Royal Holloway University of London

Doctoral Thesis

Algorithms and applications of geodynamic modelling of rapid extension processes in SE Asia

Author:
Albert de Montserrat Navarro

Supervisors:
Prof. Jason P. Morgan
Prof. Robert Hall

A thesis submitted in fulfilment of the requirements
for the degree of Doctor of Philosophy

September 2018

South East Asia Research Group
Department of Earth Sciences

Declaration

I hereby declare that except where specific reference is made to the work of others, the contents of this dissertation are original and have not been submitted in whole or in part for consideration for any other degree or qualification in this, or any other university. This dissertation is my own work and contains nothing which is the outcome of work done in collaboration with others, except as specified in the text and Acknowledgements.

Albert de Montserrat Navarro
September 2018

Acknowledgements

Firstly, I would like to acknowledge Jason P. Morgan giving me the opportunity to do this thesis, and for his guidance, support, very stimulating scientific discussions, and priceless advice during my four years at Royal Holloway. I must thank him for introducing me into a wide range of different topics and completely new for me in computational methods and geodyamics, whilst providing me the freedom to follow my own research interest during my thesis.

I would also like to acknowledge Robert Hall, who despite his initial scepticism with numerical models, made this work possible and helped me with his invaluable knowledge about SE Asia. I will always thank him for giving me the opportunities to present me research in highly stimulating scientific meetings over four different continents, and for his amazing BBQs.

I am extremely grateful with Jörg Hasenclever and Juliane Hennig-Breitfeld for their incommensurable help, contributions and rigorous review on the work done throughout my Ph.D.

Thanks to Miguel Andres Martinez, for all his help and patience during my stage of "numerical code exploration", for always letting me bother him with pointless questions, and for many conversations about how science should definitely not be done.

Thanks to Lloyd, Dom, Seb, Ben, Max, Amy, Tim, Alice and all the other members and former members of SEARG, for many moments, beers and laughs together. Extra love goes to Christof, my heart will always remember how our story started.

Thanks to my parents for their incommensurable love and support, no matter the distance. Thanks for always believe in me, I would have not reached this point of my life and become the person I am without you.

To Pau and Alba, who have been there for longer than I can recall.

Thanks all the amazing people I met in Egham during the last four years, turning this town into a surprisingly interesting place to live in. Very special thanks to Damiano, Camilla, Arnaud, Giulia, Elena, Pablo, Maria and Jorge for always being there and turning Egham into my second home. I am sure this is not the end of our journey and our paths will keep on crossing. Also, thanks to the many people I shared unforgettable moments with: Serena, Mersiye, Lucia, Amit, Rob, Harry, Nathaniel, Giacomo, George, Keiko, Francisco, Maxim, Eldert, Jorge, John P., Sandy, Raquel, Leon and Oriol. Honorific mention to Chicho Bastardo, our Lord and Saviour.

And last but not least, thanks to Silvia, for always being there, for patiently bearing with me, and for occasionally throwing electric heaters and other random furniture at me.

Abstract

The incompressible Boussinesq approximation have become a widely accepted and standardised strategy by the geodynamics community to solve the Stokes equations that describe the thermo-mechanical behaviour of Earth's interior. It is usually reasonable to assume that rocks comprising the lithosphere and mantle are (nearly) incompressible if one is focused on studying processes occurring at the uppermost part of the Earth. However, this hypothesis does not hold if attempt to compute deep mantle calculations or volumetric phase changes at lithospheric depths such as serpentinisation or melt extraction. In this thesis, I focus on the mathematical description, numerical implementation and benchmark of a fully compressible formulation of the Stokes equations so that volumetric strain can be accounted for, when necessary. Furthermore, volumetric increase rising from brittle failure is nearly always neglected. Subsequently, I have developed a visco-elasto-plastic constitutive law using an associated Drucker-Prager flow low for geodynamical processes.

Finally, I combined this tool with geochronological and geothermobarometric data to investigate the exhumation of metamorphic core complexes in Indonesia. South East Asia covers roughly the 15% of the Earth's surface and represents one of the most tectonically active regions in our planet, yet its tectonic evolution remains relatively poorly studied and understood in comparison with other heavily studied regions of the Earth. Recent episodes of extension in SE Asia have been associated with subduction initiation, sedimentary basin growth and phases of crustal melting, uplift and extremely rapid exhumation of young (< 5 Ma) metamorphic core complexes. In this Ph.D. I applied numerical tools to better comprehend some of these recent events that occurred (and many of them still ongoing) in SE Asia. Therefore, numerical models are used to better constrain the thermal conditions of the lithosphere and extension rates at which core complexes might have developed and rapidly exhumed in SE Asia. In particular, I compare available geothermobarometric data obtained from samples of the Palu Metamorphic Complex (PMC) with synthetic p-T paths computed from the numerical models.

"I am not feeling the green burning flame,
as I gaze back along footprints you have made.
I am not dreaming of more than you have shown.
You're not a foundation, you are not a stone.
But I'm afraid of the way that I'm feeling;
afraid of this new understanding now.
Afraid for the beauty within me,
and that which I hold within my hand.
And this is the ultimate secret,
that many before me have ever known.
So capture me while I am weakest;
I want to know, I want to know.
Here I am wide open, surrendering to your side.
I have laid down my armour, I have no sword at my side.
I leave behind me the ruins of the fortress I swore to defend;
I leave behind me foundations;
I'll leave you a man I'll need you to mend.
And through all the battles around me,
I never believed I would fight.
Yet here I stand, a broken soldier, shivering and naked,
in your winter light."

Footprints - Warning

Table of contents

List of figures

List of tables

1 Introduction

1.1 Plate tectonics

The dynamics of the Earth are governed by plate tectonics; in other words, the Earth is divided in a set of rigid plates whose relative motion with respect to each other is accommodated at the plate boundaries. The basics of this theory were drawn by Morgan [1968], following previous pioneering studies by Taylor [1910]; Jeffreys [1924]; Holmes [1931]; Du Toit [1937]; Wegener [1946]; Hess [1962], amongst others.

The plates are typically comprised by approximately 100 km of cool rocks, and they are classified as either oceanic or continental lithosphere. The largest fraction of the Earth's outer shell is made up of oceanic lithosphere, which is created at oceanic ridges (*divergent* plate boundaries), where two plates move away from each other. As the plates are pulled apart, hot and buoyant mantle rocks are up-welled towards the surface to fill the gap left by the divergent motion. These mantle rocks are cooled by conductive heating as they are exhumed at the spreading centre, and new oceanic lithosphere is created. As the new lithosphere moves away from the oceanic ridge, it furthers cools and thickens. Estimation of the composition of newly accreted oceanic lithosphere is an extremely challenging task from economical and technological points of view because it is covered by several kilometres of sea water. However, it is possible to study the composition of slices of oceanic lithosphere that have been uplifted and brought to the surface. These rock formations are known as *ophiolites* and are found in, for example, Oman, Cyprus, New Guinea, New Zealand and Newfoundland. Their study has revealed that oceanic lithosphere is composed by a thin layer (4-8 km), known as *oceanic crust*, of basaltic and gabroic rocks, usually covered by sediments (from a few hundred metres to a few kilometres), and underlain by mantle rocks, typically referred as *peridotites*. The oceanic crust and the cold mantle rocks are separated by the so-called Mohorovičić or *Moho* discontinuity. Since the volume of lithospheric material has to be more or less constant over time, oceanic lithosphere is cycled back to the deep mantle at subduction zones (*convergent* plate boundaries); thus the age of ocean floor available at the Earth's surface is relatively young in geological time-scales, and very rarely exceeds 200 Ma (Fig. 1.1).

On the other hand, the composition of continental plates is mainly silicic, and the main hypothesis is that a vast portion of them was created during the early stages of the Earth's history by large amounts of melt extraction. New material is accreted into the continental lithosphere by mechanisms such as intraplate volcanism or accretion at subduction zones. Since the continental material is less dense than the oceanic lithosphere, it is gravitationally stable and cannot be cycled back to the mantle by subduction processes. Mechanisms that can consume continental lithosphere and bring it back to the deep mantle are delamination of its base, and subduction of continental sediments at subduction zones.

While the composition of the uppermost section of the continental crust is accessible and relatively easy to estimate, it remains challenging to estimate the composition of the lower crust. Nonetheless, direct evidence of its composition can be obtained from mineralogical and geochemical analyses of xenolith

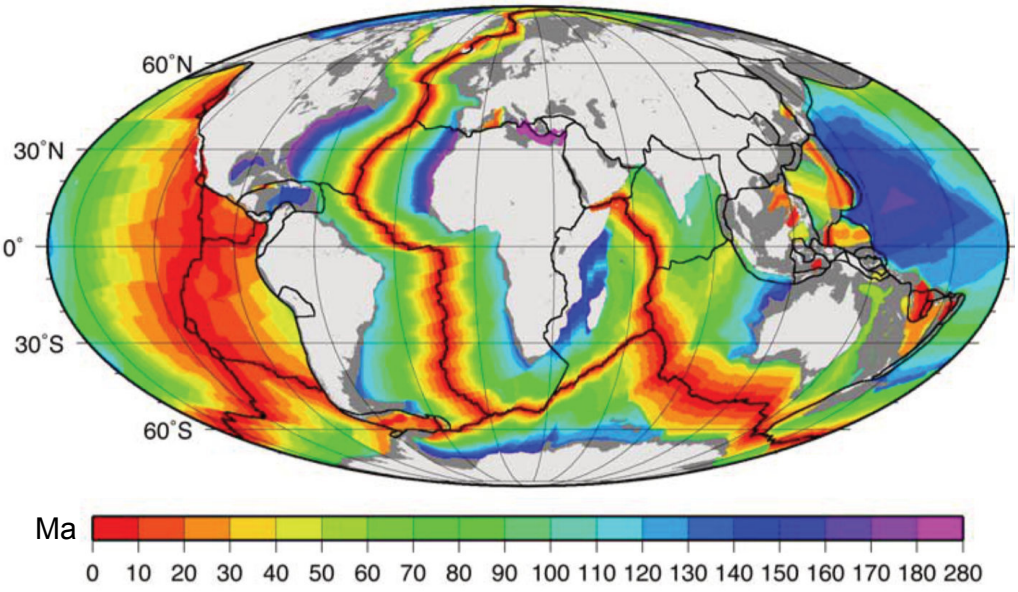

Fig. 1.1 *Oceanic floor age. From Müller et al. [2008].*

samples brought to the surface at continental volcanic centres, and from exhumed high-grade metamorphic rocks. The latter can be found in, for example, the so-called Metamorphic Core Complexes (MCCs). These are dome-shape structures comprised of metamorphosed and -frequently- partially molten mid-to-lower crust that are exhumed along a low-angle normal fault (Whitney et al. [2013] and references therein). Despite being described first in continental plates [Coney, 1974; Lister and Davis, 1989], MCCs have also been identified in oceanic plates along oceanic ridges [e.g. Cann et al., 1997; Ranero and Reston, 1999] (Fig. 1.2). Another important fraction of information of the lower crust composition is inferred from indirect measurements, as for example, the speed of elastic waves travelling through the crust [e.g Miller and Christensen, 1994; Sobolev and Babeyko, 1994; Kern et al., 1996; Musacchio et al., 1997].

1.2 Computer modelling of the Earth's dynamics

Direct observation of many geological processes, including the ones mentioned above, is often not possible or, in the best case, it is extremely difficult and expensive. Fortunately, highly valuable information of these processes can be inferred from indirect observations derived from geophysical and numerical studies. The rapid technological development produced in the last decades has made possible the proliferation of numerical models aiming at studying the dynamics of the Earth's, from the microscale to the macroscale. In spite of being simplified (quite often oversimplified) representations of thermal, mechanical and/or chemical processes, numerical models allow us to test a wide range of hypothesis at an almost insignificant economical cost, while still providing a large volume of invaluable information.

The motion and heat transfer of Earth's interior is described by the Stokes equation and the equation of conservation of energy, which comprise a set of Partial Derivative Equations (PDEs). Analytical solutions of PDEs usually exist only under specific geometry and boundary conditions, which are not representative of the bulk of geologic processes. Hence, these equations must be approximated using different numerical techniques such as the Finite Element Method (FEM) or Finite Differences (FE), which are two of the most widespread methods to tackle geodynamic problems.

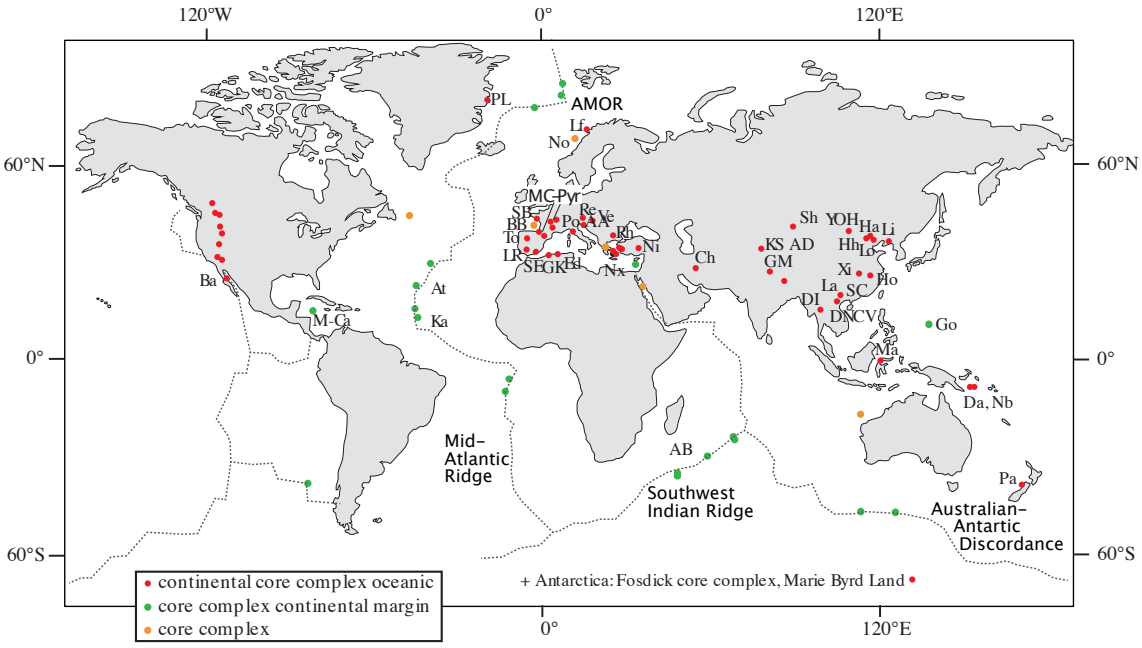

Fig. 1.2 *Map of the world showing the locations of some Phanerozoic core complexes in the continents and oceans. Key to abbreviations: AA-Alpi Apuane (Italy); AB-Atlantis Bank (SW Indian Ridge); AD-Ama Drime (Nepal); AMOR-Arctic segment of Mid-Atlantic Ridge; At-Atlantis Massif (Mid-Atlantic Ridge); Ba-Baja (Mexico); BB-Bay of Biscay; Ch-Chapedony (Iran); Da-Dayman (Papua New Guinea); DI-Doi Inthanon (Thailand); DNCV-Day Nui Con Voi (Vietnam); Ed-Edough (Algeria); GK-Grand Kabilye (Algeria); GM-Gurla Mandhata (Pamirs); Go-Godzilla; Ha-Harkin (China/Mongolia); Hh-Hohhot (China); Ho-Hongzhen (China); Ka-Kane (Mid-Atlantic Ridge); KS-Kongur Shan (Pamirs); La-Laojunshan (China); Lf-Lofoten (Norway); Li-Liaodong Peninsula (China); Ma-Malino (Indonesia); Lo-Louzidian (China); LR-Lora del Rio (Spain); M-Ca-Mid-Cayman spreading center; MC-Pyr-Massif Central (France–Pyrenees, France, Spain; includes Montagne-Noire); Nb-Normanby Island (Papua New Guinea); Ni-Niğde (Turkey); No-Norway rifted continental margin; Nx-Naxos (Greece); Pa-Paparoa (New Zealand); PL- Payer Land (Greenland); Po-Pohorje Mountains (Slovenia); Re-Rechnitz (Austria); Rh-Rhodope (Greece, Bulgaria); SB-southern Brittany (France); SC-Song Chay (China); Sh-Shaerdelan (China); SE-Sierra de las Estancias (Spain); To-Tormes (Spain); Ve- Veporic (Slovenia); Xi-Xiaoqinling (China); YOH-Yagan-Onch-Hayrhan (China/Mongolia). From Whitney et al. [2013].*

Even though the propagation of seismic waves has proven the solid state of the lithosphere and the mantle, these rheological layers behave as a viscous flow at extremely low velocities, as inferred from Global Isostasy Adjustment (GIA) studies [e.g. Peltier, 1996; Forte and Mitrovica, 1996; Mitrovica and Forte, 2004; van der Wal et al., 2015]. However, unlike hot and ductile mantle rocks, cold lithospheric material is able to release and dissipate stored elastic energy upon brittle failure, which manifests as heat release, faults, and earthquakes. This bimodal behaviour is frequently described by the mathematical model of a Maxwell body with a visco-elastic rheology, where the total strain is assumed to be the sum of its elastic and inelastic components. The mechanical response of the rocks is then defined by the so-called *constitutive equation*, which states the relationship between stress and strain for a given material. In a visco-elastic material, the dynamic viscosity is the physical parameters that controls the viscous response to applied forces, whereas the shear modulus controls the response of the elastic strain. Furthermore, the mantle and lithosphere are often treated as a *non-Newtonian* fluid, meaning that the viscosity strongly depends on temperature, compositional changes and applied stress; however, the stress dependency is sometimes omitted for computational reasons (frequently in 3D computations), and then the fluid is known as *Newtonian*. On the other hand, the shear modulus is usually considered a constant parameter that depends on the material. Nonetheless, the 'bulk' shear modulus of a rock is not strictly constant, and it will degrade if microscopic and macroscopic fractures propagate.

Several hypothesis are often considered in order to simplify the Stokes equations to make them more computationally stable and effective. First, the inertial forces are not considered. While this hypothesis holds for most tectonic processes due to extremely slow motions, it breaks if one wishes to study the propagation of elastic waves (i.e. earthquakes). Another common hypothesis is to assume that the mantle and lithosphere can be treated as (near-)incompressible bodies. This simplifies the problem, as the density becomes independent of the pressure and reduces the non-linear degree of the equations; incompressibility is incorporated by adopting the Boussinesq approximation. This approximation is suitable for many of the tectonic processes involving mantle-lithosphere deformation [e.g. Gerya and Yuen, 2007; Huismans and Beaumont, 2007; Buiter et al., 2006; Rey et al., 2009b; Huet et al., 2011; Schenker et al., 2012; Brune et al., 2012; Taramón et al., 2015; Tetreault and Buiter, 2017; Ros et al., 2017]; however, the Boussinesq approximation becomes inaccurate if density variations are larger than 10%. Deep mantle calculations are an example where the incompressibility approximation is no longer valid as the density changes exceed the accuracy threshold (density is roughly 60% higher at the core-mantle boundary) due to the enormous pressures at which rocks are subject. Moreover, a high compressibility will affect the viscous dissipation and adiabatic heating, thus swaying the thermal structure.

Compressibility was first introduced by the so-called *anelastic approximation* [Jarvis and McKenzie, 1980] to study deep mantle convection. This approach is based on the hypothesis that the dynamic pressure is very small compared to the lithostatic pressure and this allows the density to change as a function of depth, but not with time. Compressibility has been further studied [e.g. Glatzmaier, 1988; Schmeling, 1989; Bercovici et al., 1992; Tackley, 1996; King et al., 2010] in mantle convection calculations either using the anelastic approximation or its variants, such as the *truncated anelastic approximation*. However, if volumetric strain linked to phase changes is considered, the density rate might become non-negligible and the latter hypothesis breaks. Anyhow, the incompressible Boussinesq approximation prevails as the preferred hypothesis employed to reduce the degree of complexity of the Stokes equations.

1.3 Aims

The aims of this Ph.D thesis are to develop a numerical tool able to handle a general formulation in 2D of the compressible Stokes equations for a viscous flow, in order to study the effects of geological processes where volume changes and compressibility should not be overlooked. For completeness and consistency, the constitutive law is expanded so that volume changes raising from plastic deformation are also accounted for.

In parallel to the development of the new numerical tools mentioned above, numerical models are used to help to unravel the tectonic history behind the rapid exhumation and high cooling rates observed in the Palu Metamorphic Complex (PMC), one of the youngest MCCs on Earth (< 5 Ma), located in Sulawesi, Indonesia (Fig. 1.3). The PMC has been chosen as the case of study due to the possibility of comparing the numerical results with newly available geothermobarometric from rock samples coming from the PMC [Hennig et al., 2017].

1.4 Thesis outline

This thesis is divided in 7 chapters. Chapter 2 describes the methodology used in this thesis, which includes a brief description of the Finite Element Method, followed by the description and numerical implementation of the equations governing the thermo-mechanical evolution of tectonic processes. The core of this work is

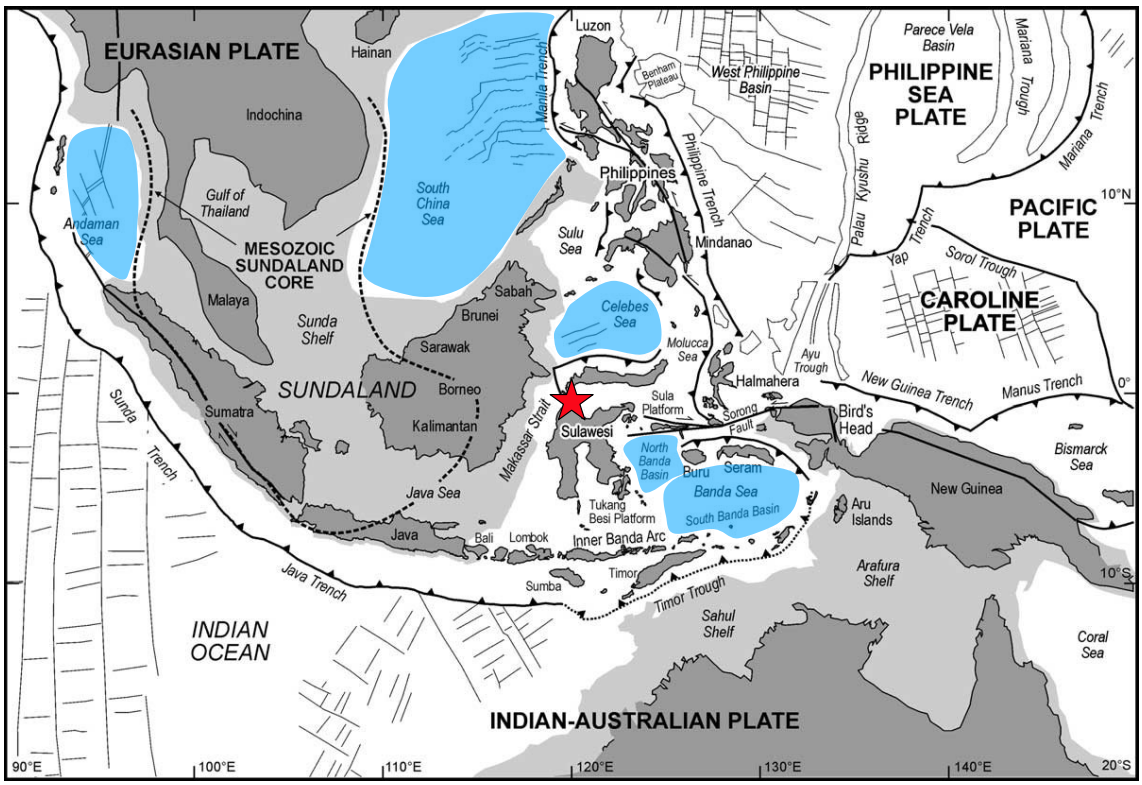

Fig. 1.3 *Geographical map showing the main geological features in SE Asia. Regions where sea-floor spreading occurred are delimited buy the shaded blue areas and the red star marks the location of the Palu Metamorphic Complex. Modified after Hall [2002].*

composed by three journal publications or manuscript drafts to be submitted into scientific journals in the near future.

Large amount of the Ph.D. focuses on the development and implementation of a general compressible formulation of the Stokes equations that accounts for volumetric strain due pressures changes and also to phase changes, such as serpentinisation and melt extraction. The description of compressible formulation and the numerical strategies to solve the resulting set of PDEs are presented in Chapter 3. A set of numerical experiments designed to validate its correct implementation is also included. This chapter consists of a manuscript draft for submission in *Geochemistry, Geophysics, Geosystems*.

While Chapter 3 focuses on solving the compressible equations governing the motion of a visco-elastic Maxwell body, the numerical model is extended in Chapter 4 by introducing a visco-elasto-plastic constitutive equation able to handle the fully non-associated (non-dilatant) and associated (dilatant) plastic limits. First, the formulation of the new constitutive law is described. Second, the results of shear band initiation obtained with this formulation are compared with other published numerical and analytical studies. And at last, the implications of plastic dilation are further extended to an example of large scale tectonic process; in this case I consider rifting of continental crust with different crustal strengths. This chapter consists of a manuscript draft for later publication in *Tectonophysics*.

In Chapter 5, numerical modelling is applied to a geological case. The Palu Metamorphic Complex (Sulawesi, Indonesia) developed and exhumed in very recent geological times (< c. 5 Ma) at rates much higher than previously known for other continental metamorphic complexes. In this chapter I investigate the conditions at which MCCs are exhumed so rapidly. I do so by comparing synthetic cooling paths computed by numerical

models against published geochronological and thermobarometric data from Hennig et al. [2017]. This chapter consists of a manuscript currently under review in *Earth and Planetary Science Letters.*

In Chapter 6 I discuss the methods and results illustrated in this thesis, and the final conclusions are drawn in Chapter 7.

2 | Numerical methods

Due to the large time and length scales of geological process, deformation of Earth's interior is often approximated by the Stokes equations that describe the thermo-mechanical behaviour of a viscous flow. The solvability of this set of partial derivative equations (PDEs) is not trivial, and requires of complex numerical techniques. All the PDEs found in this thesis are solved using the *Finite Element Method* (FEM), and implemented in the MATLAB-based code LaCoDe for bidimensional problems. FEM is a powerful and highly versatile numerical tool to approximate the continuum solution of PDEs with complex geometries and boundary conditions, and it is widely employed in engineering and other fields. The FEM is based on subdividing the domain where any given PDE needs to be solved into a set of smaller discrete regions, the so-called *elements*. The equations are first defined locally in the elements, and then they are assembled into a global system of equations where the contributions of each element are accounted for. Other numerical methods are commonly used to approximate numerically the PDEs that describe different physical processes, such as *Finite Differences Method* (FDM), *Finite Volumes Method* (FVM), *Extended Finite Element Method* (X-FEM) or *Discrete Elements Method* (DEM), but are not be considered nor discussed in this project.

In this chapter I present a description and applicability of the Lagrangian FEM to solve the Stokes equations for a visco-elasto-plastic body and other physical processes implemented in LaCoDe. A brief description of the FEM is presented in Appendix A.1, and the reader is referred to Zienkiewicz [1985]; Hughes [1987]; Bathe [2006] for a more in-depth description of the FEM.

2.1 Stokes equations: incompressible Boussinesq approximation

The general Stokes equations are defined by the coupling of the equations of conservation of momentum, conservation of energy and conservation of mass. In the following sections I will describe these equations and its numerical implementation using the FEM. Large part of this project focuses on developing a code to solve the motion of compressible visco-elastic flows. The mathematical description, numerical implementation and benchmarking of such formulation is given in Chapter 3. However, some of the models presented in this thesis (i.e. Chapter 5) employ the incompressible Boussinesq approximation. This approximation states that the flow is (nearly) incompressible and density variations only intervene in the buoyancy forces. Under this assumption, small density changes due to, for example, thermal expansion and contraction are permitted. However, the Boussinesq approximation becomes inaccurate if these density changes are $\Delta\rho/\rho > 0.1$.

In this section I present the standard mathematical formulation of an viscous flow employing the Boussinesq incompressible approximation, and the numerical implementation using the FEM. For further details in the mathematical description and numerical solutions, the reader is referred to e.g. Hughes [1987]; Donea and Huerta [2003]; Zienkiewicz and Taylor [2005]. First, the equation of conservation of energy that determines

the diffusion and advection of the temperature field is described. Then I proceed to describe the equation of conservation of momentum and conservation of mass.

2.1.1 Thermal diffusion

The time dependent equation of heat advection and diffusion with and external source of heat (or heat consumption) for an incompressible material is described by the strong form the equation of conservation of energy:

$$\rho C_p \frac{\partial T}{\partial t} + \mathbf{u}\nabla T = \kappa \nabla^2 T + Q \tag{2.1}$$

or casting out for the x and z axis:

$$\rho C_p \frac{\partial T}{\partial t} + u_x T_{,x} + u_z T_{,z} = \kappa (T_{,xx} + T_{,zz}) + Q \tag{2.2}$$

where ρ is the density, C_p is the heat capacity, T is temperature, κ is thermal conductivity and $\nabla = e_i \partial / \partial x_i$ is the nabla operator, where e_i is the standard basis. The source term Q can be positive (i.e heat generated by, for example, radiogenic decay or inelastic work) or negative (e.g. latent heat cooling during melting). In the incompressible approximation of a viscous flow we consider two sources of heat that are included in Q: 1) heat produced by radiogenic decay and 2) shear heating, which is produced by inelastic (i.e. viscous and plastic) work and it is defined as $H_{sh} = \tau_{ij}\dot{\varepsilon}_{ij}^{inel} = \tau_{ij}\left(\dot{\varepsilon}_{ij}^{viscous} + \dot{\varepsilon}_{ij}^{plastic}\right)$. It must be noted that eq. (2.2) describes the advection and diffusion of heat under an Eulerian frame of reference. Under a Lagrangian frame of reference, the advection part is done by updating the nodal positions accordingly to the velocity field, and only the diffusion terms are solved numerically, thus the advection term $\mathbf{u}\nabla T$ vanishes and the partial time derivative is equivalent to the material time derivative (i.e. $\partial(\cdot)/\partial t = D(\cdot)/Dt$), see Section 2.2 for more details. The numerical Lagrangian formulation and implementation of eq. (2.2) is described in the following subsection.

Numerical implementation

The Lagrangian time-dependent diffusion equation in a domain Ω is defined by the following boundary problem:

$$\rho C_p \frac{DT}{Dt} = \kappa \nabla^2 T + Q \tag{2.3}$$

with the boundary conditions

$$T = g \qquad \text{on } \Gamma_D \tag{2.4}$$

$$-\mathbf{n}\kappa T = q \qquad \text{on } \Gamma_N \tag{2.5}$$

where n is the unit outward normal vector to the boundary Γ and q is the heat flux. The derivation of the weak formulations of the equation of heat diffusion can be found in Appendix A.2.1 and reads as follows:

$$\int_\Omega \mathbf{N}\rho C_p \frac{D(\mathbf{N}\widetilde{T})}{Dt} d\Omega + \int_\Omega (\nabla \mathbf{N}^T)\kappa(\nabla N\widetilde{T}) d\Omega = \int_\Omega \mathbf{N} Q d\Omega - \int_{\Gamma_N} \mathbf{N} q d\Gamma_N \tag{2.6}$$

or in a compact matrix form (and dropping the wide tilde over T for more clarity):

$$\mathbf{M}\frac{DT}{Dt} + \mathbf{K}T = \mathbf{f} \tag{2.7}$$

where $\mathbf{M}$ is the mass matrix and $\mathbf{K}$ is the conductivity matrix:

$$\mathbf{M} = \int_{\Omega} \mathbf{N}^T \mathbf{N} \, d\Omega \tag{2.8}$$

$$\mathbf{K} = \int_{\Omega} \nabla^T \mathbf{N}^T \kappa \nabla \mathbf{N} d\Omega \tag{2.9}$$

$$\mathbf{f} = \int_{\Omega} \mathbf{N} \, Q d\Omega - \int_{\Gamma_N} \mathbf{N} q d\Gamma_N \tag{2.10}$$

The Galerkin method approximates the spatial dependency of the problem; however, eq. (2.7) is also time dependent equation as the mass matrix is multiplied by the time derivative of the temperature. In theory, it is possible to further use the FEM to perform the time discretisation; however, using a finite differences approach to compute the time derivatives is a common strategy due to its efficiency and simple implementation. The time derivatives are then approximated as follows:

$$\mathbf{M}\frac{DT^{n+\alpha}}{Dt} + \mathbf{K}T^{n+1} = \mathbf{f}^{n+1} \tag{2.11}$$

$$T^{n+1} = T^n + \Delta t \frac{DT^{n+\alpha}}{Dt} \tag{2.12}$$

$$\frac{DT^{n+\alpha}}{Dt} = (1-\alpha)\frac{DT^n}{Dt} + \frac{DT^{n+1}}{Dt} \tag{2.13}$$

Subscript n indicates time at t_n and $n+1$ indicates time at $t_n + \Delta t$, and Δt is the time step. Using this scheme, we obtain the following system of linear equations:

$$(\mathbf{M} + \alpha \Delta t \mathbf{K})T^{n+1} = (M - (1-\alpha)\Delta t \mathbf{K})T^n + \Delta t(\alpha \mathbf{f}^{n+1} + (1-\alpha)\mathbf{f}^n) \tag{2.14}$$

or as a more condensed expression:

$$\mathbf{K}^\star T = \mathbf{f}^\star \tag{2.15}$$

This scheme is part of the generalized trapezoidal family of methods and a more detailed description can be found in Chapter 8 of Hughes [1987]. Depending on the value of α eq. (2.14) yields to different methods of the so-called trapezoidal family: if $\alpha = 0$ it describes the forward Euler method; $\alpha = 0.5$ describes the Crank-Nicolson method; and $\alpha = 1$ describes the backward Euler method. The backward Euler method is used in all the models discussed in this thesis, unless other method is specified, because the solution depends on T and DT/Dt at $t = t_{n+1}$ and is unconditionally stable. On the other hand, the forward Euler method usually requires very small time steps to yield accurate solutions.

2.1.2 Conservation of momentum and conservation of mass

The deformation of a incompressible viscous flow is described by the coupling of the equation conservation of momentum and conservation of mass:

$$\sigma_{ij,j} = -\rho g_i \tag{2.16}$$

$$u_{i,i} = 0 \tag{2.17}$$

where σ_{ij} is the Cauchy stress tensor, and g_i is the gravitational acceleration. It should be noted that the acceleration in mantle-lithosphere processes is negligible, thus eq. (2.16) describes the conservation of momentum of an inertia-free system. It is convenient to split the Cauchy stress tensor into its deviatoric (shear component that deforms the fluid) and hydrostatic (pressure in equilibrium that does not disturb the

fluid) components:

$$\sigma_{ij} = \tau_{ij} - p\delta_{ij} \tag{2.18}$$

where τ_{ij} is the deviatoric stress tensor, δ_{ij} is the Kroenecker delta, and the pressure p is the mean of the principal stresses:

$$p = -\frac{1}{3}\sigma_{kk} \tag{2.19}$$

Substituting eq. (2.16) into eq. (2.18), the conservation of momentum yields:

$$\tau_{ij,j} - p_{,j} = \rho g_i \tag{2.20}$$

The general relationship between the stress and the deformation is given by:

$$\sigma_{ij} = \mathscr{C}_{ijkl}\dot{\varepsilon}_{ij} \tag{2.21}$$

where $\mathscr{C}_{ijkl}$ is a 4th rank tensor that includes the material properties, and $\dot{\varepsilon}_{ij}$ is the strain tensor, defined as:

$$\dot{\varepsilon}_{ij} = \frac{1}{2}\left(u_{i,j} + u_{j,i}\right) \tag{2.22}$$

Due to the symmetry of its components, the constitutive law of a viscous flow in (2.21) is reduced to:

$$\sigma_{ij} = 2\eta_s\left(\dot{\varepsilon}_{ij} - \frac{1}{3}\dot{\varepsilon}_{kk}\delta_{ij}\right) + \eta_b\dot{\varepsilon}_{kk}\delta_{ij} - p\delta_{ij} \tag{2.23}$$

where η_s is the shear viscosity, that accounts for the resistance of the material to shear strain rates and the bulk viscosity η_b determines the resistance of the fluid to compressive deformation. Therefore, the first term in eq. (2.23) describes the stresses caused by shear deformation, and the second term accounts for volumetric deformation due to normal stresses. We neglect the effects volumetric resulting from the bulk viscosity, thus the second term of the right-hand-side in eq. (2.23) vanishes:

$$\sigma_{ij} = \overbrace{2\eta\dot{\varepsilon}'_{ij}}^{\tau_{ij}} - p\delta_{ij} \tag{2.24}$$

where $\dot{\varepsilon}'_{ij} = \dot{\varepsilon}_{ij} - \frac{1}{3}\dot{\varepsilon}_{kk}\delta_{ij}$ is the deviatoric strain rate tensor. To simplify the notation, the subindex s of the shear viscosity will be dropped from now onwards, hence $\eta_s = \eta$. The incompressibility of the flow is mathematically described by a divergence-free velocity field:

$$\dot{\varepsilon}_{ii} = 0 \tag{2.25}$$

This means that the inflow into an infinitesimal volume is equal to the outflow, and therefore, the volume is preserved. Eq. (2.25) will be referred as the *incompressible constraint*. Given the expressions described above, a Stokes flow boundary problem in n dimensions is defined by the following set of coupled equations in the domain Ω:

$$\tau_{ij,j} - p_{,j} = \rho g_i \tag{2.26}$$

$$u_{i,i} = 0 \tag{2.27}$$

and the boundary conditions

$$u_i = h_i \qquad \text{on } \Gamma_D \tag{2.28}$$

$$\sigma_{ij} n_j = t_i \qquad \text{on } \Gamma_N \tag{2.29}$$

Now we can substitute eq. (2.24) in eq. (2.26) and obtain the following expressions for the x axis:

$$2\eta_{eff}\left(\dot{\varepsilon}_{xx} - \frac{1}{3}\dot{\varepsilon}_{kk}\delta_{ij}\right)_{,x} + \left(2\eta_{eff}\dot{\varepsilon}_{xz}\right)_{,z} - p_{,x} = 0 \tag{2.30}$$

and for the z axis:

$$2\eta_{eff}\left(\dot{\varepsilon}_{zz} - \frac{1}{3}\dot{\varepsilon}_{kk}\delta_{ij}\right)_{,z} + \left(2\eta_{eff}\dot{\varepsilon}_{zx}\right)_{,x} - p_{,z} = -\rho g_z \tag{2.31}$$

Using the definition of the strain tensor we obtain the strong forms of the conservation of momentum:

$$\eta_{eff}\left(\frac{4}{3}u_{x,x} - \frac{2}{3}u_{z,z}\right)_{,x} + \eta_{eff}\left(u_{x,z} + u_{z,x}\right)_{,z} - p_{,x} = 0 \tag{2.32}$$

for the x axis. And:

$$\eta_{eff}\left(\frac{4}{3}u_{z,z} - \frac{2}{3}u_{x,x}\right)_{,z} + \eta_{eff}\left(u_{x,z} + u_{z,x}\right)_{,z} - p_{,z} = -\rho g_z \tag{2.33}$$

for the z axis. Eqs.(2.32) and (2.33) are then transformed into weak form and solved using the FEM. The reader is referred to Appendix (A.2.2) or Chapter 3 for the derivation of the Stokes equations for a incompressible and compressible visco-elastic flow, respectively.

2.1.3 Numerical implementation

The resulting set of governing equations of the problem is solved numerically using the FEM to generate a system of linear equations. The governing equations (2.16) and (2.17) are transformed into their weak forms with help of the trial solutions and weighting functions employing the Galerkin approximatin (see Appendix A.2.2), reading:

$$\int_\Omega \mathbf{B}^T \mathbf{D}\mathbf{B}\widetilde{\mathbf{u}} d\Omega - \int_\Omega \mathbf{B}^T \mathbf{m}\mathbf{N}_p \widetilde{\mathbf{p}} d\Omega = \int_\Omega \mathbf{N}_u^T \left(\rho\mathbf{g} + \mathbf{B}\chi\widehat{\tau}\right) d\Omega \tag{2.34}$$

$$-\int_\Omega \mathbf{N}_p^T \mathbf{m}^T \mathbf{B}\widetilde{\mathbf{u}} d\Omega = 0 \tag{2.35}$$

where the elemental matrix $\mathbf{B}^e$ represents the strain-displacement matrix, and $\mathbf{D}^e$ is the rheology matrix that relates strain rates to deviatoric stresses:

$$\mathbf{B}^e\widetilde{\mathbf{u}}^e = \begin{bmatrix} \frac{\partial N_u}{\partial x} & 0 \\ 0 & \frac{\partial N_u}{\partial z} \\ \frac{\partial N_u}{\partial z} & \frac{\partial N_u}{\partial x} \end{bmatrix} \begin{bmatrix} u_x \\ u_z \end{bmatrix} = \begin{bmatrix} \dot{\varepsilon}_{xx} \\ \dot{\varepsilon}_{zz} \\ \dot{\varepsilon}_{xz} \end{bmatrix} \tag{2.36}$$

$$\mathbf{D}^e = \eta_{eff} \begin{bmatrix} C_1 & C_2 & 0 \\ C_2 & C_1 & 0 \\ 0 & 0 & 1 \end{bmatrix} \tag{2.37}$$

and

$$\mathbf{m}^T = [1 \quad 1 \quad 0] \tag{2.38}$$

and the coefficients in D take the values $C_1 = 4/3$ and $C_2 = -2/3$. The system of equations (2.34) and (2.35) can be conveniently written in block matrix form as:

$$\begin{pmatrix} \mathbf{A} & \mathbf{Q} \\ \mathbf{Q}^T & \mathbf{0} \end{pmatrix} \cdot \begin{pmatrix} \widetilde{\mathbf{u}} \\ \widetilde{\mathbf{p}} \end{pmatrix} = \begin{pmatrix} \mathbf{f} \\ 0 \end{pmatrix} \tag{2.39}$$

Solution scheme

Numerical complications arise due to the presence of the diagonal zeros in the full matrix eq. (2.39). A widespread method to tackle this issue consists in using the following modified continuity equation:

$$\nabla \cdot \mathbf{u} = \frac{p}{\lambda} \tag{2.40}$$

where λ is a mesh- and problem-independent parameter, commonly referred as penalty parameter. It becomes evident that $p/\lambda \to 0$ for large values of λ, and incompressibility is recovered. This so-called *penalty method* has been widely used in incompressible flow problems and a detailed description can be found in, for example, Hughes [1987]; Donea and Huerta [2003] and references therein. Introducing the penalty term in the systems of equations (A.22) yields:

$$\begin{pmatrix} \mathbf{A} & \mathbf{Q} \\ \mathbf{Q}^T & -\frac{1}{\lambda}\mathbf{M} \end{pmatrix} \cdot \begin{pmatrix} \widetilde{\mathbf{u}} \\ \widetilde{\mathbf{p}} \end{pmatrix} = \begin{pmatrix} \mathbf{f} \\ 0 \end{pmatrix} \tag{2.41}$$

where $\mathbf{M}$ is the so-called mass matrix:

$$\mathbf{M} = \int_\Omega \mathbf{N}_P^T \mathbf{N}_P d\Omega \tag{2.42}$$

The choice of the penalty number λ is not a trivial decision. A low value of λ will not ensure near-incompressibility and it will introduce errors in the pressure field. On the other hand, λ has to be large enough so that it ensures the near-incompressibility of the flow, but the constrain term p/λ may dominate the system and result in a zero-velocity field if λ is excessively high. This phenomenon is often referred as *numerical locking* or *mesh locking*, and this occurs if there are too many incompressibility constrains compared to velocity unknowns. Locking is avoided by choosing elements that satisfy the so-called LBB (or inf-sup) condition. This condition states that not all the couples of the velocity and pressure functional spaces are stable. The mathematics behind the LBB condition are out of the scope of this thesis and more details can be found in Hughes [1987]; Donea and Huerta [2003], and references therein. For incompressible flow Zienkiewicz and Taylor [2005] recommends to use $\lambda = c\eta$, with $10^7 < c < 10^{10}$, for double precision computations.

There are different possible combinations of velocity-pressure functional spaces satisfying the LBB condition; some of the most popular choices for two-dimensional elements are shown in Fig. 2.1. LaCoDe uses Crouzeix-Raviart triangular elements, where the velocity field is approximated by seven nodal points and quadratic interpolation enhanced by a cubic bubble function in the baricenter of the element. Pressure is discontinuous with three nodal points and a linear interpolation [Crouzeix and Raviart, 1973].

Locking can be alternatively avoided by under-integration of the penalty terms [Malkus and Hughes, 1978]. This method consists in using fewer integration points to calculate the numerical integrals that construct the element matrices than the number of integrations points required to exactly evaluate the integral. This results

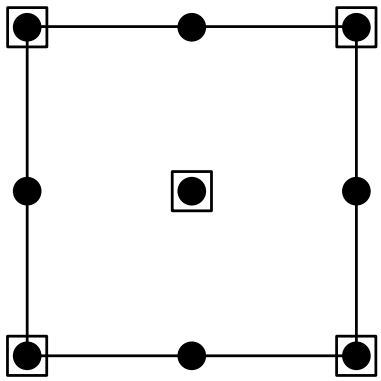

Q2Q1 (or Taylod-Hood) element:

Continuous biquadratic velocity

Continuous bilinear pressure

Quadratic convergence

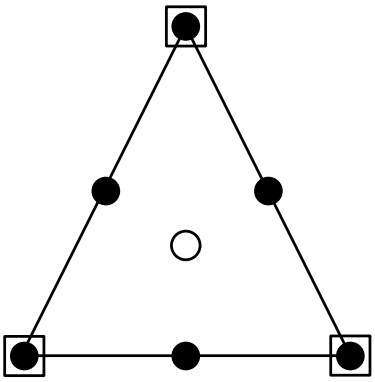

Crouzeix-Raviart element:

Continuous quadratic + cubic bubble function velocity

Discontinuous linear pressure

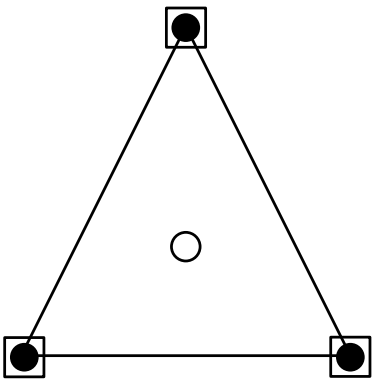

Mini element:

Continuous linear + cubic bubble function velocity

Continuous linear pressure

Pressure node Velocity node Bubble function node

Fig. 2.1 *Examples of combinations of velocity and pressure spaces that satisfy the LBB condition [Donea and Huerta, 2003].*

in a less accurate and lower order integral. By using a lower order integration scheme for the penalty term, the number of incompressibility constrains is effectively reduced.

High values of λ lead to a poorly conditioned stiffness matrix, which hinders its solvability with iterative schemes. Therefore, a lower value of λ is used in combination with a Powell-Hestenes iterative scheme [Powell, 1967; Hestenes, 1969]:

1. Choose $\widetilde{\mathbf{p}}^0 = 0$.

2. Solve the velocity field:

$$\widetilde{\mathbf{u}}^{k+1} = \left(\mathbf{A} + \lambda \mathbf{Q}\mathbf{M}^{-1}\mathbf{Q}^T - \mathbf{Q}\widetilde{\mathbf{p}}^k\right)^{-1} \mathbf{f} \tag{2.43}$$

3. Calculate pressure correction:

$$\Delta\widetilde{\mathbf{p}} = \lambda \mathbf{M}^{-1}\mathbf{Q}^T\widetilde{\mathbf{u}}^{k+1} \tag{2.44}$$

4. Update pressure:

$$\widetilde{\mathbf{p}}^{k+1} = \widetilde{\mathbf{p}}^k + \Delta\widetilde{\mathbf{p}} \tag{2.45}$$

5. Repeat steps 2-4 until $\Delta p < Tol$.

This algorithm enforces the incompressibility of the flow by correcting and updating the pressure field and the resulting forces. This solution scheme for the incompressible Stokes equations can also be understood as Augmented Lagrangian method, where the second row of the system of eqs. (2.41) is augmented by subtracting $\lambda^{-1}\mathbf{M}\widetilde{\mathbf{p}}$ and adding the following iterative scheme:

$$\begin{pmatrix} \mathbf{A} & \mathbf{Q} \\ \mathbf{Q}^T & -\frac{1}{\lambda}\mathbf{M} \end{pmatrix} \cdot \begin{pmatrix} \widetilde{\mathbf{u}} \\ \widetilde{\mathbf{p}} \end{pmatrix}^{k+1} = \begin{pmatrix} \mathbf{g}_1 \\ -\frac{1}{\lambda}\mathbf{M}\widetilde{\mathbf{p}}^k \end{pmatrix} \tag{2.46}$$

Upon convergence $\mathbf{M}\widetilde{\mathbf{p}}^{k+1} = \mathbf{M}\widetilde{\mathbf{p}}^k$ and the incompressibility constraint is satisfied.

2.1.4 Non-linear rheologies

The Stokes equations described in the previous section describe the thermo-mechanical behaviour of a linear visocous (or visco-elastic) flow. However, the deformation of tectonic evenets is better characterised by rheological laws such as diffussion creep, dislocation creep and/or plastic failure. These mechanisms depend on variables such as strain rate, temperature, pressure or differential stress, thus introducing different degrees of non-linearities into the Stokes equations. In this section, I present the mathematical description, implementation and solution scheme for these non-linear rheological laws. The plasticity presented in this chapter correspond to a non-dilatant formulation using the Prandtl-Reus flow law. The formulation of a dilatant plasticity is presented in Chapter 4.

Viscous creep

Two mechanisms for viscous deformation are included in the model: diffusion creep and dislocation creep [Poirier, 1985; Karato et al., 2001]. Diffusion creep occurs at low stress levels, when atoms diffuse through inside the crystal grains and along the grain boundaries, causing deformation of the rock. Deformation due to dislocation creep is caused by the migration of dislocations through the crystal lattice of the rock. Both creep mechanisms are strain rate-, temperature- and pressure- dependent:

$$\dot{\varepsilon} = A\sigma_d^n \exp\left(\frac{E_a + pV_a}{nRT}\right) \tag{2.47}$$

where A is the pre-exponential parameter, E_a is the activation energy, V_a is the activation volume and R is the universal gas constant. The pre-exponential parameter $A = Bd^{-m} f_{H_2O}^r \exp(\alpha\phi)$ takes in consideration the

Table 2.1 *Mechanical parameters for dislocation and diffusion creep.*

Rheology	Creep	log_{10}(A) ($Pa^{-n}s^{-1}$)	n	E ($kJmol^{-1}$)	Reference
Wet quartzite	Dislocation	-28	4.0	223	Gleason and Tullis [1995]
Mafic granulite	Dislocation	-21.05	4.2	445	Gleason and Tullis [1995]
Dry olivine	Dislocation	-15.56	3.5	530	Wilks and Carter [1990]
Wet olivine	Dislocation	-15.05	3.5	480	Hirth and Kohlstedt [2003]
Dry olivine	Diffusion	-8.65	1.0	375	Hirth and Kohlstedt [2003]
Wet olivine	Diffusion	-8.66	1.0	335	Hirth and Kohlstedt [2003]

grain size d, grain size exponent m, water fugacity f_{H_2O}, water fugacity exponent r, melt fraction factor α and melt fraction ϕ. Using the constitutive law of viscous flow:

$$\tau_{II} = 2\eta\dot{\varepsilon}_{II} \tag{2.48}$$

the correspondent dislocation and diffusion viscosities can be computed substituting eq. (2.47) in (2.48) :

$$\eta_{dif} = \frac{1}{2}(A)^{-\frac{1}{n}}(\dot{\varepsilon}_{II}^{dif})^{\frac{1}{n}-1}\exp\left(\frac{E_a + pV_a}{nRT}\right) \tag{2.49}$$

$$\eta_{dis} = \frac{1}{2}(A)^{-\frac{1}{n}}(\dot{\varepsilon}_{II}^{dis})^{\frac{1}{n}-1}\exp\left(\frac{E_a + pV_a}{nRT}\right) \tag{2.50}$$

where n is the power-law exponent, the subindex II indicates the square root of the second invariant of an arbitrary tensor $a_{II} = \sqrt{\frac{1}{2}a_{ij}a_{ij}}$. The power-law exponent for diffusion creep is $n = 1$, thus yielding an expression for the diffusion viscosity that does depend on strain; on the other hand, theoretical values of the power-law exponent for dislocation are $n = 3-4$ and yields a non-linear equation. An effective creep viscosity is now built as:

$$\frac{1}{\eta} = \frac{1}{\eta_{dif}} + \frac{1}{\eta_{dis}} \tag{2.51}$$

In this way, the smallest viscosity will have the largest contribution to the effective viscosity, with deformation dominated by the mechanism that has the smallest activation stress. The viscous strain tensor is then $\dot{\varepsilon}_{ij}^{visc} = \dot{\varepsilon}_{ij}^{dif} + \dot{\varepsilon}_{ij}^{dis}$ and, using the definitions (2.49) and (2.50), the diffusion and dislocation strain tensors are respectively computed as:

$$\dot{\varepsilon}_{ij}^{dif} = \frac{\tau_{ij}}{2\eta_{dif}}; \quad \dot{\varepsilon}_{ij}^{dif} = \frac{\tau_{ij}}{2\eta_{dif}} \tag{2.52}$$

Values of the parameters in eqs. (2.49) and (2.50) used in this thesis are summarised in Table 2.1. It must be noted that these values have been obtained in laboratory conditions from either uniaxial or triaxial experiments, meaning that the strain rate and differential stress at which they were calculated, is not equivalent to the square root of the second invariant of a given tensor (i.e. strain and deviatoric stress). The differential stress in these experiments is defined as:

$$\sigma_d = \sigma_1 - \sigma_3 \tag{2.53}$$

where σ_1 and σ_3 are the maximum and minimum eigenvalues (in other words, the maximum and minimum principal stresses) of the stress tensor and the conditions:

$$\sigma_1 \neq \sigma_2 = \sigma_3 \tag{2.54}$$

where 1 represents the vertical axis and 2 and 3 are the horizontal axis. For a uniaxial experiment $\sigma_2 = \sigma_3 = 0$, whereas σ_2 and σ_3 are the confining pressure for a triaxial experiment. The strain rate in these experiments is then the axial strain $\dot{\varepsilon}_1$. Under these conditions, the deviatoric strain yields:

$$\tau = \begin{bmatrix} \sigma_1 - \frac{\sigma_1 - 2\sigma_3}{3} & 0 & 0 \\ 0 & \sigma_3 - \frac{\sigma_1 - 2\sigma_3}{3} & 0 \\ 0 & 0 & \sigma_3 - \frac{\sigma_1 - 2\sigma_3}{3} \end{bmatrix} \tag{2.55}$$

and the square root of its second invariant is:

$$\tau_{II} = \sqrt{\frac{1}{2}\left(\left[\frac{2}{3}\sigma_1 - \frac{2}{3}\sigma_3\right]^2 + 2\left[\frac{1}{3}\sigma_3 - \frac{1}{3}\sigma_1\right]^2\right)} \tag{2.56}$$

which simplifies to:

$$\tau_{II} = \frac{1}{\sqrt{3}}\sigma_d \tag{2.57}$$

If one assumes uniform deformation along the axis 2 and 3 and incompressibility:

$$-\frac{1}{2}\dot{\varepsilon}_1 = \dot{\varepsilon}_2 = \dot{\varepsilon}_3 \tag{2.58}$$

and the square root of the second invariant of the strain rate tensor yields:

$$\dot{\varepsilon}_{II} = \sqrt{\frac{1}{2}\left(\dot{\varepsilon}_1^2 + 2\left[-\frac{1}{2}\dot{\varepsilon}_1\right]^2\right)^2} \tag{2.59}$$

which simplifies to

$$\dot{\varepsilon}_1 = \frac{2}{\sqrt{3}}\dot{\varepsilon}_{II} \tag{2.60}$$

The power law eq. (2.47) can be now generalized in terms of the square roots of the second invariants of stress and strain rate using eqs. (2.57) and (2.60):

$$\tau_{II} = C(A)^{\frac{1}{n}}(\dot{\varepsilon}_{II})^{\frac{1-n}{n}} \exp\left(\frac{E+PV}{nRT}\right) \tag{2.61}$$

where C is a conversion factor:

$$C = (2)^{\frac{1}{n}}(3)^{-\frac{n+1}{2n}} \tag{2.62}$$

Plastic deformation

Materials undergo non-recoverable plastic deformation if the yield stress is exceeded. The stress at which a material fails is defined by the yield surface $\mathscr{F}(\tau_{ij}, q)$, a scalar function of the deviatoric stress and the softening parameter q, which limits the maximum stress possible within the material.

For points of the material where deformations are purely visco-elastic $\mathscr{F} < 0$, whereas $\mathscr{F} = 0$ at yield. If the stress field at any point of the domain is such that $\mathscr{F} > 0$, the stress must be brought back to the yield

surface. Plastic strain rate is defined by the plastic multiplier $\dot{\gamma} > 0$ and the plastic potential $\mathscr{G}$:

$$\dot{\varepsilon}_{ij}^{\prime(pl)} = \dot{\gamma}\frac{\partial \mathscr{G}}{\partial \tau_{ij}} \tag{2.63}$$

The addition of plastic strain rates to eq. (A.40) leads to the visco-elasto-plastic constitutive equation:

$$\dot{\varepsilon}_{ij}^{\prime} = \frac{\tau_{ij}}{2\eta} + \frac{1}{2G}\frac{D\tau_{ij}}{Dt} + \dot{\gamma}\frac{\partial \mathscr{G}}{\partial \tau_{ij}} \tag{2.64}$$

In this section we adopt the deviatoric, corner-free and non-associative ($\mathscr{F} \neq \mathscr{G}$) Prandtl-Reus flow rule (e.g. Zienkiewicz and Taylor [2005]). This flow rule takes the von Mises yield surface as the flow potential:

$$\mathscr{G} = \tau_{II} \tag{2.65}$$

and therefore

$$\frac{\partial \tau_{II}}{\partial \tau_{ij}} = \frac{\tau_{ij}}{2\tau_{II}} \tag{2.66}$$

Plastic volumetric strain can be included by using an associative flow rule ($\mathscr{F} = \mathscr{G}$). This topic is further described and discussed in Chapter 4. Using the Prandtl-Reus flow rule, and after some algebraic manipulations, we can obtain obtain the following expression:

$$\tau_{ij}\left(\frac{1}{2\eta} + \frac{1}{2G\Delta t} + \frac{\dot{\gamma}}{2\tau_{II}}\right) = \dot{\varepsilon}_{ij}^{\prime} + \frac{\tau_{ij}^{n}}{2G\Delta t} + \frac{\tau_{ij}^{rot}}{2G} \tag{2.67}$$

where τ_{ij}^{rot} are the terms in eq. (A.41) associated to rigid body rotations. Assuming that at yield $\tau_{II} = \tau_y$:

$$\tau_{ij} = \eta_{vpl}\left(2\dot{\varepsilon}_{ij}^{\prime} + \frac{\tau_{ij}^{n}}{G\Delta t} + \frac{\tau_{ij}^{rot}}{G}\right) \tag{2.68}$$

where η_{vpl} is the effective visco-elasto-plastic viscosity given by:

$$\eta_{vpl} = \frac{\eta G \tau_y \Delta t}{G\tau_y\Delta t + \eta\,\tau_y + \eta\,\dot{\gamma} G\Delta t} \tag{2.69}$$

Or alternatively, the effective visco-elasto-plastic viscosity can be computed directly from eq. (2.68) as:

$$\eta_{vpl} = \frac{\tau_{ij}}{2\dot{\varepsilon}_{ij} + \frac{\tau_{ij}^{n}}{G\Delta t} + \frac{\tau_{ij}^{rot}}{G}} \tag{2.70}$$

In order to be consistent with our description of visco-elastic deformations, eq. (2.70) is rewritten in terms of η_{eff} and χ, giving the expression of the effective visco-elasto-plastic viscosity:

$$\eta_{vpl} = \frac{\tau_y}{2\dot{\varepsilon}_{II} + \chi\widehat{\tau}_{II}} \tag{2.71}$$

Thus at yield, the constitutive visco-elasto-plastic constitutive law is given by

$$\tau_{ij} = 2\langle\eta\rangle\dot{\varepsilon}_{ij} + \chi\widehat{\tau}_{ij} \tag{2.72}$$

and

$$\langle\eta\rangle = \begin{cases} \eta_{eff} & \text{for } \mathscr{F} \leq 0 \\ \eta_{vpl} & \text{for } \mathscr{F} > 0 \end{cases} \tag{2.73}$$

If one wishes to recover the plastic strain, $\dot{\gamma}$ can be computed as:

$$\dot{\gamma} = \tau_y \left(\frac{1}{\eta_{vpl}} - \frac{1}{\eta_{G\Delta t}} - 1 \right) \tag{2.74}$$

Plastic strain rate is then recovered after substitution of eq. (2.74) in (2.63):

$$\dot{\varepsilon}_{ij}^{\prime(pl)} = \frac{1}{2} \left(\tau_y \left[\frac{1}{\eta_{vpl}} - \frac{1}{\eta_{G\Delta t}} - 1 \right] \right) \frac{\tau_{ij}}{\tau_{II}} \tag{2.75}$$

Yield surface

The yield surface is a scalar function that defines the domain of admissible stresses, thus defining the yield stress. There is a vast range of proposed yield surfaces; however, in geodynamics it is common to use pressure-sensitive yield criterion. I therefore adopt the pressure-dependent Drucker-Prager [Drucker and Prager, 1952] yield criterium to describe the yield stress, for which $\mathscr{F}$ is defined as:

$$\mathscr{F} = \tau_{II} - p \sin\phi - c \cos\phi \leq 0 \tag{2.76}$$

where ϕ is the friction angle and c is the cohesion. To avoid shear bands forming at 45°, we consider that the strength of the material depends on the total pressure [Kaus, 2010]. A common alternative to Drucker-Prager is the isotropic Mohr-Coulomb [Coulomb, 1773] yield surface:

$$\mathscr{F} = (\sigma_1 - \sigma_3) + (\sigma_1 + \sigma_3) \sin\phi - 2c \cos\phi \leq 0 \tag{2.77}$$

where σ_1 and σ_3 are the maximum and minimum principal stresses, respectively. The Drucker-Prager yield surface is represented by a cone in the space of principal stresses, whereas Moh-Coulomb is a hexagonal pyramid. This means that both functions have an apex aligned with the hydrostatic axis. The derivative at the apex is a singularity and should be computed very carefully. This issue can be bypassed by combining Drucker-Prager or Mohr-Coulomb for high stress/pressure values with the von Mises yield surface [Mises, 1913] for low stress/pressure values. Therefore, the following two-surface yield criterion is defined (Fig. 2.2):

$$\mathscr{F} = \begin{cases} \tau_{II} - p \sin\phi - c \cos\phi & \tau_{II} > c \\ \tau_{II} - c & \tau_{II} \leq c \end{cases} \tag{2.78}$$

for a mixed Drucker-Prager - von Misses yield surface, or:

$$\mathscr{F} = \begin{cases} \mathscr{F} = (\sigma_1 - \sigma_3) + (\sigma_1 + \sigma_3) \sin\phi - 2c \cos\phi & \tau_{II} > c \\ \tau_{II} - c & \tau_{II} \leq c \end{cases} \tag{2.79}$$

for a mixed Mohr Coulomb - von Misses yield surface. I must note that the Mohr-Coulomb yield surface is available in LaCode, howeever, it is not employed in the work presented in this thesis.

Strain softening

The accumulate plastic strain is commonly employing as the softening parameter [de Souza Neto et al., 2011]. Strain softening can be applied to both friction angle and cohesion; however, in this thesis, strain softening is only applied to the friction angle. The friction angle is then reduced as a linear function of the softening parameter, defined as competition between the plastic strain and a healing term [Moresi and

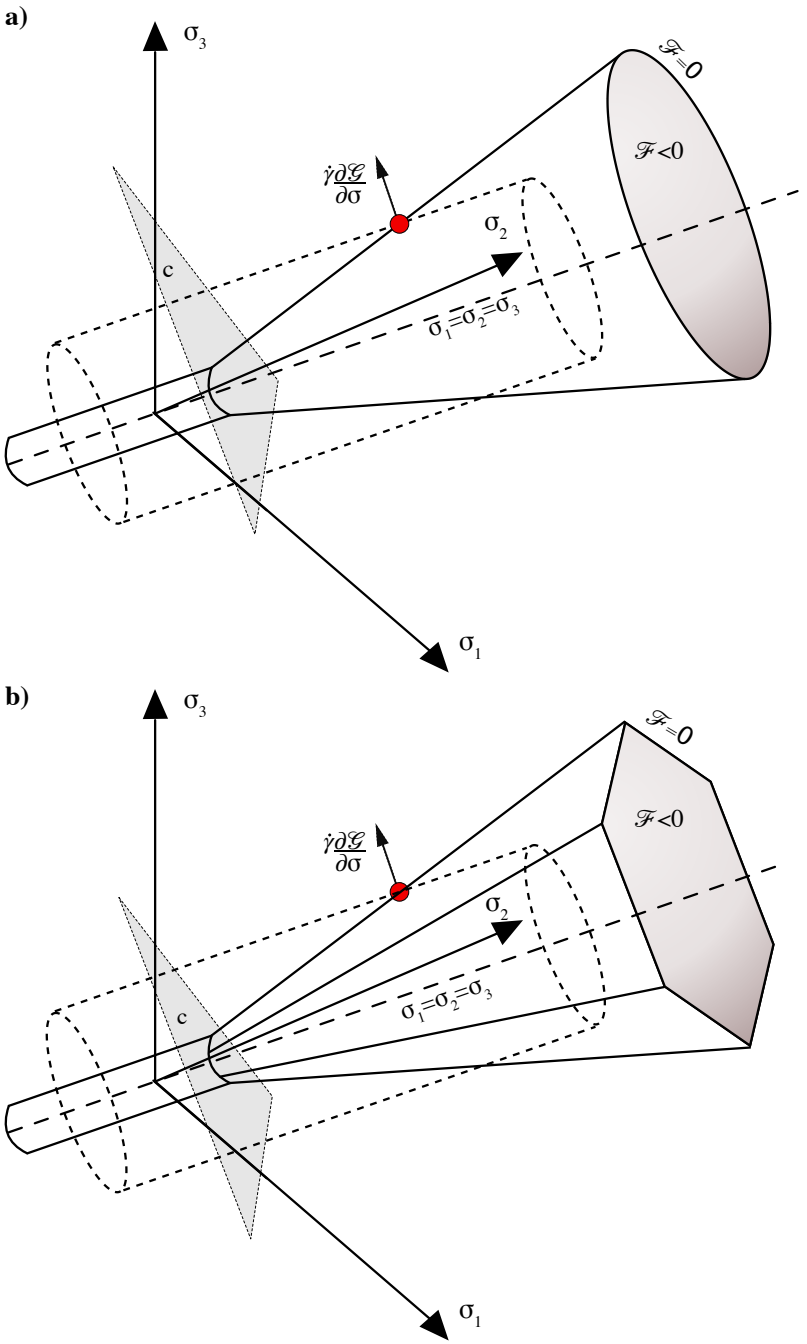

Fig. 2.2 *Graphical representation of the mixed yield surface in the principal stress space:* ***(a)*** *Drucker-Prager and* ***(b)*** *Mohr-Coulomb yield surface define the strength envelope at high pressure/differential stress values, and Von Misses defines the strength envelope for stresses so that $\tau_{II} < c$. The dashed line represents the hydrostatic axis $\sigma_1 = \sigma_2 = \sigma_3$.*

Mühlhaus, 2006]:

$$q = E_{ij}^{pl} = \int \left(\dot{\gamma} \frac{\tau_{ij}}{2\tau_y} - q_h(\tau_{ij}, \eta) \right) dt \tag{2.80}$$

where the healing term $q_h(\tau, \eta)$ is a scalar function proportional to the background viscous strain:

$$q_h(\tau_{ij}, \eta) = \vartheta \frac{\tau_{II}}{\eta} \tag{2.81}$$

and $0 < \vartheta < 1$ is a scalar function of pressure and temperature. Unless specified, initial friction angles of $\phi_0 = 35^\circ$ and minimum angle of friction of $\phi_\infty = 15^\circ$ are used in the numerical experiments presented in

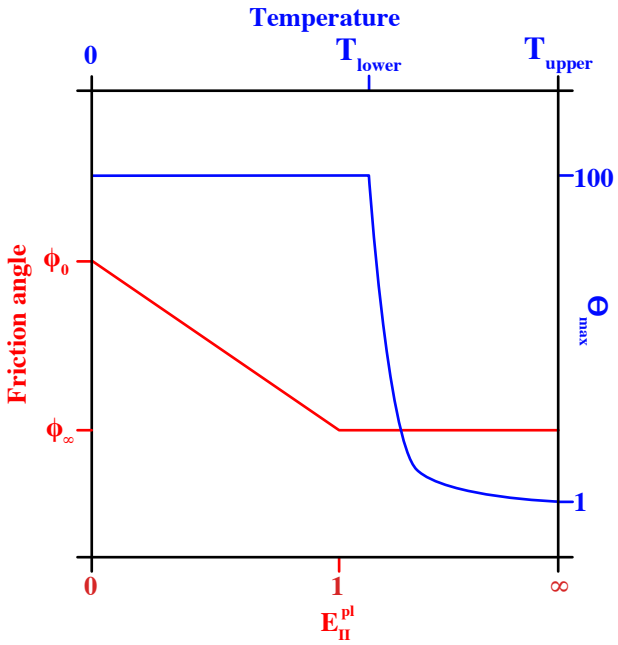

Fig. 2.3 *In red: linear dependence of plastic softening on finite plastic strain. In blue: temperature dependency of the maximum viscous pre-exponential factor.*

this thesis. The maximum amount of softening is reached at $E_{II} = 1$, thus no further softening is applied for larger deformations.

The factor Θ is introduced in the equations of diffusion and dislocation to weaken the viscous deformations due to grain size reduction by dislocation mechanism and crystallographic orientations [Karato and Wu, 1993; Hansen et al., 2012]:

$$\eta = \Theta \frac{1}{2} A^{(\frac{1}{n})} \dot{\varepsilon}_{II}^{(\frac{1}{n}-1)} \exp\left(\frac{E+PV_a}{nRT}\right) \tag{2.82}$$

The pre-exponential Θ factor depends linearly on the second invariant of the strain tensor. The pre-exponential factor (Fig. 2.3) takes values of $1 \leq \Theta \leq \Theta_{max}$, with Θ_{max} being a scalar function of temperature:

$$\Theta_{max}(T) = \begin{cases} 100 & \text{if } T \leq T_{lower} \\ exp\left(\frac{T-T_{upper}}{T_{lower}}\right) & \text{if } T_{lower} < T < T_{upper} \\ 1 & \text{if } T > T_{upper} \end{cases} \tag{2.83}$$

where T_{lower} and T_{upper} are the lower and upper limits that define the exponential decay, respectively.

2.1.5 Non-linear iterations

In geodynamical problems, rheological non-linearities are typically present (e.g. dislocation creep, plastic deformation, temperature-dependent density). These non-linearities are treated by nesting the linear solver within a set of Picard iterations. Non-linear iterations are terminated when the value of the residual of the velocity is below a certain tolerance. The residual is defined as:

$$R = \frac{\| u^i - u^{i-1} \|_\infty}{\| u^i \|_\infty} \leq Tol \tag{2.84}$$

where $\| \cdot \|_\infty$ is the infinity norm and i is the non-linear iteration index.

2.2 Advection scheme

Let us first define the material time derivative as:

$$\frac{D\psi}{Dt} = \frac{\partial \psi}{\partial t} + u \cdot \nabla \psi \tag{2.85}$$

where $\partial(\cdot)/\partial t$ indicates the partial time derivative of the function $(\cdot)$, and $\psi = \psi(x,y,z)$. As described previously in this chapter, LaCoDe solves the governing equations of a compressible and incompressible viscous flow using a Lagrangian frame of reference. Under this assumption, any fluid particle is followed by the observer as it moves through space and time. For this reason, the advection term $u \cdot \nabla \psi$ in eq. vanishes, and the material time derivative is equivalent to the partial time derivative. On the other hand, the observer is fixed and does not follow the flow particles as they move through time and space under a Eulerian frame of reference. In the Eulerian formulation of the Stokes equations for a visco-elastic flow, the advection term must be included in the equations of conversvation of momentum, conservation of mass, and in the Jaumann derivative of the elastic stress.

In the context of the Lagrangian FEM, the elements are deformed, at the end of every time step, once the velocity and temperature fields are computed, by simply performing the following calculation for every node of the FEM mesh (Fig. 2.4a):

$$x_i = x_i + u_i dt \tag{2.86}$$

Since LaCoDe uses 7-nodes triangular elements, the edges of the elements may not remain completely straight and the inner node may not be located at the barycentre of the element, after the mesh is advected (Fig. 2.4b). This effect might lead to highly distorted elements after few time steps. To avoid an excessive use of remeshing techniques, the position of the nodes located at the centre of the edges is recalculated so that the edges are straight, and the 7th node inside the element is brought back to the barycentre (Fig. 2.4c).

2.3 Remeshing

One of the drawbacks of using a Lagrangian formulation is that large deformation of the mesh eventually leads to highly distorted elements. This issue is overcome by mapping the necessary fields (i.e. temperature, density, accumulated strain) onto a newly generated high-quality mesh. To reduce the associated computational cost and interpolation errors, the new mesh is generated only when the quality of the mesh is below a given threshold. Therefore, the remeshing algorithm is called only if $q_n < .25$, $\alpha < 7^\circ$ and $\beta > 170^\circ$, for at least one element. Where α and β are the smallest and largest angles, respectively, and q_n is a quality factor defined as:

$$q_n = \frac{4\sqrt{3}A}{||ab||^2 + ||ac||^2 + ||bc||^2} \tag{2.87}$$

where A is the area, and a, b and c are the vertices of the triangle. The remeshing scheme and mapping of the fields onto the new mesh and the accuracy of the remeshing scheme are described in Chapter 3. The remeshing algorithm currently implemented in LaCoDe is optimised to work with the mesh generator Triangle [Shewchuk, 1996] for perfect body-fitting meshes, and with an adaptive mesh generator [Liu et al., 2018] for non-body-fitting meshes.

In the first case, the interface between two different bodies (e.g. the contact between two rheological phases) is tracked through time. When remeshing is necessary, the nodes at this interface are used as a boundary condition in order to generate the new mesh. Perfect body-fitting meshes are extremely convenient in the context of the FEM to model the mechanical behaviour of a composite body. However, this approach might

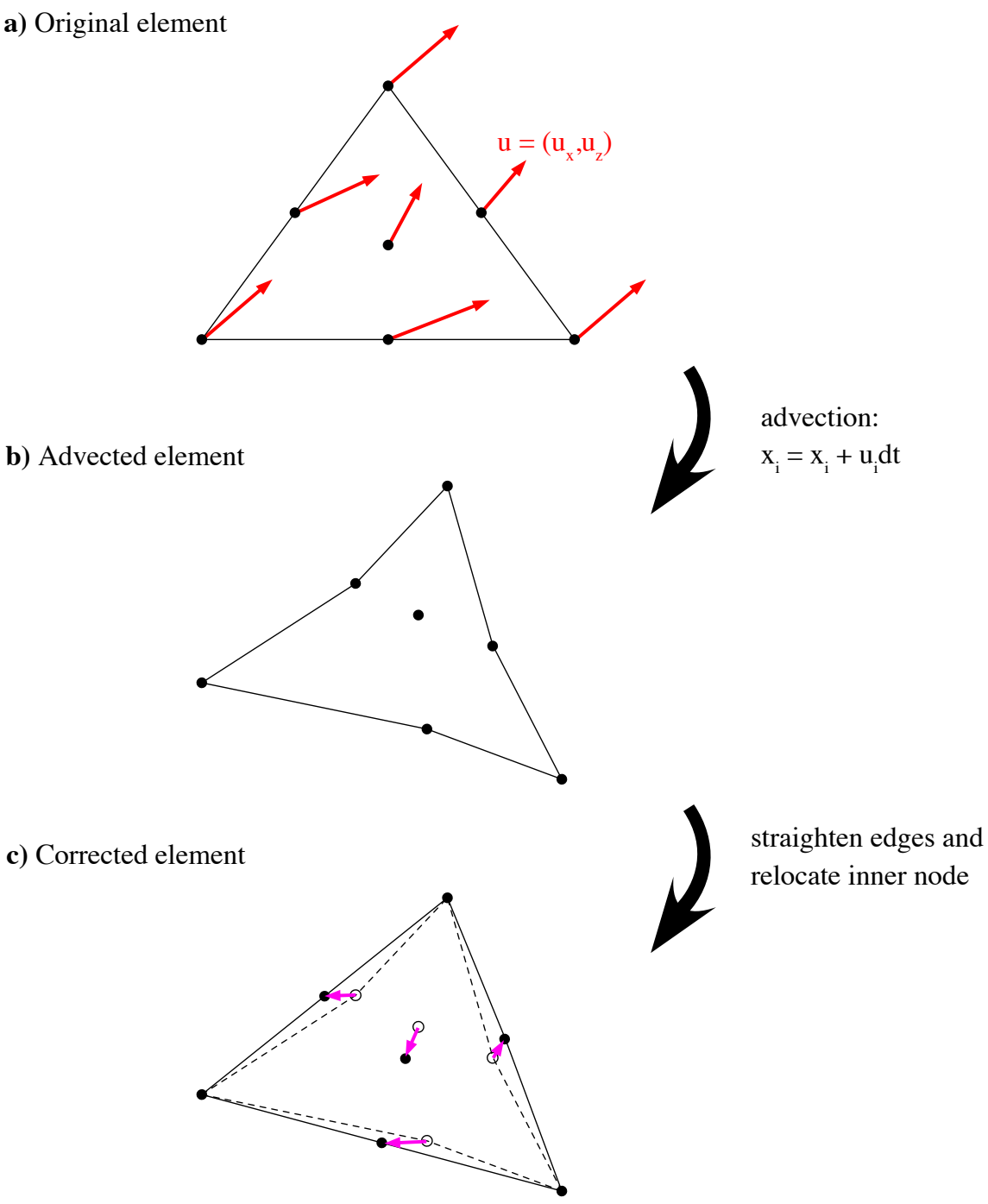

Fig. 2.4 *Advection scheme:* ***(a)*** *Undeformed 7-node Crouzeix-Raviart triangular element. The red arrows represent the velocity vectors.* ***(b)*** *Deformed element after applying the advection scheme.* ***(c)*** *The element is corrected by straightening its edges and relocating the central node back to its baricenter. The dashed triangle and empty circles represent the element and the nodes pre-correction, respectively.*

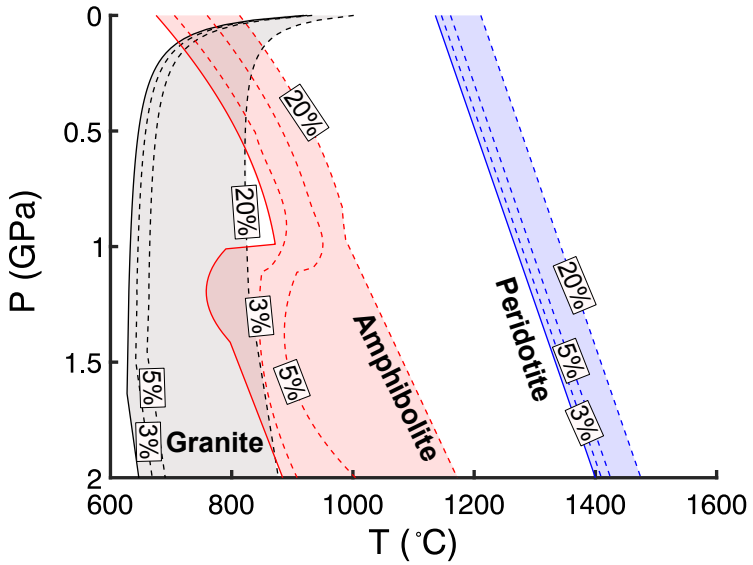

Fig. 2.5 *Solidus of a hydrated granite [Boettcher and Wyllie, 1968]* ***(in black)****, fluid-absent MORB-derived amphibolite [López and Castro, 2001]* ***(in red)*** *and fertile peridotite [Phipps Morgan, 2001b]* ***(in blue)****. Dashed lines represent the solidus at different degrees of melt fraction.*

be problematic if two different interfaces cross each other. For example, during continental break-up, the mesh comprising the upper crust, lower crust and mantle lithosphere is subject to extensive extension and thinning, which may result in the crossing of the interfaces between these rheological bodies nearby the spreading centre. This problem is fixed in LaCoDe by imposing a minimum distance between layers of around 100 and 1000 m, depending on the spatial resolution of the model. This issue can also be bypassed in LaCoDe by using an adaptive mesh generator. In this case, the interfaces between two distinct bodies do not perfectly match their contact, instead they are defined as higher resolution areas, and the code generates a cloud of randomly generated tracers (at least 6 tracers per element) that store the rheological phase. In every time step, the velocity field is interpolated onto the tracers, which are advected following the same procedure as for the FEM mesh. Then the rheological phase of a single element is defined as the median of the tracers inside the element. Employing this approach, rheological layers that were laterally continuous at the beginning of the simulation can actually break-up, thus avoiding problems of crossing interfaces.

2.4 Other processes

The code includes two additional features of significant relevance to geological processes: melt generation and serpentinisation. Their correspondent parametrisation is briefly described in the following sections.

2.4.1 Partial melting

The production of partial melt is calculated following Phipps Morgan [2001b]. The mantle solidus temperature T^s is defined as:

$$T^s = T^s_o + \left(\frac{\partial T^s}{\partial p}\right)_F p + \left(\frac{\partial T^s}{\partial F}\right)_P F \tag{2.88}$$

where T^s_o is the solidus temperature at the surface, $\partial T^s/\partial P$ is the solidus-pressure gradient, $\partial T^s/\partial F$ is the solidus-depletion gradient and F is melt fraction. Melting is produced in a parcel of the model if $T > T^s$, and two mechanisms are responsible for the production partial melting: 1) temperatures above the solidus,

Table 2.2 *Thermodynamic properties for mantle material. Values from Phipps Morgan [2001b]*

Lithology	T_o^s (°C)	$\partial T^s/\partial p$ (°C/GPa)	$\partial T^s/\partial f$ (°C)	ΔH
Fertile peridotite	1081	132	250	550
Refractory peridotite	1136	132	250	550

and 2) decompression. The decompression melt productivity for a lithology i within a lithology j is given by [Phipps Morgan, 2001b]:

$$-\frac{\partial F_i}{\partial p} = \frac{\frac{\partial T_i^s}{\partial p} - \frac{\alpha T}{\rho C_p} + \frac{T}{C_p}\phi_j \Delta S_j \left(\frac{\partial T_i^s}{\partial p} - \frac{\partial T_j^s}{\partial p}\right)}{\frac{T}{C_p}\phi_i \Delta S_j \left(\frac{\partial T_i^s/\partial F_i}{\partial T_j^s/\partial F_j}\right) + \frac{\partial T_i^s}{\partial F_i}} \tag{2.89}$$

where ΔS is the entropy of the solid-melt phase change, which can be related to the latent heat of melting ΔH, for a pure substance, as $\Delta H = T\Delta S$. A single component melting is considered in this thesis and the amount of decompression melting is defined as:

$$dF_{pressure} = dP\left(-\frac{\frac{\partial T^s}{\partial p}}{\frac{\Delta H}{C_p} + \frac{\partial T^s}{\partial F}}\right) \tag{2.90}$$

where the adiabatic term is missing because the temperatures are potential temperature. The temperature change during decompression melting is given by:

$$\frac{dT}{dP} = \frac{\partial T_s^i}{\partial p} + \frac{\partial T_s^i}{\partial F_i}\frac{dF_i}{dp} \tag{2.91}$$

The amount of melt under isobaric conditions is given by [Nielsen and Hopper, 2004]:

$$dF_{temp} = \frac{T^m - T^s}{\frac{\Delta H}{C_p} + \frac{\partial T^s}{\partial F}} \tag{2.92}$$

where T^m is the mantle temperature and the total amount of instantaneous melt is $dF = dF_{pressure} + dF_{temp}$. The total amount of melting produced in a parcel is then the summation of dF over time:

$$F = \Delta t \sum_{t=1}^{n} dF^t \tag{2.93}$$

where the superscript t is the time step and n is the total number of time steps. For undepleted mantle, the wet solidus (fertile peridotite in Table 2.2) is used initially, and the dry solidus (refractory peridotite in Table 2.2) is used after 2% melting [Braun et al., 2000]. Partial melting of the crustal is calculated in the same manner as melting of the mantle; however crustal T^s have been parametrised from solidus-liquidus curves obtained with experimental studies. For the work correspondent to Chapter 4, two different source of crustal melting are considered (see Figure 2.5): 1) a hydrated granite [Boettcher and Wyllie, 1968]; and 2) a fluid-absent MORB-derived amphibolite [López and Castro, 2001].

Since buoyancy forces due to melt production are relatively small, they can be included in the equation of state under the Boussinesq approximation:

$$\rho(T,P) = \rho_o(1 + \alpha(T - T_o) - \beta F) \tag{2.94}$$

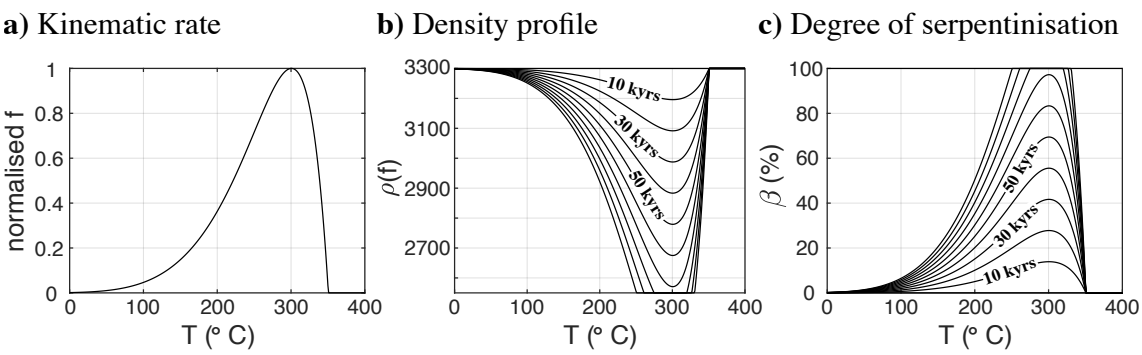

Fig. 2.6 ***(a)*** *Kinematic rate as a function of temperature. Evolution of the* ***(b)*** *density and* ***(c)*** *degree of serpentinisation with temperature and time.*

where ρ_o and T_o are the density and temperature at the surface temperature and zero pressure, respectively, α is the thermal expansivity, F is the depletion and β is defined as:

$$\beta = 1 - \frac{\rho_{molten}}{\rho_{solid}} \tag{2.95}$$

where ρ_{solid} and ρ_{molten} are the reference densities of the rock in its solid and molten states. The density of molten crust is taken $\rho = 2400\ kg/m^3$ and $\rho = 2900\ kg/m^3$ for molten mantle material [Gerya and Meilick, 2011].

2.4.2 Serpentinisation

Serpentinisation reactions occur when cold lithospheric mantle rocks react with seawater within the temperature limits (< 350 °C) of the serpentine group minerals (Fig. 2.6) and represent a relevant chemico-mechanical process that takes place in some tectonic events such as continental break-up and subducting slabs. The low friction angle and volumetric strain associated to these reactions is known to weaken the strength of the lithosphere [Escartin et al., 1997, 2001] and theorised to control the development of decollements at the crust-mantle boundary in slow-spreading oceanic ridges [Pérez-Gussinyé and Reston, 2001]. Additionally, serpentinisation occurring at oceanic transform faults associated to slow-spreading oceanic ridges may have a significant impact on global marine biogeochemical cycles (Rüpke and Hasenclever [2017], and references therein). Serpentinisation have been also identified between the outer rise and the trench of subducting slabs [Ranero et al., 2003], and the volumetric strain of associated to the formation of serpentine group minerals is inferred to enhance the bending of the subducting slab [Phipps Morgan, 2001a]. Moreover, it is commonly accepted that the deep (at ∼250-300 km) dehydration of the slab is responible for triggering arc melting [Rüpke et al., 2004], and the associated decrease of volyme may aid the unbending of the slab.

Two different mechanism are responsible of bringing seawater into contact with mantle rocks: i) exhumation of ultra mafic rocks, and ii) active faults that cut through the crust and reach the mantle lithosphere, resulting in the formation of conduits of seawater that reaches and reacts with mantle lithospheric rocks. The later mechanism has been observed under thinned continental crust in slow-spreading oceanic ridges [e.g. Pérez-Gussinyé and Reston, 2001; Rüpke et al., 2013; Rüpke and Hasenclever, 2017], and the amount of sewater reaching the mantle is thought to be controlled by the amount of displacement along the faults [Bayrakci et al., 2016]. Serpentinisation ocurring at a crustal scale in subducting slabs has also been linked to active normal faults related to the bending slab [Ranero et al., 2003].

In LaCoDe, the degree of serpentinisation of the mantle is calculated in every time step for those parcels of the model under brittle failure (i.e. points of the model where $\tau = \tau_y$) and within the serpentinisation pressure and temperature stability conditions. The serpentinisation reaction is implemented assuming a temperature-dependent kinetic rate [Malvoisin et al., 2012]:

$$f(T) = C_o A \exp\left(-\frac{b}{T}\right)\left(1 - exp\left[-c\left(\frac{1}{T} - \frac{1}{T_o}\right)\right]\right) \tag{2.96}$$

with $A = 808.3$, $b = 3640$ K, $T_o = 623.6$ K, $c = 8759$ K. The rate of density change due to serpentinization is then:

$$\frac{\partial \rho}{\partial t} = -f\rho_{ol} \tag{2.97}$$

The phase change is then incorporated to a pressure and temperature dependant equation of state:

$$\rho(p,T,f) = \rho_o(1 - \alpha(T - T_o) + K^{-1}p - f\Delta t) \tag{2.98}$$

where ρ_o and T_o are the reference density and temperature, respectively, and K is the bulk modulus. Serpentinisation is an exothermic reaction, thus a term Q_{serp} that represents the rate heat generation by the reaction of serpentenisation is added to the equation of conservation on energy [Emmanuel and Berkowitz, 2006]:

$$Q_{serp} = H_{serp}\frac{\partial \rho_{ol}}{\partial t} \tag{2.99}$$

where H is the thermal energy released during the hydration (or dehydration) reaction per unit mass of serpentinised mineral. It must be noted that density changes due to serpentinisation reactions may become larger than 10% with respect the reference density. Therefore, one should be extremely cautious (and drop the pressure term) if the eq. (2.98) is used under the incompressible Boussinesq approximation.

2.5 Code structure

The incompressible thermo-mechanical problem described in this chapter is solved using the code LaCoDe. This code is written in MATLAB and uses the optimised approached described in [Dabrowski et al., 2008] to build the block matrices that constitute the system of linear equations. Previous versions of LaCoDe included non-Newtonian flow and elastic deformation for an incompressible material. For this thesis, I have enhanced incompressible version of LaCoDe by adding plastic deformation, plastic softening and shear heating. I have also written a different version of LaCoDe that includes a fully compressible formulation (see Chapter 3 for a description and discussion). The global workflow of LaCoDe for the incompressible Boussinesq approximation is summarised in Fig. 2.7. The structure of the code can be sub-divided in three parts:

Pre-processor

In this part the thermo-mechanical properties and geometry defining the problem is defined. A triangular mesh is generated using the mesh generator Triangle [Shewchuk, 1996] or an adaptive mesh generator [Liu et al., 2018]. The velocity and temperature boundary conditions are also prescribed in this section of the code.

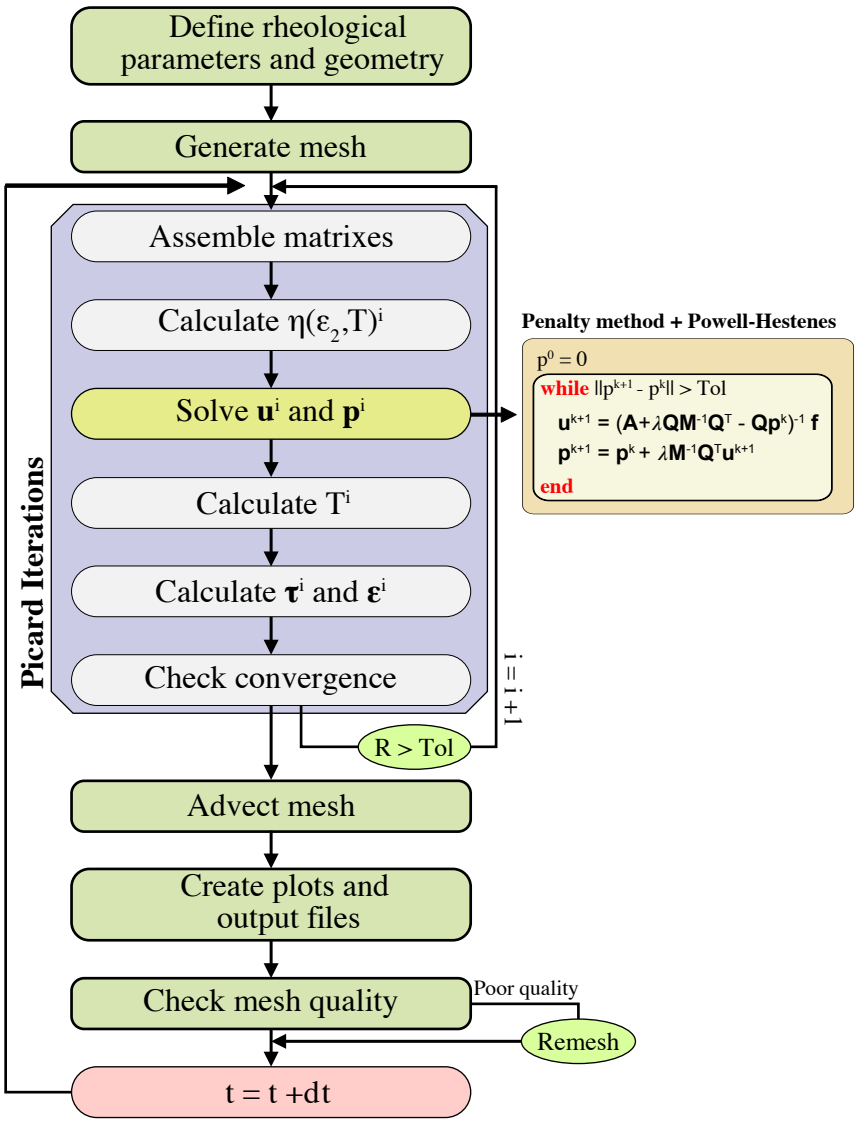

Fig. 2.7 *Global work flow of the LaCoDe for the incompressible Boussinesq approximation, and details of the linear solver (combination of penalty method and Powell-Hestenes iterations).*

Processor

This part of the codes solves the incompressible Stokes equations and thermal diffusion to obtain the velocity, pressure and temperature fields. After advection of the mesh, a remeshing algorithm is called if it is too distorted (this procedure is described in Chapter 3).

Post-processor

Other variables are here calculated from the velocity, pressure and temperature; for example: stress and strain fields or partial melting. Visualization algorithms are called to produce plots of the results of the models.

3 | LaCoDe: a Lagrangian two-dimensional thermo-mechanical code for large strain compressible viscoelastic geodynamical modelling

Albert de Montserrat, Jason P. Morgan and Jörg Hasenclever. LaCoDe: a Lagrangian two-dimensional thermo-mechanical code for large strain compressible viscoelastic geodynamical modelling. Planned for submission to *Tectonophysics*.

Authors contribution

AdM and JM designed the mathematical description of a compressible visco-elastic flow and the numerical implementation was introduced by AdM in collaboration with JM and JH. AdM designed and analysed the results of the numerical experiments in discussion with JM and JH. AdM wrote the manuscript under the supervision of JM and JH.

LaCoDe: a Lagrangian two-dimensional thermo-mechanical code for large strain compressible visco-elastic geodynamical modeling

Albert de Montserrat[a], Jason P. Morgan[b], Jörg Hasenclever[c]

[a]*SE Asia Research Group, Department of Earth Sciences, Royal Holloway University of London, Egham, United Kingdom*
[b]*Royal Holloway University of London, Department of Earth Sciences, Egham, United Kingdom*
[c]*Institute of Geophysics, Hamburg University, Hamburg, Germany*

Abstract

We present the numerical code LaCoDe (Lagrangian Compressible Deformation) for two-dimensional problems for mantle-lithosphere geodynamic modeling. Unlike a great number of mantle modeling codes that are based on the incompressible Boussinesq approximation, LaCoDe adopts a compressible continuity equation, including the volumetric strains linked to elastic compression. LaCoDe is a finite element method code that typically uses a Lagrangian frame of reference. It solves the Stokes equations for a non-Newtonian visco-elastic rheology. A remeshing algorithm is implemented to track and transfer the physical parameters of the material from a heavily distorted mesh into to an updated one. In this paper, we first describe the equations governing the deformation of Earth materials with detailed description of the algorithm and its numerical implementation. We then benchmark the accuracy of LaCoDe by comparing numerical results with analytical solutions for bending of a thin elastic beam under a constant uniform load, viscous inclusions, Rayleigh-Taylor instabilities, stress build-up in a visco-elastic Maxwell body, and Couette flow with viscous flow. The Rayleigh-Taylor test is further used to demonstrate the accuracy of the remeshing algorithm. Finally, we show the importance of including volumetric strain in some crust-lithospheric deformation cases, such as magma-free slow-spreading ridges and subducting slabs. Additionally, we find that the ex-

tra non-linearities introduced by the compressible Stokes equations are better solved using nested sets of Picard iterations.

Keywords:

, Modeling of large-strain visco-elastic deformation, Compressible formulation

1. Introduction

Rocks are exposed to thermal, mechanical and chemical processes that induce volumetric changes. Obvious examples are mechanical compression and decompression, thermal expansion, and phase changes resulting from partial melting and serpentinization. Even though stresses related to compressibility may play an important role in rock deformation and failure, the incompressible Boussinesq approximation of the governing equations is the most common approach used in geodynamical modeling of coupled lithospheric-mantle systems. This approximation is considered to be reasonably valid under lithospheric conditions and offers a simple and straightforward numerical implementation, hence its popularity. The Boussinesq approximation is considered to be appropriate if: 1) the size of the domain is shorter than any physical scale height (i.e. $D_f = |f_m^{-1} df_o/dz|^{-1}$, where f is any state variable, f_m is the space average of f, and f_o is the variation in the absence of motion (Spiegel and Veronis, 1959)); 2) the density of the material does not change more than 10% with respect to its reference value (Gray and Giorgini, 1976); and, 3) volume-change-related stresses are small with respect to the lithostatic pressure and deformation-linked stresses.

These approximations are usually valid for lithospheric-scale models, but may be violated in certain scenarios. For instance, it is well known that metamorphic phase changes occurring at crustal conditions can induce significant changes in density in localised regions that far exceed the maximum density changes thought to be appropriate for the Boussinesq approximation. In the case of partial serpentinization, for example, density can be reduced by up to 18%, and the associated volumetric strains can cause rocks to fail. This

mechanism potentially reduces the strength of the lithosphere by 30% (Escartin et al., 1997), or even more when intact rock is replaced by a serpentinized fault. Volume-change-linked stresses related to phase changes may therefore have a significant influence on the localisation of deformation when brittle failure is an important rheological feature.

The first studies proposing a compressible formulation for mantle deformation (Jarvis and McKenzie, 1980; Quareni et al., 1986; Yuen et al., 1987) made use of the so-called anelastic approximation. These studies were aimed at understanding the behaviour of deep mantle convection, while implications for lithospheric failure and deformation were not considered. In the last decades numerous studies focused on the development of numerical tools to investigate lithospheric and upper mantle geodynamical processes (e.g. Christensen, 1987; Braun and Sambridge, 1994; Fullsack, 1995; Schmalholz et al., 2001; Moresi et al., 2003; Petrunin and Sobolev, 2006; Gerya and Yuen, 2007; von Tscharner and Schmalholz, 2015). However, all of these studies employed the Boussinesq incompressible approximation. To date, relatively little effort has been made to include and discuss the effects of volumetric strains at the lithospheric scale. To our knowledge, SLIM3D (Popov and Sobolev, 2008) and DynEarthSol2D (Choi et al., 2013) are the only available numerical models that include elastic compressibility. However, these studies do not assess its implications for lithospheric scale processes.

We propose a new compressible formulation that has been implemented in the 2-D geodynamic code LaCoDe (Hasenclever, 2010; Hasenclever et al., 2011). LaCoDe solves for visco-elastic deformation, thermal convection and melting processes. It is written in MATLAB and uses an optimized assembly based on the 'blocking' and vectorization approaches described in Dabrowski et al. (2008). Stokes equations are solved using a Lagrangian mixed velocity-pressure approach with the Finite Element Method (FEM). An additional feature of LaCoDe, not discussed here, is a free-surface algorithm (Andrés-Martínez et al., 2015) that allows the tracking of the evolution of topographic relief.

The purpose of this paper is to assess the stability of the numerical im-

plementation of a visco-elastic rheology that does not assume the incompressible Boussinesq approximation and emphasize its relevance for some geological events at a lithospheric scale. We first describe the new formulation and its numerical implementation. Then we test the accuracy of our code with a series of benchmarks for viscous and elastic deformation: 1) bending of an elastic cantilever under a uniform load, 2) deformation around a viscous inclusion, 3) Rayleigh-Taylor instability, 4) steady-state thermal convection, 5) build-up of stress in a visco-elastic Maxwell body, 6) Coutte-flow of a fluid with temperature-dependent viscosity and viscous heating effects. We then present two examples of tectonic processes where compressibility might be an important mechanism: 1) volumetric strain linked to phase changes, and 2) comparison of a compressible and incompressible subducting slab. Finally, we prove that when non-linear rheologies are employed with a compressible formulation, it is more convenient to use nested Picard iterations.

2. Governing equations for compressible flow

Mantle-lithosphere deformation are considered to be a thermo-mechanical process described by the equations of continuity, conservation of momentum and conservation of energy, respectively, in a domain Ω:

$$\frac{\partial \sigma_{ij}}{\partial x_j} = -\rho g_i \tag{1}$$

$$\frac{D\rho}{Dt} + \rho \frac{\partial u_i}{\partial x_i} = q_m \tag{2}$$

$$\rho C_p \frac{DT}{Dt} = \frac{\partial}{\partial x_i}\left(\kappa \frac{\partial T}{\partial x_i}\right) + \alpha T \frac{Dp}{Dt} + H_q + H_{sh} \tag{3}$$

where ρ is density, x_i are the spatial coordinates with the indexes i, j referring to the directions x and z in a two-dimensional Cartesian coordinate system, respectively, u_i are the velocity components, σ_{ij} is the Cauchy stress tensor, g_i is the gravitational acceleration, C_p is heat capacity, T is temperature, κ is thermal conductivity, α is thermal expansivity, H_q is a heat source, and shear

heating is defined as the energy released by the inelastic work $H_{sh} = \sigma_{ij}\varepsilon_{ij}^{inel}$. The function $q_m = q(x,t)$ in eq. (2) describes the rate of mass being added (local source of mass: $q_m > 0$) or subtracted (local sink of mass: $q_m < 0$) from a region, with dimensions of mass per unit volume and unit time. Note that, when a Lagrangian frame of reference is adopted, the material time derivative $D(\cdot)/Dt$ is equal to the partial time derivative $\partial(\cdot)/\partial t$.

The set of equations (1), (2) and (3) describe the thermo-mechanical behaviour of a compressible viscous flow. Several approximations of these equations have been widely employed to address the compressibility of the mantle, such as the anelastic approximation (ALA) or the truncated anelastic approximation (TALA) (e.g. Jarvis and McKenzie, 1980; Bercovici et al., 1992; King et al., 2010). On the other hand, models studying geodynamic processes at a lithospheric scale (e.g. from rifting of continental crust tor subduction zones) widely employ the so-called incompressible Boussinesq approximation, where the continuity equation is simplified as divergence-free. In the (T)ALA approximations the dynamic pressure is assumed negligible with respect the hydrostatic pressure ($p_{dyn} << p_{total}$), leading to a depth-dependent density. We propose a formulation where the continuity equation is directly computed using its Lagrangian form, employing an equation of state that depends on the total pressure:

$$\rho(T,p) = \rho_o \left[1 - \alpha(T - T_o) + K^{-1}(p - p_o)\right] \tag{4}$$

where ρ_o, T_o, p_o are the reference density, temperature and pressure, K is the bulk modulus and p is total pressure. It is convenient to define a the reference density, for example, using the Adams-Williamson equation, or an approximation of the hydrostatic pressure, so that the volumetric changes are with respect to the reference state. If one wishes, density changes due to phase changes can be incorporated to the equation of state. The density time derivative in the continuity equation is then computed in an implicit manner, so that eq. (2) is approximated as:

$$\frac{\partial u_i^{n+1}}{\partial x_i} = \frac{1}{\rho^{n+1}} \left(q_m - \frac{\rho^{n+1} - \rho^n}{\Delta t} \right) \tag{5}$$

where the superscript n indicates the time step iteration, and Δt is the time step. The time derivative of the density introduces a non-linearity in the system of equations and eq. (2) can also be solved either in an explicit manner. A comparison between both approaches has been discussed in Heister et al. (2017) and, a priori, it is not obvious whether one approach is numerically more stable and/or more efficient than the other. By definition, the explicit approach would require less non-linear iterations than the implicit approach; however, Heister et al. (2017) concluded that both approaches yield equally accurate results at similar computational time requirements.

2.1. Mixed formulation

The implementation of a mixed formulation to solve the Stokes equations splits the Cauchy stress tensor into its deviatoric and hydrostatic components:

$$\sigma_{ij} = \tau_{ij} - p\delta_{ij} \tag{6}$$

where τ_{ij} is the deviatoric stress tensor, δ_{ij} is the Kroenecker delta and the pressure is the mean of the principal stresses $p = -\sigma_{kk}/3$. Using eq. (6), the conservation of momentum is written in terms of the deviatoric stress and pressure:

$$\frac{\partial \tau_{ij}}{\partial x_j} - \frac{\partial p}{\partial x_i} = -\rho g_i \tag{7}$$

2.2. Constitutive equation of a visco-elastic fluid

The viscous constitutive law is conveniently expressed in terms of deviatoric stress τ_{ij} and deviatoric strain rate $\dot{\varepsilon}_{ij}$:

$$\tau_{ij} = 2\eta\dot{\varepsilon}_{ij} \tag{8}$$

where η is the shear viscosity, and the deviatoric strain rate tensor is defined as:

$$\dot{\varepsilon}_{ij} = \frac{1}{2}\left(\frac{\partial u_i}{\partial x_j} + \frac{\partial u_j}{\partial x_i}\right) - \frac{1}{3}\frac{\partial u_k}{\partial x_k}\delta_{ij} \tag{9}$$

Elastic deformation is incorporated by adopting a Maxwell material model, where the visco-elastic deviatoric strain rate is the sum of the viscous and elastic

strain rates:

$$\dot{\varepsilon}_{ij} = \dot{\varepsilon}_{ij}^{visc} + \dot{\varepsilon}_{ij}^{el} = \frac{\tau_{ij}}{2\eta} + \frac{\breve{\tau}_{ij}}{2G} \tag{10}$$

where G is the shear modulus and $\breve{\tau}_{ij}$ is the objective deviatoric stress rate (e.g. Hashiguchi and Yamakawa, 2012). The Zaremba-Jaumann derivative is used to compute the objective deviatoric stress rate in eq. (10):

$$\breve{\tau}_{ij} = \frac{\partial \tau_{ij}}{\partial t} - \omega_{ik}\tau_{kj} + \tau_{ik}\omega_{kj} \tag{11}$$

where $\omega_{ij} = 1/2(\partial u_i/\partial x_j - \partial u_j/\partial x_i)$ is the spin tensor associated with the rigid body rotation. Following the implementation of large-strain elastic deformation described by Moresi et al. (2003) and Kaus (2010), $\breve{\tau}_{ij}$ is approximated by an implicit discretisation of the time derivative:

$$\breve{\tau}_{ij} \approx \frac{\tau_{ij}^{n+1} - \tau_{ij}^{n}}{\Delta t} - \omega_{ik}^{n}\tau_{kj}^{n} + \tau_{ik}^{n}\omega_{kj}^{n} \tag{12}$$

Substitution of eq. (12) into eq. (10) with subsequent rearrangement of the terms leads to the visco-elastic constitutive law:

$$\tau_{ij} = 2\eta_{eff}\dot{\varepsilon}_{ij} + \chi\widehat{\tau}_{ij} \tag{13}$$

where

$$\eta_{eff} = \frac{1}{\frac{1}{\eta} + \frac{1}{G\Delta t}} \tag{14}$$

$$\chi = \frac{1}{1 + \frac{G\Delta t}{\eta}} \tag{15}$$

$$\widehat{\tau}_{ij} = \tau_{ij}^{n} + (\omega_{ik}^{n}\tau_{kj}^{n} - \tau_{ik}^{n}\omega_{kj}^{n})\Delta t \tag{16}$$

were the "real" viscosity has been substitued by an effective viscosity η_{eff} that includes the elastic terms. A pure viscous rheology is recovered if $\Delta t \to \infty$. Note that the visco-elastic deformation obtained per time step depends on the size of the time step. However, the deformation after a certain simulation time has to be independent of the chosen time step.

2.3. Viscous creep

Two mechanisms for viscous deformation are included in our model: diffusion creep and dislocation creep (Poirier, 1985; Karato et al., 2001). Diffusion creep occurs at low stress levels, when atoms diffuse inside the crystal grains and along the grain boundaries, resulting deformation of the rock. Deformation due to dislocation creep is caused by the migration of dislocations through the crystal lattice of the rock. Both creep mechanisms are strain rate-, temperature- and pressure- dependent:

$$\eta_{dif} = \frac{1}{2}(A)^{-\frac{1}{n}}(\dot{\varepsilon}_{II}^{dif})^{\frac{1}{n}-1}\exp\left(\frac{E_a + pV_a}{nRT}\right) \tag{17}$$

$$\eta_{dis} = \frac{1}{2}(A)^{-\frac{1}{n}}(\dot{\varepsilon}_{II}^{dis})^{\frac{1}{n}-1}\exp\left(\frac{E_a + pV_a}{nRT}\right) \tag{18}$$

where A is the pre-exponential parameter, n is the power-law exponent (with $n = 1$ for diffusion creep and, theoretically, $n \approx 3$ for dislocation creep), $\dot{\varepsilon}_{II} = \sqrt{(1/2)\dot{\varepsilon}_{ij}\dot{\varepsilon}_{ij}}$ is the square root of the second invariant of the deviatoric strain rate tensor, E_a is the activation energy, V_a is the activation volume and R is the universal gas constant. We now build an effective creep viscosity, using diffusion and dislocation viscosities in parallel:

$$\frac{1}{\eta} = \frac{1}{\eta_{dif}} + \frac{1}{\eta_{dis}} \tag{19}$$

In this way, the smallest viscosity will have the largest contribution to the effective viscosity, with deformation dominated by the mechanism that has the smallest activation stress. The viscous strain tensor is then $\dot{\varepsilon}_{ij}^{visc} = \dot{\varepsilon}_{ij}^{dif} + \dot{\varepsilon}_{ij}^{dis}$ and, using the definitions (17) and (18), the diffusion and dislocation strain tensors are respectively computed as:

$$\dot{\varepsilon}_{ij}^{dif} = \frac{\tau_{ij}}{2\eta_{dif}}; \quad \dot{\varepsilon}_{ij}^{dif} = \frac{\tau_{ij}}{2\eta_{dif}} \tag{20}$$

3. Numerical implementation

LaCoDe solves the resulting set of governing equations of the thermo-mechanical problem using the FEM to generate the system of matrix equations (e.g. Hughes,

1987; Zienkiewicz and Taylor, 2005). Discretizing the domain into elements, the primary variables u, p and T are approximated using the shape functions N_u for velocity, N_p for pressure and N_T for temperature:

$$u(x,y) \approx \sum_{a=1}^{n} N_u^a(x,y)\widetilde{u}_a \tag{21}$$

$$p(x,y) \approx \sum_{a=1}^{n} N_P^a(x,y)\widetilde{p}_a \tag{22}$$

$$T(x,y) \approx \sum_{a=1}^{n} N_T^a(x,y)\widetilde{T}_a \tag{23}$$

where the subscript a is the nodal index and n is the number of nodes in the element. Employing the Galerkin procedure, the governing eqs. (1), (2) and (3) are transformed into their weak forms using the shape functions as trial functions.

The choice of the approximation space for the coupled velocity-pressure problem has to be taken carefully so that the so-called LBB (or *inf-sup*) condition is satisfied. Some combinations of approximation spaces for velocity and pressure will violate such condition and result in spurious pressure modes and/or non-converged flow solutions. In LaCoDe, the LBB condition is satisfied by using Crouzeix-Raviart triangular elements (Crouzeix and Raviart, 1973), where the velocity field is approximated by seven nodal points and quadratic interpolation enhanced by a cubic bubble function in the baricenter of the element (Fig. .1). Pressure is discontinuous with three nodal points describing a linear interpolation within each element.

In the following sections we detail the strong forms of the Stokes and thermal diffusion equations as well as their numerical implimentation, where we drop the $\widetilde{\cdot}$ from the approximated fields in order to simplify the notation. The reader is referred to FEM texbooks (e.g. Hughes, 1987; Zienkiewicz and Taylor, 2005) for more details on the method and the description of the weak formulation of the Stokes and thermal diffusion equations.

3.1. FEM formulation of thermal diffusion

The time derivatives in eq. (3) are approximated using a backward Euler discretisation:

$$\rho C_p \left(\frac{T^{n+1} - T^n}{\Delta t} \right) = \frac{\partial}{\partial x_i} \left(k \frac{\partial T^{n+1}}{\partial x_i} \right) + \alpha T^{n+1} \frac{p^{n+1} - p^n}{\Delta t} + H_r + H_{sh} \quad (24)$$

Using FEM for the spatial discretization in the space and rearranging eq. (24), we can express it in a compact matrix notation:

$$\mathbf{K}_T \mathbf{T} = \mathbf{f}_T \quad (25)$$

where the stiffness matrix is:

$$\begin{aligned} \mathbf{K}_T = \int_\Omega \nabla \mathbf{N}_T k \nabla \mathbf{N}_T d\Omega + \frac{1}{\Delta t} \int_\Omega \mathbf{N}_T^T \rho^{n+1} C_p \mathbf{N}_T d\Omega + \\ \frac{1}{\Delta t} \int_\Omega \mathbf{N}_T^T \alpha \mathbf{N}_u (\mathbf{p}^{n+1} - \mathbf{p}^n) \mathbf{N}_T d\Omega \end{aligned} \quad (26)$$

and the right-hand-side vector:

$$\mathbf{f}_T = \frac{1}{\Delta t} \int_\Omega \mathbf{N}_T^T \rho^{n+1} C_p T^n \mathbf{N}_T d\Omega + \int_\Omega \mathbf{N}_T H_r d\Omega + \int_\Omega \mathbf{N}_T H_{sh} d\Omega \quad (27)$$

We use the same shape functions for temperature as velocity, i.e. $N_T = N_u$.

3.2. FEM formulation of Stokes equations

The motion of a compressible visco-elastic flow is described by the Stokes equations (1) and (2). The weak forms of the Navier-Stokes equations can be expressed in matrix form as:

$$\int_\Omega \mathbf{B}^T \mathbf{D} \mathbf{B} \mathbf{u}^{n+1} d\Omega - \int_\Omega \mathbf{B}^T \mathbf{m} \mathbf{N}_p \mathbf{p}^{n+1} d\Omega = \int_\Omega \mathbf{N}_u^T \rho \mathbf{g} d\Omega - \int_\Omega \mathbf{B}^T \chi \widehat{\tau} d\Omega \quad (28)$$

$$\int_\Omega \mathbf{N}_p^T \mathbf{m}^T \mathbf{B} \mathbf{u}^{n+1} d\Omega = \int_\Omega \mathbf{N}_P^T \left(\frac{1}{\rho^{n+1}} \left(q_m - \frac{\rho^{n+1} - \rho^n}{\Delta t} \right) \right) d\Omega \quad (29)$$

The elemental matrix $\mathbf{B}^e$ represents the strain-displacement matrix and $\mathbf{D}^e$ is the rheology matrix that relates strain rates to deviatoric stresses:

$$\mathbf{B}^e \mathbf{u}^e = \begin{bmatrix} \frac{\partial N_u}{\partial x} & 0 \\ 0 & \frac{\partial N_u}{\partial z} \\ \frac{\partial N_u}{\partial z} & \frac{\partial N_u}{\partial x} \end{bmatrix} \begin{bmatrix} u_x \\ u_z \end{bmatrix} = \begin{bmatrix} \dot{\varepsilon}_{xx} \\ \dot{\varepsilon}_{zz} \\ \dot{\varepsilon}_{xz} \end{bmatrix} \quad (30)$$

$$\mathbf{D}^e = \eta_{eff} \begin{bmatrix} C_1 & C_2 & 0 \\ C_2 & C_1 & 0 \\ 0 & 0 & 1 \end{bmatrix} \tag{31}$$

$$\mathbf{m}^T = [1 \quad 1 \quad 0] \tag{32}$$

The $\mathbf{m}^T$ vector is necessary when the cross derivatives in the last row in of the matrix $\mathbf{B}$ are not necessary. In the compressible case the coefficients in the rheology matrix $\mathbf{D}^e$ take values of $C_1 = 4/3$ and $C_2 = -2/3$. The weak forms (28) and (29) can then be written in a compact matrix notation as:

[Figure 1 about here.]

$$\begin{pmatrix} \mathbf{A} & \mathbf{G} \\ \mathbf{G}^T & \mathbf{0} \end{pmatrix} \cdot \begin{pmatrix} \mathbf{u} \\ \mathbf{p} \end{pmatrix} = \begin{pmatrix} \mathbf{f}_1 \\ \mathbf{f}_2 \end{pmatrix} \tag{33}$$

where:

$$\mathbf{A} = \int_\Omega \mathbf{B}^T \mathbf{D} \mathbf{B} d\Omega \tag{34}$$

$$\mathbf{G} = -\int_\Omega \mathbf{B}^T \mathbf{m} \mathbf{N}_p d\Omega \tag{35}$$

$$\mathbf{f}_1 = \int_\Omega \mathbf{N}_u^T \rho \mathbf{g} d\Omega - \int_\Omega \mathbf{B}^T \chi \widehat{\tau} d\Omega \tag{36}$$

$$\mathbf{f}_2 = \int_\Omega \mathbf{N}_P^T \left(\frac{1}{\rho^{n+1}} \left(q_m - \frac{\rho^{n+1} - \rho^n}{\Delta t} \right) \right) d\Omega \tag{37}$$

and the right-hand-side vector f_2 contains the non-zero divergence terms related to density changes.

3.3. Solution scheme of Stokes equations

The expression (33) mathematically describes the so-called *saddle point* problem. Numerical complications arise due to the presence of the diagonal zero-block in the full matrix, which makes the matrix positive semi-definite, and thus it cannot be solved directly with numerical algorithms such as Conjugate Gradient or Cholesky factorization. LaCoDe solves the Stokes equation

using the Augmented Lagrangian method (Rockafellar, 1974), which consists of subtracting $\lambda^{-1}\mathbf{Mp}$ from the left- and right-hand-side of the continuity equation, and introducing the following iterative scheme:

$$\begin{pmatrix} \mathbf{A} & \mathbf{G} \\ \mathbf{G}^T & -\lambda^{-1}\mathbf{M} \end{pmatrix} \cdot \begin{pmatrix} \mathbf{u} \\ \mathbf{p} \end{pmatrix}^{k+1} = \begin{pmatrix} \mathbf{f}_1 \\ \mathbf{f}_2 - \lambda^{-1}\mathbf{M}\mathbf{p}^k \end{pmatrix} \tag{38}$$

where k is the iteration counter, λ is an artificial compressibility term penalising the new pressure term in the second row of the global matrix and has units of dynamic viscosity, and $\mathbf{M}$ is the mass matrix defined as:

$$\mathbf{M} = \int_\Omega \mathbf{N}_p^T \mathbf{N}_p d\Omega \tag{39}$$

The choice of λ is not trivial, as the block matrix might become ill-posed or numerical locking might occur if λ is either to high or too low. A value of $\lambda = max(\eta)$ has been proven to work well in our benchmarks. Upon convergence, $\mathbf{p}^{k+1} = \mathbf{p}^k$ and the system of equations (33) is recovered. The new system of equations (38) allows the elimination of the pressure field, and the first and second rows of the system are solved in a segregated manner. Rearranging the second equation we obtain the expression for the updated pressure:

$$\mathbf{p}^{k+1} = \mathbf{p}^k + \mathbf{M}^{-1}(\lambda \mathbf{G}^T \mathbf{u}^{k+1} - \mathbf{f}_2) \tag{40}$$

and after substitution of eq. (40) into the first equation in the system (38) we obtain the following linearised expression for the velocity field:

$$\mathbf{u}^{k+1} = \mathbf{K}^{-1}\mathbf{f}^{k+1} \tag{41}$$

where the stiffness matrix $\mathbf{K}$ is defined as:

$$\mathbf{K} = \left(\mathbf{A} + \mathbf{G}\lambda\mathbf{M}^{-1}\mathbf{G}^T\right) \tag{42}$$

and the force vector in the righ-hand-side is:

$$\mathbf{f}^{k+1} = \mathbf{f}_1 + \mathbf{G}\left(\lambda\mathbf{M}^{-1}\mathbf{f}_2 - \mathbf{p}^k\right) \tag{43}$$

The expression (40) is clearly non-linear because the density in $\mathbf{f}_2$ depends on the pressure via the equation of state. We treat this non-linearity by adding

a set of Picard iterations and freezing the density during the Powell-Hesteness iterations:

$$\overbrace{\nabla \cdot \mathbf{u}^{k+1} + \frac{1}{\lambda}\mathbf{p}^{k+1}}^{\text{new velocity and pressure}} = \underbrace{\frac{1}{\rho(\mathbf{P}^m, \mathbf{T}^m)}}_{\text{previous Picard iteration}} \cdot \left(q_m - \frac{\overbrace{\rho(\mathbf{P}^m, \mathbf{T}^m)}^{\text{previous Picard iteration}} - \overbrace{\rho(\mathbf{P}^n, \mathbf{T}^n)}^{\text{previous time step}}}{\Delta t} \right) = \mathbf{f}_2^m \tag{44}$$

where the superscripts k, m and n are the counters of the Powell-Hestenes, Picard and time iterations, respectively. Eqs. (40) and (41) are thus solved iteratively combining Powell-Hestenes and Picard iterations in the following scheme (Fig. .2):

1. $\mathbf{p}^0 = 0$ for $n = 1$, and $\mathbf{p}^0 = \mathbf{p}^{n-1}$ for $n > 1$.
2. Calculate: $\mathbf{K}$.
3. Calculate: $\mathbf{f}_2^m$
4. Calculate: $\mathbf{f}^{k+1}$
5. Solve: $\mathbf{u}^{k+1} = \mathbf{K}^{-1}\mathbf{f}^{k+1}$
6. Update pressure: $\mathbf{p}^{k+1} = \mathbf{p}^k + \mathbf{M}^{-1}(\lambda \mathbf{G}^T \mathbf{u}^{k+1} - \mathbf{f}_2^m)$
7. Check convergence of the continuity equation. If $|| - \mathbf{Q}^T\mathbf{u} - \mathbf{g}_2||_\infty >$Tol, and repeat steps 4 and 7.
8. If $||\mathbf{f}_2^m - \mathbf{f}_2^{m+1}||_\infty$¿Tol, repeat steps 3 to 7.

where $|| \cdot ||_\infty$ is the infinity norm. We note that for $\mathbf{p}^0 = 0$, the equations are equivalent to the penalty method. The solution scheme presented here is equivalent to the resulting schemes from Uzawa iterations (Arrow et al., 1958; Zienkiewicz, 1985) and later extended in the context of optimization independently by Hesteness (Hestenes, 1969) and Powell (Powell, 1967).

[Figure 2 about here.]

3.4. Iteration scheme for non-linear rheology

The problem described in Section 3.3 becomes even more non-linear if temperature and/or a non-Newtonian rheology are also considered. We propose two different approaches to tackle highly non-linear problems (Fig. .2): i) all the non-linearities are treated within a single loop of Picard iterations (Approach 1); and, ii) the rheological and density non-linearities are split into two levels of nested Picard iterations (Approach 2). While Approach 2 is likely to increment the total number of linear and non-linear iterations for a single time step, the rheological non-linearities are performed in a presumably better converged flow solution. The rheology iterations are stopped when the residual R is below a given tolerance:

$$R = \frac{||u^{i+1} - u^i||_\infty}{||u^{i+1}||_\infty} \leq Tol \tag{45}$$

where i is the rheology iteration counter, and we take a typical value of $Tol = 10^{-3}$. We note that this iterative scheme is able to handle other kinds of rheology non-linearities not included in this paper, such as plastic deformation. The efficiency of both methods is compared in Section 5.2.

4. Remeshing

One of the drawbacks of using a Lagrangian formulation is that large deformation of the mesh may lead to highly distorted elements. This issue is overcome by mapping the necessary variable fields onto a newly generated high quality mesh. One could perform a remeshing after every time step, but to reduce the associated computational cost and interpolation errors, a new mesh is generated only when the quality of the mesh is below a given threshold. Let us define a triangle with the area A, vertices a, b and c, and the smallest and largest angles α and β, respectively. We define the quality factor of the triangle to be:

$$q_n = \frac{4\sqrt{3}A}{||ab||^2 + ||ac||^2 + ||bc||^2} \tag{46}$$

where q_n is a measurement of how close a triangle is to be equilateral. The remeshing algorithm is called only if one (or several) triangular element has $q_n < Tol_q$, $\alpha < Tol_\alpha$ or $\beta > Tol_\beta$. Unless specified, we use values of $Tol_{q_n} = 0.25$, $Tol_\alpha = 7^\circ$ and $Tol_\beta = 170^\circ$.

For fields that are computed at the nodes (i.e. temperature), the 6-node elements are split into 3-nodes elements and the fields are linearly interpolated into the new nodal positions. The information of the fields associated with the elements (i.e. stress, density) is stored at the integration points of the elements and they are mapped onto the new mesh using the following procedure:

1. Find the element of the old mesh containing the new integration point using the quick search algorithm *tsearch2* (*Mutils* package: http://milamin.sourceforge.net/downloads).
2. Calculate local coordinates of the new integration point with respect to the element in the old mesh.
3. The field $\Psi(x, y)$ is mapped element-to-element onto the old nodes of using linear shape functions:

$$\Psi_a(x, y) = (N^a(\xi, \eta))^{-1} \Psi(x', y') \tag{47}$$

   where a is the nodal index, ξ and η are the local coordinates of the shape function and x' and y' are the coordinates of the integration point of the old mesh.
4. The nodal values of target field $\Psi_a(x, y)$ are mapped onto the new integration point using the shape functions:

$$\Psi(x^*, y^*) = \sum_{a=1}^{n} N^a(\xi, \eta) \Psi_a(x, y) \tag{48}$$

   where ξ and η are the local coordinates of the shape function and x^* and y^* are the coordinates of the integration point of the new mesh.

While this scheme works particularly well for perfect body-fitting meshes, for which each element of the new and old meshes belongs to a single material phase, other approaches may be better suited for non-body-fitting meshes. The accuracy of this remeshing scheme is demonstrated in Section 5.1.3.

[Figure 3 about here.]

5. Results

We present a set of benchmarks and numerical experiments to test the implementation of the formulation described above. We first demonstrate the accuracy of LaCoDe, comparing the results of these experiments with analytical solutions and results from previously published studies. These benchmarks are: i) bending of a thin beam under a distributed load (Turcotte and Schubert, 2014); ii) deformation around a viscous inclusion (Schmid and Podladchikov, 2003); iii) Rayleigh-Taylor instability (van Keken et al., 1997); iv) stress build-up in a visco-elastic Maxwell body (Gerya and Yuen, 2007); and v) solution of a Couette-flow with viscous heating and temperature-dependent viscosity (Turcotte and Schubert, 2014). Then, we investigate the effectiveness of the two approaches to solve problems with non-linear rheologies described in Section 3.4. Finally, two tectonic scenarios where the effect of compressibility effects is relevant are presented: i) an example of volumetric strain produced by phase changes; ii) subduction of a compressible slab.

5.1. Benchmarks

5.1.1. Cantilever beam under a uniform load

In this benchmark we compare the numerical results of a bending elastic thin plate, clamped at one end, against an analytical solution for a perfectly-elastic material (Turcotte and Schubert, 2014). We also use this benchmark to compare the accuracy of the non-linearised and linearised formulations in resolving elastic problems. The ratio between the thickness and length of the cantilever is taken to be 1/10 in order to satisfy the thin beam hypothesis. The density of the beam is $\rho = 150\ kg/m^3$ (an approximate value for the density contrast between the upper and lower crust) and the shear modulus is $G = 36\ GPa$. The analytical solution for the maximum deflection ω is,

$$\omega = \frac{3}{24}\frac{\rho g h L^4}{D} \tag{49}$$

where h and L are the height and length, respectively, and D is the so-called flexural rigidity of the plate. The latter can be expressed in terms of the Youngs

modulus E and the Poisson ratio ν: $D = Eh^3/12(1-\nu^2)$. The maximum horizontal stress in the cantilever is given by:

$$\sigma_{xx}^{max} = \frac{3gL^2}{h} \tag{50}$$

[Figure 4 about here.]

To test the mesh-dependence and the accuracy of our code we use structured meshes with different configurations of triangular elements, see Fig. .4a. We use triangles with a ratio height/length of 1 and we run the model for different numbers of elements in the vertical direction. The deformed beam and the resulting stress field of the beam with $\nu = 0.25$ are shown in Fig. .4b. The maximum deflection of the cantilever (Fig. .4c) is well-resolved for different degrees of elastic compressibility ($0.25 \leq \nu \leq 0.4999$). Convergence to the analytical solution is achieved with only 8 elements in the vertical direction with relative errors $e_\omega < 1\%$ for all the Poisson ratios and different mesh configurations. Maximum horizontal stresses show high relative errors for coarse meshes but rapidly converge to the analytical solution with $e_{\sigma_{xx}} < 2\%$ for meshes with 10 elements in the vertical direction. A good accuracy of the solver is demonstrated in both the compressible or incompressible limits. Relative errors for $\nu < 0.45$ are consistent with the results obtained employing quadrilateral elements with 4 nodes by Popov and Sobolev (2008) and 8 nodes by Quinteros et al. (2009).

5.1.2. Viscous inclusion

The model set-up (Fig. 4a) consists of a circular viscous inclusion with radius $R = 0.1$ embedded in a homogeneous matrix under pure shear boundary conditions in a square domain $\Omega = [-1,1]x[-1,1]$. The aim of this numerical experiment is to assess the accuracy of the pressure and velocity fields in cases with strong viscosity jumps. The dimensionless viscosity of the inclusion is $\eta_1 = 10^3$ and $\eta_2 = 1$ for the matrix. The domain is discretised using an unstructured mesh of triangular elements. The edges of the elements match with the interface between the inclusion and the matrix, resulting in elements belonging either to the inclusion or to the matrix. This near-perfect body-fitting mesh is the most

accurate way for the FEM to model this test (Deubelbeiss and Kaus, 2008). Velocity boundary conditions are imposed on the edges of the domain. These are obtained from the analytical solution for the velocity field (Schmid and Podladchikov, 2003) with a background strain rate $\dot{\varepsilon}_b = 1$ (Appendix B).

[Figure 5 about here.]

Total root-mean-square (rms) errors are calculated to assess the numerical accuracy of this test:

$$e_p^t = \sqrt{\frac{\int_\Omega (P - P^{ana})^2 d\Omega}{\int_\Omega (P^{ana})^2 d\Omega}} \tag{51}$$

$$e_u^t = \sqrt{\frac{\int_\Omega (u_x - u_x^{ana})^2 + (u_z - u_z^{ana})^2 d\Omega}{\int_\Omega ||u^{ana}||^2 d\Omega}} \tag{52}$$

$$e_p^{t*} = \sqrt{\int_\Omega (P - P^{ana})^2 d\Omega} \tag{53}$$

$$e_u^{t*} = \sqrt{\int_\Omega (u_x - u_x^{ana})^2 + (u_z - u_z^{ana})^2 d\Omega} \tag{54}$$

where the superscript *ana* denotes the analytical values. Pressure errors decrease with increasing numerical resolution (Fig. Appendix Db), with minimum values of rms error of $e_p^t = 2.3 \cdot 10^{-2}$ for high resolution meshes with DOF ¿ 10^5. The velocity field is accurately calculated even for coarse meshes ($DOF = 10^3$) and shows little dependence in the number of DOF, with minimum errors of $e_u^t = 3.6 \cdot 10^{-4}$ in the finest mesh (DOF ¿ 10^5). Figs. Appendix D c-d show the pressure and velocity along the horizontal plane $y = 0$ for different numerical resolutions. Coarse meshes with low number of DOFs show accurate pressure solutions in the matrix, whereas near the inclusion there is an evident drop in the accuracy of the numerical solution. High spatial resolutions (DOF ¿ 10^4) lead to smoother pressure solutions around the inclusion. The velocity along the same plane displays higher levels of accuracy, with a smooth solution around the viscosity jump even for low numerical resolutions.

Fig. Appendix D shows the analytical and numerical solutions for pressure and velocity, as well as the e_p^{t*} and e_u^{t*} distribution for the pressure and velocity fields with respect to the analytical solution. As discussed above, the highest pressure errors are located around the the contact between the inclusion and the matrix and the minimum pressure errors are distributed along the four diagonals of the domain and within the inclusion. Velocity errors are smoothly distributed over the matrix and the minimum error values occur inside the inclusion. The maximum numerical values of pressure and velocity show a difference of 2.4450% and 0.2559%, respectively, with respect to the analytical solution. These results are comparable with previous numerical benchmarks (e.g. Deubelbeiss and Kaus, 2008; von Tscharner and Schmalholz, 2015).

[Figure 6 about here.]

5.1.3. Rayleigh-Taylor instability

The purpose of this test is to benchmark viscous deformation due to convection driven by density contrasts (van Keken et al., 1997). The large deformation produced in this experiment provide an excellent way to validate not only the viscous deformation, but also the implementation of the remeshing algorithm. Both fluids are assumed to be isoviscous with equal viscosity but different density. In this test we use the dimensionless equation of conservation of momentum:

$$\frac{\partial \tau_{ij}}{\partial x_j} + \frac{\partial P}{\partial x_j} = R_b \Gamma n_j \tag{55}$$

[Figure 7 about here.]

where n_j is the unit vector in the direction j and R_b is the compositional "Rayleigh number" $R_b = \Delta\rho g h^3/\kappa\eta_r$, where η_r is the reference viscosity. Γ is a step function with $\Gamma = 1$ for the layer at the bottom and $\Gamma = 0$ for the top layer. The domain consists of a box of height h and width λ. The thickness of the bottom layer is 0.2 with an initial perturbation between the two phases given by:

$$\omega = 0.02 \cos\left(\frac{\pi x}{\lambda}\right) \tag{56}$$

Table 1: Values of growth rate, maximum rms velocity and its correspondenting time. $\delta\gamma$ and δu_{rms}^{max} denote the difference in % of the growth rate and maximum rms velocity with respect to the 'best' results from van Keken et al. (1997) (PvK code with 80x80 C1 elements).

initial num. els.	**DOF**	γ	$\delta\gamma$	u_{rms}^{max}	δu_{rms}^{max}	t^{max}
1808	10754	0.01221	0.28%	0.003110	0.61%	215
7093	42592	0.01222	0.20%	0.003080	0.36%	212
17960	107468	0.01222	0.20%	0.003075	0.52%	211

The aspect ratio of the domain ($\lambda = 0.9142$) is chosen such that a harmonic perturbation with wavelength 2λ is the most unstable, giving the largest growth rate. Displacements are restricted at the bottom and top boundaries and tangential free-slip is allowed along the lateral boundaries (Fig. .7a).

We consider only an isoviscous case with $\eta_r/\eta_o = 1$ and $\rho_r/\rho_o = 1.3$. Throughout the evolution of the flow we calculate the evolution with time of root-mean-square velocity:

$$u_{rms}(t) = \sqrt{\frac{1}{h\lambda}\int_0^{\lambda}\int_0^{1} ||u||^2 dxdz} \tag{57}$$

We use the 'best' results from van Keken et al. (1997) as a reference (Pvk code with 80x80 C1 finite elements) to validate the results obtained with LaCoDe. The Rayleigh-Taylor instability shows the same evolution (Fig. .7a-e) as the one shown by the reference results. Only a few discrepancies are found in the geometry of the secondary and tertiary diapirs in the late stages of the flow evolution. Models with coarse meshes are able to predict accurate values of the maximum rms velocity, but predict maximum rms velocities for the secondary diapir that are 13% higher than the values obtained with a finer mesh (Fig. .7f). The growth rate of the instability γ at $t = 0$ and the maximum rms velocity (Table 5.1.3) are in agreement with the reference values, with errors smaller than 1%. The increase in the difference of the maximum u_{rms} for the case with 17960 elements is due to a numerical resolution 2.8 times higher than the one employed in the reference case, presumably leading to a more accurate solution.

The remeshing algorithm is called when the quality of any element or ele-

ments of the mesh is below the quality threshold. The two fluids are discretised in the space such that their interface represents a sharp contact, with individual elements belonging to a single phase. The interface is tracked with time, and it is used to define the geometry of the new mesh. The interface between the two fluids undergoes a high amount of stretching during the evolution of the flow and it is refined during the remeshing so that its spatial resolution is constant (i.e. a new node is added to the interface if the space between two consecutive nodes is larger than a specified distance), producing a considerable increase of the number of elements in later stages.

In this numerical experiment it is sufficient to generate a new mesh and there is no actual need to transfer information from the new mesh into the new one. However for benchmarking purposes, we perform the mapping of the second invariant of the accumulated strain E_{II} onto the new high quality mesh. Fig. .7g,h shows an accurate mapping of E_{II} from the old mesh onto the new mesh. The quality of the remeshing algorithm is assessed by comparing the finite strain field before and after remeshing. In order to compare the pre- and post-remeshing results, both fields are sampled in high-resolution rectangular grid of 1000 by 1000 nodal points, where the root-mean-square error of the mapped field is computed (Fig. .7i).

5.1.4. Stress build up in a visco-elastic Maxwell body

Visco-elastic deformation is demonstrated by repeating the numerical experiment of build-up of stress in a Maxwell body under pure shear deformation (Gerya and Yuen, 2007). A constant background strain rate $\dot{\varepsilon} = 10^{-15}\ s^{-1}$ is prescribed at the boundaries of a body with a 100 by 100 km domain (Fig. .8a). The mechanical parameters are: $G = 10$ GPa, $\eta = 10^{22}$ Pa $\cdot$ s and gravity is switched off. We take $\nu = 0.4999$ in order to approximate an incompressible material. The build-up of the stress is described by the following analytical expression:

$$\tau = 2\dot{\varepsilon}_{II}(1 - exp(-\frac{Gt}{\eta})) \tag{58}$$

The analytical and numerical time-stress curves overlap (Fig. .8b,c), demonstrating the high accuracy of the implementation of the Maxwell rheology.

[Figure 8 about here.]

5.1.5. Couette flow with viscous heating and temperature dependent viscosity

[Figure 9 about here.]

The aim of this test is to demonstrate the accuracy of the numerical solution of thermal diffusion and the coupling of the Stokes equations with the conservation of energy for fluids with temperature-dependent viscosity and shear heating. The set-up of the model is consists of the Couette flow in a rectangular channel (Fig..9a). The motion of the flow is driven by shear along the top boundary of the channel with the following boundary conditions: no-slip motion ($u(z = 0) = 0$) and constant temperature ($T(z = 0) = T_0$) at the lower boundary, zero vertical pressure gradient ($\partial P/\partial z = 0$), constant shear stress and $\partial T/\partial x = 0$ at the lateral boundaries of the model. The size of the model is $\Omega = [0, 90]$x$[0, 12]$ km. This length-to-depth ratio is sufficiently large to avoid errors in the flow due to boundary effects. The model is started with T_0 across the whole domain. The analytical solution of this problem is described in the Appendix Appendix D.

The dependence of the maximum non-dimensional temperature change in the channel θ with the Brinkman number Br is used to compare the analytical solution with the numerical results, taking values of $E_a = 150$ J/mol, $R = 8.35$, $A = 10^{15}$ Pa·s, $K = 2$ W/m/K and $T_0 = 1000$ K. The results obtained with LaCoDe show an excellent agreement with the analytical solution (Fig..9), demonstrating the capability of the code to model coupled thermo-mechanical problems with non-linear rheologies and shear heating.

5.2. Non-linear rheology iterations: single vs nested Picard iterations

We test the accuracy and efficiency of these two solution schemes with two different numerical experiments: A) a visco-elastic rectangular body under pure

shear with a non-Newtonian rheology including diffusion and dislocation creep; and, B) a set-up for a subduction problem with a non-Newtonian visco-elastic rheology. In both problems, we keep track and compare the number of linear and non-linear iterations, residual velocity and computational time during the first five time steps for Test A, and six time steps for the Test B (this corresponds to the number of time steps before remeshing is required). Details of the model set-up, boundary conditions and thermo-mechanical parameters are found in Appendix Appendix A.

[Figure 10 about here.]

Results from Test A (Fig. .10a) show that, as expected, Approach 2 leads to a higher number of Powell-Hestenes iterations compared to dealing with all non-linearities in the same loop as in Approach 1, resulting in typically ~ 1.5 times more linear iterations $\sim 25\%$ more computational time per iteration. Despite being somewhat more expensive, Approach 2 yields a better-converged solution.

The efficiency of Approach 1 and 2 is further checked with the more realistic Test B, where a rheologically layered domain adds new degrees of complexity to the problem. In this case we have capped the maximum number of the outer level of Picard iterations to 60. Approach 2 converges typically within 17-30 outer Picard iterations, whereas Approach 1 constantly reaches the maximum allowed number of iterations and results in a poorly-converged solution (Fig. .10b). In this case, every time step using Approach 2 needs to perform about 2 or 3 times the number of linear iterations performed by Approach 1; however, approximately half of the rheological non-linear iterations are required, yielding a slightly cheaper solution scheme.

Considering these results, we infer that treating all the non-linearities in one level of Picard iterations (Approach 1) is more efficient in terms of total number of iterations; however, this approach yields larger residuals of the velocity field (Fig. .10). Approach 2 also becomes substantially cheaper than Approach 1 as the complexity of the problem increases because a lower number of outer Picard iterations is required. We therefore recommend to use the solution scheme as

in Approach 2 for complex and highly non-linear problems.

5.3. Numerical experiments with a compressible crust and mantle

5.3.1. Volumetric strain induced by serpentinization

The phase change from peridotite to serpentinite is accompanied by a considerable reduction in density. In this experiment, we simulate a visco-elastic oceanic lithosphere in which serpentinization occurs to different degrees. The transformation of mantle peridotites to serpentinite occurs within a specific range of pressure and temperature and with an inflow of sea water into the material. However, in the model shown here, we simplify this process by imposing a rate of density change in a target region, at a rate that reaches the maximum degree of serpentinization after 1 Myr. This experiment is designed to explore the impact of the sudden reduction of density and change of volume on the stress and strain fields.

The model is 300 km long by 100 km deep and is stretched under pure shear boundary conditions, with a full extension rate of $u_{ext} = 1$ mm/yr. Serpentinization occurs within the 40 km by 10 km rectangular area located at the centre of the model. The rheology is visco-elastic with $\eta = 10^{23}$ Pa s, $G = 36GPa$ and $\nu = 0.3$. The density of the serpentinized material is calculated as a linear function of β (Escartin et al., 2001):

$$\rho(\beta) = \rho_{serp}\left(1 - \frac{\beta}{100}\right)(\rho_o - \rho_{serp}) \tag{59}$$

where β is the percent of serpentinization. We take a $\rho_o = 3300$ kg/m^3 characteristic of mantle material and $\rho_{serp} = 2550\ kg/m^3$. We run a set of models with different values of degree of serpentinization ($\beta = 0$, 20 and 40%).

[Figure 11 about here.]

It is known that at these values of serpentinization, significant weakening of the lithosphere might occur (Escartin et al., 1997). Considering a pressure dependent failure criterion such as Drucker-Prager , $\tau_y = p\sin(\phi) + C\cos(\phi)$, and assuming a friction angle $\phi = 30°$ and cohesion $C = 30$ MPa (dashed

line in Fig..11b), it becomes evident that the stress linked to the volumetric increased caused by serpentinization reactions can easily exceed the yield stress at shallow depths (at ~ 2 km for $\beta = 20\%$ and ~ 10 km for $\beta = 20\%$; Fig..11b), thus localising, or enhancing, inelastic deformation in faults and shear bands. Topographic expressions in the sea-floor could also be linked to the production of serpentinite at shallow depths (Fig..11c). Our models predict topographic highs from 0.3 km and 0.7 km for a partially serpentinized material for $\beta = 20\%$ and $\beta = 40\%$, respectively.

For comparison, we include a model with $\beta = 40\%$ using the incompressible Boussinesq approximation (i.e. the continuity equation is approximated as $\nabla \cdot \mathbf{u} = 0$). The incompressible approximation is not able to resolve the volumetric strains and the flow solution only accounts for the buoyancy forces produced by the serpentinization. Therefore, the strain field is barely affected by the phase change and the stress field is incorrect, showing even lower stresses than for $\beta = 0\%$ (Fig..11b). Furthermore, the pressure dependence of the density in this model is switched off or it would become unstable after few time steps.

Even though the model considered here is very simple, and more realistic set-ups and conditions might change the values of the effect of serpentinization (e.g. plastic deformation, rheological layering, etc.), it serves as an example for how the volumetric strain produced by a phase change can potentially weaken the crust and localise brittle deformation. Therefore, weakening by serpentinization may play a crucial role to shape the kinematics of magma-poor margins and the bending/unbending of subducting plates (Phipps Morgan, 2001). This numerical example also shows that the incompressible Boussinesq approximation is not able to deal with large density changes and predicts unrealistic strain and stress fields. Instead, a compressible formulation should be used.

5.3.2. Subduction of a compressible slab

[Figure 12 about here.]

In subduction zones, the cold subducting plate is rapidly buried to great depths. Hence the subducting slab is subject to considerable pressure changes that imply

large variations of the density. In this test, we investigate how large these density variations can be for a compressible mantle and lithosphere, and whether they eventually become large enough ($> 10\%$) so that the Boussinesq approximation becomes inaccurate. We employ a non-Newtonian visco-elastic rheology and the mechanical parameters, set-up and boundary conditions for subduction are described in Appendix A.2. The thermal ages of the oceanic and continental lithospheres are 70 Ma and 400 Ma, respectively. For completeness, we compare results of obtained with compressible ($\nu = 0.30$) and incompressible mantle-lithosphere. In the latter, incompressibility is approximated by using a Poison ratio of $\nu = 0.4999$. In the compressible case, ridge push boundary conditions are applied until 4 Ma. At this moment, the tip of the slab is dense enough for slab-pull to become effective, and no additional forces are required to sustain the subduction of the oceanic lithosphere. The density in the incompressible case is lower, and ridge push boundary conditions need to be prescribed until 5 Ma.

At 3.5 Ma, while ridge push is still active, the compressible oceanic lithosphere has subducted 297 km and the dip at its tip is 60° (Fig. .12a). After slab-pull becomes effective, the trench starts to retreat and the slab rolls-back. At 7.1 Ma, the pressure at the tip of the slab is high enough to produce density variations with respect to the reference state that exceed the accuracy threshold of the Boussinesq approximation (Fig. .12a). At this point the trench has retreated 114 km, the slab is 14° steeper, and has further subducted down to 477 km depth (Fig. .12a).

In the incompressible case, the oceanic lithosphere has subducted to a depth comparable to the compressible case. However, the dip of the incompresible slab is 10° less. Furthermore, at 7.1 Ma the incompressible slab will subduct only another 73 km (even if ridge push lasts an additional million year), whereas the compressible slab subducts extra 180 km with respect to the depth at 3.5 Ma.

This simple numerical experiments illustrates how compressibility is a mechanical feature that is certainly important to account for in models of subducting slabs. The enormous pressures that build up at the tip of the slab lead to

density variations of more than 10% that affects the timing and effectiveness of slab pull, and the dynamics of subduction.

6. Discussion and summary

1. An implicit approach of the general compressible Stokes equation can be well resolved using iterative solvers such as the Augmented Lagrangian Method.
2. The dependency on density of the compressible continuity equation introduces an additional non-linearity into the problem, with respect to the incompressible approximation, thus increasing the total number of iterations per time step. We find that for non-Newtonian rheologies, one could treat all the non-linearities within one Picard loop. However, as the complexity of the problem increases, it becomes convenient to split the non-linearities with a rheological nature from the ones raising from the continuity equation into two levels of Picard iterations, as it leads to faster convergence rates and better resolved solutions. Even if not considered in this paper, the latter scheme holds if other non-linear rheological features are incorporated in the model, such as plastic deformation.
3. While the Boussinesq approximation is a valid hypothesis for simple modeling of crustal deformation, more complex models that aim to study processes such as phase changes or subduction of oceanic lithosphere will require a modification of the Boussinesq approximation to accommodate the effects of volumetric strains and volume-change-linked stresses.
4. Benchmarks for elastic deformation and stresses show that the formulation presented here is able to model elasticity both for compressible materials and in the incompressible limit.
5. The accuracy of LaCoDe for viscous deformation has been demonstrated. The velocity and pressure fields from the viscous inclusion test are consistent the analytical solutions. The benchmarks of compositional convection is also in agreement with previous benchmarks.

6. The agreement of the numerical and analytical solution of a Couette flow with viscous heating and temperature dependent viscosity demonstrates the accuracy of LaCoDe to solve thermo-mechanical problems.
7. The inclusion of a self-consistent volume change source term is a powerful tool that opens an opportunity to study the effects of overpressure caused by the inflow and outflow of mass into geological features (e.g. serpentinization and melt extraction). Exploring these processes will be the goal of future work.

Appendix A. Model set-up and boundary conditions for tests in Section 3.4

Appendix A.1. Test A: Pure shear deformation of a non-Newtonian visco-elastic body

The initial size of the models is a 500 km by 400 km rectangular box with an initial temperature profile as shown in (Fig. .13a). We use a non-Newtonian visco-elastic with the thermo-mechanical parameters of wet olivine (Table Appendix A.2). Pure shear far-field boundary conditions are prescribed in the boundaries of the model (i.e. half and full extension rate are prescribed at the lateral and bottom boundaries of the domain, respectively), the boundaries of the model are thermally insulated and tangential free slip condition are prescribed at the lateral and bottom boundaries. Temperature is fixed at 0 $^{\circ}C$ and 1300 $^{\circ}C$ at the surface and bottom of the model. A free-surface algorithm is employed to calculate the dynamic response of the topography (Andrés-Martínez et al., 2015). The domain of the model is discretised by an unstructured mesh of 13828 triangular elements (42271 DOFs).

Appendix A.2. Test B: Subduction initiation

The set-up of Test B correspond to a subduction problem with a size of 3000 km by 1500 km. The oceanic and continental lithosphere are 80 km and 140 km thick, respectively. The motion of the bottom and lateral sides is fixed, and convergence boundary velocity conditions are prescribed in a vertical profile along

the oceanic lithosphere 500 km before the trench. We use a non-Newtonian visco-elastic rheology with a wet quartzic crust, dry olivine continental lithosphere and wet olivine for the oceanic lithosphere and asthenosphere. All the boundaries except the surface are thermally insulating; bottom and top temperatures are constant at 0 $°C$ and 1300 $°C$ at the surface; and free surface boundary conditions are prescribed at the top of the model. The initial thermal structure is given by continental lithosphere with a thermal age of 500 Ma and an oceanic lithosphere with a thermal age of 75 Ma. To ease the subduction initiation, we introduce a weak layer between the oceanic and continental lithospheres with a constant viscosity of $5 \cdot 10^{19}$ Pa·s. The domain of the model is discretised by an unstructured mesh of 17927 triangular elements (55107 DOFs).

[Figure 13 about here.]

Table A.2: Rheological parameters. Wet quartzite from Gleason and Tullis (1995) and dry olivine and wet olivine from Hirth and Kohlstedt (2003), respectively.

Parameter	Units	Wet Olivine	Dry Olivine	Wet Quartzite
c	MPa	20	20	20
ρ	kgm^{-3}	3300	3300	2850
G	GPa	74	74	36
α	-	$3 \cdot 10^{-5}$	$3 \cdot 10^{-5}$	$2.4 \cdot 10^{-5}$
H_Q	Wm^{-3}	0	0	$0.2 \cdot 10^{6}$
K	$Wm^{-3}K^{-3}$	3.3	3.3	2.5
$log_{10}(A)$	$Pa^{-n}s^{-1}$	-15.56	-15.56	-28
E	$KJmol^{-3}$	480	530	223
$log_{10}(V_o)$	m^3mol^{-3}	-6	-6	1
n_{dis}	-	3.5	3.5	4
n_{dif}	-	1	1	0

Appendix B. Analytical solution for a thin beam under uniform load

The general equation describing the deflection ω of an elastic cantilever of length L and thickness h is given by:

$$D\frac{d^4\omega}{dx^4} = q(x) - p\frac{d^2\omega}{dx^2} \tag{B.1}$$

where $q(x)$ is the load and p is the pressure. Considering $p = 0$ and a constant and uniform load, eq. (B.1) yields:

$$\frac{d^4\omega}{dx^4} = \frac{q}{D} \tag{B.2}$$

Eq. (B.2) can be integrated using the following boundary conditions: 1) $\omega = 0$ at $x = 0$ (fixed end); 2) $d\omega/dx = 0$ at $x = 0$; 3) $d\omega^2/dx^2 = 0$ at $x = L$; and, 4) $dM/dx = V$, where M is the bending momentum and V is the shear force. After some algebra, the solution can be written as:

$$\omega = \frac{qx^2}{D}\left(\frac{x^2}{24} + \frac{Lx}{6} + \frac{L^2}{4}\right) \tag{B.3}$$

with the q being the gravitational load $q = g\rho Lh$. The horizontal stress along the cantilever is given by the expression:

$$\sigma_{xx} = \frac{E}{1-\nu^2}\varepsilon_{xx} \tag{B.4}$$

the horizontal strain is given by:

$$\varepsilon_{xx} = -z\frac{d^2\omega}{dx^2} \tag{B.5}$$

and the bending momentum at $x = 0$ is:

$$M = -\frac{qL^2}{h} \tag{B.6}$$

The maximum bending stress at $x = 0$ in a cantilever, centred at $z = 0$, occurs at $z = \pm h/2$ and it is obtained combining eqs. (B.4), (B.5) and (B.6):

$$\sigma_{xx}^{max} = \frac{3qL^2}{h^2} \tag{B.7}$$

Appendix C. Analytical solution for a viscous inclusion

The analytical solution of a viscous inclusion within a homogeneous matrix is based on Muskhelishvili's complex variable stress-function method and solution (Muskhelishvili, 1953) for 2D elasticity. Here we present a brief description with the solution under pure shear conditions. A more detailed description in the geological literature is found in Schmid and Podladchikov (2003). The coordinates are expressed in the complex plane:

$$z = x + iy \tag{C.1}$$

where $i = \sqrt{-1}$. For a slow incompressible viscous flow in plane strain, the velocity field can be expressed in terms of the complex functions $\phi(z)$ and $\psi(z)$:

$$u_x + iu_z = \frac{\phi(z) - z\overline{\phi'(z)} - \overline{\psi(z)}}{2\eta} \tag{C.2}$$

where the overbar refers to the complex conjugate and the prime refers to the derivative with respect to z. Under pure shear boundary conditions the functions $\phi(z)$ and $\psi(z)$ in the matrix are given by:

$$\phi_m(z) = -\frac{2\dot{\varepsilon}Ar_c^2}{z} \tag{C.3}$$

$$\psi_m(z) = -2\dot{\varepsilon}\eta_m z - \frac{2\dot{\varepsilon}Ar_c^4}{z^3} \tag{C.4}$$

with

$$A = \frac{\eta_m\left(\eta_c - \eta_m\right)}{\eta_c + \eta_m} \tag{C.5}$$

where r_c is the radius of the inclusion and η_m and η_c are the viscosities of the matrix and the inclusion, respectively. Inside the inclusion:

$$\phi_c(z) = 0 \tag{C.6}$$

$$\psi_c(z) = -4\dot{\varepsilon}\frac{\eta_c\eta_m}{\eta_c + \eta_m}z \tag{C.7}$$

Substitution of eqs. (C.3) and (C.4) into (C.2) yields the analytical solution for the velocity field in the matrix:

$$u_x + iu_z = \frac{\dot{\varepsilon} A r_c^2}{\eta_m} \left[-\frac{1}{z} + \frac{z}{\overline{z^2}} - \frac{1}{\overline{z^3}} - \frac{\overline{z}\eta_m}{A r_c^2} \right] \tag{C.8}$$

Substitution of (C.6) and (C.7) into (C.2) give the analytical solution for the velocity inside the inclusion:

$$u_x + iu_z = -\frac{4\dot{\varepsilon}}{2\eta_c} \frac{\eta_c \eta_m}{\eta_c + \eta_m} \overline{z} \tag{C.9}$$

The general expression of the pressure field is given by:

$$p = -2Re(\phi'(z)) \tag{C.10}$$

with $Re(\cdot)$ denoting the real part of $(\cdot)$. Under pure shear boundary conditions the pressure field in the inclusion is $p_c = 0$ and the pressure in the matrix is given by:

$$p_m = -2Re\left(\frac{2\dot{\varepsilon} A r_c^2}{z^2} \right) \tag{C.11}$$

Appendix D. Analytical solution for a Couette flow with viscous heating and temperature dependent viscosity

The non-Newtonian viscosity of the flow is controlled by the following equation (Turcotte and Schubert, 2014):

$$\eta = A \exp\left[\frac{E_a}{R T_0} \left(1 - \frac{T - T_0}{T_0} \right) \right] \tag{D.1}$$

where E_a is the activation energy, R is the gas constant and A is a pre-exponential factor that depends on the material. The analytical solution of the temperature field of the flow is described by the following set of equations (Turcotte and Schubert, 2014):

$$x = \frac{L}{B} ln \left[\frac{(D - B)(C - B)}{(D - B)(C + B)} \right] \tag{D.2}$$

$$B = ln \left[\frac{1 + \left(1 - \frac{2Br}{B^2}\right)^2}{1 + \left(1 + \frac{2Br}{B^2}\right)^2} \right] \tag{D.3}$$

$$C = \sqrt{2(\phi_1 - \phi(x))Br} \tag{D.4}$$

$$D = \sqrt{2(\phi_1 - 1)Br} \tag{D.5}$$

$$\phi(x) = exp(\theta(x)) \tag{D.6}$$

$$\theta(x) = \frac{E_a T(x) - T_0}{RT_0^2} \tag{D.7}$$

$$\phi_1 = \frac{B^2}{2Br} = exp(\theta_1) \tag{D.8}$$

$$\theta_1 = \frac{E_a(T_1 - T_0)}{RT_0^2} \tag{D.9}$$

$$Br = \frac{(\sigma_{xz1}L)^2 E_a}{KART_0^2} exp\left(-\frac{E_a}{RT_0}\right) \tag{D.10}$$

where Br is the non-dimensional Brinkman number, θ is the non-dimensional temperature change, σ_{xz1} is the shear stress at the top boundary, K is the thermal conductivity and T_1 is the temperature at the top boundary. If non-negative values of B are chosen, the Brinkman number can be calculated as (Gerya, 2009):

$$Br = \frac{B^2}{2}\left[1 - \left(\frac{exp(B) - 1}{exp(B) + 1}\right)\right] \tag{D.11}$$

For a given σ_{xz} the solution is non-unique and two flows with different temperature and velocity exist. However, a unique solution exists if a given velocity is prescribed at the upper boundary. Therefore, we prescribe a constant horizontal velocity boundary u^* at the upper boundary instead of imposing a constant shear stress.

References

Andrés-Martínez, M., Morgan, J. P., Pérez-Gussinyé, M., Rüpke, L., 2015. A new free-surface stabilization algorithm for geodynamical modelling: Theory and numerical tests. Physics of the Earth and Planetary Interiors 246, 41–51.

Arrow, K. J., Hurwicz, L., Uzawa, H., Chenery, H. B., 1958. Studies in linear and non-linear programming. Stanford University Press.

Bercovici, D., Schubert, G., Glatzmaier, G. A., 1992. Three-dimensional convection of an infinite-prandtl-number compressible fluid in a basally heated spherical shell. Journal of Fluid Mechanics 239, 683–719.

Braun, J., Sambridge, M., 1994. Dynamical Lagrangian Remeshing (dlr): a new algorithm for solving large strain deformation problems and its application to fault-propagation folding. Earth and Planetary Science Letters 124 (1), 211–220.

Choi, E., Tan, E., Lavier, L., Calo, V. M., 2013. DynEarthSol2D: An efficient unstructured finite element method to study long-term tectonic deformation. Journal of Geophysical Research: Solid Earth 118 (5), 2429–2444.

Christensen, U. R., 1987. Some geodynamical effects of anisotropic viscosity. Geophysical Journal International 91 (3), 711–736.

Crouzeix, M., Raviart, P.-A., 1973. Conforming and nonconforming finite element methods for solving the stationary stokes equations i. Revue française d'automatique, informatique, recherche opérationnelle. Mathématique 7 (3), 33–75.

Dabrowski, M., Krotkiewski, M., Schmid, D. W., 2008. MILAMIN: MATLAB-based finite element method solver for large problems. Geochemistry, Geophysics, Geosystems 9 (4), 1–24.

Deubelbeiss, Y., Kaus, B., 2008. Comparison of Eulerian and Lagrangian numerical techniques for the stokes equations in the presence of strongly varying viscosity. Physics of the Earth and Planetary Interiors 171 (1), 92–111.

Escartin, J., Hirth, G., Evans, B., 1997. Effects of serpentinization on the lithospheric strength and the style of normal faulting at slow-spreading ridges. Earth and Planetary Science Letters 151 (3), 181–189.

Escartin, J., Hirth, G., Evans, B., 2001. Strength of slightly serpentinized peridotites: Implications for the tectonics of oceanic lithosphere. Geology 29 (11), 1023–1026.

Fullsack, P., 1995. An arbitrary Lagrangian-Eulerian formulation for creeping flows and its application in tectonic models. Geophysical Journal International 120 (1), 1–23.

Gerya, T., 2009. Introduction to numerical geodynamic modelling. Cambridge University Press.

Gerya, T. V., Yuen, D. A., 2007. Robust characteristics method for modelling multiphase visco-elasto-plastic thermo-mechanical problems. Physics of the Earth and Planetary Interiors 163 (1), 83–105.

Gleason, G. C., Tullis, J., 1995. A flow law for dislocation creep of quartz aggregates determined with the molten salt cell. Tectonophysics 247 (1), 1–23.

Gray, D. D., Giorgini, A., 1976. The validity of the Boussinesq approximation for liquids and gases. International Journal of Heat and Mass Transfer 19 (5), 545–551.

Hasenclever, J., 2010. Modeling mantle flow and melting processes at mid-ocean ridges and subduction zones. Development and application of numerical models.

Hasenclever, J., Morgan, J. P., Hort, M., Rüpke, L. H., 2011. 2D and 3D numerical models on compositionally buoyant diapirs in the mantle wedge. Earth and Planetary Science Letters 311 (1), 53–68.

Hashiguchi, K., Yamakawa, Y., 2012. Introduction to finite strain theory for continuum elasto-plasticity. John Wiley & Sons.

Heister, T., Dannberg, J., Gassmöller, R., Bangerth, W., 2017. High accuracy mantle convection simulation through modern numerical methods–ii: realistic models and problems. Geophysical Journal International 210 (2), 833–851.

Hestenes, M. R., 1969. Multiplier and gradient methods. Journal of optimization theory and applications 4 (5), 303–320.

Hirth, G., Kohlstedt, D., 2003. Rheology of the upper mantle and the mantle wedge: A view from the experimentalists. Inside the subduction Factory, 83–105.

Hughes, T., 1987. The Finite Element Method: linear static and dynamic finite element analysis, 1st Edition. Englewood Cliffs: Prentice-Hall.

Jarvis, G. T., McKenzie, D. P., 1980. Convection in a compressible fluid with infinite Prandtl number. Journal of Fluid Mechanics 96 (3), 515–583.

Karato, S.-i., Riedel, M. R., Yuen, D. A., 2001. Rheological structure and deformation of subducted slabs in the mantle transition zone: implications for mantle circulation and deep earthquakes. Physics of the Earth and Planetary Interiors 127 (1), 83–108.

Kaus, B. J., mar 2010. Factors that control the angle of shear bands in geodynamic numerical models of brittle deformation. Tectonophysics 484 (1-4), 36–47.

King, S. D., Lee, C., Van Keken, P. E., Leng, W., Zhong, S., Tan, E., Tosi, N., Kameyama, M. C., 2010. A community benchmark for 2-d cartesian compressible convection in the earth's mantle. Geophysical Journal International 180 (1), 73–87.

Moresi, L., Dufour, F., Mühlhaus, H.-B., 2003. A Lagrangian integration point Finite Element Eethod for large deformation modeling of viscoelastic geomaterials. Journal of Computational Physics 184 (2), 476–497.

Muskhelishvili, N., 1953. Some Basic Problems Of The Mathematical Theory Of Elasticity. Oxford University Press, Bombay.

Petrunin, A., Sobolev, S. V., 2006. What controls thickness of sediments and lithospheric deformation at a pull-apart basin? Geology 34 (5), 389–392. URL http://geology.gsapubs.org/content/34/5/389.abstract

Phipps Morgan, J., 2001. The role of serpentinization and serpentinization in bending and unbending the subducting slab. AGU 82, F1154.

Poirier, J.-P., 1985. Creep of crystals: high-temperature deformation processes in metals, ceramics and minerals. Cambridge University Press.

Popov, A. A., Sobolev, S. V., 2008. SLIM3D: A tool for three-dimensional thermomechanical modeling of lithospheric deformation with elasto-visco-plastic rheology. Physics of the Earth and Planetary Interiors 171 (1-4), 55–75.

Powell, M. J., 1967. " A method for non-linear constraints in minimization problems". UKAEA.

Quareni, F., Yuen, D. A., Saari, M. R., 1986. Adiabaticity and viscosity in deep mantle convection. Geophysical Research Letters 13 (1), 38–41.

Quinteros, J., Ramos, V. a., Jacovkis, P. M., 2009. An elasto-visco-plastic model using the Finite Element Method for crustal and lithospheric deformation. Journal of Geodynamics 48 (2), 83–94.

Rockafellar, R. T., 1974. Augmented lagrange multiplier functions and duality in nonconvex programming. SIAM Journal on Control 12 (2), 268–285.

Schmalholz, S., Podladchikov, Y., Schmid, D., 2001. A spectral/finite difference method for simulating large deformations of heterogeneous, viscoelastic materials. Geophysical Journal International 145 (1), 199–208.

Schmid, D. W., Podladchikov, Y. Y., 2003. Analytical solutions for deformable elliptical inclusions in general shear. Geophysical Journal International 155 (1), 269–288.

867 Spiegel, E. A., Veronis, G., 1959. On the Boussinesq approximation for a com-
868 pressible fluid. Astrophysical Journal 131, 442.

869 Turcotte, D. L., Schubert, G., 2014. Geodynamics. Cambridge University Press.

870 van Keken, P., King, S., Schmeling, H., Christensen, U., Neumeister, D., Doin,
871 M.-P., 1997. A comparison of methods for the modeling of thermochemical
872 convection. Journal of Geophysical Research: Solid Earth 102 (B10), 22477–
873 22495.

874 von Tscharner, M., Schmalholz, S., 2015. A 3-D Lagrangian Finite Element
875 algorithm with remeshing for simulating large-strain hydrodynamic instabil-
876 ities in power law viscoelastic fluids. Geochemistry, Geophysics, Geosystems
877 16 (1), 215–245.

878 Yuen, D. A., Quareni, F., Hong, H.-J., 1987. Effects from equation of state and
879 rheology in dissipative heating in compressible mantle convection. Nature
880 326 (6108), 67.

881 Zienkiewicz, O., 1985. Iterative method for constrained and mixed approxima-
882 tion. An inexpensive improvement of F.E.M. performance. Computer Methods
883 in Applied Mechanics and Engineering 51, 3–29.

884 Zienkiewicz, O. C., Taylor, R. L., 2005. The Finite Element Method for Solid
885 and Structural Mechanics, 6th Edition. Elsevier.

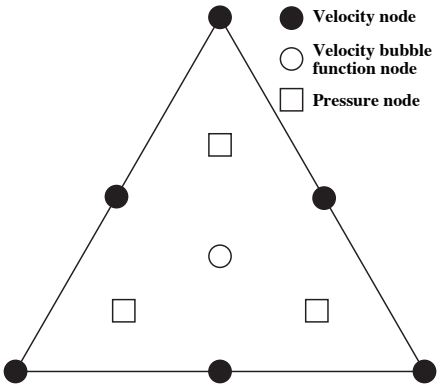

Figure .1: Crouzeix-Raviart triangular element. These elements are characterised by continuous quadratic velocities with cubic bubble function in the baricenter of the triangle and discontinuous linear pressure and show quadratic convergence.

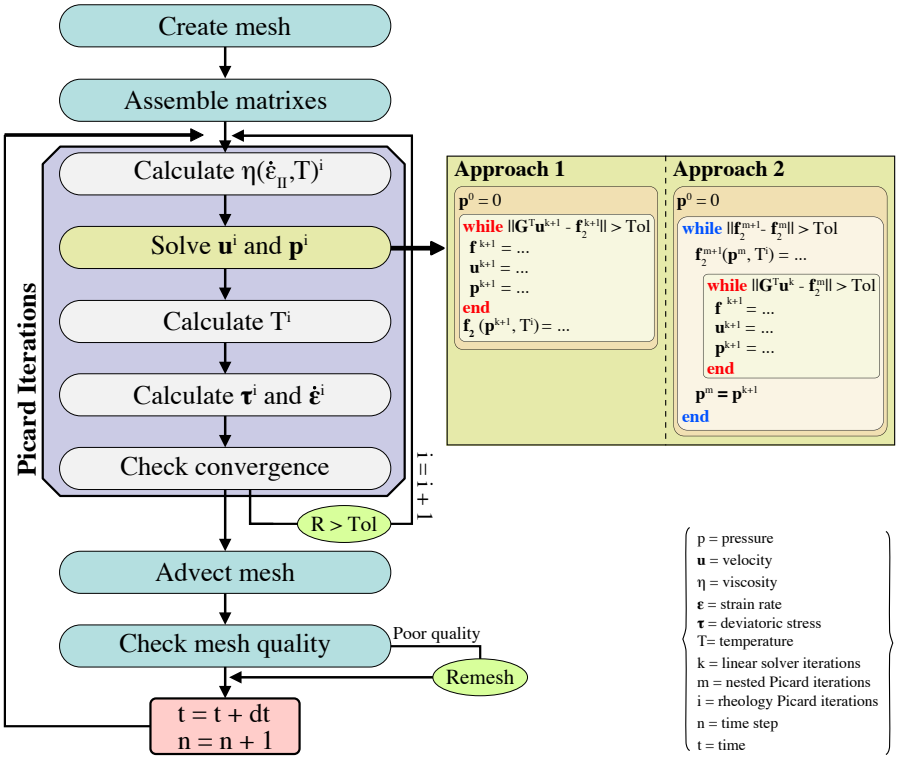

Figure .2: Global work flow of the code.

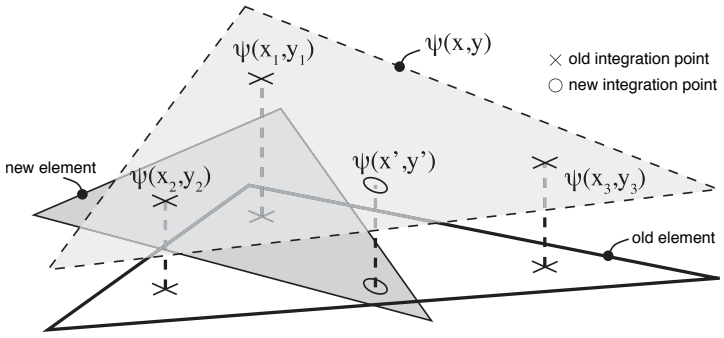

Figure .3: The information stored at the integration points of the elements of the old mesh is mapped into the new elements using the shape functions as interpolation functions. For simplicity, the field $\Psi(x, y)$ depicted in this sketch is assumed to be linear.

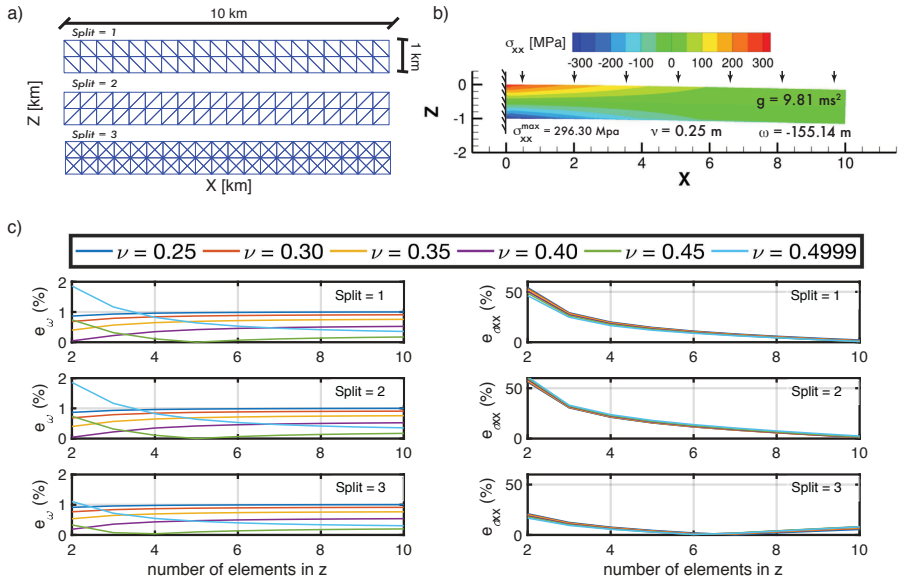

Figure .4: **a)** Structured triangular meshes with different element orientations. **b)** Set-up for the cantilever problem and flexure and stress field after loading for $\nu = 0.25$. **c)** Relative errors of the maximum deflection and bending stress for a thin beam embedded in one side and subjected to a uniform loading.

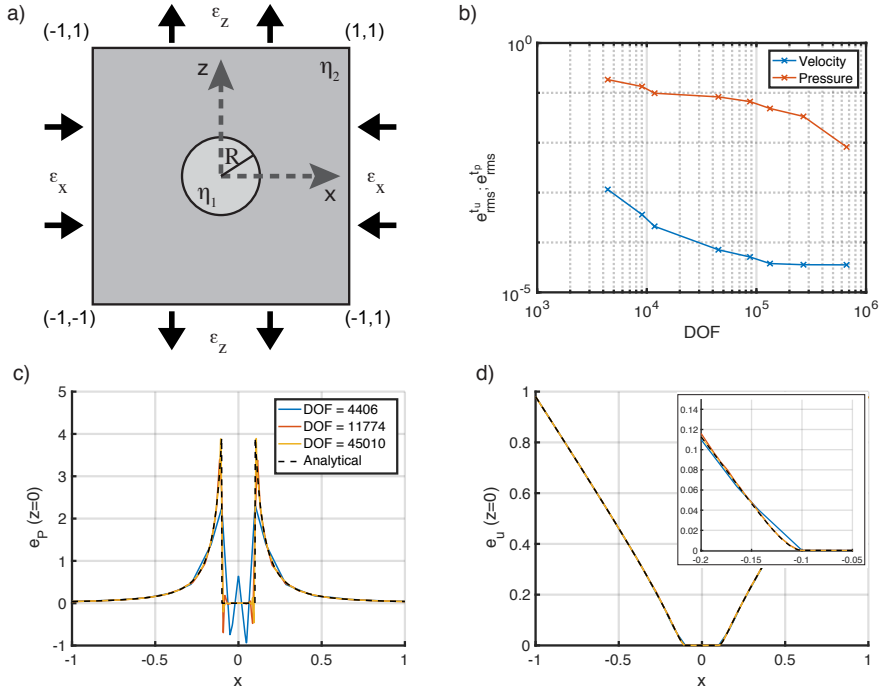

Figure .5: **a)** Set-up of a viscous inclusion with radius R and viscosity η_1 within a homogeneous matrix with viscosity η_2 and equal height and width. **b)** The domain is discretised with triangular elements so that the edges of the elements near-perfectly fit the boundary between the inclusion and the matrix. Comparison of the analytical solution for **c)** pressure and **d)** velocity along the plane $z = 0$ for numerical solutions with increasing numbers of DOF. The inset in d) shows the smooth transition in the velocity field with increasing number of DOF.

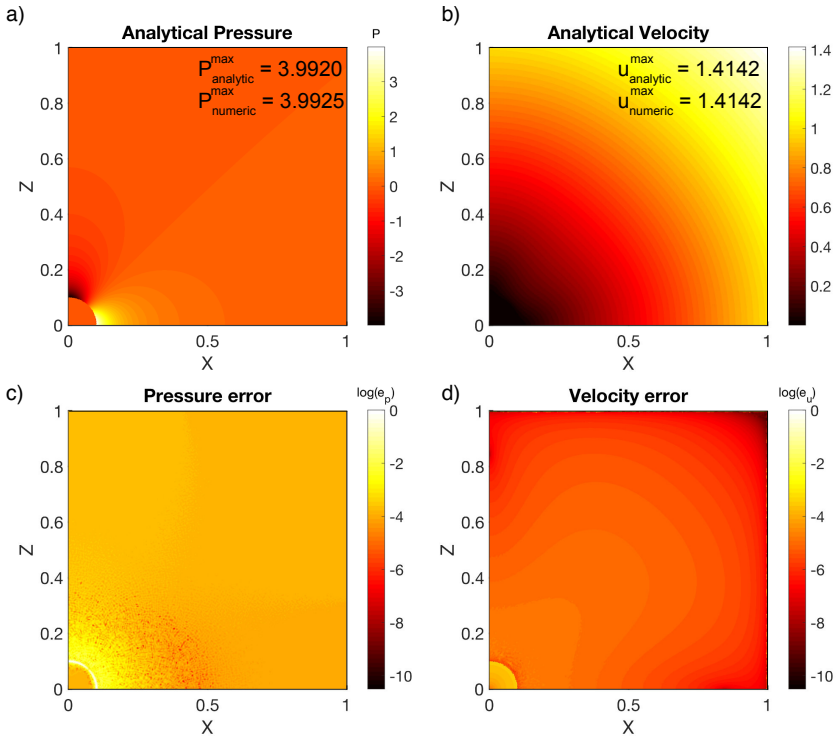

Figure .6: Numerical solutions of the **a)** pressure and **b)** velocity fields; and distribution of the logarithmic rms error of **c)** pressure and **d)** velocity. The zoom-in in d) shows the zero velocity error in the boundaries of the domain. Due to the symmetry of the pressure and velocity fields, only the upper-right corner of the domain ($\Omega' = [0,1]x[0,1]$) is shown in this figure. The results shown here correspond to a mesh with $6.65 \cdot 10^5$ DOF.

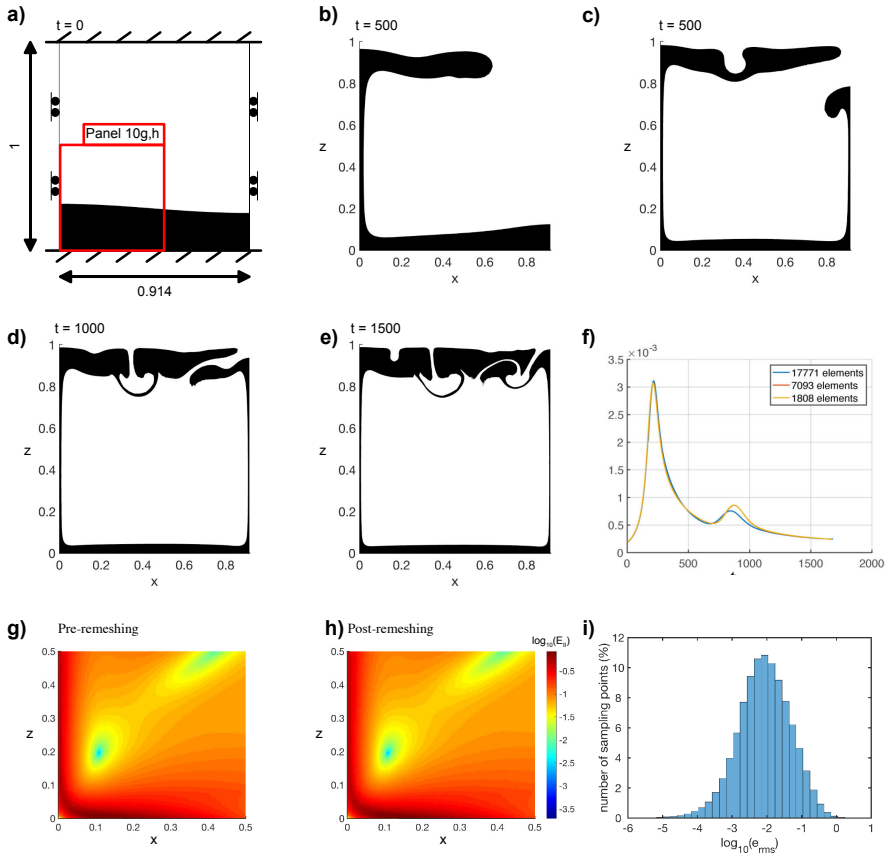

Figure .7: **a-e)** Temporal evolution of the Rayleigh-Taylor instability. **g)** Evolution of u_{rms}. Remeshing of the domain is necessary when the mesh becomes highly distorted. Note that the red lines is overlapped by the blue line. **g-h)** Comparison between the second invariant of strain E_{II} field in a mesh with heavily distorted elements and the accumulated square root of second invariant of the strain rate interpolated into a new mesh. **i)** Histogram showing the logarithm of the error between the accumulated square root of second invariant of the strain rate, pre and post remeshing

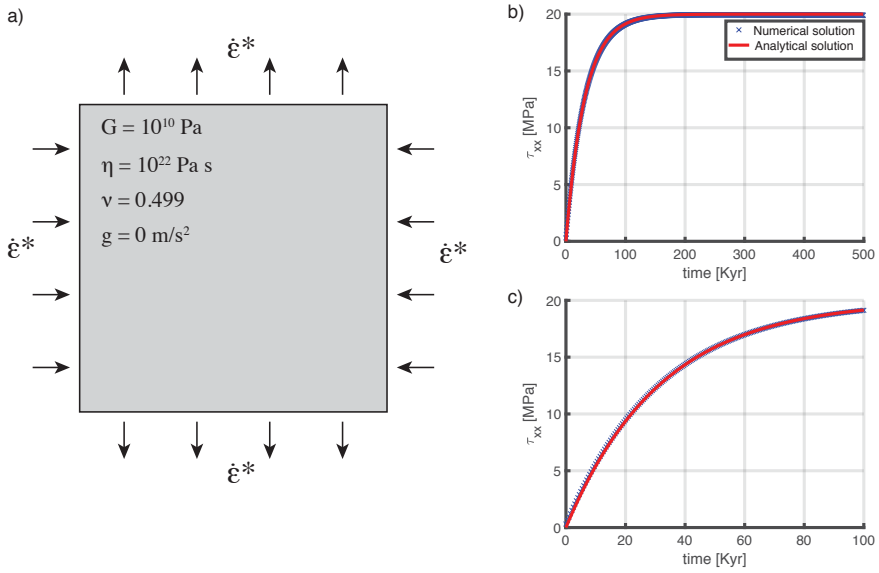

Figure .8: **a)** Set-up for the stress build-up experiment: a rectangular body is deformed with a constant background strain rate under pure shear boundary conditions. **b)** Comparison of the stress between the analytical solution and the numerical results. **c)** Zoom in the stress-time curve in the visco-elastic regime.

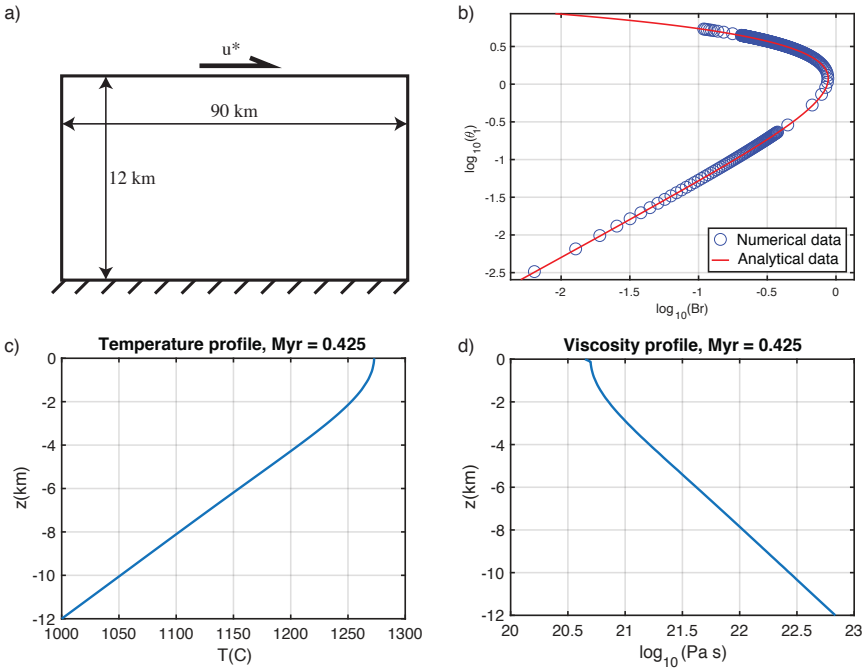

Figure .9: **a)** Set-up for Couette flow: the velocity at the bottom is u=0 and constant velocity u^* is prescribed at the top boundary. **b)** Analytical and numerical relationship between the Brinkman number and the non-dimensional temperature at the top of the Couette flow. Vertical **c)** temperature and viscosity **d)** profiles after 0.425 Myrs.

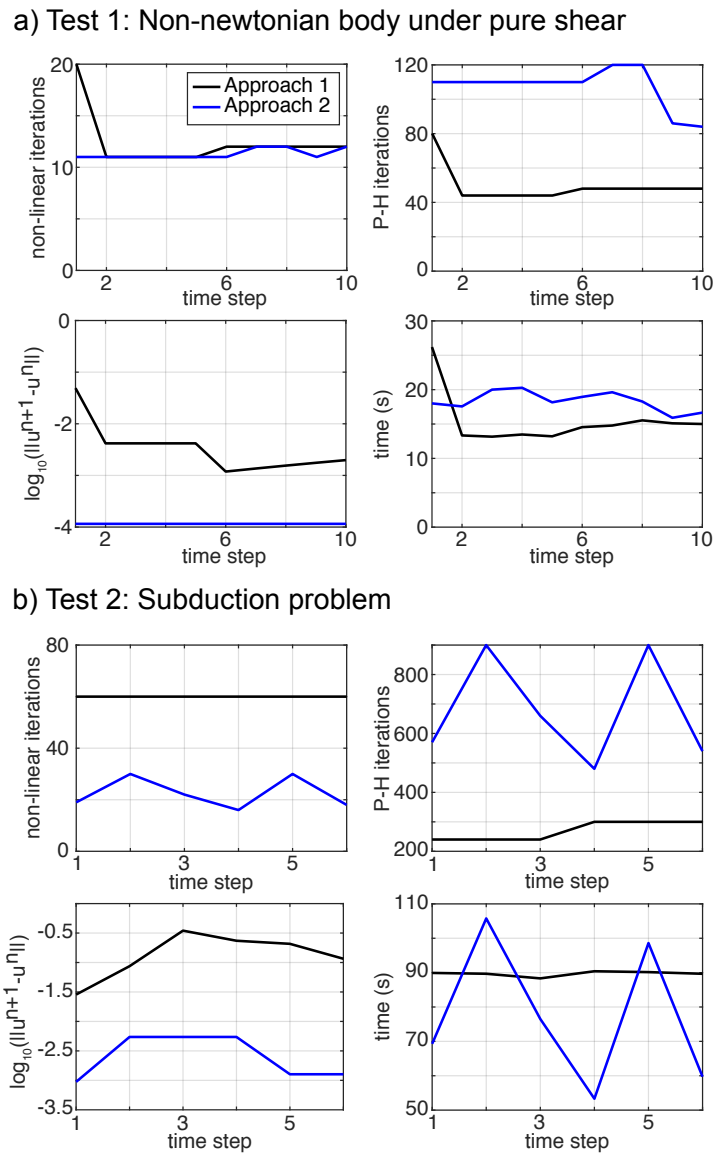

Figure .10: Comparison of the number of non-linear and linear iterations, residual velocity and computational time between Approach 1 and Approach 2 for **a)** Test A and **b)** Test B. The average computational times per time iteration for Test A are 15.43 s for Approach 1 and 18.34 s for Approach 2, whereas Test B yields average times of 89.68 s and 77.20 s for Approach 1 and 2, respectively.

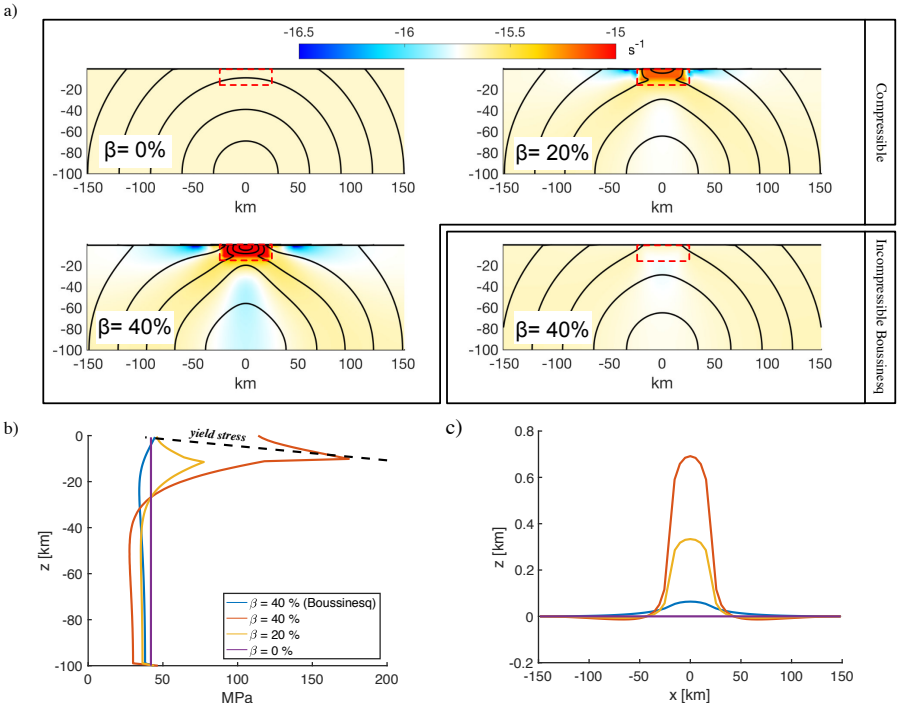

Figure .11: **a)** Results for different values of β. The density depends linearly on the degree of serpentinization: $\beta = 0, 20$ and 40 kg/m^3. The color maps represent the square root of the second invariant of the stress and the thick black lines are isolines of the velocity field. The change of density occurs within area delimited by the dashed red rectangle. **b)** Vertical profile of τ_{II} at x = 0; the dashed line represents the yield stress given by a pressure dependent yield surface: $\tau_y = p \sin\phi + C\cos\phi$. **c)** Comparison of the topographic relief for different degrees of serpentinization. All the results shown here correspond to $t = 1$ Myr.

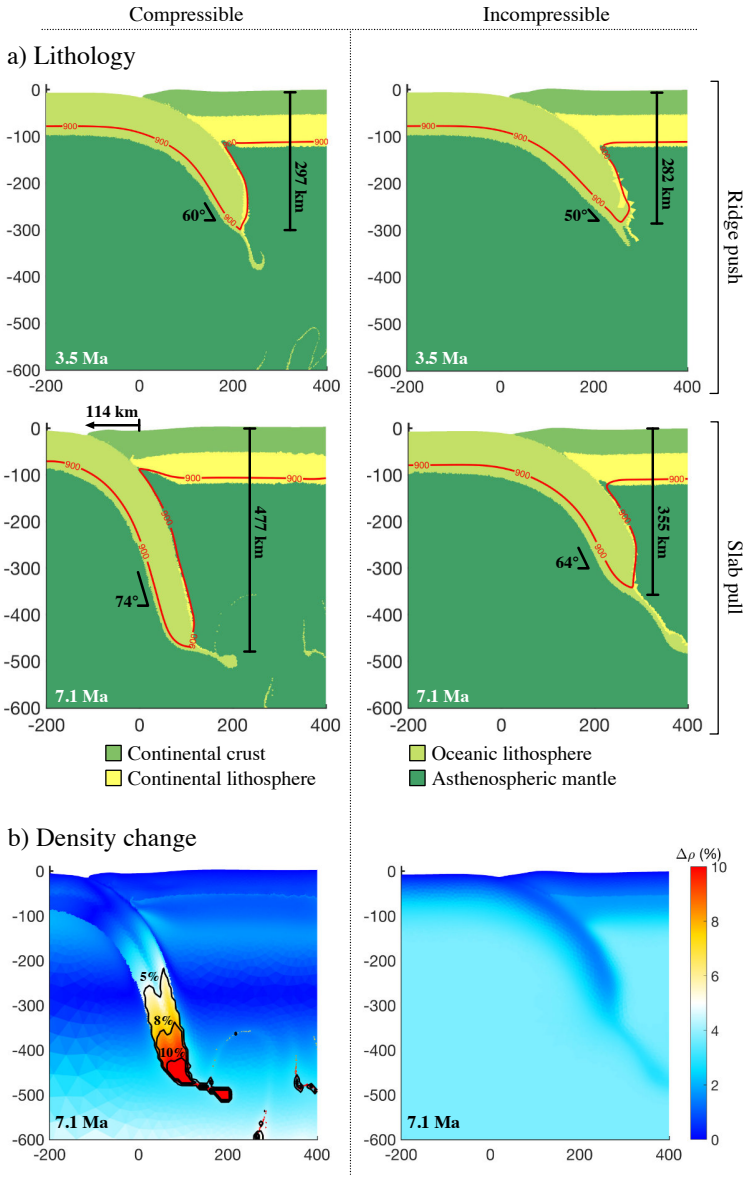

Figure .12: **a)** Snapshots of the subducting slab at 4.0 and 7.1 Ma for compressible ($\nu = 0.3$) and incompressible materials ($\nu \approx 0.5$). The red line represents the 900°C isotherm. **b)** Density variations with respect the reference state at 7.1 Ma.

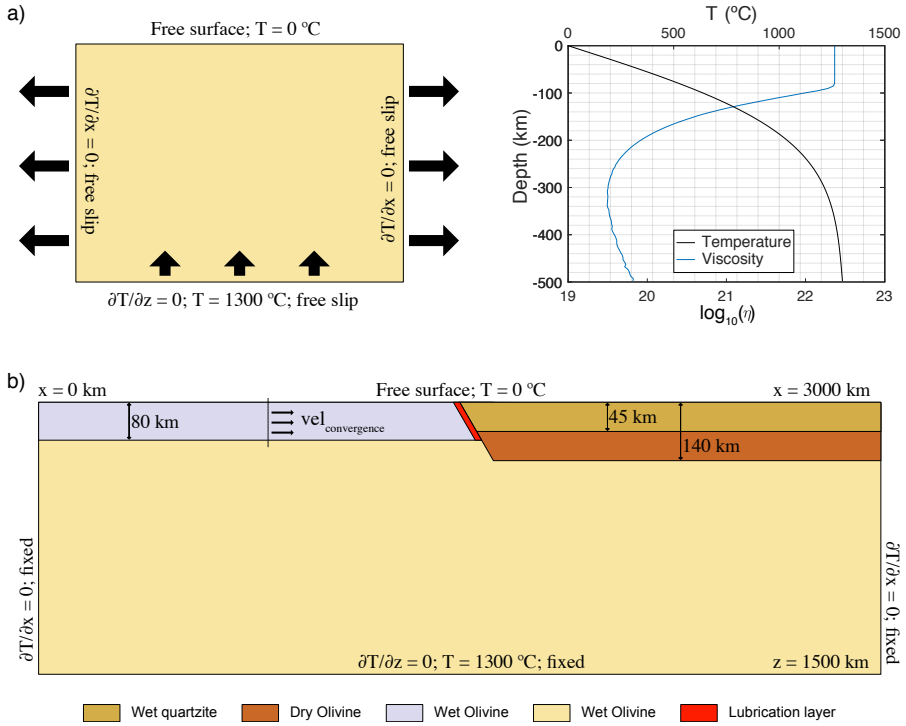

Figure .13: a) Model set-up, boundary conditions and vertical temperature and viscosity profiles of Test A. b) Model set-up and boundary conditions of Test B.

4 | Effects of dilatant pressure-dependent plasticity in geodynamic models

Albert de Montserrat and Jason P. Morgan. Effects of dilatant pressure-dependent plasticity in geodynamic models. Planned for submission to *Tectonophysics.*

Authors contribution

AdM designed the research in discussion with JM. AdM derived and implemented the new constitutive visco-elasto-plastic equation into the numerical code. AdM first designed the numerical experiments to validate the proposed formulation and its implementation. In discussion with JM, AdM programmed and interpreted the tectonic models to further test the implications of plastic dilation in tectonic processes. AdM wrote the manuscript in collaboration with JM.

Effects of dilatant pressure-dependent plasticity in geodynamic models

Albert de Montserrat[a], Jason P. Morgan[b]

[a]*SE Asia Research Group, Department of Earth Sciences, Royal Holloway University of London, Egham, United Kingdom*
[b]*Royal Holloway University of London, Department of Earth Sciences, Egham, United Kingdom*

Abstract

Volumetric expansion at microscopic and macroscopic scales upon brittle failure has been long accepted to occur in most of the rocks that comprise the continental crust. At greater depths, pressure-solution and melt-wall rock reactions could lead to net mass removal along an active shear zone. However, the mathematical description of models that attempt to mimic the development of faults as observed in geomaterials is often simplified by omitting dilation effects. With this model simplification, different numerical studies have successfully replicated shear bands that are oriented within the range of stable angles provided by analytical solutions; at the same time, they have failed to provide a unified answer, as the orientation of the fault has been proven to be highly sensitive to the employed numerical technique and spatial resolution. We show that, with dilation, an associated flow law combined with a Drucker-Prager failure criterion efficiently generates orientation angles tightly bound to analytical solutions without any compromise in computational cost. In addition, we modify the resulting set of equations to accommodate the possibility of compaction within shear zones as could occur by geological mechanisms such as pressure solution or wall rock reactions during fluid migration along a shear zone. Should chemically linked volume reduction occur along a fault zone, this would influence lithosphere deformation by leading to to more rapid localisation of lithosphere scale shear zones.

Keywords:

1. Introduction

The Earth exhibits strong bimodal mechanical behaviour. While the deformation and convection of the deep and hot mantle is governed by power-law ductile flow (e.g. Karato and Wu, 1993), tectonic processes such as subduction zones, continental rifting or mountain building, involve the deformation of cold and shallow lithospheric rocks and are characterised by a combination of elastic deformation and brittle failure. The development of constitutive models that capture ductile-brittle deformation and yield results compatible with geological and laboratory observations has been a key technical hurdle to overcome for better model-based understanding of geological processes at both micro and macro scales.

A wide spectrum of brittle failure models is commonly employed in engineering problems in order to simulate the non-recoverable deformation of metals, rocks, concrete, soils and other granular materials. In spite of the discontinuous nature of fractures and shear zones, continuum approaches such as the Finite Element Method (FEM) or Finite Difference Method (FDM) are the most widespread numerical tools used in geodynamics to tackle the brittle failure of geomaterials during tectonic processes. The deformation of any given material is described by its so-called constitutive law, which defines the response of the material to external forces. Due to its relative simplicity, an isotropic visco-elasto-plastic constitutive law based on a Maxwell model has been established as a powerful instrument to study coupled ductile-brittle deformation at geological time and length scales (e.g. Braun et al., 2008; Buck, 1991; Buiter et al., 2006; Choi et al., 2013; Fullsack, 1995; Gerya and Yuen, 2007; Huismans and Beaumont, 2007; Kaus, 2010; Lemiale et al., 2008; Moresi et al., 2007; Popov and Sobolev, 2008; Brune et al., 2014; Ros et al., 2017). Another reason to favour this model is that it requires of only two well-constrained physical parameters, namely the material's cohesion and friction angle; while there is a lack of constraints on the mechanical parameters, at geological scales, that de-

fine other constitutive models (for example, the fracture energy required damage models to define the amount of inelastic work a material can withstand before it fractures).

Plastic deformation is controlled by a scalar function, the *yield surface* or *yield criterion*, that limits the amount of stored stress in any given material. Although there have been a large number of yield-surfaces proposed for different materials, the yield stress in geodynamics is typically defined by a pressure-sensitive Mohr-Coulomb (Coulomb, 1773) or Drucker-Prager (Drucker and Prager, 1952) yield surface. While there is a noteworthy amount of research focused on the numerical implementation of visco-elasto-plastic models that mimic the observed angles and length-scales of shear bands and fractures (e.g. Moresi et al., 2007; Lemiale et al., 2008; Buiter et al., 2006; Buiter, 2012; Kaus, 2010; Popov and Sobolev, 2008; Spiegelman et al., 2016), current results exhibit wide variability. For example, Moresi et al. (2007) observed that shear bands were initiating at 45° using the Drucker-Prager model, independent of friction angle. It was later pointed out that the numerical resolution has to be sufficiently fine (Lemiale et al., 2008) and that mechanical heterogeneities have to be sufficiently well-resolved (Kaus, 2010) for analytical Coulomb angles to be recovered. In addition, the community benchmark presented by Buiter et al. (2006) illustrates that, even though the results obtained from different codes are comparable, there is a non-unique solution for visco-plastic flow, that strongly depends on the choice of numerical technique, which in turns hinders the reproducibility of these numerical results. Furthermore, even the convergence of visco-plastic models containing a dynamic pressure-sensitive yield criterion is under debate (Spiegelman et al., 2016).

It is known that plastic yielding in granular materials and rocks is (with some exceptions such as serpentinite (Escartin et al., 1997)) accompanied by a volumetric increase referred to as *dilatancy* (Brace and Byerlee, 1966; Vermeer and De Borst, 1984; Scholz, 2002). This mechanism was neglected in the studies previously mentioned, and has received little attention to date. Interestingly, Moresi et al. (2007) attributes the invariability of the orientation of the shear

bands to the suppression of volumetric changes, and Choi and Petersen (2015) conclude that an associated Mohr-Coulomb models yields shear band orientations tightly bounded to the predicted Coulomb angles. However, a thorough analysis of the potential role of plastic volume changes in tectonic processes is still lacking.

The aim of this paper is to investigate the effects of plastic dilation in strain localisation and shear band formation and discuss the implications of these effects for macro-deformation at the scale of faults and lithospheric processes. We start by describing a visco-elasto-plastic constitutive law for geodynamic problems that includes a non-elastic volume change via a so-called associated Drucker-Prager flow law. We then demonstrate the viability of this formulation with shear-induced dilatancy to reproduce shear band orientations in good agreement with the analytical predictions from bifurcation analyses (Vermeer and De Borst, 1984; Rudnicki and Olsson, 1998), in model conditions that do not require a spatial resolution as fine as that required in previous numerical studies.

We further extend our analysis to a rift-like scenario to illustrate potential feedbacks between plastic dilation and tectonic processes (or even fault-slip linked "contraction"). Our results suggest that dilatant and non-dilatant plasticity lead to rifted conjugate margins with a relatively comparable final geometry and faulting history, but the volume increase in associated plasticity results in the strengthening of the lithosphere and delays crustal break-up and mantle exhumation. In contrast, if shear zone motions are accompanied by fault-normal contraction or dissolution, the lithosphere experiences enhanced fault localisation and more rapid break-up. In all cases, the thermal evolution is also altered.

2. Plasticity model

Materials undergo non-recoverable plastic deformation if the stress at any material point is such that the yield stress is exceeded. The deviatoric plastic

strain rate is then defined as:

$$\dot{\varepsilon}^{plastic} = \lambda \frac{\partial \mathbb{G}}{\partial \tau} \tag{1}$$

where $\lambda \geq 0$ is a plastic multiplier, $\mathbb{G}$ is the plastic potential, τ is the deviatoric stress tensor and $\dot{\varepsilon}^{plastic}$ is the plastic component of the deviatoric strain rate tensor:

$$\dot{\varepsilon} = \frac{1}{2}(\nabla \mathbf{u} + (\nabla \mathbf{u})^T) - \frac{1}{3}(\nabla \cdot \mathbf{u}) \tag{2}$$

The elastic domain is defined by the yield surface $\mathbb{F}(\sigma, \xi, h)$, which limits the maximum stress possible and is a scalar function of the Caucy stress tensor σ, a set of material parameters ξ, and the hardening/softening parameter h. The choice of h is not trivial and will be discussed later on. In domains where deformation is purel elastic $\mathbb{F} < 0$, whereas $\mathbb{F} = 0$ at yield. If the stress field at any point of the domain is such that $\mathbb{F} > 0$, the stress needs to be corrected and brought back to the yield surface ($\mathbb{F} = 0$). In this study we employ a two-surface yield surface, combining the von Mises (Mises, 1913) and Drucker-Prager (Drucker and Prager, 1952) criteria:

$$\mathbb{F} = \begin{cases} \alpha(\sigma) - p(\sigma)\sin(\phi(h)) - c\cos(\phi(h)) & \text{if } c \leq \tau_{II} \quad \text{(Drucker-Prager)} \\ \alpha(\sigma) - H & \text{if } c > \tau_{II} \quad \text{(von Mises)} \end{cases} \tag{3}$$

where ϕ is the friction angle, c is the cohesion, the pressure is defined as $p = -tr(\sigma)\mathbf{I}/3$, τ is the deviatoric stress tensor and the subscript II denotes the square root of the second invariant (i.e. $\mathbf{C}_{II} = \sqrt{(1/2)\mathbf{C} : \mathbf{C}}$, where $\mathbf{C}$ is any given tensor). The Drucker-Prager criterion is a pressure dependant yield surface and is a smooth (corner free) approximation of the Mohr-Coulomb surface. On the other hand, the von Mises law is pressure-insensitive and states that plastic flow begins whenever $\alpha(\sigma)$ reaches a critical value H. In the principal stress space, Drucker-Prager has a conic shape, whereas von Mises is described by a cylinder (Fig.1). The parameter $\alpha(\sigma)$ is commonly taken to be the square root of the second invariant of the deviatoric stress tensor. We also take $H = c$,

thus assuming that the yield stress at low stress levels is ultimately defined by the cohesion of the material.

2.1. Flow law

Plasticity models can be classified in two types according to the choice of the plastic potential. If the yield surface is taken to be the plastic potential ($\mathbb{F} = \mathbb{G}$), this is commonly referred as *associative* plasticity and the material follows the so-called normality rule: the plastic strain increment vector is normal and moves outwards from the failure surface. If the plastic potential and yield surface are different ($\mathbb{F} \neq \mathbb{G}$), this is known as *non-associative* plasticity and the normality rule is not obeyed.

In the geodynamic community, plasticity is often assumed to be non-associative and the Prandlt-Reus flow rule is the preferred tool to solve plastic deformation for Maxwell visco-elasto-plastic bodies. An extensive bibliography describing this formulation is available and the reader is referred to, for example, Moresi et al. (2003); Gerya and Yuen (2007); Popov and Sobolev (2008); Kaus (2010); Buiter (2012) for further details. On the contrary, in this paper we focus on the use of an associated Drucker-Prager flow law model to solve plastic deformation for problems of mantle-lithosphere deformation.

Taking $\mathbb{F} = \mathbb{G}$, the derivative of the plastic potential with respect to the stress field yields:

$$\frac{\partial \mathbb{G}}{\partial \tau} = \begin{cases} \frac{\tau}{2\tau_{II}} + \frac{1}{3}\sin\phi\mathbf{I} & \text{if } c \leq \tau_{II} \\ \frac{\tau}{2\tau_{II}} & \text{if } c > \tau_{II} \end{cases} \tag{4}$$

where $\mathbf{I}$ is the identity matrix. Because $\mathbb{F}$ is defined to be a continuous piecewise function, $\mathbb{G}$ is continuous piecewise derivable and we do not have to deal with the derivative at the apex of the Drucker-Prager yield surface. If one wishes to use a model with only the Drucker-Prager yield surface for the whole stress domain, the derivative at the apex must be done carefully. Due to the pressure dependence of the Drucker-Prager yield surface, the plastic strain rate is no longer purely deviatoric and the stress derivative of the Drucker-Prager yield

surface results in both volumetric and deviatoric components:

$$\dot{\varepsilon}^{plastic} = \begin{cases} \lambda \left(\Upsilon^v + \Upsilon^d \right) & \text{if } c \leq \tau_{II} \\ \lambda \Upsilon^d & \text{if } c > \tau_{II} \end{cases} \tag{5}$$

where $\Upsilon^v = (1/3) \sin\psi \mathbf{I}$ and $\Upsilon^d = \tau / 2\tau_{II}$. If $c > \tau_{II}$, the corresponding yield surface is von Mises, which results in zero volumetric plastic strain. The volumetric plastic deformation predicted by associated flow rule is often found to be excessively high and the friction angle in the volumetric plastic strain rate component is commonly replaced by the so-called dilatancy angle $\psi \leq \phi$. It is obvious to see that if $\psi = 0^\circ$ non-associated flow rule is recovered and $\Upsilon^v = 0$ for $c \leq \tau_{II}$.

[Figure 1 about here.]

3. Rheological model for a visco-elasto-plastic body with an associated Drucker-Prager flow rule

Adopting a Maxwell model to describe the deformation of a visco-elasto-plastic body, the total deviatoric strain rate is given by the summation of its elastic and inelastic components:

$$\dot{\varepsilon} = \dot{\varepsilon}^{viscous} + \dot{\varepsilon}^{elastic} + \dot{\varepsilon}^{plastic} \tag{6}$$

which yields the following the visco-elasto-plastic constitutive equation:

$$\dot{\varepsilon} = \frac{\tau}{2\eta} + \frac{1}{2G}\frac{D\tau}{Dt} + \lambda \frac{\partial \mathbb{G}}{\partial \sigma} \tag{7}$$

where η is the viscosity and G is the shear modulus. The time derivative of the deviatoric stress tensor is computed by approximating the Jaumann derivative in an implicit manner (e.g. Kaus, 2010):

$$\frac{D\tau}{Dt} \approx \frac{\tau - \tau^o}{\Delta t} - \omega^o \tau^o + \tau^o \omega^o \tag{8}$$

where the super-script o refers to the previous time step, Δt is the time step, and $\omega = 1/2(\nabla \mathbf{u} - (\nabla \mathbf{u})^T)$ is the skew symmetric part of the velocity gradient

tensor, commonly known as spin tensor, that rotates the stored stress tensor. After substitution of eq. 4 into 7, the general visco-elasto-plastic constitutive equation reads:

$$\dot{\varepsilon} = \frac{\tau}{2\eta} + \frac{1}{2G}\frac{D\tau}{Dt} + \lambda\left(\frac{\tau}{2\tau_{II}} + \frac{1}{3}\sin\psi\mathbf{I}\right) \tag{9}$$

To calculate the unknown plastic multiplier, we rearrange the previous equation using eq. 8, consider that at yield $\tau = \tau_y$, and take the second invariants of $\dot{\varepsilon}$ and $\widehat{\tau}$:

$$\lambda = \frac{2\dot{\varepsilon}_{II} + \frac{1}{G\Delta t}\widehat{\tau}_{II} - \tau_y\left(\frac{1}{\eta} + \frac{1}{G\Delta t}\right)}{1 + \frac{2}{3}\sin\psi\mathbf{I}} \tag{10}$$

where $\widehat{\tau} = \tau^o + (\omega^o\tau^o - \tau^o\omega^o)\Delta t$. Now that λ is known, we can rearrange eq. 9 to obtain the following stress-strain relationship:

$$\tau = \eta_{vpl}\left(2\dot{\varepsilon} + \theta\widehat{\tau} - \frac{2}{3}\lambda\sin\psi\mathbf{I}\right) \tag{11}$$

where $\theta = (G\Delta t)^{-1}$. The effective visco-elasto-plastic viscosity can be computed directly from eq. 11 assuming yielding conditions:

$$\eta_{vpl} = \frac{\tau_y}{2\dot{\varepsilon}_{II} + \theta\widehat{\tau}_{II} - \frac{2}{3}\lambda\sin\psi\mathbf{I}} \tag{12}$$

Knowing that $\psi = 0°$ for $c > \tau_{II}$, we can build a piecewise effective viscosity that covers the whole stress domain:

$$\eta_{vpl} = \begin{cases} \tau_y/\left(2\dot{\varepsilon}_{II} + \theta\widehat{\tau}_{II} + \frac{2}{3}\lambda\sin\psi\mathbf{I}\right) & \text{if } c \leq \tau_{II} \\ \tau_y/\left(2\dot{\varepsilon}_{II} + \theta\widehat{\tau}_{II}\right) & \text{if } c > \tau_{II} \end{cases} \tag{13}$$

where the effective viscosity for $c > \tau_{II}$ is equivalent to the expression obtained by emplying the Prandtl-Reus flow rule. Finally, we can build a general constitutive relationship for visco-elasto-plastic materials as:

$$\tau = 2\eta^*\dot{\varepsilon} + \theta\eta^*\widehat{\tau} - \langle 1\rangle\frac{2}{3}\lambda\sin\psi\mathbf{I} \tag{14}$$

where $\eta^* = \eta_{vpl}$ and $\langle 1\rangle = 1$ for $\tau > \tau_y$, and $\eta^* = \eta_{eff}$ and $\langle 1\rangle = 0$ for $\tau \leq \tau_y$. The effective viscosit is defined as (e.g. (Kaus, 2010)):

$$\eta_{eff} = \frac{1}{\frac{1}{\eta} + \frac{1}{G\Delta t}} \tag{15}$$

3.1. Strain softening

To mimic the post-peak stress drop often seen in granular materials and rocks, strain softening, as a function of the softening parameter h, is applied to some of the mechanical properties that define the strength of the material. As commonly used in geodynamics (e.g. Huismans and Beaumont, 2002; Buiter, 2012; Choi and Petersen, 2015), we take the accumulated plastic strain as the softening parameter, and the initial values of ϕ and ψ are linearly reduced with with increasing accumulated plastic strain. The latter is defined as:

$$\mathbf{E}^{pl} = \int \sqrt{\frac{1}{2}\dot{\varepsilon}^{plastic} : \dot{\varepsilon}^{plastic}} dt \tag{16}$$

where the colon represents a dyadic contraction of the plastic strain-rate tensor. The friction angle is chosen so that $\phi(\mathbf{E}^{pl} = 0) = \phi_0$ and $\phi(\mathbf{E}^{pl} \geq \mathbf{E}^{pl}_{max}) = \phi_\infty$. Strain softening is also applied to the dilatancy angle following Choi and Petersen (2015), who inferred that ϕ and ψ should have initially their maximum *undamaged* value so that a shear band can form at a Coulomb angle. Another reasons in favour of reducing the dilatancy angle are that, with increasing slip: 1) faults do not have an everlasting expansive behaviour (Detournay, 1986) and will evolve from associated plastic state towards non-associative plastic deformation;and 2) mass (i.e. fluids) within the dilatant shear band can diffuse into the new pore spaces and thereby decrease the ambient pore pressure Rudnicki (1988). These effects are coarsely simulated by linearly reducing the dilatancy angle with increasing accumulated plastic strain so that $\psi(\mathbf{E}^{pl} \geq \mathbf{E}^{pl}_{max}) = \psi_\infty = 0°$, and a non-associated state is recovered. There is a general lack of studies to constrain the values of $\mathbf{E}^{pl}_{max}$ and ϕ_∞; however, it is common to adopt values within the range of $0.25 \leq \mathbf{E}^{pl}_{max} \leq 1.25$ and $2 \leq \phi_\infty \leq 15$. In the models further presented in this paper, we adopt $\mathbf{E}^{pl}_{max} = 1$ and $\phi_\infty = 15$. Alternatively, one could use the accumulated plastic work as to define the softening curve (de Souza Neto et al., 2011). However, we do not investigate this option here.

4. Numerical code

[Figure 2 about here.]

We use the LaCoDe code (de Montserrat et al., 2018), based on a Lagrangian formulation of the Finite Element Method, to solve the coupled equations of conservation of momentum, conservation of mass and conservation of energy:

$$\nabla\sigma = \rho\mathbf{g} \tag{17}$$

$$\rho\frac{D\rho}{Dt} + \nabla\cdot\mathbf{u} = 0 \tag{18}$$

$$\rho C_p\frac{DT}{Dt} = k\nabla^2 T + H_Q + H_{sh} \tag{19}$$

where ρ is the density, $\mathbf{g}$ is the gravitational acceleration, $\mathbf{u}$ is the velocity field, C_p is specific heat, T is temperature, κ is thermal conductivity, H_Q is radioactive heating and H_{sh} is shear heating. Density corrections are calculated using a temperature and pressure dependent equation of state:

$$\rho(T,p) = \rho_o\left(1-\alpha\left(T-T_{ref}\right)+\frac{p}{K}\right) \tag{20}$$

where ρ_o is the reference density, α is the thermal expansivity, T_{ref} is the reference temperature and K is the bulk modulus. We use a non-Newtonian rheology to describe diffusion and dislocation creep, where the viscosity is given by a strain rate- and temperature- dependent power law (Poirier, 1985; Karato et al., 2001):

$$\eta = \frac{1}{2}(A)^{-\frac{1}{n}}\left(\dot{\varepsilon}_{II}\right)^{\frac{1}{n}-1}\exp\left(\frac{E_a+pV_a}{nRT}\right) \tag{21}$$

where A is a pre-exponential parameter, n is a power-law exponent, E_a is activation energy, V_a is activation volume and R is the universal gas constant. The second invariant of the deviatoric strain rate in eq. 21 corresponds to either the diffusion or dislocation creep deviatoric strain rate tensor. A resultant composite viscosity is obtained as:

$$\eta = \frac{1}{\frac{1}{\eta_{dif}}+\frac{1}{\eta_{dis}}} \tag{22}$$

where deformation is dominated by the mechanism with the smallest activation stress.

Eq. 19 describes the conservation of mass for a compressible material where volumetric deformation is linked to density changes. When at yield, eq. 19 is modified to include the volumetric deformation from the dilatant plasticity:

$$\frac{D\rho}{Dt} + \rho\nabla \cdot \mathbf{u} = \rho\lambda\Upsilon^{v} \tag{23}$$

For a (nearly) incompressible material, the material time derivative of the density in eq. 23 vanishes, and the extended Boussinesq approximation will be recovered:

$$\nabla \cdot \mathbf{u} = \lambda\Upsilon^{v} \tag{24}$$

Using a mixed formulation to solve the Stokes equations, the Cauchy stress is split into its deviatoric and volumetric components:

$$\sigma = \tau + p \tag{25}$$

and using eqs. 11 and 25, the equation of conservation of momentum yields:

$$\nabla\left(2\eta^{*}\dot{\varepsilon}\right) + \nabla\mathbf{p} = \rho\mathbf{g} - \nabla\left(\theta\eta^{*}\widehat{\tau}_{II}\right) + \nabla\left(\langle 1\rangle\eta^{*}\frac{2}{3}\lambda\sin\phi\mathbf{I}\right) \tag{26}$$

Eqs. 23 and 26 are solved combining Powell-Hestenes iterations with the penalty method (e.g. Dabrowski et al., 2008). Rheological (non-Newtonian viscous creep and plasticity) and density (compressible continuity equation) non-linearities are treated with Picard iterations.

5. Shear band initiation

[Figure 3 about here.]

The implementation of the associated and non-associated flow rules is tested with a numerical experiment modelling shear band initiation. Similar tests can be found in, for example, Popov and Sobolev (2008); Kaus (2010); Choi and Petersen (2015); Spiegelman et al. (2016). The domain of this numerical

experiment is a 20 by 10 km rectangular visco-elasto-plastic box with a density of 2700 kg/m^3 that simulates the uppermost part of the crust. The mechanical parameters are G = 30 GPa, c = 30 MPa, $\nu \approx 0.5$, and a uniform viscosity $\eta = 10^{23}$ Pa·s. An extension rate of 1 cm/year is prescribed at the right hand-side edge of the domain, and free-slip boundary conditions are prescribed at the bottom and left boundaries. The surface of the model is traction-free (i.e. a free surface). A mechanical heterogeneity of 1 by 1 km is introduced at the bottom-centre of the model, so that shear bands will nucleate around it. The friction angle of this weak region is set to be $\phi = 0°$, while $\phi_0 = 30°$ elsewhere. We perform a suite of tests with the arbitrary values of the dilatancy angle $\psi_0 = \phi_0$, $\psi_0 = \phi_0/2$ and $\psi_0 = 0°$, with strain softening applied to the friction ($\phi_\infty = 15°$) and dilatancy angle ($\psi_\infty = 0°$). The models are run only until the mesh is so distorted that a remeshing algorithm would be necessary.

To avoid any geometrical bias derived from a preferred orientation of the mesh, the domain is discretised into triangular elements that are regularly and symmetrically distributed along the domain. This mesh is constructed by 1) dividing the domain in a regular grid formed by rectangles, and 2) splitting the rectangles into four triangles with a common vertex at the centre of the rectangle. The effect of spatial resolution on associated plasticity is assed by running the model with different numerica resolutions: fine ($4 \cdot 10^4$ triangular elements), intermediate ($2.25 \cdot 10^4$ triangular elements) and coarse (10^4 triangular elements). The aspect ratio (height/base) of the triangular elements is 0.25 for all meshes considered.

5.1. Results

[Figure 4 about here.]

From bifurcation analysis using a Mohr Coulomb failure criterion, Vermeer and De Borst (1984) deduced three mechanically stable angles for shear bands: 1) $\theta = 45° + \frac{\psi}{2}$, Roscoe (1970); 2) $\theta = 45° + \frac{\phi}{2}$, Coulomb (1773) ; and 3) $\theta = 45° + \frac{\phi+\psi}{4}$, Arthur et al. (1977). Again from a bifurcation analysis, but this time

employing a Drucker-Prager criterion, Rudnicki and Olsson (1998) obtained the alternative expression for a stable shear band orientation:

$$\theta = 45^\circ + \frac{1}{2}\arcsin\alpha \tag{27}$$

where $\alpha = (\phi + \psi)/2$ in the incompressible case under extension and pure shear boundary conditions.

All the models are able to consistently produce a single pair of well-converged conjugate shear bands that initiate at the mechanical heterogeneity (Fig .3). Depending on the spatial resolution, shear bands initiate at approximately $57.5-60.5^\circ$ for associated ($\psi = \phi$) models (Table 5.1). On the other hand, non-associated ($0 < \psi < \phi$) models yields shear bands with orientations around $55.5 - 57.5^\circ$, whereas non-dilatant models yield shear bands at $51.5 - 53.5^\circ$. In spite of some minor angle deviations for $\psi \neq \phi$, these values show that the plastic formulation presented here using a associated Drucker-Prager flow rule yields shear bands in close agreement with the orientations predicted by Rudnicki (1988), rather than the Coulomb, Arthur or Roscoe angles (Fig .4a).

The build up of volumetric plastic strain within the shear bands translates into a relative structural hardening with increasing dilatancy angle. This can be inferred from the stress-strain curves (Fig .4b, where the vertical axis represents the integrated stress along the right edge of the model): while for $\psi_0 = 0^\circ$ the model shows an immediate post-peak strain-softening behaviour with a sharp drop of stress, dilatant models are able to sustain near-peak stress conditions shortly after yielding, and their stress drop is more sustained and progressive. Strain softening is not observed in the case of $\psi_0 = 0^\circ$ because the models are run only until the quality of the mesh becomes too poor, therefore, in this particular case, strain softening has not kicked in enough to become noticeable in the stress-displacement curve.

The plastic strain within the shear bands increases with the dilatancy angle as a result of a non-zero volumetric plastic strain rate. This enhances strain localisation within the shear bands, resulting in higher strain rate in the yielded material. One would expect that higher plastic strain rates will be reflected

Table 1: Shear band orientation as a function of the dilatancy angle ψ for different spatial resolutions.

	Shear band orientation (°)			Mohr-Coulomb (°)			Drucker-Prager (°)
ψ (°)	10000 els.	22500 els.	40000 els.	Coulomb	Arthur	Roscoe	Rudnicki
30	55	59.5	60.5	60	60	60	60.8
15	54	57.5	57.5	60	56.25	52.5	56.6
0	51.5	53	53.5	60	52.5	45	52.6

Table 2: Vertical fault desplacement and width of the graben. Values are normalised with respect the case $\psi = 0°$.

	Normalised vertical fault displacement		
ψ (°)	10000 els.	22500 els.	40000 els.
30	0.87	0.89	0.91
15	1.02	1.01	1.01
0	1	1	1

on the topographic profile as larger vertical fault displacements. However, for associated models ($\phi = \psi$) the build up of volumetric strain within the shear bands introduces a vertical motion in the hanging wall block that limits vertical fault displacement (Fig.4c; Table 5.1).

Another effect of dilatant plasticity is that the additional inelastic strain rate results in higher inelastic work dissipation, which translates to higher temperatures due to additional shear heating. This could have consequences in, for example, numerical models of rifted margins, as it might further enhance strain localisation when using a temperature-dependent viscosity.

6. Case study: rifting of continental crust

In the previous section we examined the effects of dilatant plasticity on shear band initiation in small scale models. However, it is not obvious what *a priori* effects this behaviour will have on large scale geodynamic problems, or whether it even has is any noticeable effects at all. We therefore further explore the effect of dilatant plasticity on strain localisation, fault geometry, thermal structure,

and structural evolution of an evolving rift.

6.1. Model set-up

The domain consists of a 500 by 500 km box (Fig.5) divided into distinct rheological layers: wet quartzitic upper crust (UC), dry olivine upper mantle (UM) and wet olivine lower mantle (LM). We further asses the impact of dilation on lower crusts (LC) with different strengths: i) a weak end member (wet quartzite), and ii) a strong end member (mafic granulite). The corresponding rheological parameters are shown in Table 6.1. Pure shear far-field boundary conditions are prescribed at the boundaries of the model (i.e. half and full extension rate at the lateral and bottom boundaries of the domain, respectively), and a tangential free slip condition is employed at the lateral and bottom boundaries; the top boundary of the domain is treated as a free surface (Andrés-Martínez et al., 2015). Temperature is kept fixed at 0°C at the surface and at 1200° C below 120 km depth. In order to localise deformation at the centre of the model at the onset of extension and to avoid artefacts arising from boundary effects, we introduce a thermal Gaussian-shape perturbation in the lower crust at 35 km depth. The half extension rate prescribed at the edges of the domain is 32.5 mm/yr.

We note that the set-up of the models is representative of typical numerical experiments aiming at modelling different rifting scenarios; however, the aim of these models is to assess solely the effects of associative plasticity on lithospheric stretching. Therefore, we will not explore the detailed evolution of rifting in these models.

[Figure 5 about here.]

6.2. Strong lower crust: fault geometry and model evolution

Models with a mafic granulite lower crust result in a pair of asymmetric conjugate rifted margins (Fig.6). After an initial phase of widely distributed faulting strain localises in a pair of main conjugate normal faults that cut throughout

the whole crust, coupling crust and upper mantle, and deformation is accommodated by pure shear. As the crust stretches, strain further localises in the E-dipping conjugate normal fault. The W-dipping normal fault becomes progressively inactive and the deformation mode switches to simple shear. In this stage, many secondary shear zones develop in the rifting region, along with a high strain listric fault that root into the main one. Further extension results in the rotation of the main normal fault and progressive crustal thinning of one of the margins, whereas the crust of the other conjugate margin is sharply thinned. Due to the rapid extension rate, the upwelling of mantle material is quite fast and crustal break-up and mantle exhumation are reached at about 2.5-2.7 Ma.

The effect of dilatant plasticity on the fault distribution is most noticeable in the 2 and 2.2 Ma snapshots (Fig.6a). Localisation of plastic strain is enhanced and dilatancy angles of $\psi > 0°$ yield a higher number of well-defined shear zones at crustal depths. Structural hardening is produced by the blocks of unyielded material being *locked* by the expansion of the shear zones, becoming more noticeable after the rifting develops (2.0 Ma and onwards). This effect is ultimately responsible for a delay in the evolution of the rifting. Consequently, mantle exhumation occurs earlier (at c. 2.5 Ma) for $\psi = 0°$, whereas mantle is not exhumed until c. 2.6 and 2.7 Ma after onset of extension for $\psi = 15°$ and $\psi = 30°$, respectively. Plastic strain is less effectively localised in the non-dilatant model which results in smoother relief (Fig.7a,b,c). In contrast, dilatant

Table 3: Rheological parameters. The upper and lower crust are weak wet quartzite (Gleason and Tullis, 1995), the upper and lower mantle are dry olivine and wet olivine (Hirth and Kohlstedt, 2003), respectively.

Parameter	Description (Units)	Wet olivine	Dry olivine	Mafic granulite	Wet quartzite
ψ_0/ψ_∞	°	30/0	30/0	30/0	30/0
ϕ_0/ϕ_∞	°	30/15	30/15	30/15	30/15
c	Cohesion (Mpa)	20	20	20	20
A	Pre-exponential factor ($Pa^{-n}s^{-1}$)	$10^{-15.56}$	$10^{-15.56}$	$10^{-21.05}$	10^{-28}
E	Activacion energy ($KJmol^{-3}$)	$480{\cdot}10^3$	$530{\cdot}10^3$	$445{\cdot}10^3$	$223{\cdot}10^3$
V_o	Activation volume(m^3mol^{-3})	10^{-4}	10^{-6}	0	0
n_{dis}	Power-law exponent (dislocation creep)	3.5	3.5	4.2	4
n_{dif}	Power-law exponent (diffusion creep)	1	1	0	0

models present a rougher surface due to more effective faulting at shallow depths; however, the amplitude of the relief is slightly smaller as a result of the structural hardening.

[Figure 6 about here.]

[Figure 7 about here.]

6.3. Weak lower crust: fault geometry and model evolution

[Figure 8 about here.]

As is well known from previous numerical studies of rifted margins (e.g. Huismans and Beaumont, 2011, 2014; Ros et al., 2017; Tetreault and Buiter, 2017), a weak lower crust results in different margin evolution with respect to models with a strong end member. In early stages, strain localises into a set of widely distributed shear zones. After c. 1.5 Ma, strain localises into two high strain rate regions located at the flanks of the weak seed which results in the development of two basins. These high strain regions are characterised by several sets of conjugate normal faults. Due to its weak mechanical behaviour, ductile flow predominates in the lower crust and focussed shear zones do not continue into the mantle lithosphere. Hence the conjugate normal faults die out in the upper section of the lower crust and the crust and mantle lithosphere remain mechanically decoupled within the rifting region. Further stretching is accompanied by ductile flow of the lower crust that leads to a thickening of the upper crust and thinning of the lower crust at the centre of the model, with two domes of lower crustal material forming at $\sim$ 45 km away from the centre.

Extension is accompanied by ascent of lower mantle material and break-up of the mantle lithosphere occurs prior to crustal break-up at c. 1.5 Ma. As stretching continues, the deeper mantle asthenosphere flows laterally towards regions where the crust is weaker (i.e. where a considerable amount of upper crust has been removed and replaced by weak and hot lower crust), eventually leading to crustal break-up and mantle exhumation, and resulting in two highly asymmetric rifted margins.

Wet quartzite is mechanically weaker than mafic granulite, hence it more readily deforms by ductile flow than by brittle failure. Therefore, the effects of associative plasticity are less evident here than for the strong end member case in terms of rift evolution. Nonetheless, strain localises better in associated models when plastic deformation is efficient enough (Fig.8, 2.2 Ma). The overall ductile behaviour of these models results in smooth topographies with two major basins and very little difference between dilatant and non-dilatant models (Fig.7d,e,f).

6.4. Thermal evolution

Plastic dilation may not only affect the deformation history of conjugate rifted margins, but has consequences for the thermal evolution due to two main mechanisms: 1) dilatant hardening leads to a locking of non-yielded material in between shear zones; as a consequence, the locking strengthens the crust and slows down the upwelling of mantle material, thereby delaying mantle exhumation and crustal break-up with respect to non-dilatant models; and, 2) dilatant plastic strain leads to a higher inelastic strain rate and therefore higher heating due to inelastic work. The first mechanism promotes the cooling of the model as vertical motion is reduced with increasing dilation. The second mechanism enhances thermal localisation, as the heating from inelastic work would increase with increasing dilatancy angle. The resulting thermal evolution is determined by the competition between both mechanisms.

For a strong lower crust, plastic deformation is very effective and shear heating becomes the dominant mechanism for intermediate degrees of dilation ($\psi = 15°$), resulting in a higher geotherm at lithospheric depths in comparison with a non-associated model. However, hardening cooling dominates for a highly dilatant ($\psi = 30°$) crust, thus leading to cooler thermal structures (Fig.9a). For a weak lower crust, the plastic contribution to shear heating is lower than viscous dissipation and volumetric locking becomes a more efficient as a cooling mechanism with increasing dilatancy angle (Fig.9c). Nonetheless, independent of the strength of the lower crust, the surface heat flow is significantly reduced as

a consequence of increasing dilation within the faults at shallow crustal depths (Fig.9b,d) as the result of cooling derived from the structural hardening being more effective than shear heating.

[Figure 9 about here.]

6.5. Depth dependant dilatancy angle

As argued by Detournay (1986), dilation is not only a function of plastic strain, but also of confining stress. The effect of confining stress was further noted by Medhurst (1997), from triaxial tests on multi-scale coal samples, and Ribacchi (2000) from standard triaxial tests on limestone samples with variable fractures. We investigate this argument by introducing a depth-dependent dilatancy angle. As in Alejano and Alonso (2005), at null confining pressure we consider that the dilation and friction angle are the same, i.e. $\psi_0(z=0) = \phi_0$. The dilatancy angle is then linearly reduced as a function of depth until a certain depth limit, i.e. $\psi_0(z = z_{limit}) = 0°$. We perform a sensitivity test of the depth-dependency of the dilatancy angle in the model with a strong lower crust taking values of $z_{limit} = 60, 40$ and 20 km (Fig.10).

A similar initial phase of distributed faulting at the initial stages of deformation ($\leq$ 1.7 Ma) is observed in all the models with different depths of dilatation efficiency. For $z_{lim} \leq 40$ km, strain localises in two main conjugate shear zones that cut through the whole crust, coupling its deformation with the mantle lithosphere (Fig.10a, 2.0 Ma). With further extension, the W dipping shear zone becomes inactive and strain is localised in the remaining main shear zone. The latter rotates to lower dipping angles and listric faults that root on this main detachment begin to develop (Fig.10a, 2.2 Ma), thereby forming a single basin (Fig.11b,c). At this stage, deformation shifts from pure shear to simple shear. At c. 2.7 the lithosphere breaks-up and mantle is exhumed, resulting in two asymmetric conjugate margins (Fig.10b).

In contrast, models with a depth limit deeper than the base of the crust for dilatant plasticity show a different history of brittle deformation after the initial

phase of distributed faulting ($\leq$ 1.7 Ma). At c. 2 Ma, strain has localised in two shear zones that start at the centre of the surface with opposite orientations. These faults also root into the base of the lower crust, coupling deformation between the crust and mantle lithosphere. This different set of main shear zones results in two mini basins with an uplifted crustal block in between them (Fig.10a, 2.2 Ma; Fig.11a). Due to the stronger hardening effects, lithospheric break-up and mantle exhumation is delayed until c. 3 Ma. However, this model also results in a pair of asymmetric conjugate margins (Fig.10b).

The depth at which dilation ceases is also reflected in the thermal signature in the models (Fig.10c): shallower depth limits for dilation yield higher peaks of surface heat flow, whereas for deeper depth limits the peak of surface heat flow at the same time is approximately three times smaller.

[Figure 10 about here.]

[Figure 11 about here.]

7. Compaction of shear bands

Opposite to the porosity increase due to the brittle-faulting-linked dilatancy, other mechanisms lead to mass loss or compaction are known to occur within shear zones. Some of these processes include pressure solution (e.g. Renard et al., 2000; Bos et al., 2000; Gratier et al., 2011) and reactive fluid or melt migration along faults and fractures. While the physical and mathematical description of these mechanisms is not represented by the equations developed for an associated Drucker-Prager flow rule, we can simulate the effect of compaction within shear bands by changing the sign of the right-hand-side of eq. (23). We must emphasize this is a more a "thought experiment" than a quantitative simulation of the effects of fault-slip-linked mass removal processes.

In this case, the compaction of yielded material leads to a structural softening of the crust, enhancing strain localisation and leading to focussed shear bands with higher strain rates (Fig. .12). The faulting history of the crust follows the

same pattern as described in Sections 6.2 and 6.3. However, the enhancement of strain localisation during the early stages of extension (0.9-1.4 Ma) in the model with a weak lower crust results in two narrower basins at the flanks of an non-deformed crustal block (Fig. .12b).

As described in the earlier sections, an associated (dilatant) plastic model causes a structural hardening that slows down the deformation history of the lithosphere. In contrast, compaction within shear zones will leads to structural softening that speeds up the evolution of deformation. This results in break-up of the lithosphere occurring around 30% (c. 1.75 Ma) and 42% (c. 2.15 Ma) earlier for the strong and weak lower crust cases, respectively, with respect to previous models with $\psi = 0°$.

[Figure 12 about here.]

8. Discussion

The admissible shear band orientation lies within the range of Roscoe-Arthur-Coulomb angles, and orientations outside this range are not expected. Using a Drucker-Prager yield surface, Lemiale et al. (2008) inferred that high spatial resolutions are required in order to obtain shear bands at Coulomb angles. This was later affirmed by Kaus (2010), who attested that the mechanical heterogeneity has to be well resolved with at least 5-10 elements. In contrast, Choi and Petersen (2015) obtained shear bands spread around Arthur and Roscoe angles for non-associated $\phi_0 \neq \psi_0$ flow rules using a Mohr-Coulomb failure criterion. Our analysis based on the formulation presented in this work using a Drucker-Prager criterion is in agreement with the results from Choi and Petersen (2015) for $\phi_0 = \psi_0$, with shear band orientations that yield Coulomb angles; however, our results show shear bands tightly bounded to the analytical solution derived by Rudnicki and Olsson (1998). Coulomb angles also form with $\psi = 15°$ and the orientations are scattered around the Coulomb-Arthur-Roscoe spectrum only in the non-dilatant case.

The stress-displacement curves obtained from the shear band initiation illustrate the structural hardening inherent from associated models and the post-peak softening, as described by Vermeer and De Borst (1984) and also in agreement with hardening models addressing, for example, earthquake instabilities (Rudnicki (1988) and references therein).

As discussed in Spiegelman et al. (2016), visco-plastic Stokes problems may become ill-posed for pressure-dependant rheologies (e.g. Drucker-Prager) and Picard iterations might stall at large residuals. In spite of the deep implications of this issue for geodynamical models of lithospheric deformation, this difficulty did not arise during this work. However, following the conclusions drawn by Spiegelman et al. (2016), we must emphasize the importance of cautiousness when interpreting results that may not reflect fully converged numerical experiments. To enhance the convergence rate, the extension rate applied to the model is typically linearly increased during the first ten time-steps until it reaches 1 cm/yr. Strong convergence may not be fully reached in the initial time steps; however, convergence improves significantly after a few time steps and consistent patterns of shear bands develop.

The solution of the associative Drucker-Prager flow rule still exhibits a considerable mesh-dependent effects where shear band orientations in models with a fine and coarse mesh can have up to 5° of difference. One proposed remedy for this algorithmic issue consists adjusting the softening modulus as a function of element size. This was first proposed Pietruszczak and Mroz (1981) for shear softening in plasticity and by Bažant and Oh (1983) for tensile softening caused by smeared cracking. These techniques lead to improved element-size insensitivity; however, the solution can still depend on the assumed element shape and orientation. This computational issue has been overcome by applying so-called non-local continuum plasticity models (Bažant et al., 1988). In these models, stress is no longer determined uniquely by the strain history and temperature at that given point alone but also depends on the strain history of surrounding material points, with interactions exceeding a certain length-scale being neglected. Although effective computationally, this approach still involves

ad-hoc, non-physical assumptions. Mesh-dependent effects on strain localisation problems remain unresolved and are clearly a key phenomenon that still needs to be properly addressed in geodynamic models using (visco-)plastic rheologies.

Numerical examples of rifting of continental crust suggest a non-trivial effect of plastic dilation on large scale geodynamic problems. Even though the geometry of numerical fault evolution during continental rifting does not seem to be greatly altered by associated plasticity, the resulting hardening creates a strengthening of the crust that leads to a delay in the evolution of the margins, consequently delaying crustal break-up and mantle exhumation. The surface heat flow and thermal structure of the models is also altered as a result of the competition between shear heating and cooling resulting from the structural hardening.

As pointed out from experimental observations, the dilation of rocks depends on the confining pressure (e.g. Medhurst, 1997; Ribacchi, 2000), or in other words, depth. Our experiments with linear depth-dependent dilatancy angle suggest that there is not much difference between models where dilation becomes negligible at upper ($z_{lim} = 20$ km) and lower crustal depths ($z_{lim} = 40$ km); the only apparent difference between these models is a small delay in the evolution of deformation, and a slightly lower surface heat flow peak. However, a different faulting history is observed if brittle fault dilation can remain effective at lithospheric depths ($z_{lim} = 60$ km); for these the heat signature at the surface is considerably reduced.

In spite of the mathematical and physical incompleteness of the formulation presented in this paper to properly describe compaction effects in shear bands due to processes such as pressure solution or reactive fluid migration through fractures, a small modification of the continuity equation allows as to explore the geodynamic consequences of relative mass loss within a shear zone at a lithospheric scale. Our results show that this effect leads to a strong structural softening of the lithosphere that speeds up the deformation of the crust and asthenospheric upwelling. From this, we suggest that volume losses to reactive fluid migration along shear zones could play a significant role driving the defor-

mation of the lithosphere during tectonic events, and that this process deserves a more complete thermo-mechanical treatment and exploration.

Depth-dependent associated plasticity may also be important in other tectonic settings such as in subduction zones, as it could enhance plate-bending and increase the porosity of fracture zones, thus facilitating fluid circulation. It could also influence in the seismic cycle, as failure/earthquake occurrence can be delayed by the resultant structural hardening.

9. Summary

- Plastic models with a Drucker-Prager yield function and an associative flow rule yield shear bands that dip at the angles predicted by Rudnicki and Olsson (1998), whereas a non-associative deviatoric Prandtl-Reus flow rule yields shear band orientations scattered within the wider range of Coulomb-Arthur-Roscoe angles.

- Volumetric expansion within the shear bands results in a structural hardening of the faulting domain.

- The evolution and final geometry of rifted margin experiment does not show significant structural differences between dilatant and non-dilatant models.

- The slower vertical motion of mantle upwelling induced by the structural hardening of the lithosphere leads to relative cooling in the models, whereas volumetric plastic strain introduces an extra local source of heat derived from inelastic work. The thermal structure and surface heat flow in dilatant models is therefore altered with respect to non-dilatant models. For a strong lower crust, brittle deformation is highly effective and dilatant models yield similar temperature fields for the range of dilatancy angles considered in this paper. However, plasticity is less effective in models with a weak lower crust and shear heating dominates for $\psi_0 = 15°$, whereas the

model with $\psi_0 = 30°$ is cooler, due to the slower upwelling rates of mantle material.

- The evolution of the faults and shear zones of a model with a depth-dependent dilatancy angle with $\psi_0 = \phi_0$ at null confining pressure represents an intermediate state between using constant $\psi_0 = 30°$ and constant $\psi_0 = 15°$. During the early stages of extension, this model is very similar to a model with constant $\psi_0 = 30°$, while it evolves towards a similar strain rate state as the model with $\psi_0 = 15°$ as strain softening kicks in.

References

Alejano, L., Alonso, E., 2005. Considerations of the dilatancy angle in rocks and rock masses. International Journal of Rock Mechanics and Mining Sciences 42 (4), 481–507.

Andrés-Martínez, M., Morgan, J. P., Pérez-Gussinyé, M., Rüpke, L., 2015. A new free-surface stabilization algorithm for geodynamical modelling: Theory and numerical tests. Physics of the Earth and Planetary Interiors 246, 41–51.

Arthur, J., Dunstan, T., Al-Ani, Q., Assadi, A., 1977. Plastic deformation and failure in granular media. Geotechnique 27 (1), 53–74.

Bažant, Z., Lin, F.-B., et al., 1988. Non-local yield limit degradation. International Journal for Numerical Methods in Engineering 26 (8), 1805–1823.

Bažant, Z. P., Oh, B. H., 1983. Crack band theory for fracture of concrete. Matériaux et construction 16 (3), 155–177.

Bos, B., Peach, C. J., Spiers, C. J., 2000. Slip behavior of simulated gouge-bearing faults under conditions favoring pressure solution. Journal of Geophysical Research: Solid Earth 105 (B7), 16699–16717.

Brace, W., Byerlee, J., 1966. Stick-slip as a mechanism for earthquakes. Science 153 (3739), 990–992.

Braun, J., Thieulot, C., Fullsack, P., DeKool, M., Beaumont, C., Huismans, R., 2008. Douar: A new three-dimensional creeping flow numerical model for the solution of geological problems. Physics of the Earth and Planetary Interiors 171 (1-4), 76–91.

Brune, S., Heine, C., Pérez-Gussinyé, M., Sobolev, S. V., 2014. Rift migration explains continental margin asymmetry and crustal hyper-extension. Nature Communications 5, 4014.

Buck, W. R., 1991. Modes of continental lithospheric extension. Journal of Geophysical Research: Solid Earth 96 (B12), 20161–20178.

Buiter, S. J., 2012. A review of brittle compressional wedge models. Tectonophysics 530, 1–17.

Buiter, S. J., Babeyko, A. Y., Ellis, S., Gerya, T. V., Kaus, B. J., Kellner, A., Schreurs, G., Yamada, Y., 2006. The numerical sandbox: comparison of model results for a shortening and an extension experiment. Geological Society, London, Special Publications 253 (1), 29–64.

Choi, E., Petersen, K. D., 2015. Making coulomb angle-oriented shear bands in numerical tectonic models. Tectonophysics 657, 94–101.

Choi, E., Tan, E., Lavier, L., Calo, V. M., 2013. Dynearthsol2d: An efficient unstructured finite element method to study long-term tectonic deformation. Journal of Geophysical Research: Solid Earth 118 (5), 2429–2444.

Coulomb, C., 1773. Sur l'application des règles des maximis et minimis à quèlques problèmes de statique relatifs à l'architecture. Mémoires de Mathématique et de Physique. 7, 343–382.

Dabrowski, M., Krotkiewski, M., Schmid, D. W., 2008. MILAMIN: MATLAB-based finite element method solver for large problems. Geochemistry, Geophysics, Geosystems 9 (4), 1–24.

de Montserrat, A., Morgan, J. P., Hasenclever, J., 2018. M2tri: a lagrangian two-dimensional thermo-mechanical code for large strain compressible viscoelastic geodynamical modelling.

de Souza Neto, E. A., Peric, D., Owen, D. R., 2011. Computational methods for plasticity: theory and applications. John Wiley & Sons.

Detournay, E., 1986. Elastoplastic model of a deep tunnel for a rock with variable dilatancy. Rock Mechanics and Rock Engineering 19 (2), 99–108.

Drucker, D. C., Prager, W., 1952. Soil mechanics and plastic analysis or limit design. Quarterly of applied mathematics 10 (2), 157–165.

Escartin, J., Hirth, G., Evans, B., 1997. Nondilatant brittle deformation of serpentinites: Implications for mohr-coulomb theory and the strength of faults. Journal of Geophysical Research: Solid Earth 102 (B2), 2897–2913.

Fullsack, P., 1995. An arbitrary lagrangian-eulerian formulation for creeping flows and its application in tectonic models. Geophysical Journal International 120 (1), 1–23.

Gerya, T. V., Yuen, D. A., 2007. Robust characteristics method for modelling multiphase visco-elasto-plastic thermo-mechanical problems. Physics of the Earth and Planetary Interiors 163 (1-4), 83–105.

Gleason, G. C., Tullis, J., 1995. A flow law for dislocation creep of quartz aggregates determined with the molten salt cell. Tectonophysics 247 (1), 1–23.

Gratier, J.-P., Richard, J., Renard, F., Mittempergher, S., Doan, M.-L., Di Toro, G., Hadizadeh, J., Boullier, A.-M., 2011. Aseismic sliding of active faults by pressure solution creep: Evidence from the San Andreas Fault Observatory at Depth. Geology 39 (12), 1131–1134.

Hirth, G., Kohlstedt, D., 2003. Rheology of the upper mantle and the mantle wedge: A view from the experimentalists. Inside the subduction Factory, 83–105.

679 Huismans, R., Beaumont, C., 2007. Roles of lithospheric strain softening and
680 heterogeneity in determining the geometry of rifts and continental margins.
681 Geological Society, London, Special Publications 282 (1), 111–138.

682 Huismans, R., Beaumont, C., 2011. Depth-dependent extension, two-stage
683 breakup and cratonic underplating at rifted margins. Nature 473 (7345), 74.

684 Huismans, R. S., Beaumont, C., 2002. Asymmetric lithospheric extension: The
685 role of frictional plastic strain softening inferred from numerical experiments.
686 Geology 30 (3), 211–214.

687 Huismans, R. S., Beaumont, C., 2014. Rifted continental margins: The case for
688 depth-dependent extension. Earth and Planetary Science Letters 407, 148–
689 162.

690 Karato, S.-i., Riedel, M. R., Yuen, D. A., 2001. Rheological structure and de-
691 formation of subducted slabs in the mantle transition zone: implications for
692 mantle circulation and deep earthquakes. Physics of the Earth and Planetary
693 Interiors 127 (1), 83–108.

694 Karato, S.-i., Wu, P., 1993. Rheology of the upper mantle: A synthesis. Science
695 260 (5109), 771–778.

696 Kaus, B. J., 2010. Factors that control the angle of shear bands in geodynamic
697 numerical models of brittle deformation. Tectonophysics 484 (1-4), 36–47.

698 Lemiale, V., Mühlhaus, H.-B., Moresi, L., Stafford, J., 2008. Shear banding
699 analysis of plastic models formulated for incompressible viscous flows. Physics
700 of the Earth and Planetary Interiors 171 (1-4), 177–186.

701 Medhurst, T. P., 1997. Estimation of the in situ strength and deformability of
702 coal for engineering design.

703 Mises, R. v., 1913. Mechanik der festen körper im plastisch-deformablen zu-
704 stand. Nachrichten von der Gesellschaft der Wissenschaften zu Göttingen,
705 Mathematisch-Physikalische Klasse 1913 (4), 582–592.

Moresi, L., Dufour, F., Mühlhaus, H.-B., 2003. A lagrangian integration point finite element method for large deformation modeling of viscoelastic geomaterials. Journal of Computational Physics 184 (2), 476–497.

Moresi, L., Quenette, S., Lemiale, V., Meriaux, C., Appelbe, B., Mühlhaus, H.-B., 2007. Computational approaches to studying non-linear dynamics of the crust and mantle. Physics of the Earth and Planetary Interiors 163 (1), 69–82.

Pietruszczak, S., Mroz, Z., 1981. Finite element analysis of deformation of strain-softening materials. International Journal for Numerical Methods in Engineering 17 (3), 327–334.

Poirier, J.-P., 1985. Creep of crystals: high-temperature deformation processes in metals, ceramics and minerals. Cambridge University Press.

Popov, A., Sobolev, S., 2008. Slim3d: A tool for three-dimensional thermomechanical modeling of lithospheric deformation with elasto-visco-plastic rheology. Physics of the Earth and Planetary Interiors 171 (1-4), 55–75.

Renard, F., Gratier, J.-P., Jamtveit, B., 2000. Kinetics of crack-sealing, intergranular pressure solution, and compaction around active faults. Journal of Structural Geology 22 (10), 1395–1407.

Ribacchi, R., 2000. Mechanical tests on pervasively jointed rock material: insight into rock mass behaviour. Rock mechanics and rock engineering 33 (4), 243–266.

Ros, E., Pérez-Gussinyé, M., Araújo, M., Thoaldo Romeiro, M., Andrés-Martínez, M., Morgan, J. P., 2017. Lower Crustal Strength Controls on Melting and Serpentinization at Magma-Poor Margins: Potential Implications for the South Atlantic. Geochemistry, Geophysics, Geosystems 18 (12), 4538–4557.

Roscoe, K. H., 1970. The influence of strains in soil mechanics. Geotechnique 20 (2), 129–170.

Rudnicki, J., Olsson, W., 1998. Reexamination of fault angles predicted by shear localization theory. International Journal of Rock Mechanics and Mining Sciences 35 (4-5), 512–513.

Rudnicki, J. W., 1988. Physical models of earthquake instability and precursory processes. pure and applied geophysics 126 (2-4), 531–554.

Scholz, C. H., 2002. The mechanics of earthquakes and faulting. Cambridge university press.

Spiegelman, M., May, D. A., Wilson, C. R., 2016. On the solvability of incompressible stokes with viscoplastic rheologies in geodynamics. Geochemistry, Geophysics, Geosystems 17 (6), 2213–2238.

Tetreault, J., Buiter, S., 2017. The influence of extension rate and crustal rheology on the evolution of passive margins from rifting to break-up. Tectonophysics.

Vermeer, P. A., De Borst, R., 1984. Non-associated plasticity for soils, concrete and rock. HERON, 29 (3), 1984.

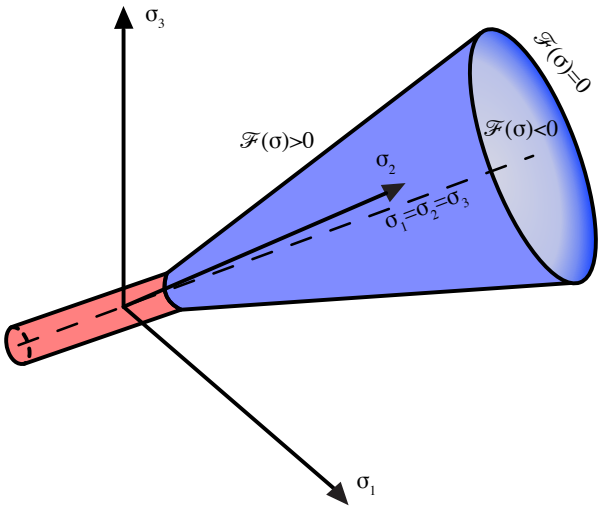

Figure .1: Sketch of the combined Drucker-Prager (in blue) and von Mises (in red) yield surface.

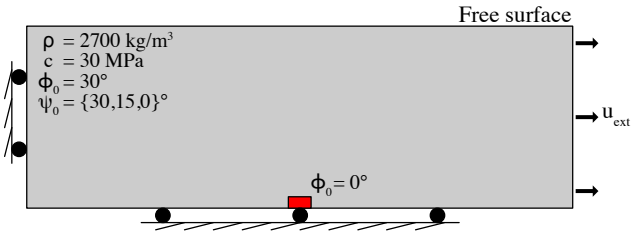

Figure .2: Set-up of the shear band initiation model. The region in red represents a mechanical heterogeneity with $\phi = 0°$.

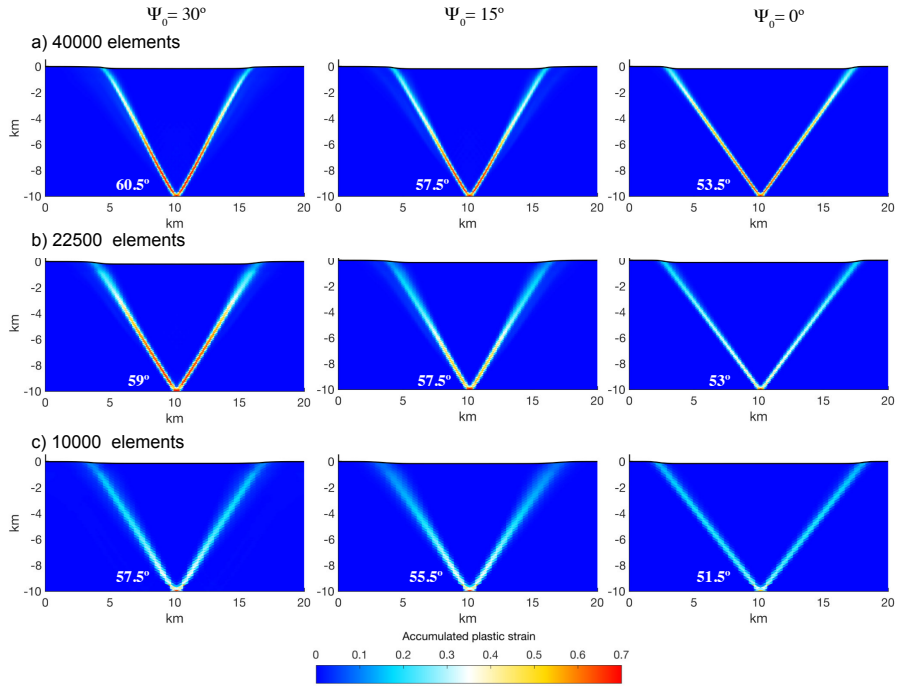

Figure .3: Shear band results for associative and non-associated flow rules with $\psi = 30°$, $\psi = 15°$ and $0°$. Models have a resolution of **a)** 40000, **b)** 22500 and **c)** 10000 triangular elements with an aspect ratio (height/base) of 0.25. Strain softening is applied to ϕ and ψ in all models. The colour maps represent the rate square root of the second invariant of the accumulated plastic strain rate $\mathbf{E}^{pl}$.

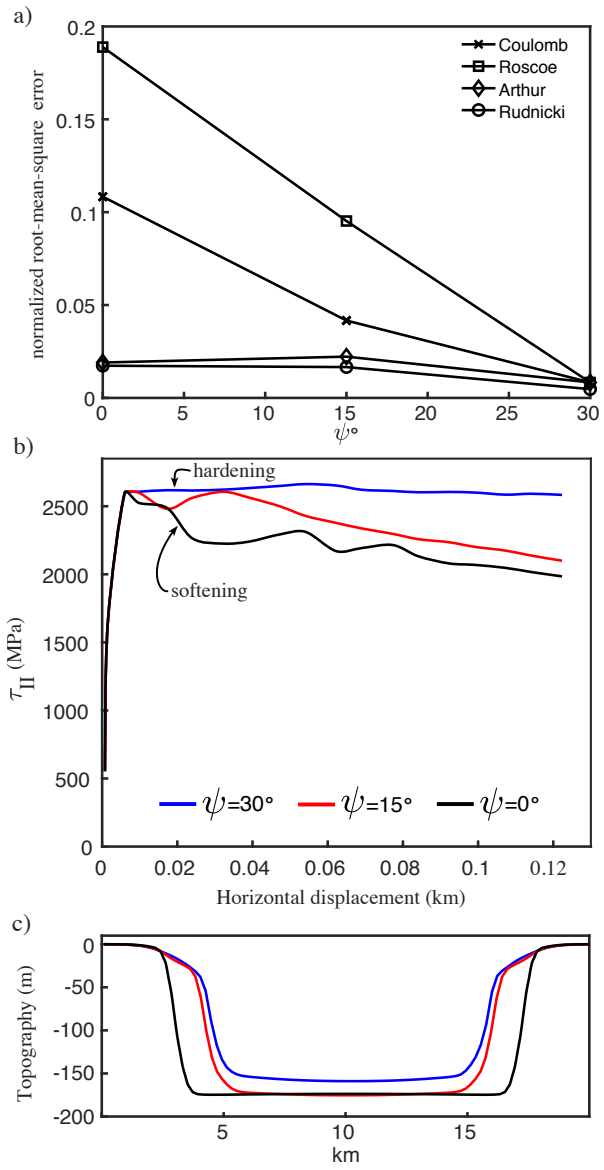

Figure .4: **a)** Normalised root-mean-square (rms) error between the numerical orientations of the shear bands and the analytical Coulomb, Roscoe, Arthur and Rudnicki angles. **b)** Stress-horizontal displacement curve. The vertical axis corresponds to the stress integrated along a vertical profile at the right boundary of the domain. **c)** Topographic expression for all models; the vertical axis of the plot is vertically exaggerated. The results in a), b) and c) correspond to the high-resolution models (40000 elements).

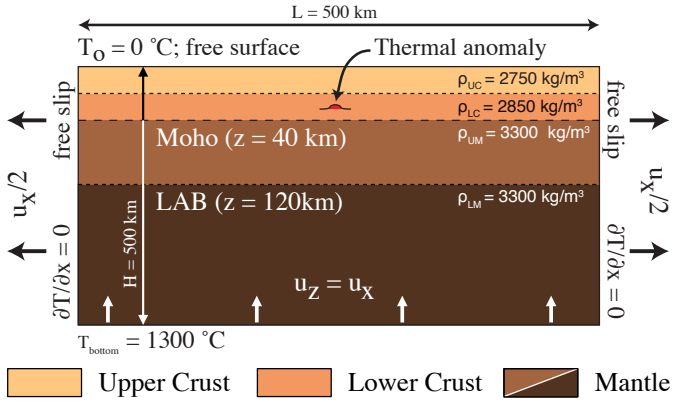

Figure .5: Model set-up. The model is stretched using pure shear boundary conditions. To localise the deformation in the centre of the model, a thermal anomaly is introduced in the middle of the lower crust at $x = 0$ km. The rheological parameters are given in Table 6.1.

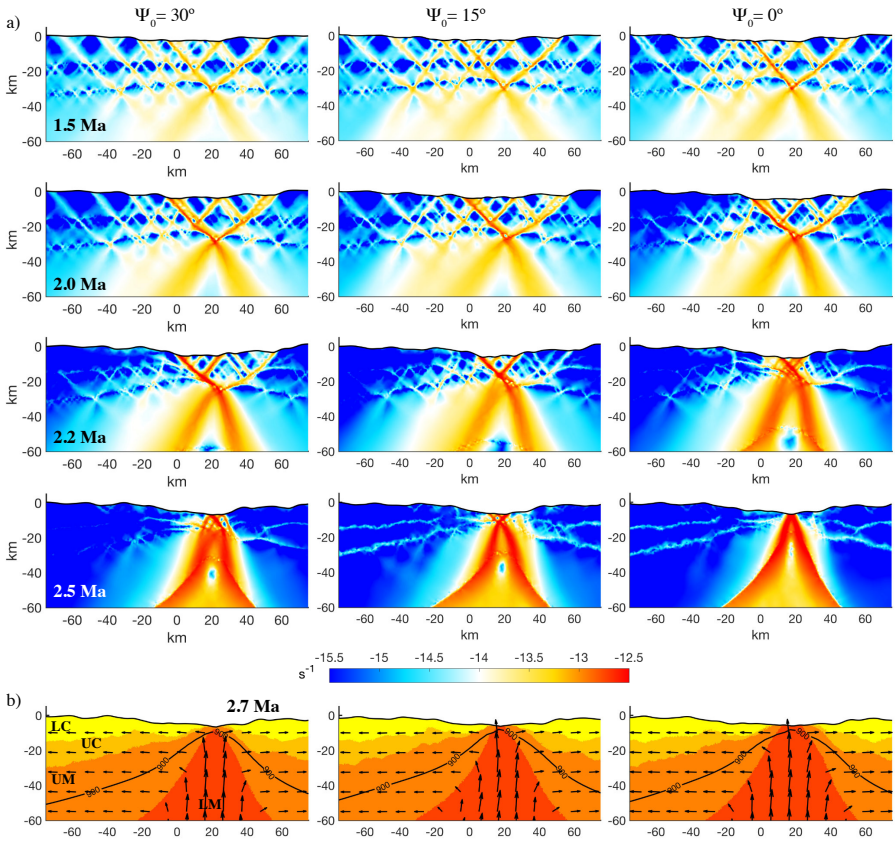

Figure .6: Models with a mafic granulite lower crust (strong end member). **a)** Evolution of the square root of the second invariant of strain rate ($\dot{\varepsilon}_{II}$) for $\psi_0 = 30°$, $15°$ (associative plasticity) and $0°$ (non-associative plasticity). **b)** Comparison of the geometry of the model at 2.5 Ma. Colour maps indicate the different rheological layers and arrows indicate velocity.

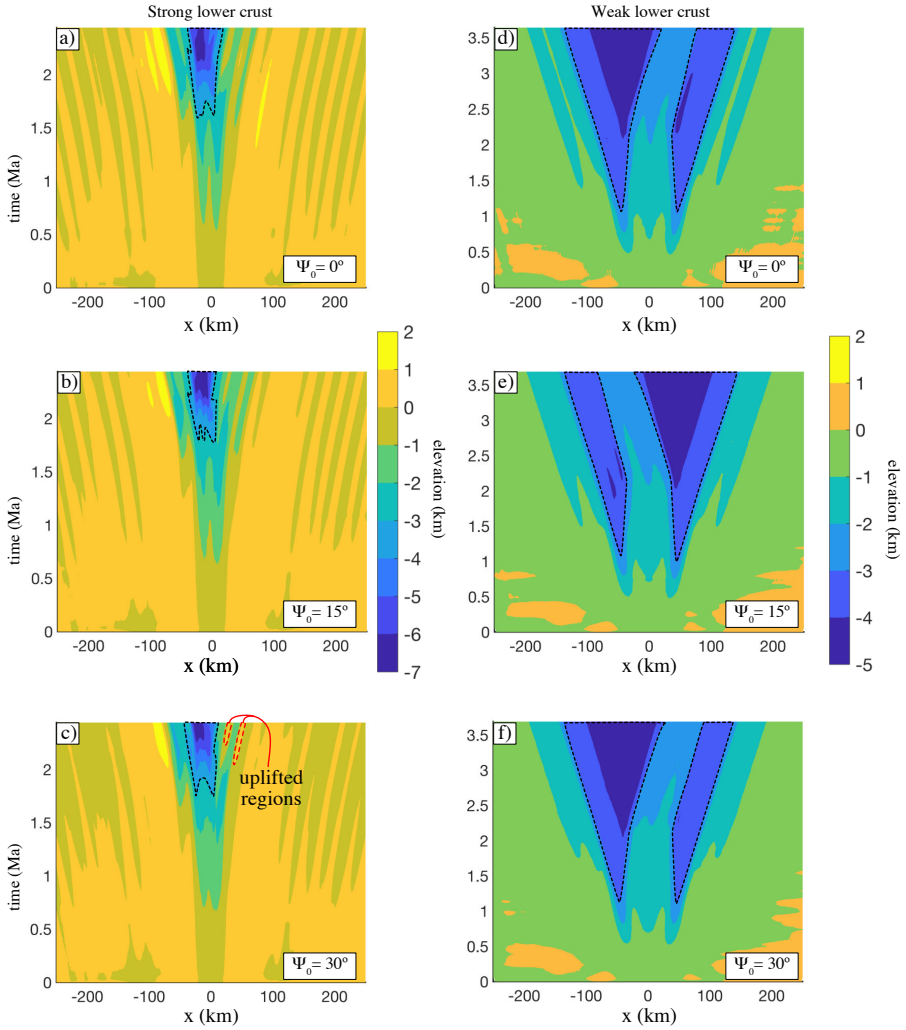

Figure .7: Surface evolution with time for a strong **a)** lower crust and **b)** weak lower crust for different values of dilatancy angle. Areas within black and red dashed polygons indicate deep water basins and uplifted regions, respectively.

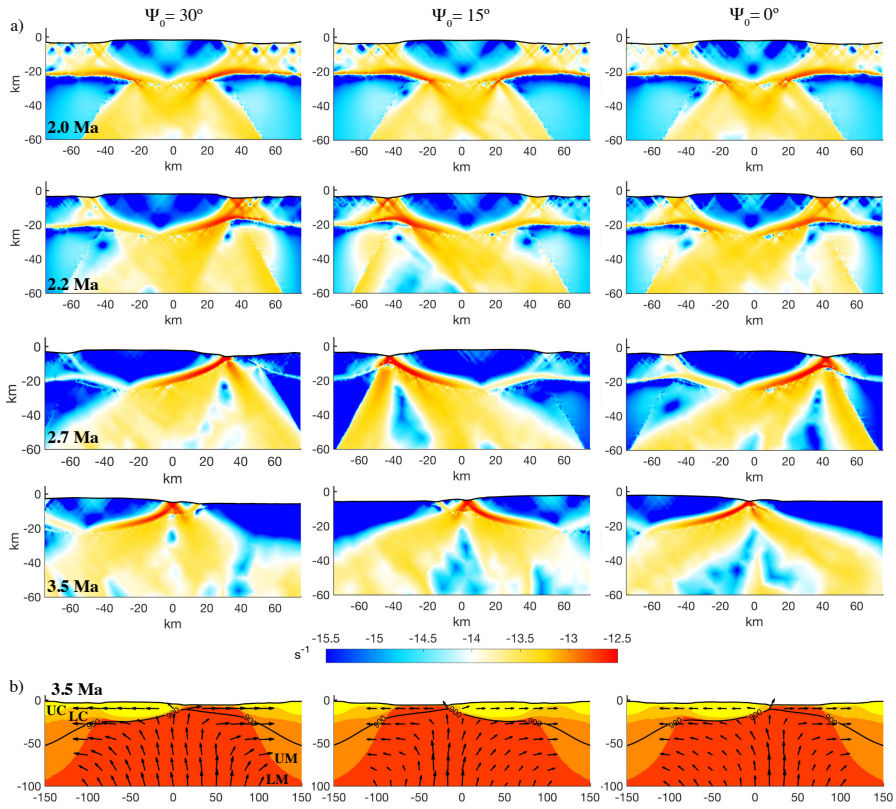

Figure .8: Models with a wet quartzitic lower crust (weak end member). **a)** Evolution of the square root of the second invariant of strain rate ($\dot{\varepsilon}_{II}$) for $\psi_0 = 30°$, 15° (associative plasticity) and 0° (non-associative plasticity). **b)** Comparison of the geometry of the model at 2.5 Ma. Colour maps indicate the different rheological layers and arrows indicate velocity. **c)** Values of the dilatancy angle at 2.5 Ma.

5 | Rapid cooling and exhumation of lower crust. Insights from numerical models and application to SE Asia.

Albert de Montserrat, Juliane Hennig-Breitfield, Jason P. Morgan and Robert Hall. Rapid cooling and exhumation of lower crust. Insights from numerical models and application to SE Asia. Under revision in *Earth and Planetary Science Letters, April 2018.*

Authors contribution

AdM, JM and RH defined the research. AdM designed the numerical experiments and analysed the results in discussion with JH, JM and RH. AdM wrote the manuscript in collaboration with JH, JM and RH.

Rapid cooling and exhumation of lower crust. Insights from numerical models and application to SE Asia

Albert de Montserrat[a], Juliane Hennig-Breitfeld[a], Jason P. Morgan[b], Robert Hall[a]

[a] *SE Asia Research Group, Department of Earth Sciences, Royal Holloway University of London, Egham, United Kingdom*
[b] *Department of Earth Sciences, Royal Holloway University of London, Egham, United Kingdom*

Abstract

Recent episodes of extension in SE Asia have been associated with rapid sedimentary basin growth, and phases of crustal melting, uplift and extremely rapid exhumation of young (Early-Late Pliocene) metamorphic complexes. We combine geochronological and geothermobarometric data with two-dimensional numerical models to investigate exhumation of metamorphic core complexes in Sulawesi, Indonesia. The lithospheric thermal conditions and extension rates at which these developed and later exhumed are poorly known. Therefore, we explore a wide range of potential initial conditions with different permutations of extension rate and initial Moho temperature. The numerical models show that high Moho temperatures are key to shaping the architecture of the stretched lithosphere. Hot and weak lower crust fails to transmit stress and brittle deformation to deeper regions, resulting in a strong decoupling between crust and lithospheric mantle. In this case, deformation is dominated by ductile flow, yielding the exhumation of one-to-several partially molten lower crustal bodies. Continental break-up is often inhibited by the ductile behaviour of the lower crust, and is only achieved after considerable cooling of the lithosphere. Further comparison between the observed and synthetic model T-t paths confirms that extremely rapid exhumation of lower crustal bodies should be linked to very fast extension rates ($\sim$75 mm/yr) and Moho temperatures (>740 °C) higher than those in more commonly studied rift settings (e.g. Atlantic opening,

East African Rift, Australia-Antarctica opening).

Keywords: SE Asia, Sulawesi, Palu Metamorphic Complex, Fast exhumation of lower crust, Slow, rapid and ultra-rapid metamorphic complexes

1. Introduction

SE Asia represents one of the most tectonically active regions of the Earth, as the result of the convergence of the Eurasian, Indo-Australian and Philippine Sea plates. Recent thermobarometric studies have revealed SEA as the host of arguably the youngest continental Metamorphic Core Complexes (MCCs) in Sulawesi (Hennig et al., 2014, 2016, 2017; van Leeuwen et al., 2016), Seram (Pownall, 2015; Pownall et al., 2017) and D'Entrecasteaux Islands (Little et al., 2011; Baldwin et al., 2004) ever reported, as the consequence of a series of extensional episodes during the Neogene (Spakman and Hall, 2010; Hall, 2011, 2012; Pownall et al., 2013; Hennig et al., 2014).

A two-phase thermal history of the lower crustal rocks, consisting of an initial phase of slow cooling, followed by a brief (few million years) period of rapid cooling, at rates of 60-280 °C/Ma, have been reported in extension-driven Cordilleran-type MCCs in the Basin and Range province (e.g. John and Howard, 1995), Cyclades (e.g. Scott et al., 1998) and North China Craton (e.g. Yang et al., 2007), as well as in MCCs in the Canadian Cordillera thought to have been developed by gravitational collapse (e.g. Vanderhaeghe et al., 2003). Although this two-phase thermal history has been attributed to variations in denudation rate, localised thermal perturbations or changes in the geometry of the detachment faults, the nature of the pulses of rapid cooling remain poorly understood.

Recent thermobarometric and geochronological data from rocks of the Palu Metamorphic Complex (PMC) in Sulawesi (Hennig et al., 2017), indicate that cooling rates in MCCs can be higher than those previously reported ($\geq$ 540 °C/Ma). Unfortunately, and despite the increasing number of geological and geophysical studies carried out in the last decades, the initial thermal structure,

and extension rates, responsible for the development of the PMC and other MCCs in SEA remains poorly constrained.

A numerical approach has become a powerful tool to investigate different aspects that control the formation of the MCCs, such as partial melting and extension rates Rey et al. (2009), inherited crustal layering Huet et al. (2011a) and wedge structures Huet et al. (2011b), origin of the heat source necessary for migmatisation Schenker et al. (2012), and role of the density and viscosity of the deep crust Korchinski et al. (2018). The thermobarometric history of MCCs has been also explored by numerical models, and synthetic p-T paths have yielded reasonable comparisons with natural counterparts (Huet et al., 2011a,b; Schenker et al., 2012). However, the cooling history of the MCCs have received little attention from a numerical point of view.

In this paper, we use two-dimensional thermo-mechanical numerical models to study the thermal history of rocks comprising MCCs and what extension rates are necessary to reproduce the cooling rates observed in the geological record. In particular, we compare synthetic T-t paths against available thermochronological data from the PMC (Hennig et al., 2017). To find the best fit with the natural cooling paths, we run a suite of numerical models with different permutations of initial conditions, namely extension rate and initial Moho temperature.

We further investigate whether the volume and distribution of crustal melting plays a crucial role in the thermal history of continental MCCs. For this reason, we consider two solidi with that lead to different volumes of partially molten crust. An initial volume of partial melting is not prescribed anywhere in the model, thus partial melting is self-consistently produced according to pressure and temperature conditions.

The different combinations of Moho temperature and extension rate result in the formation of continental core complexes with distinct thermal histories showing that: i) slow extension rates lead to cooling rates of 60-300 °C/Ma, and ii) high cooling rates as in the PMC >300-540 °C/Ma) are reproduced in models under rapid and ultra-rapid extension ($\geq$35 mm/yr).

2. Extension of Central Sulawesi: rapid exhumation of the Palu Metamorphic Complex

[Figure 1 about here.]

The western continental margin of Sundaland in Sulawesi is formed by Australian crust that rifted from the Australian margin during the Late Jurassic and was accreted to Sundaland in the Late Cretaceous (Smyth et al., 2007; Hall et al., 2009; Hall, 2011). Rifting from Borneo occurred in the Eocene (Hamilton, 1979; Weissel, 1980), related to widespread extension in SE Asia which opened the Celebes Sea followed by formation of the North Sulawesi volcanic arc (Hall, 2012).

At c. 45 Ma, Australia started to move northward. The collision of the northern promontory of the Australian margin, called the Sula Spur (Klompe, 1954), with the forearc of North Sulawesi volcanic arc started in the Early Miocene at c. 23 Ma (Spakman and Hall, 2010; Hall, 2011). Northward movement of Australia continued after the collision until c. 17 Ma, when eastward propagation of a tear in the slab from the Java trench was accompanied by rapid subsidence and rollback of the subduction zone into the Banda embayment (Spakman and Hall, 2010; Hall, 2018). Banda rollback led to widespread extension above the subducting slab, resulting in the formation of oceanic crust and opening of the North Banda Sea between 12.5 and 7 Ma (Hinschberger et al., 2000), and caused extension-related magmatism in West Sulawesi (Polvé et al., 1997; Hennig et al., 2016). Rocks associated with this magmatism are not well known and were described as a high- potassium suite, which includes nepheline gabbros, quartz-syenites, and monzodiorites of presumed Middle to Late Miocene age (Priadi et al., 1994; Polvé et al., 1997; Elburg et al., 2003). Extension led to crustal thinning and weakening in the study area, which defines the starting conditions for our numerical model that is based on a hot and relatively thin lithosphere.

The PMC is located in the neck of Sulawesi (Fig. D.1a,b). The metamorphic rocks of the PMC were initially interpreted to be Permo-Triassic basement rocks

recording a major rift phase on the margin of New Guinea (Sukamto, 1973; van Leeuwen and Muhardjo, 2005). More recent studies from U-Pb zircon dating of schists of the PMC revealed that some of these rocks have Eocene protoliths, and therefore must be younger (van Leeuwen et al., 2016; Hennig et al., 2016). The PMC is typically divided into a metapelite unit in the west and a gneiss unit in the east Sukamto (1973); van Leeuwen and Muhardjo (2005). The metamorphic grade increases to the east, and the gneiss unit is comprised mainly of high-grade metamorphic rocks: biotite granite-gneisses and biotite-amphibole granite-gneisses, and subordinate pyroxene gneisses, marbles and migmatites.

Radiometric dating of magmatic and metamorphic rocks of the PMC showed evidence of contemporaneous Pliocene magmatism, metamorphism and exhumation, suggesting the PMC must have developed in an extensional setting that includes significant stretching of the upper plate and rapid exhumation of deep crust; features that resemble a metamorphic core complex in an extensional setting (van Leeuwen and Muhardjo, 2005; Hennig et al., 2014, 2017). The detachment fault has not been observed and its inferred position is in mountains in the neck of Sulawesi where there is dense rainforest vegetation, and accessibility is limited. Mylonitic shear zones observed in biotite hornfels and slates in the northern PMC are interpreted as related to subordinate detachment faults (Hennig et al., 2017). The metapelites of the PMC are strongly deformed and the youngest metamorphism has pervasively overprinted older fabrics. Some textural evidence for near-isothermal decompression was observed by staurolite, andalusite, and cordierite or pinite porphyroblasts which are sometimes mantled by white mica coronas, indicating disequilibrium to secondary low-pressure conditions.

T-t paths of S-type magmatic and metamorphic rocks (Fig. D.1d) from the PMC have been estimated by combining U-Pb zircon rim ages from biotite-amphibole gneiss Hennig et al. (2016) with $^{40}Ar/^{39}Ar$ cooling ages of amphibole and biotite from amphibolite and biotite schist (Hennig et al., 2017), yielding remarkably high cooling rates (Fig. D.1d) that suggest an unusually rapid exhumation during the Late Pliocene to Pleistocene (Hennig et al., 2017). At the

same time there was the youngest extension phase affecting northern Sulawesi due to northward subduction rollback of the North Sulawesi trench. Previously, this rollback was explained as a response to clockwise rotation of the North Arm (Hamilton, 1979; Silver et al., 1983; Surmont et al., 1994) and left-lateral movement along the Palu-Koro fault at the western end of the trench (Walpersdorf et al., 1998; Socquet et al., 2006). However, new studies reveal a more complex history related to development of subduction, and the deepest part of the subducted slab is located in the centre of the subduction zone (Hall, 2018). Our numerical experiments are aimed to model the period of the last 3-5 Ma of exhumation of the PMC, during which the subducted slab was deep and dense enough to drive subduction rollback.

3. Numerical modelling of stretched crust

3.1. Numerical code

We use a modified version of the viscous flow solver MILAMIN (Dabrowski et al., 2008), based on a Lagrangian formulation of the Finite Element Method, to solve the coupled equations of conservation of momentum, conservation of mass and conservation of energy. Incompressibility is incorporated by using the Boussinesq approximation and the mechanical behaviour of the rocks is modelled as a Maxwell body with a visco-elasto-plastic rheology: viscous deformation is described by a power-law constitutive equation, and plastic deformation is computed employing a pressure dependent Drucker-Prager yield surface. Strain localisation is enhanced by the reduction of the angle of friction as a linear function of the accumulated plastic strain (e.g. de Souza Neto et al., 2011). A brief description of the numerical formulation is provided in Appendix A.

3.2. Model set-up and initial conditions

[Figure 2 about here.]

The domain of the models consists in 500 by 400 km rectangular box (Fig. D.2a) that is divided in four laterally homogeneous rheological layers: a 35

km thick crust comprised of a wet quartzitic upper crust (UC) and lower crust (LC), a 85 km thick dry olivine lithospheric mantle (LM) and wet olivine asthenospheric mantle (AM). The rheological and mechanical parameters used to describe the thermo-mechanical behaviour of these layers are shown in Table 3.2. Pure shear far-field boundary conditions (BCs) are prescribed on the boundaries of the model (half extension rate prescribed at the side boundaries, and full extension rate at the bottom), with a shear stress-free BC employed on the lateral and bottom boundaries. The top boundary of the domain is treated as a free surface. We introduce a Gaussian-shape thermal perturbation to promote strain localisation after onset of extension. This thermal weak seed is emplaced at the centre of the model to avoid boundary effects that might corrupt the results. At the onset of the extensional event that led to the formation of the PMC the crust had already undergone a previous stretching event. For this reason, we define a relatively thin crust of 35 km.

The thermal gradient in the Banda Sea region is poorly constrained. However, the lithosphere must have been very hot during the extensional event that triggered the development and exhumation of the PMC (Hall, 2018). To provide better constraints on over the initial thermal gradient, we explore a set of different permutations of initial Moho temperature: 1) cold: 710 °C; 2) intermediate: 844 °C ; 3) warm: 911 °C ; and 4) hot: 1040 °C.

We also consider a range of different extension rates: 1) slow: 10 mm/yr; 2) rapid: 35 mm/yr; and, 3) ultra-rapid: 75 mm/yr. The rapid and ultra-rapid rates are faster than the ones used in previous numerical studies of the formation of MCCs (e.g. Huet et al., 2011a; Rey et al., 2011; Schenker et al., 2012), and are chosen to investigate the plausible range of extension rates responsible for the evolution of the Banda Sea region during the last 5-10 Ma.

3.3. Partial melting

Partial melting is computed using the approach described by Morgan (2001) when pressure and temperature conditions of any parcel of the model exceed the solidus temperature (Fig.D.2b). Partial melting occurring at the LC is calcu-

Table 1: Rheological parameters. The upper and lower crust are weak wet quartzite (Gleason and Tullis, 1995), the upper and lower mantle are dry olivine and wet olivine (Hirth and Kohlstedt, 2003), respectively. Density values within brackets indicate the density of a fully molten rock.

Parameter	Description	Lower Mantle	Upper Mantle	Lower Crust	Upper Crust
c	Cohesion (Mpa)	20	20	20	20
ϕ_o	Peak friction angle (°)	30	30	30	30
ϕ_∞	Minimum friction angle (°)	15	15	15	15
ρ	Density (kgm^{-3})	3300 (2900)	3300 (2900)	2850 (2400)	2700 (2400)
G	Shear modulus (GPa)	74	74	40	36
α	Thermal expansivity	$3 \cdot 10^{-5}$	$3 \cdot 10^{-5}$	$2.4 \cdot 10^{-5}$	$2.4 \cdot 10^{-5}$
H_Q	Radioactive heating (Wm^{-3})	0	0	$0.2 \cdot 10^{6}$	$1.3 \cdot 10^{6}$
K	Thermal conductivity ($Wm^{-3}K^{-3}$)	3.3	3.3	2.5	2.1
A	Pre-exponential factor ($Pa^{-n}s^{-1}$)	$10^{-15.56}$	$10^{-15.56}$	10^{-28}	10^{-28}
E	Activacion energy ($KJmol^{-3}$)	480	530	223	223
V_o	Activation volume(m^3mol^{-3})	10^{-4}	10^{-6}	0	0
n_{dis}	Power-law exponent (dislocation creep)	3.5	3.5	4	4
n_{dif}	Power-law exponent (diffusion creep)	1	1	0	0

lated using the solidus (Solidus A) of a hydrated granite (Boettcher and Wyllie, 1968), and decompression melting of the mantle is calculated according to the solidus of a fertile peridotite (Morgan, 2001). Additionally, we investigate the evolution of MCCs in reduced crustal partial melting conditions by considering the solidus (Solidus B) of a fluid-absent MORB-derived amphibolite (López and Castro, 2001). We note that this solidus does not correspond to the LC rheology used in the models and has been chosen merely as an end member of low partial melting productivity. Segregation of the melt from its source is not considered and we assume that it moves *en masse* (Teyssier and Whitney, 2002). Rosenberg and Handy (2005) pointed out that the viscosity of crustal rocks is significantly reduced for $F > 7\%$, independent of the melting or crystallizing state of the rock. Following this conclusion, the viscosity of crustal rocks in the models is linearly reduced as a function of melt fraction. Density is also linearly reduced with increasing melt fraction.

4. Dynamics of lower crustal exhumation

A total of 24 model calculations have been performed for all the possible combination of initial Moho temperature, extension rate and LC solidus stated in Section 3.2 . All these models develop a LC dome that is exhumed along a detachment fault. The dynamics of the formation of these domes share some common features that are observed in all the models:

[Figure 3 about here.]

1. An initial stage (total extension: $\leq 4\%$) dominated by either pure shear (under slow extension; Fig. D.3.1a) or simple shear (under rapid and ultra-rapid extension; Fig. D.3.1b), resulting in two conjugate normal faults that root in the LC, producing a single graben.
2. Between 4-6 % of total extension (Fig. D.3.2), the LC dome starts to develop, and the conjugate normal faults are abandoned. During this stage, ductile flow of basal crustal material feeds the dome, resulting in a gradual thinning of the LC at the flanks of the dome. Strain localises in a detachment fault that starts at the centre of the graben and roots at the top of the crustal dome. At this stage, some secondary shear bands may develop, but crustal deformation remains mainly accommodated by the detachment fault.
3. As extension continues (total extension: 6-8%), the detachment fault rotates, reaching low angles (15-20°) close to the surface, whereas the dip remains within 50-60° at mid-crustal depths. Ductile flow of the LC keeps filling the gap left by the stretched UC and the dome is progressively exhumed along the detachment (Fig. D.3.3).
4. Exhumation of the LC dome occurs typically after 8-10% of extension and it is followed by a period of lateral spreading (Fig. D.3.4).

After 10-15% of extension, the evolution of the models differs depending on the initial conditions. Moreover, the topography of the Moho, formation of secondary domes, partial melting production, and thermal history also vary

according to the initial conditions. The results are further summarised in the following sections.

4.1. Cold models: $T_{Moho} = 710\ ^{\circ}C$

[Figure 4 about here.]

The dynamics of extension and crustal dome formation during the early stages (extension $< 10\%$) are as described above. Synchronous with the growth of the dome, the upwelling of mantle material leads to a positive topography of the Moho underneath the crustal dome, and decompression melting takes place in the ascended mantle at about 50 km depth. In the late stages of extension ($> 10\%$), shear zones penetrate into the Moho, coupling the deformation between lithosphere and asthenosphere and leading to exhumation of mantle material and, consequently, mantle exhumation and formation of oceanic crust (Fig. D.4a). Melting of the LC is not predicted under these thermal conditions for models employing the Solidus B and the final state of the model corresponds to two conjugate margins with a gradually thinned crust.

4.2. Intermediate models : $T_{Moho} = 844\ ^{\circ}C$

Under this initial thermal structure (Fig. D.4b), the detachment remains active throughout the period of domal growth and it is only abandoned after the upper crust is broken apart and lateral spreading of the dome begins. In contrast to models with a cold initial geotherm the elevated temperature of the LC inhibits the transmission of stress to the Moho. As a consequence, and even though the Moho bends upwards due to upwelling of asthenospheric material, the crust never ruptures. The base of LC remains under partial melting conditions, and molten material is advected towards the surface as the dome grows, resulting in a mushroom-shaped region of partially molten crust.

During the first stages of the development of the LC dome in rapid and ultra-rapid models (≥ 35 mm/yr), the asthenosphere flows upwards and localises right underneath the dome. With further extension, the rise of asthenospheric material concentrates below one of the flanks of the dome, and as a consequence,

the LC experiences conductive heating at the contact with the lower mantle, leading to additional partial melting production and Ultra High Temperature (UHT) conditions. These heated rocks form a secondary dome that is progressively exhumed along a new detachment fault that roots in the LC. These secondary domes are not predicted by slow extension rates. Further extension of the model produces extreme thinning of the LC and decompressional melting of the mantle, located underneath the dome or the (if there is any) secondary dome. Mantle exhumation is only reached at very late stages of deformation (extension $> 45\%$), after significant crustal thinning and cooling.

In slow and intermediate temperature models, ductile flow of the deep crust inhibits crustal thinning and the Moho remains flat during the growth and exhumation of the LC dome. Under these conditions, doming of the Moho and decompression melting of the mantle are only observed after c. 18 Ma, triggered by the ascent of asthenospheric material.

4.3. Warm and hot models : $T_{Moho} \geq 911\ ^{\circ}C$

Strain localises in the LC as a detachment fault, leading to the formation of a LC dome. After the dome has been exhumed to the surface along the detachment and the latter becomes inactive, strain localises in new detachments along the model. These detachment faults are associated with the development of LC domes. As a consequence of the high temperatures, stress is not transmitted through the LC, the crust remains uncoupled from the mantle, and the topography of the Moho remains almost flat (Fig. D.5a,b). Exceptionally, the topography of the Moho of warm models under fast extension (≥ 35 mm/yr) is slightly bent upwards.

During the growth and exhumation of the LC, there is no melt productivity in the mantle, and UHT conditions at the base of the crust are reached only for $u_{ext} \geq 35$ mm/yr. In this set of experiments, decompression melting of the asthenosphere and mantle exhumation is observed only at c. 15 Ma and c. 8 Ma for rapid and ultra-rapid extension, respectively, after hyperextension of the crust and a considerable cooling.

4.4. p-T paths of lower crustal rocks

Synthetic p-T paths (supplementary Figs. 1 and 2) are obtained by tracking the evolution through time of pressure and temperature of a set of passive markers located within the LC. We refer to the markers initially located at 19, 27 and 34 km depth as shallow, mid and deep markers respectively (see Fig.D.8a,b for their location). The shape of the p-T paths shows a high sensitivity to extension rate as fast extension rates promote near-isothermal decompression. In contrast, the initial Moho temperature does not have a significant influence in the shape of the p-T paths and only increases (or reduces) the average temperature of the curves.

Similar p-T paths are observed in rapid and ultra-rapid models with cold-to-warm ($710 \leq T_{Moho} \leq 911$ °C) initial Moho temperatures, where a bimodal thermobarometric history of the LC rocks record is recorded. While deep and mid markers record an initial phase of near-isothermal decompression (down to 0.2 GPa), shallow markers experience an initial phase of decompressional heating as the result of heat advection, reaching peak conditions of 550-600 °C and c. 0.3 GPa.The markers cross from the kyanite to the sillimanite to the andalusite stability field during isothermal decompression, with the exception of shallow rock domes that cross from kyanite directly into the andalusite stability field. In contrast, slow models show significant differences in the p-T records between cold ($T_{Moho} = 710$ °C) and intermediate-to-warm ($844 \leq T_{Moho} \leq 911$ °C) initial Moho temperatures. In the cold case, near-isothermal decompression of deep markers occurs from about 0.85 GPa to 0.45 GPa, and mid and shallow markers record cooling following a path subparallel to the kyanite-andalusite transition. In warmer models ($T_{Moho} \geq 844$ °C), deep markers record decompressing heating with peak conditions of 0.6-0.75 GPa and 750-800 °C, followed by cooling along a geothermal gradient of c. 10 °C/km that switches to c. 35 °C/km at c. 0.3 GPa, until final exhumation. Despite not being exhumed to the surface, shallow markers located at the flanks of the LC dome record isobaric heating during the early stages of extension.

In all models, we observe that deep markers are always under partial melting

conditions during near-isothermal decompression and recrystallize at 0.15-0.2 GPa for rapid and ultra-rapid extension, and between 0.3-0.4 GPa for slow models.

p-T paths do not show a significant dependence on the solidus of the LC. The most significant difference is that for models with Solidus B, recrystallization of rock domes that underwent partial melting occurs at a lower pressure of c. 0.1 GPa, in the stability field of andalusite.

4.5. Cooling rates of lower crustal rocks

The shape of synthetic T-t paths (Fig. D.7Supplementary Fig. 3 and 4) shows a positive (and non-linear) correlation with extension rate and Moho temperature, and to a lesser extent, volume of partial melting of the crust.

Deep dome rocks record a brief period (c. 0.5 Ma) of heating (from +50 °C in the cold models, and up to +150 °C for hotter Moho temperature) before experiencing rapid cooling along average cooling rates of about 2000 °C/Ma, 350 °C/Ma and 40-50 °C/Ma for ultra-rapid (75 mm/yr), rapid (35 mm/yr) and slow (10 mm/yr) extension rates, respectively. On the other hand, mid and shallow dome rocks do not experience any initial heating, and average cooling occurs at 1000-1500 °C/Ma, 200-250 °C/Ma and 70-100 °C/Ma for the same range of extension rates. This period of rapid cooling takes place at c. 0.7 Ma (ultra-rapid), c. 1.5 Ma (rapid) and c. 4 Ma (slow) after the onset of extension for deep dome rocks and after c. 0.3 (ultra-rapid), c. 0.5 Ma (rapid) and 1-2 Ma (slow) for shallow dome rocks. We further note that the initial period of heating of deep dome rocks is not observed in the slow models with initial Moho temperatures lower than 911 °C. This range of cooling rates is consistent for all cold-to-warm models ($T_{Moho} \leq 911$ °C); the only significant difference between them is the peak temperature during decompressional heating of the deep dome rocks, which increases with the Moho temperature.

A significant difference in the cooling paths is observed for the hottest models ($T_{Moho} = 1040$ °C). Deep crustal rocks of models employing the Solidus A undergo an initial period of 3-4 Ma of considerable heating (> 150°C) after

onset of extension, followed by rapid cooling at 350-400 °C/Ma. Mid and shallow dome rocks record residual heating and are rapidly cooled as they are advected towards shallow depths, with cooling rates of 200-475 °C/Ma (ultra-rapid), 200-250 °C/Ma (rapid) and 60-100 °C/Ma (slow). On the other hand, mid and shallow markers at the flanks of the LC dome barely experience any heating or cooling throughout the duration of the model. Cooling paths of hot models using Solidus B show a similar trend to the ones using Solidus A; however, cooling of mid and shallow dome rocks occurs within a much shorter period of time (near-instantaneously for rapid and ultra-rapid models).

4.6. Influence of extension rate on the evolution of metamorphic complexes

[Figure 5 about here.]

For a set of models with the same initial thermal structure, different aspects such as geometry, timing of crustal break-up, volume of partial melting, p-T and T-t paths of the LC and UHT conditions are affected by the extension rate to different extents.

First, the evolution and final architecture of models with a cold initial Moho temperature differ under slow, rapid and ultra-rapid extension (Fig. D.4a). In slow models, the growth and exhumation of the LC dome is accompanied by the ascent of the asthenosphere, followed by the break-up of the crust after significant extension ($> 40\%$) and consequent seafloor spreading, resulting in two asymmetric conjugate margins. Under rapid extension, a secondary dome is formed due to the asymmetric ascent of the asthenosphere, and the detachment faults associated to both primary and secondary remain simultaneously active until the crust is completely broken apart by the exhumation of the mantle at c. 3.9 Ma, resulting in two symmetric conjugate margins. Ultra-rapid models display a similar evolution to rapid models; however, these models yield two asymmetric conjugate margins after crustal break-up and sea-flow spreading take place (c. 3 Ma). The architecture of the crust and the dynamics of extension of intermediate, warm and hot models show little variability with different

extension rates. However, fast extension rates promote doming of the topography of the Moho synchronous with the growth of the LC dome; the age of break-up of the upper crust shows a negative correlation with extension rate (Fig. D.7a).

Second, fast extension rates speed up the vertical velocity of the lower mantle, thus enhancing the amount and onset of decompression melt of asthenospheric material. Similarly, with Solidus B, crustal partial melting is enhanced by fast extension. On the other hand, if Solidus A is considered, the base of the crust is under partial melting conditions from the onset of extension, and similar amounts of melting are predicted for all the extension rates considered here.

Third, p-T and T-t paths exhibit a considerable sensitivity to extension rate. Rocks at the core of the LC dome record near-isothermal decompression from about to 0.85 GPa to 0.1-0.2 GPa during fast extension ($\geq$ 35 mm/yr), whereas they experience decompressional heating followed by cooling after reaching peak conditions of c. 0.6 GPa and 750-825 °C under slow extension. Average cooling rates are remarkably higher during fast extension, with maximum rates for deep dome rocks of 40-50 °C/Ma under slow extension, and 1500-2000 °C/Ma for ultra-rapid extension.

Finally, UHT conditions are only predicted for $u_{ext} \geq 35$ mm/yr and initial Moho temperatures of $T_{Moho} \geq 940$ °C.

4.7. Influence of lower crustal melting

While Solidus A and B predict similar volumes of crustal partial melting ($F_{max} = 25 - 35$ %) for warm and hot models, major volumetric differences are observed for $T_{Moho} \leq 844$ °C. Since similar volumes of partial melting of the crust are predicted for models with Solidus A and B and initial $T_{Moho} \geq 911$ °C, the crust undergoes similar levels of weakening due to the presence of partial melting (i.e. the viscosity fields are very similar), and thus the choice of the solidus has little effect on potential geometrical discrepancies between these models. In the colder models, Solidus A predicts maximum partial melting

fractions of at least 20%, whereas for the Solidus B, partial melting of the crust only takes places at advanced stages of deformation for intermediate models when hot asthenospheric material reaches the bottom of the crust. Partial melting of the crust is not observed for the coldest models for Solidus B.

Geometrical differences linked to partial melting of the crust are only evident amongst models with very different volumes of partially molten crust (i.e. $T_{Moho} \leq 844$ °C). A weakened base of the LC due to partial melting leads to the growth and consequent exhumation of a secondary dome of LC rocks and UHT conditions at the base of the crust at the stages of crustal break-up with an asymmetric flow of the asthenosphere (Fig.D.6a). None of these features are observed in the near-absence of partially molten crust (Fig.D.6b).

[Figure 6 about here.]

5. Comparison of the numerical models with the Palu Metamorphic Complex

[Figure 7 about here.]

The geometry of the PMC is well reproduced by the exhumation of a LC dome as predicted by the numerical models. The formation of several extension-driven LC domes and secondary domes on the flank of the primary dome is compatible with the presence of other metamorphic complexes in the region, including the Gumbasa, Wana and Karossa Metamorphic Complexes, that are exposed within less than 80 km south-west from the southernmost tip of the PMC (Fig. D.1b).

To constrain the extension rates and Moho temperatures at the onset of the extensional event that drove the later exhumation of the PMC, we compare the observed cooling paths from samples of magmatic and metamorphic rocks in Hennig et al. (2017) with synthetic cooling paths obtained from our numerical models. Analysis of the error (Appendix D) between these paths (Fig. D.8) reveals that extension of the crust in this region must have taken place at very fast extension rates of c. 75 mm/yr and initial Moho temperatures of c. 710 °C.

The p-T evolution in the ultra-rapid model with initial T_{Moho} = 710 °C and Solidus A is consistent with the high temperature/low pressure mineral assemblages found in the PMC: deep dome rocks are under partial melting conditions and recrystallize at low pressure (c. 0.2 GPa) shortly after onset of extension (c. 0.8 Ma). An emplacement depth of c. 13 km has been suggested for S-type granitoids assuming a linear geothermal gradient of 30 °C/km (Hennig et al., 2017). However, synthetic p-T paths for rapid and ultra-rapid extension predict partial melting conditions at depths below 4-7 km for rocks comprising the dome. This discrepancy can be explained by the choice of the geothermal gradient used to estimate the emplacement depth: a linear geotherm of 30 °C/km is compatible with the crustal geotherm predicted by the numerical experiments far away from the MCC, whereas the geotherm within the MCC is significantly steeper and non-linear at crustal depths, thus yielding higher temperatures at shallower depths.

Shallow LC markers ($z_{marker}(t = 0) = 19$ km) located initially at the flanks of the dome experience a brief period of isothermal decompression followed by isobaric- and decompression- heating. Some of the mid crustal rocks are incorporated into a secondary dome. Ascent of asthenosphere underneath the secondary dome brings rocks at the Moho under UHT and partial melting conditions for a brief period of time. Although exhumed granulite facies rocks are found along the Palu-Koro Fault Zone, they pre-date the formation and exhumation of the PMC and may be associated with the rollback in the Banda Sea region (Spakman and Hall, 2010).

Magmatic and metamorphic rocks of the PMC have been estimated to have been exhumed at rates of 1-4 mm/yr (Hennig et al., 2017). However, these values are small, similar to other MCC that presumably formed and exhumed at slower extension rates, such as the Naxos MCC, which has an estimated exhumation rate of the order of 1-10 mm/yr (Duchene et al., 2006)) and has been numerically modelled using extension rates of 10 mm/yr (Huet et al., 2011b). Maximum exhumation rates obtained from our models (Fig. D.8b) suggest maximum values of 25-50 mm/yr for fast extension ($\geq$ 35 mm /yr). It

is possible that the estimated exhumation rates for the PMC are capturing only the last stages of exhumation, thus yielding lower rates.

6. Discussion

Even though our numerical experiments yield different types of crustal deformation, the development of LC domes is predicted for the whole range of Moho temperatures considered here. These results reinforce the idea that MCC are able to develop in relatively cold crust (Schenker et al., 2012). MCC in relatively cold crustal conditions have been also predicted by models with an inherited reversed lithological layering (Huet et al., 2011b). Rey et al. (2009) pointed out that a point-like heterogeneity resulted in symmetric extension, whereas a fault-like weak zone yielded asymmetric extension. Interestingly, our results illustrate how a Gaussian-shaped thermal anomaly can lead to different degrees of asymmetry. We argue that this discrepancy may be mainly related to the use of a different rheological law (elasticity is not considered in Rey et al. (2009)) and implementation of strain softening.

All the models described in this paper predict similar kinematics at early stages of deformation, dominated by conjugate normal faults rooting in the LC. Our results suggest a substantial difference between the evolution of models with initial $T_{Moho} = 710$ °C and models with hotter initial conditions. In the first case, extension is accompanied by the upwelling of the asthenosphere and decompression melting of the mantle underneath the LC dome. Subsequently, shear zones penetrate the Moho due to the embrittlement of the LC caused by lower temperatures, resulting in break-up of the LC dome and mantle exhumation. In contrast, hotter crustal temperatures ($T_{Moho} \geq 844$ °C) and fast extension (≥ 35 mm/yr) inhibit the transmission of stress to the Moho a more vigorous ductile flow of the lower crust, maintaining a relatively flat Moho topography. In these latter cases, crustal break-up is only reached after considerable cooling and extreme thinning of the crust.

Depending on its origin, we can distinguish two kinds of MCCs: 1) a primary

LC dome (Fig. D.3) and 2) a secondary asthenospheric-heat induced MCC (Fig. D.9). The first are common to all our numerical experiments. As concluded by Huet et al. (2011b), they are driven by strain localization in the LC due to a thermal or mechanical heterogeneity and far-field extensional forces, rather than by buoyancy forces. On the other hand, fast extension rates ($\leq$ 35 mm/yr) promote an asymmetric upwelling of the asthenosphere. As the asthenosphere reaches the base of the LC at the flanks of the positive topography of the Moho (offset by 30-50 km with respect to the centre of the primary dome), it produces a shift of the ductile flow at the base of the LC, redirecting the crustal flow towards the flank of the of primary dome and ending the phase of lateral spreading of the dome. Conductive heating of the bottom of the LC induced by contact with hot asthenosphere material leads to UHT conditions, additional production of partially molten crust, development of a secondary asthenospheric-heat induced dome, and localization of strain in a new detachment fault. This kind of secondary dome is only predicted for intermediate temperatures, as colder conditions lead to crustal break-up, and hotter crustal temperatures favour ductile flow and lateral migration of the LC. Asthenospheric-heat induced MCCs have been previously described and compared to the Rhodope Metamorphic Complex by Schenker et al. (2012).

p-T path diagrams of primary and secondary domes reveal different thermal histories. As characteristic of many migmatitic MCC (Rey et al., 2011; Huet et al., 2011a; Schenker et al., 2012), rocks of the primary dome are rapidly advected near-vertically towards the surface and record near-isothermal decompression to shallow depths, followed by recrystallization at low pressure and rapid cooling (a small amount of heating might be possible for deep dome rocks; see red markers and red p-T paths in Fig. D.8a). On the other hand, the secondary dome is comprised of LC rocks located beneath the upper-lower crust boundary that migrate laterally and are incorporated into the secondary dome (black markers in Fig. D.8a). These later rocks experience near-isobaric heating, induced by heat advection, at pressures of 0.4-0.5 GPa and from $\sim$400 to $\sim$600 °C. This is followed by near-isothermal decompression to 0.1-0.2 GPa, and

a last phase of isobaric cooling.

[Figure 8 about here.]

Computed maximum cooling rates (Fig. D.7c) for slow models are consistent with many thermochronological data from different MCC all over the world (e.g. John and Howard (1995); Scott et al. (1998); Vanderhaeghe et al. (2003); Yang et al. (2007)), yielding cooling rates of 70-300 °C/Ma. An increase of the extension rate from slow to rapid and ultra-rapid extension results in cooling rates of 700-4000 °C/Ma, an increase of almost one order of magnitude, yielding cooling rates closer to the ones observed in the metamorphic complexes exhumed under very rapid exhumation, as inferred for the PMC Hennig et al. (2017). Exceptionally, the hottest models using Solidus B yield maximum cooling rates of >5000 °C/Ma for rapid and ultra-rapid extension.

As obvious as it might seem, we further note that rocks located a few km away with respect to the centre of the metamorphic complex (e.g. as the markers located at ±15 km) experience a slower and slightly longer period of cooling. Furthermore, these rocks can experience reheating if they are reincorporated into secondary domes.

[Figure 9 about here.]

7. Conclusions

- Our numerical results on extension of thinned crust with different permutations of initial thermal structure and extension rates considered in this work yield formation of lower crustal domes, suggesting that anomalously elevated thermal conditions are not a pre-requisite for the formation of MCCs in thinned crust.

- Three different final modes of model architecture are observed: 1) localised doming of the lower crust with synchronous upwelling of the asthenosphere, followed by crustal break up and resulting in two conjugate

margins; 2) localised doming of the lower crust accompanied by doming of the Moho, occasionally followed by secondary asthenospheric-heat induced lower crustal dome; and 3) doming of the lower crust with a flat Moho.

- Two different kinds of lower crustal domes are identified: 1) a primary lower crustal dome driven by far-field forces and lower crustal flow; and 2) a secondary asthenospheric-heat induced MCC. Rocks comprising the latter domes record different p-T-t histories: primary lower crustal dome rocks show very rapid vertical ascend towards the surface reflected by near-isothermal p-T paths followed by rapid cooling at shallow depths, whereas asthenospheric-heat induced MCC rocks experience isobaric heating at intermediate pressure and 400-600 °C followed by decompression heating to peak conditions (c. 0.2 GPa and 700-750 °C). These secondary domes are only observed for $T_{Moho} \geq 844$ °C and rapid and ultra-rapid extension.

- Extension rate plays a crucial role in shaping the thermobarometric history of MCCs, as increasing extension promotes near-isothermal decompression and shorter periods of rapid cooling.

- Crystallization of the partially molten core of fast MCC in a thinned crust occurs at low pressure (0.15-0.2 GPa) and intermediate pressure (0.3-0.4 GPa) for slow MCC.

- Rocks with a solidus corresponding to a granite are weakened by partial melting even for the lowest Moho temperature considered here. Rocks with a lower water content require hotter conditions for partial melting to occur, and they remain stronger. The geometry is affected by the volume of crustal melting; however, MCCs are still predicted in absence of partial melting. This suggests that advection of lower crust towards the surface is driven by the ductile flow of hot lower crust that fills the space left by the stretching and break-up of the lower crust, rather than by buoyancy forces alone.

Acknowledgements

This study was supported by the SE Asia Research Group which is funded by a consortium of oil companies. We gratefully thank two anonymous reviewers for their thorough comments which greatly improved the manuscript.

Appendix A. Numerical formulation

The thermo-mechanical behaviour of Earth's interior is described the equations of conservation of momentum, conservation of mass, and conservation of energy, respectively:

$$\nabla\sigma = \rho\mathbf{g} \tag{A.1}$$

$$\nabla \cdot \mathbf{u} = 0 \tag{A.2}$$

$$\rho C_p \dot{T} = k\nabla^2 T + H \tag{A.3}$$

where σ is the Cauchy stress tensor, ρ is the density, $\mathbf{g}$ is the gravitational acceleration, $\mathbf{u}$ is the velocity field, C_p is specific heat, T is temperature, κ is thermal conductivity, H is a source term that includes radioactive and shear heating. The set of equations A.2-A.3 is solved on a deformation Lagrangian mesh using a version of MILAMIN (Dabrowski et al., 2008) that has been modified to include elastic deformation and non-linear rheologies, namely diffusion creep, dislocation creep and plastic deformation.

Viscous deformation is calculated assuming a strain rate- and temperature-dependent power law rheology for diffusion creep and dislocation creep (Karato et al., 2001):

$$\eta = \frac{1}{2}(A)^{-\frac{1}{n}}(\dot{\varepsilon}_{II})^{\frac{1}{n}-1}\exp\left(\frac{E+pV_a}{nRT}\right) \tag{A.4}$$

where the deviatoric strain rate is $\dot{\varepsilon} = \left[1/2(\nabla\mathbf{u} + (\nabla\mathbf{u})^T) - 1/3(\nabla\cdot\mathbf{u})\right]$ and the sub index II denotes the square root of the J_2 invariant (i.e. $\mathbf{C}_{II} = \sqrt{(1/2)\mathbf{C}:\mathbf{C}}$ and $\mathbf{C}$ is any given tensor), A is a pre-exponential parameter, n is a power-law exponent, E is activation energy, p is pressure, V_a is activation volume and R is the universal gas constant. The second invariant of the deviatoric strain

rate in eq.(A.4) corresponds to the deformation of either diffusion or dislocation deviatoric strain rate tensor. A resultant composite viscosity is obtained:

$$\eta = \frac{1}{\frac{1}{\eta_{dif}} + \frac{1}{\eta_{dis}}} \tag{A.5}$$

By adopting this composite viscous rheology, deformation is dominated by the mechanism that has the smallest activation stress.

Stress produced by elastic deformation is a large contributor to the global deformation-budget in the uppermost layers of the Earth, thus the necessity to add elastic deformation to the constitutive law if we aim to study the kinematics of the lithosphere. The visco-elastic constitutive law is given by:

$$\tau = 2\eta_{eff}\dot{\varepsilon} + \chi\widehat{\tau} \tag{A.6}$$

with

$$\eta_{eff} = \frac{1}{\frac{1}{\eta} + \frac{1}{G\Delta t}} \tag{A.7}$$

$$\chi = \frac{1}{1 + \frac{G\Delta t}{\eta}} \tag{A.8}$$

$$\widehat{\tau} = \tau^o + (\omega^o\tau^o - \tau^o\omega^o)\Delta t \tag{A.9}$$

where η_{eff} is the effective visco-elastic viscosity, the super-script o refers to values at the previous time step, Δt is the time step, G is the shear modulus and $\omega = 1/2(\nabla\mathbf{u} - (\nabla\mathbf{u})^T)$ is the skew symmetric part of the velocity gradient tensor, commonly known as spin tensor.

Plastic deformation (i.e. fault-like behaviour of the rocks) is computed adopting the pressure dependent Drucker-Prager yield surface $\mathbb{F}$:

$$\mathbb{F} = \tau_{II} - p\sin(\phi) - c\cos(\phi) \tag{A.10}$$

where τ_y is the yield stress. If the stress is such that $\mathbb{F} > 0$, the stress is brought back to the yield surface ($\mathbb{F} = 0$) using the deviatoric, corner-free and non-associative Prandtl-Reus flow rule. For points in the domain where $\mathbb{F} = 0$, the effective plastic viscosity η_{pl} is then given by:

$$\eta_{pl} = \frac{\tau_y}{2\dot{\varepsilon}_{II} + \chi\widehat{\tau}_{II}} \tag{A.11}$$

The incompressible Boussinesq approximation is assumed, thus volumetric strains and/or buoyancy forces due to pressure effects are not included in the numerical formulation. However, density changes and buoyancy forces derived from thermal expansion (and partial melting, see Appendix B) are permitted in the incompressible approximation. Therefore, we use a temperature dependent equation of state:

$$\rho = \rho_o \left(1 - \alpha(T - T_o)\right) \tag{A.12}$$

where ρ_o is the reference density and α is the coefficient of thermal expansion.

Appendix B. Partial melting

The production of partial melting is calculated following Morgan (2001). The mantle solidus temperature T^s is defined as:

$$T^s = T^s_o + \left(\frac{\partial T^s}{\partial p}\right)_F p + \left(\frac{\partial T^s}{\partial F}\right)_P F \tag{B.1}$$

where T^s_o is the solidus temperature at the surface, $\partial T^s/\partial P$ is the solidus-pressure gradient, $\partial T^s/\partial F$ is the solidus-depletion gradient and F is melt fraction. Melting is produced in a parcel of the model if $T > T^s$, and two mechanisms (or their combination) are responsible for melt productivity: 1) an increase in the material due to thermal diffusion; and 2) variations in the solidus curve due to changes in pressure or melt fraction. The decompression melt productivity for a lithology i within a lithology j is given by (Morgan, 2001) :

$$-\frac{\partial F_i}{\partial p} = \frac{\frac{\partial T^s_i}{\partial p} - \frac{\alpha T}{\rho C_p} + \frac{T}{C_p}\phi_j \Delta S_j \left(\frac{\partial T^s_i}{\partial p} - \frac{\partial T^s_j}{\partial p}\right)}{\frac{T}{C_p}\phi_i \Delta S_j \left(\frac{\partial T^s_i/\partial F_i}{\partial T^s_j/\partial F_j}\right) + \frac{\partial T^s_i}{\partial F_i}} \tag{B.2}$$

where ΔS is the entropy of the solid-melt phase change, which can be related to the latent heat of melting ΔH, for a pure substance, as $\Delta H = T\Delta S$. We consider only a single-component melting, thus the amount of decompression melting is:

$$dF_p = dP \left(-\frac{\frac{\partial T^s}{\partial p}}{\frac{\Delta H}{C_p} + \frac{\partial T^s}{\partial F}}\right) \tag{B.3}$$

where the adiabatic term is missing because the temperatures are potential temperature. The temperature change during decompression melting is given by:

$$\frac{dT}{dp} = \frac{\partial T_s^i}{\partial p} + \frac{\partial T_s^i}{\partial F_i}\frac{dF_i}{dp} \tag{B.4}$$

The amount of melt under isobaric conditions is given by:

$$dF_T = \frac{T^m - T^s}{\frac{\Delta H}{C_p} + \frac{\partial T^s}{\partial F}} \tag{B.5}$$

where T^m is the mantle temperature and the total amount of instantaneous melt is $dF = dF_p + dF_T$. The total amount of melting produced in a parcel is then the summation of dF over time:

$$F = \sum_{t=1}^{n} dF^t \tag{B.6}$$

where the superscript t is the time step and n is the total number of time steps. For undepleted mantle, the wet solidus is used initially, and the dry solidus is used after 2% melting (Braun et al., 2000). Buoyancy forces due to melt production are included in the following temperature and depletion dependant equation of state (EOS):

$$\rho(T, P) = \rho_o(1 + \alpha(T - T_o) - \beta F) \tag{B.7}$$

where F is the melt fraction and β is defined as:

$$\beta = 1 - \frac{\rho_{molten}}{\rho_{solid}} \tag{B.8}$$

where ρ_{solid} and ρ_{molten} are the reference densities of the rock in its solid and molten states. We consider the density of molten crust to be $\rho = 2400\ kg/m^3$ and $\rho = 2900\ kg/m^3$ for molten mantle material (values taken from (Gerya and Meilick, 2011)).

Appendix C. Strain softening

We define the accumulated plastic strain as :

$$\mathbf{E}^{pl} = \int_t \dot{\lambda}\frac{\partial \mathbb{G}}{\partial \tau_{ij}} dt \tag{C.1}$$

where $\dot{\lambda} \geq 0$ is the so-called plastic multiplier, and $\mathbb{G} = \tau_{II}$ is the plastic potential. Strain softening is then applied to the brittle domain by reducing the friction angle ϕ as a linear function of the finite plastic strain, with $\phi(\mathbf{E}^{pl} = 0) = 30^{\circ}$ and $\phi(\mathbf{E}^{pl} \geq 1) = 15^{\circ}$.

Appendix D. Error between synthetic and natural cooling paths

To compare the synthetic and observed cooling path, we define the following error

$$e = \min\left(\frac{N^{nat} - N_i^{syn}}{N^{nat}}\right) 100 \tag{D.1}$$

where the error e is given in percentage, N^{nat} is the natural cooling rate and N_i^{syn} is a vector that contains the synthetic cooling paths at the i-times.

References

Baldwin, S. L., Monteleone, B. D., Webb, L. E., Fitzgerald, P. G., Grove, M., June Hill, E., 2004. Pliocene eclogite exhumation at plate tectonic rates in eastern Papua New Guinea. Nature 431, 263 – 267.
URL `http://dx.doi.org/10.1038/nature02846`

Boettcher, A., Wyllie, P., 1968. Melting of granite with excess water to 30 kilobars pressure. The Journal of Geology 76 (2), 235–244.

Braun, M. G., Hirth, G., Parmentier, E., 2000. The effects of deep damp melting on mantle flow and melt generation beneath mid-ocean ridges. Earth and Planetary Science Letters 176 (3-4), 339–356.

Dabrowski, M., Krotkiewski, M., Schmid, D. W., 2008. MILAMIN: MATLAB-based finite element method solver for large problems. Geochemistry, Geophysics, Geosystems 9 (4), 1–24.

de Souza Neto, E. A., Peric, D., Owen, D. R., 2011. Computational methods for plasticity: theory and applications. John Wiley & Sons.

Duchene, S., Aissa, R., Vanderhaeghe, O., 2006. Pressure-temperature-time evolution of metamorphic rocks from Naxos (Cyclades, Greece): constraints from thermobarometry and Rb/Sr dating. Geodinamica Acta 19 (5), 301–321.

Elburg, M., van Leeuwen, T., Foden, J., et al., 2003. Spatial and temporal isotopic domains of contrasting igneous suites in Western and Northern Sulawesi, Indonesia. Chemical Geology 199 (3), 243–276.

Gerya, T. V., Meilick, F., 2011. Geodynamic regimes of subduction under an active margin: effects of rheological weakening by fluids and melts. Journal of Metamorphic Geology 29 (1), 7–31.

Gleason, G. C., Tullis, J., 1995. A flow law for dislocation creep of quartz aggregates determined with the molten salt cell. Tectonophysics 247 (1), 1–23.

Hall, R., 2011. Australia-SE Asia collision: plate tectonics and crustal flow. Geological Society, London, Special Publications 355 (1), 75–109.

Hall, R., 2012. Late Jurassic–Cenozoic reconstructions of the Indonesian region and the Indian Ocean. Tectonophysics 570, 1–41.

Hall, R., 2017. Southeast asia: New views of the geology of the malay archipelago. Annual Review of Earth and Planetary Sciences 45, 331–358.

Hall, R., 2018. The subduction initiation stage of the Wilson cycle. Geological Society, London, Special Publications 470.

Hall, R., Clements, B., Smyth, H. R., 2009. Sundaland: basement character, structure and plate tectonic development. In: Proceedings Indonesian Petroleum Association, 33^{rd} Annual Convention, IPA09-G-134. pp. 1–27.

Hamilton, W. B., 1979. Tectonics of the Indonesian region. No. 1078. US Govt. Print. Off.

Hennig, J., Advokaat, E., Rudyawan, A., Hall, R., 2014. Large sediment accumulations and major subsidence offshore; rapid uplift on land: Consequences

of extension of Gorontalo Bay and northern Sulawesi. Proceedings Indonesian Pretoleum Association, 38^{th} Annual Convention and Exhibition (IPA14-G-304).

Hennig, J., Hall, R., Armstrong, R. A., 2016. U-Pb zircon geochronology of rocks from west Central Sulawesi, Indonesia: Extension-related metamorphism and magmatism during the early stages of mountain building. Gondwana Research 32 (Supplement C), 41 – 63.

Hennig, J., Hall, R., Forster, M. A., Kohn, B. P., Lister, G. S., 2017. Rapid cooling and exhumation as a consequence of extension and crustal thinning: Inferences from the Late Miocene to Pliocene Palu Metamorphic Complex, Sulawesi, Indonesia. Tectonophysics 712, 600–622.

Hinschberger, F., Malod, J.-A., Réhault, J.-P., Dyment, J., Honthaas, C., Villeneuve, M., Burhanuddin, S., 2000. Origine et evolution du bassin Nord-Banda (Indonesie): apport des donnees magnetiques. Comptes Rendus de l'Académie des Sciences-Series IIA-Earth and Planetary Science 331 (7), 507–514.

Hirth, G., Kohlstedt, D., 2003. Rheology of the upper mantle and the mantle wedge: A view from the experimentalists. Inside the subduction Factory, 83–105.

Huet, B., Le Pourhiet, L., Labrousse, L., Burov, E., Jolivet, L., 2011a. Formation of metamorphic core complex in inherited wedges: A thermomechanical modelling study. Earth and Planetary Science Letters 309 (3), 249–257.

Huet, B., Le Pourhiet, L., Labrousse, L., Burov, E., Jolivet, L., 2011b. Post-orogenic extension and metamorphic core complexes in a heterogeneous crust: the role of crustal layering inherited from collision. Application to the Cyclades (Aegean domain). Geophysical Journal International 184 (2), 611–625.

John, B. E., Howard, K. A., 1995. Rapid extension recorded by cooling-age

patterns and brittle deformation, Naxos, Greece. Journal of Geophysical Research: Solid Earth 100 (B6), 9969–9979.

Karato, S.-i., Riedel, M. R., Yuen, D. A., 2001. Rheological structure and deformation of subducted slabs in the mantle transition zone: implications for mantle circulation and deep earthquakes. Physics of the Earth and Planetary Interiors 127 (1), 83–108.

Klompe, T. H., 1954. The structural importance of the Sula Spur (Indonesia). Indonesian Journal of Natural Sciences 110, 21–40.

Korchinski, M., Rey, P. F., Mondy, L., Teyssier, C., Whitney, D. L., 2018. Numerical investigation of deep-crust behavior under lithospheric extension. Tectonophysics 726, 137–146.

Little, T., Hacker, B., Gordon, S., Baldwin, S., Fitzgerald, P., Ellis, S., Korchinski, M., 2011. Diapiric exhumation of Earth's youngest (UHP) eclogites in the gneiss domes of the D'Entrecasteaux Islands, Papua New Guinea. Tectonophysics 510 (1-2), 39–68.

López, S., Castro, A., 2001. Determination of the fluid–absent solidus and supersolidus phase relationships of MORB-derived amphibolites in the range 4-14 kbar. American Mineralogist 86 (11-12), 1396–1403.

Morgan, J. P., 2001. Thermodynamics of pressure release melting of a veined plum pudding mantle. Geochemistry, Geophysics, Geosystems 2 (4).

Polvé, M., Maury, R., Bellon, H., Rangin, C., Priadi, B., Yuwono, S., Joron, J., Atmadja, R. S., 1997. Magmatic evolution of Sulawesi (Indonesia): constraints on the Cenozoic geodynamic history of the Sundaland active margin. Tectonophysics 272 (1), 69–92.

Pownall, J., 2015. UHT metamorphism on Seram, eastern Indonesia: reaction microstructures and P–T evolution of spinel-bearing garnet–sillimanite granulites from the Kobipoto Complex. Journal of Metamorphic Geology 33 (9), 909–935.

763 Pownall, J., Hall, R., Watkinson, I., 2013. Extreme extension across Seram and
764 Ambon, eastern Indonesia: evidence for Banda slab rollback. Solid Earth
765 4 (2), 277.

766 Pownall, J. M., Hall, R., Armstrong, R. A., 2017. Hot lherzolite exhumation,
767 UHT migmatite formation, and acid volcanism driven by Miocene rollback of
768 the Banda Arc, eastern Indonesia. Gondwana Research 51, 92–117.

769 Priadi, B., Polvé, M., Maury, R., Bellon, H., Soeria-Atmadja, R., Joron, J.,
770 Cotten, J., 1994. Tertiary and Quaternary magmatism in Central Sulawesi:
771 chronological and petrological constraints. Journal of Southeast Asian Earth
772 Sciences 9 (1-2), 81–93.

773 Rey, P., Teyssier, C., Whitney, D., 2009. Extension rates, crustal melting, and
774 core complex dynamics. Geology 37 (5), 391–394.

775 Rey, P. F., Teyssier, C., Kruckenberg, S. C., Whitney, D. L., 2011. Viscous
776 collision in channel explains double domes in metamorphic core complexes.
777 Geology 39 (4), 387–390.

778 Rosenberg, C., Handy, M., 2005. Experimental deformation of partially melted
779 granite revisited: implications for the continental crust. Journal of metamor-
780 phic Geology 23 (1), 19–28.

781 Schenker, F., Gerya, T., Burg, J.-P., 2012. Bimodal behavior of extended con-
782 tinental lithosphere: Modeling insight and application to thermal history of
783 migmatitic core complexes. Tectonophysics 579, 88–103.

784 Scott, R. J., Foster, D. A., Lister, G. S., 1998. Tectonic implications of rapid
785 cooling of lower plate rocks from the Buckskin-Rawhide metamorphic core
786 complex, west-central Arizona. Geological Society of America Bulletin 110 (5),
787 588–614.

788 Silver, E. A., McCaffrey, R., Smith, R. B., 1983. Collision, rotation, and the
789 initiation of subduction in the evolution of Sulawesi, Indonesia. Journal of
790 Geophysical Research: Solid Earth 88 (B11), 9407–9418.

Smyth, H., Hamilton, P., Hall, R., Kinny, P., 2007. The deep crust beneath island arcs: inherited zircons reveal a Gondwana continental fragment beneath East Java, Indonesia. Earth and Planetary Science Letters 258 (1-2), 269–282.

Spakman, W., Hall, R., 2010. Surface deformation and slab-mantle interaction during Banda arc subduction rollback. Nature Geoscience 3 (8), 562.

Sukamto, R., 1973. Reconnaissance geologic map of Palu Area, Sulawesi-scale 1: 250,000. Geological Survey of Indonesia, Directorate of Mineral Resources, Geological Research and Development Centre, Bandung, Open File (Unpublished).

Surmont, J., Laj, C., Kissel, C., Rangin, C., Bellon, H., Priadi, B., 1994. New paleomagnetic constraints on the Cenozoic tectonic evolution of the North Arm of Sulawesi, Indonesia. Earth and Planetary Science Letters 121, 629–638.

Teyssier, C., Whitney, D. L., 2002. Gneiss domes and orogeny. Geology 30 (12), 1139–1142.

van Leeuwen, T M sand Allen, C. M., Elburg, M., Massonne, H.-J., Palin, J. M., Hennig, J., 2016. The Palu Metamorphic Complex, NW Sulawesi, Indonesia: Origin and evolution of a young metamorphic terrane with links to Gondwana and Sundaland. Journal of Asian Earth Sciences 115, 133–152.

van Leeuwen, T. M., Muhardjo, 2005. Stratigraphy and tectonic setting of the Cretaceous and Paleogene volcanic-sedimentary successions in northwest Sulawesi, Indonesia: implications for the Cenozoic evolution of Western and Northern Sulawesi. Journal of Asian Earth Sciences 25 (3), 481–511.

Vanderhaeghe, O., Teyssier, C., McDougall, I., Dunlap, W. J., 2003. Cooling and exhumation of the Shuswap Metamorphic Core Complex constrained by $^{40}Ar/^{39}Ar$ thermochronology. Geological Society of America Bulletin 115 (2), 200–216.

Weissel, J. K., 1980. Evidence for Eocene oceanic crust in the Celebes Basin. The Tectonic and Geologic Evolution of Southeast Asian Seas and Islands, 37–47.

Yang, J.-H., Wu, F.-Y., Chung, S.-L., Lo, C.-H., Wilde, S. A., Davis, G. A., 2007. Rapid exhumation and cooling of the Liaonan metamorphic core complex: Inferences from $^{40}Ar/^{39}Ar$ thermochronology and implications for Late Mesozoic extension in the eastern North China Craton. Geological Society of America Bulletin 119 (11-12), 1405–1414.

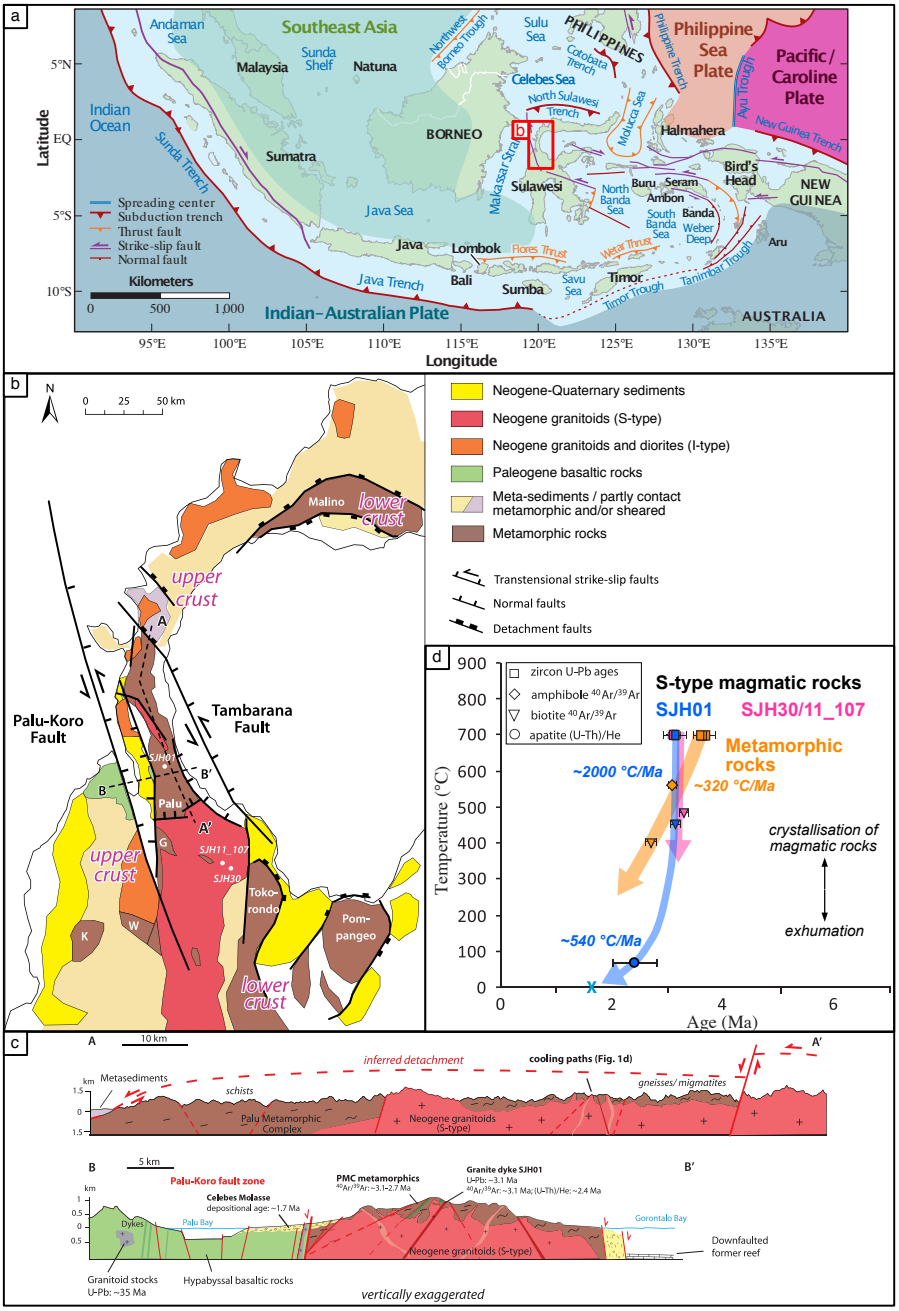

Figure D.1: **(a)** Geological map of SE Asia. The strongly coloured areas correspond to rigid plates, whereas the pale blue shaded region should be treated as micro-plates. After Hall (2017). **(b)** Simplified geological map of west Central Sulawesi showing the location of the Palu, Malino, Tokorondo, Pompangeo, Gumbasa (G), Wana (W) and Karossa (K) metamorphic complexes. **(c)** Cross-section along the A-A' and B-B' transects in panel *(b)*. From Hennig et al. (2017). **(d)** Cooling paths of S-type granites (blue and pink) and metamorphic rocks (orange) of the Neck and mid Central Sulawesi (modified from Hennig et al. (2017)). The blue cross marks the depositional age of 1.7 Ma reported for the Celebes Molasse by van Leeuwen and Muhardjo (2005).

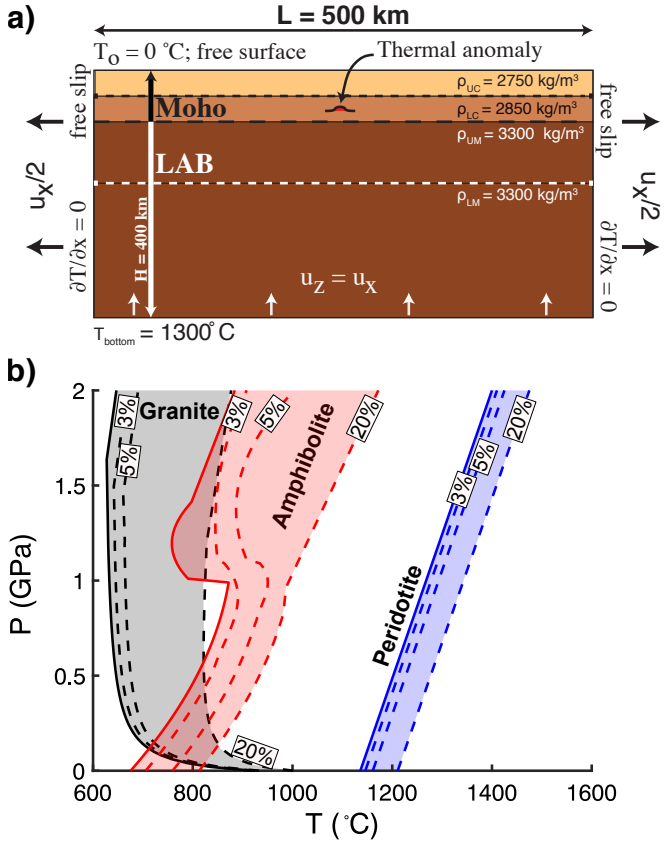

Figure D.2: **a** Model set-up. The model is stretched using pure shear boundary conditions and the temperature at the surface and bottom of the domain are fixed at a constant value. To localise the deformation in the center of the model, a thermal anomaly is introduced in the middle of the lower crust at $x = 0$ km. The domain is comprised of four laterally homogeneous rheological layers: a 17.5 km thick upper crust (UC), a 17.5 km thick lower crust (LC), a 85 km thick lithospheric mantle (LM) and a 280 km thick asthenospheric mantle (AM). The rheological parameters are given in Table 3.2. **b** Solidus of a granite with excess water (Boettcher and Wyllie, 1968) (in black), fluid-absent MORB-derived amphibolite (López and Castro, 2001) (in red) and fertile peridotite (Morgan, 2001) (in blue). Dashed lines represent the solidus at different degrees of melt fraction.

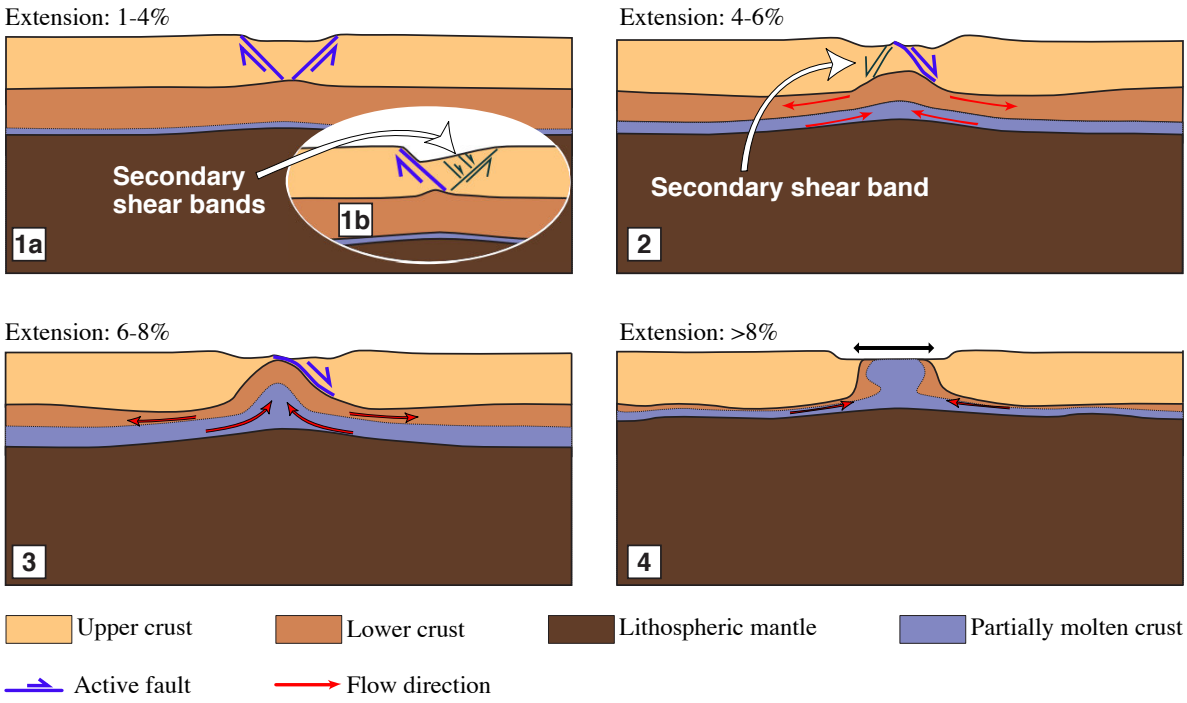

Figure D.3: Sketch illustrating the general dynamics of the formation and exhumation of lower crustal domes. **(1)** The initial stage (total extension: $\leq 4\%$) is dominated by either pure shear (under slow extension; 1a) or simple shear (under rapid and ultra-rapid extension; 1b), resulting in two conjugate normal faults that root in the LC, producing a single graben. **(2)** The conjugate normal faults are abandoned and the LC dome starts to develop. Ductile flow of basal crustal material feeds the dome, resulting in a gradual thinning of the LC at the flanks of the dome. Strain localises in a detachment fault that starts at the centre of the graben and roots at the top of the crustal dome. **(3)** The detachment fault rotates, reaching low angles close to the surface, but maintaining dips between 50-60° at mid crustal depths. Ductile flow of the lower crust progressively fills the gap left by the stretched upper crust, and the dome is gradually exhumed along the detachment fault. **(4)** Exhumation of the lower crustal dome occurs typically after $8 - 10\%$ of extension and it is followed by a period of lateral spreading. This sketch is an idealised representation of the formation of LC domes, some features (such as the topography of the Moho) might differ depending on the initial conditions of the model.

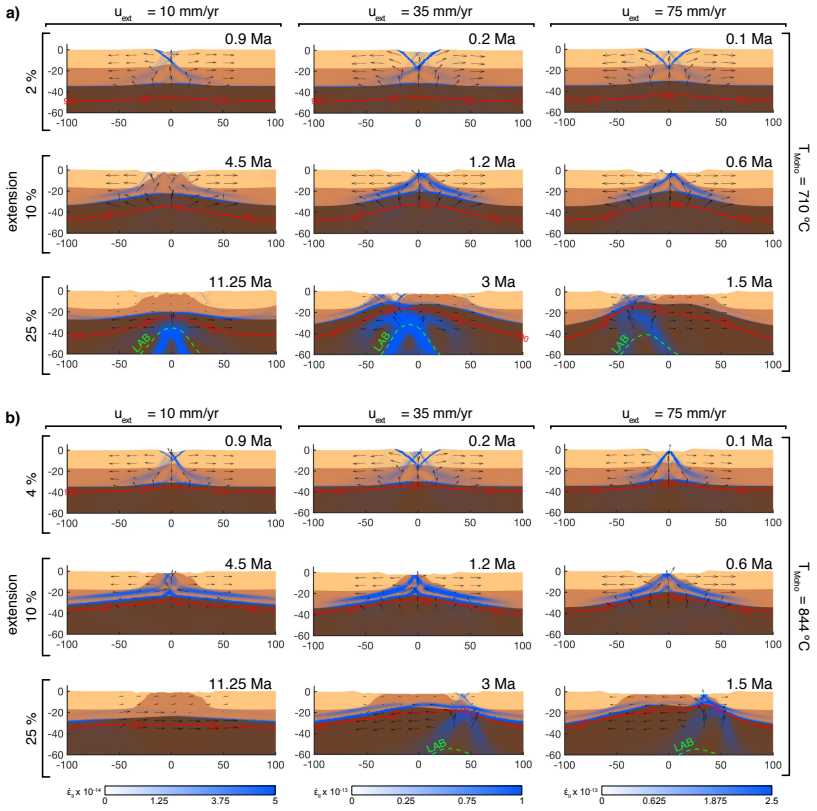

Figure D.4: Snapshots of illustrating the evolution of the **(a)** cold (T_{Moho} = 710 °C) and **(b)** intermediate (T_{Moho} = 844 °C) models for slow (10 mm/yr), rapid (35 mm/yr) and ultra-rapid (75 mm/yr) extension rates. Note that the colour map corresponds to different lithologies, and the strain rate is shown as a blue shading. The thick red line corresponds to the 900 °C isotherm and the green dashed line marks to the Lithosphere Asthenosphere Boundary (LAB). The black vectors represent the velocity field. These models have been computed using the Solidus A. The results of models with Solidus B are found in the supplementary material.

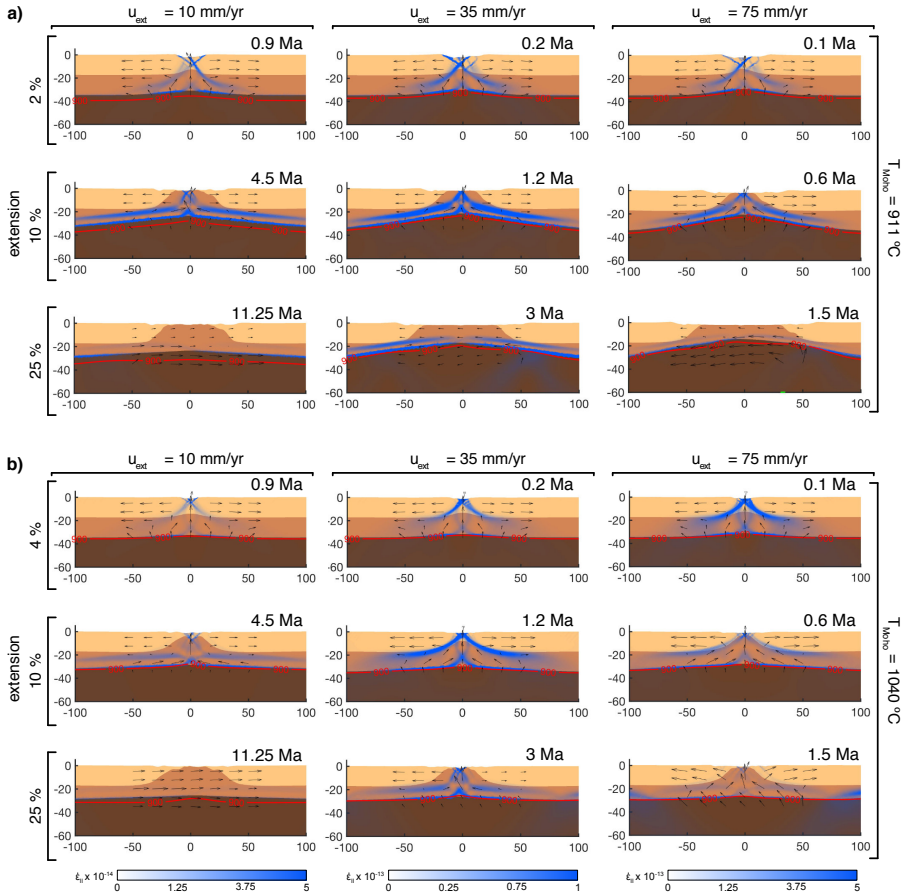

Figure D.5: Snapshots of illustrating the evolution of the **(a)** cold (T_{Moho} = 911 °C) and **(b)** intermediate (T_{Moho} = 1040 °C) models for slow (10 mm/yr), rapid (35 mm/yr) and ultra-rapid (75 mm/yr) extension rates. Note that the colour map corresponds to different lithologies, and the strain rate is shown as a blue shading. The thick red line corresponds to the 900 °C isotherm and the green dashed line marks to the Lithosphere Asthenosphere Boundary (LAB). The black vectors represent the velocity field. These models have been computed using the Solidus A. The results of models with Solidus B are found in the supplementary material.

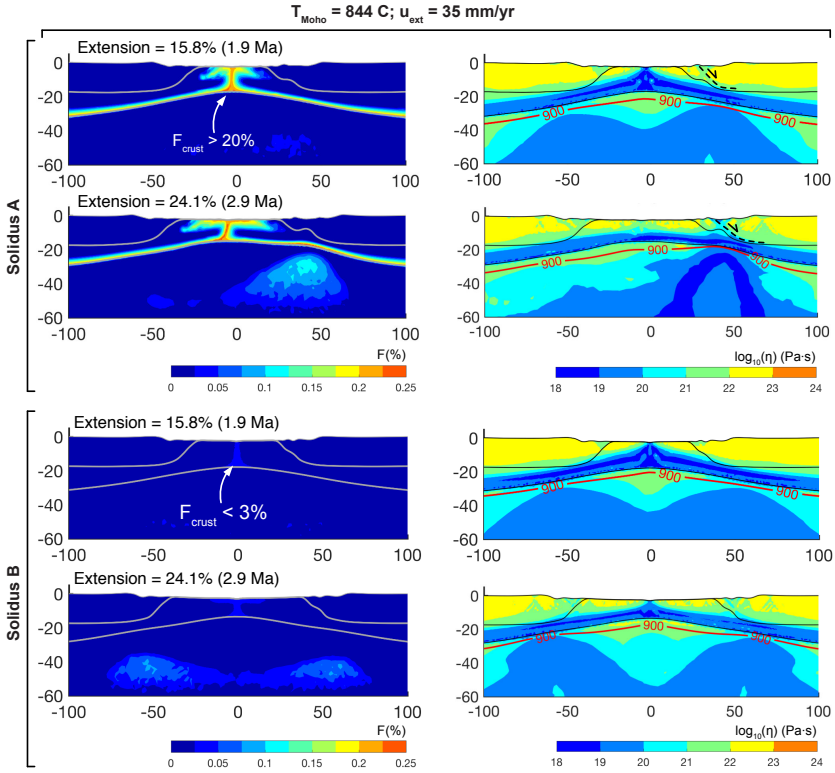

Figure D.6: Snapshots of the evolution the model with an initial intermediate temperature T_{Moho} = 844 °C under rapid (35 mm/yr) stretching boundary conditions for models employing the Solidus A and Solidus B . The colour maps of the figures at the left-hand-side correspond to the percentage of melt fraction and the figures at the right-hand-side show the logarithmic viscosity field.

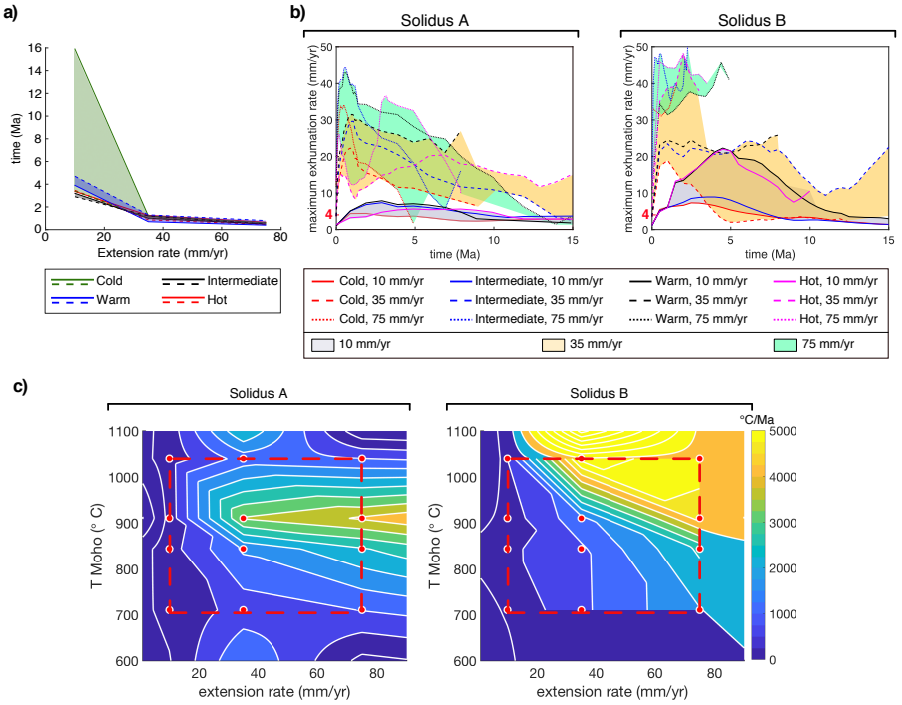

Figure D.7: **(a)** Exhumation times as a functions of extension rate and initial Moho temperature. Dashed lines and thick lines correspond to models employing Solidus A and B, respectively. **(b)** Maximum exhumation rates of the lower crust for the different combinations of extension rate, initial Moho temperature and crustal solidi. Shaded regions represent the envelope of maximum extension rates for models with equal extension rate. **(c)** Contours of the maximum cooling rates obtained from the synthetic T-t paths for models with the Solidus A and B. Red circles indicate the combination of Moho temperature and velocity chosen for the numerical models. Isolines within the red dashed rectangle are result from interpolation of data from our numerical models and isolines outside the rectangle are projected maximum cooling rate values

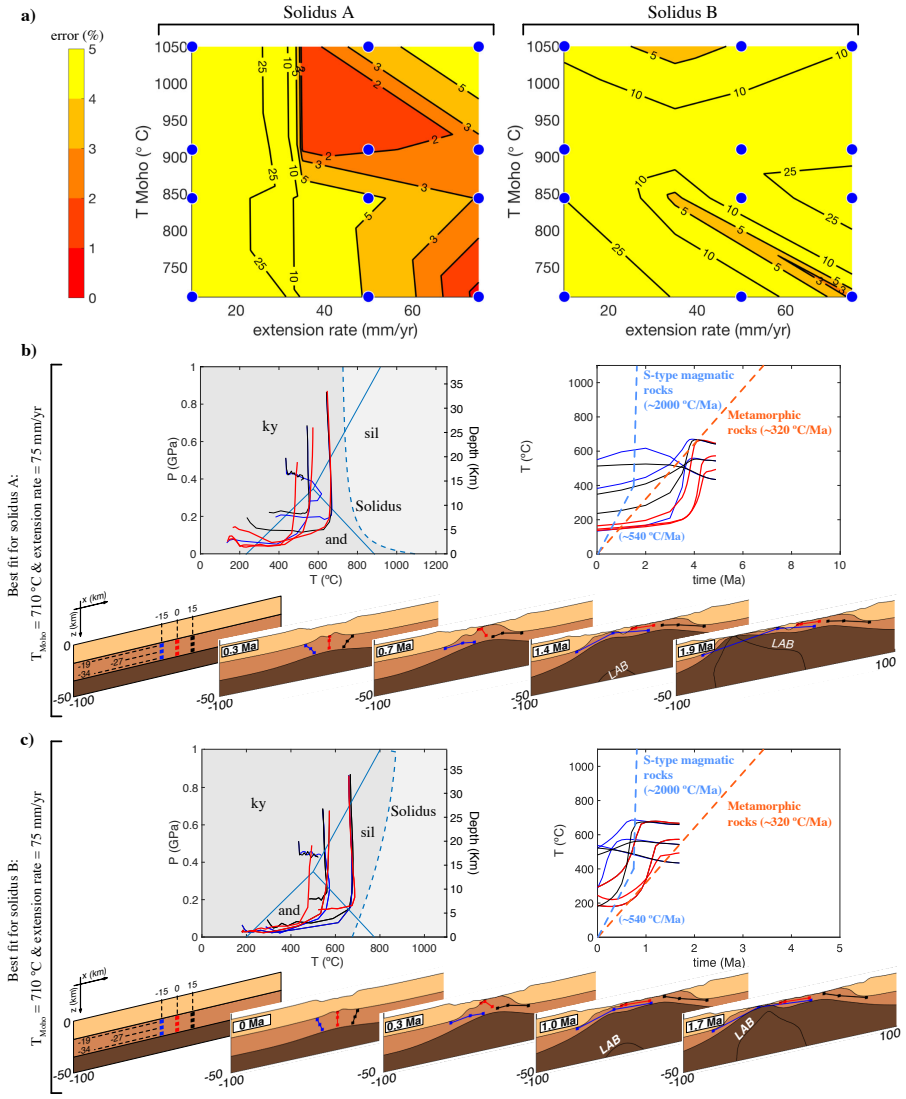

Figure D.8: **(a)** Isolines of the combined error of the magmatic and metamorphic natural paths of samples of the Palu MMC (Hennig et al., 2017) with respect to to the synthetic T-t paths. Blue dots indicate the combinations of initial Moho temperature and extension rate used in the numerical experiments. p-T and T-t paths corresponding the best fit of the synthetic cooling paths with the natural cooling paths for models using **(b)** the Solidus A and **(c)** Solidus B. The colour plots in *(b)* and *(c)* show the different rheological layers, and the blue, black and red dots are the markers where the pressure and temperature are tracked through time. These markers are located initially forming a grid with x = -15, 0, 15 km and z = -19, -27 and 39 km. Tracers are located at both sides of the centre of the model ($x = \pm 15$ km) to capture any asymmetry during exhumation.

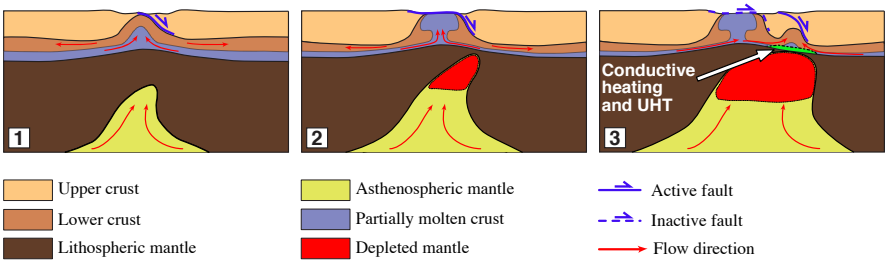

Figure D.9: Sketch showing the development of a secondary asthenospheric-heat induced core complex found for initial Moho temperatures of 710-844° and rapid and ultra-rapid extension ($\geq$ 35 mm/yr). **1** Exhumation of the lower crust is accompanied by an asymmetric ascent of asthenospheric material. **2**. The lower crustal MCC is exhumed along the detachment normal fault; the asthenospheric material continues to raise and undergoes decompression melting. **3** The asthenospheric material reaches the lower crust and conductive heating leads to UHT conditions and a peak of partial melting in the lower crust. The material in this region becomes more buoyant and is eventually exhumed along a new detachment fault.

Supplementary material

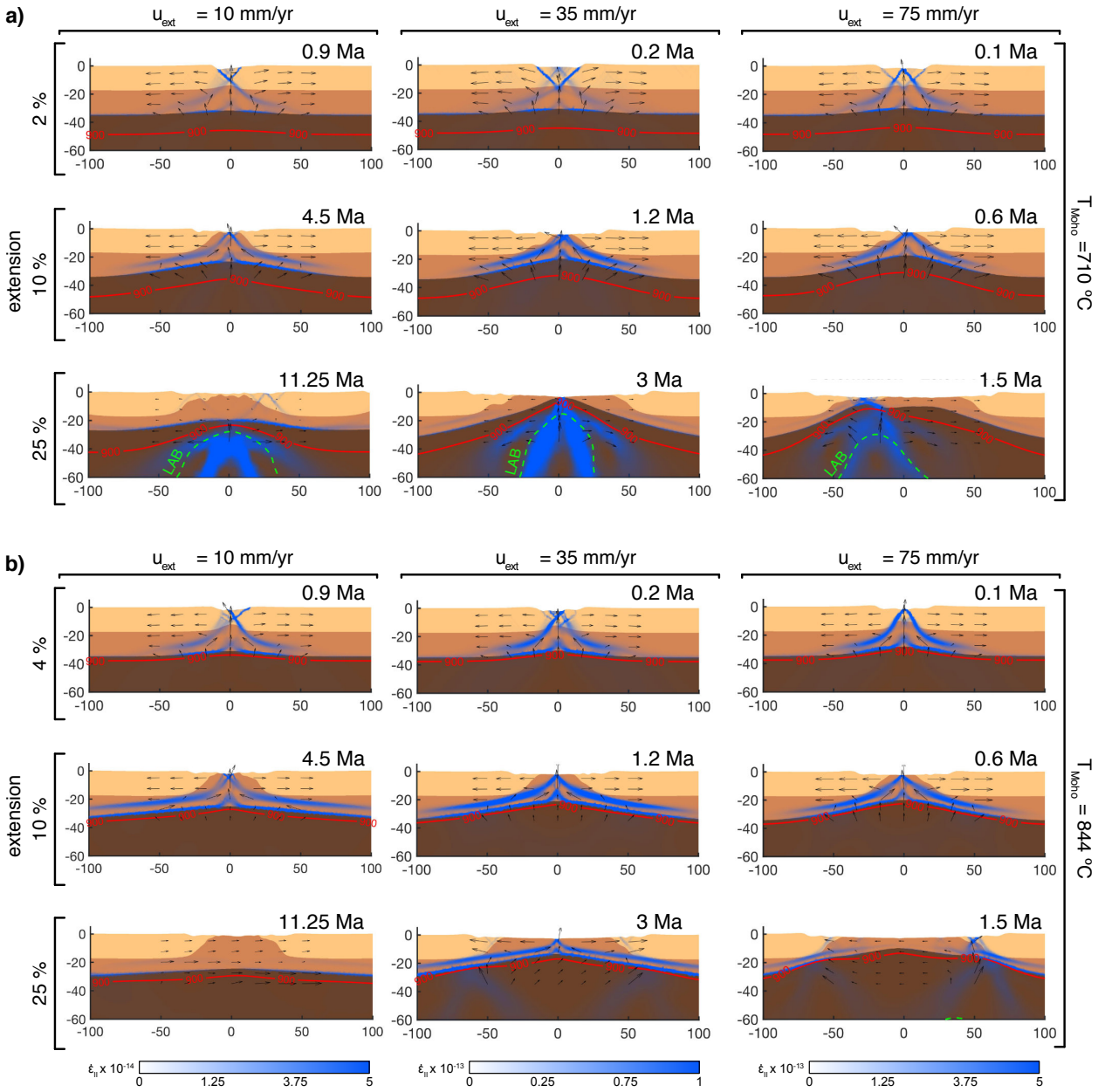

Figure 1: Snapshots of illustrating the evolution of the **(a)** cold (T_{Moho} = 710 °C) and **(b)** intermediate (T_{Moho} = 844 °C) models for slow (10 mm/yr), rapid (35 mm/yr) and ultra-rapid (75 mm/yr) extension rates. Note that the colour map corresponds to different lithologies, and the strain rate is shown as a blue shading. The thick red line corresponds to the 900 °C isotherm and the green dashed line marks to the Lithosphere Asthenosphere Boundary (LAB). The black vectors represent the velocity field. These models have been computed using the Solidus B.

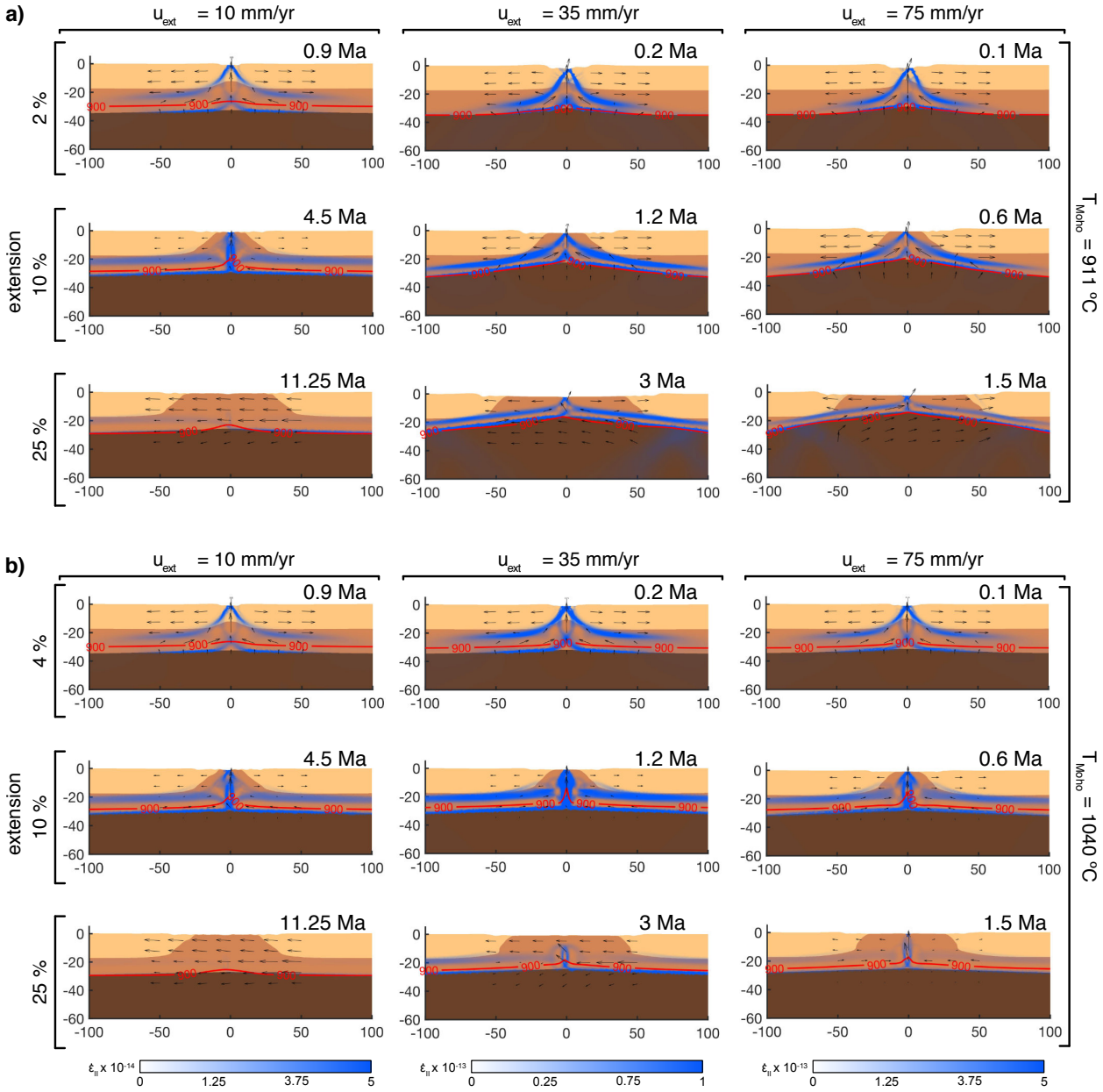

Figure 2: Snapshots of illustrating the evolution of the **(a)** cold (T_{Moho} = 911 °C) and **(b)** intermediate (T_{Moho} = 1040 °C) models for slow (10 mm/yr), rapid (35 mm/yr) and ultra-rapid (75 mm/yr) extension rates. Note that the colour map corresponds to different lithologies, and the strain rate is shown as a blue shading. The thick red line corresponds to the 900 °C isotherm and the green dashed line marks to the Lithosphere Asthenosphere Boundary (LAB). The black vectors represent the velocity field. These models have been computed using the Solidus B.

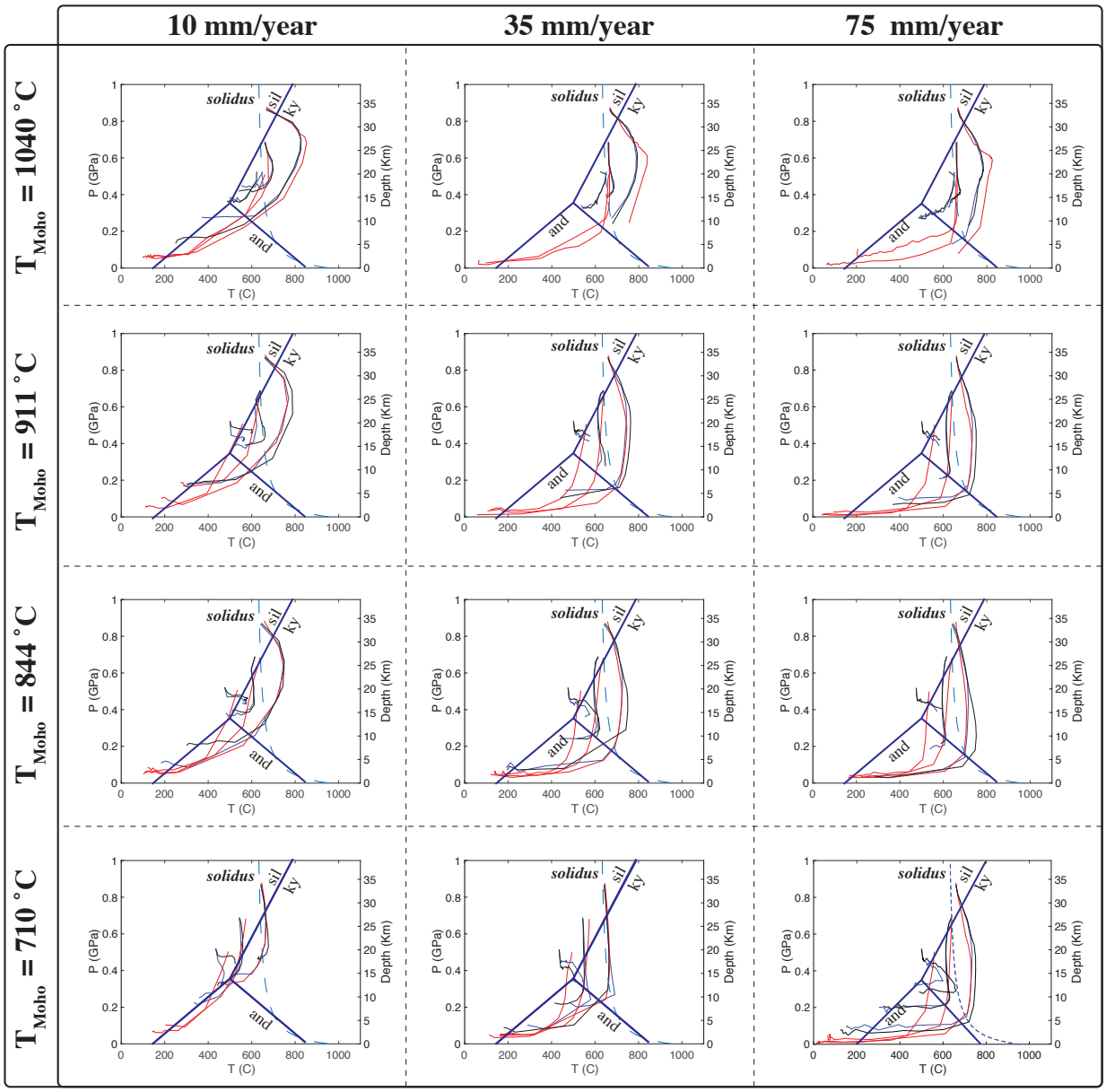

Figure 3: p-T paths corresponding to Solidus A.

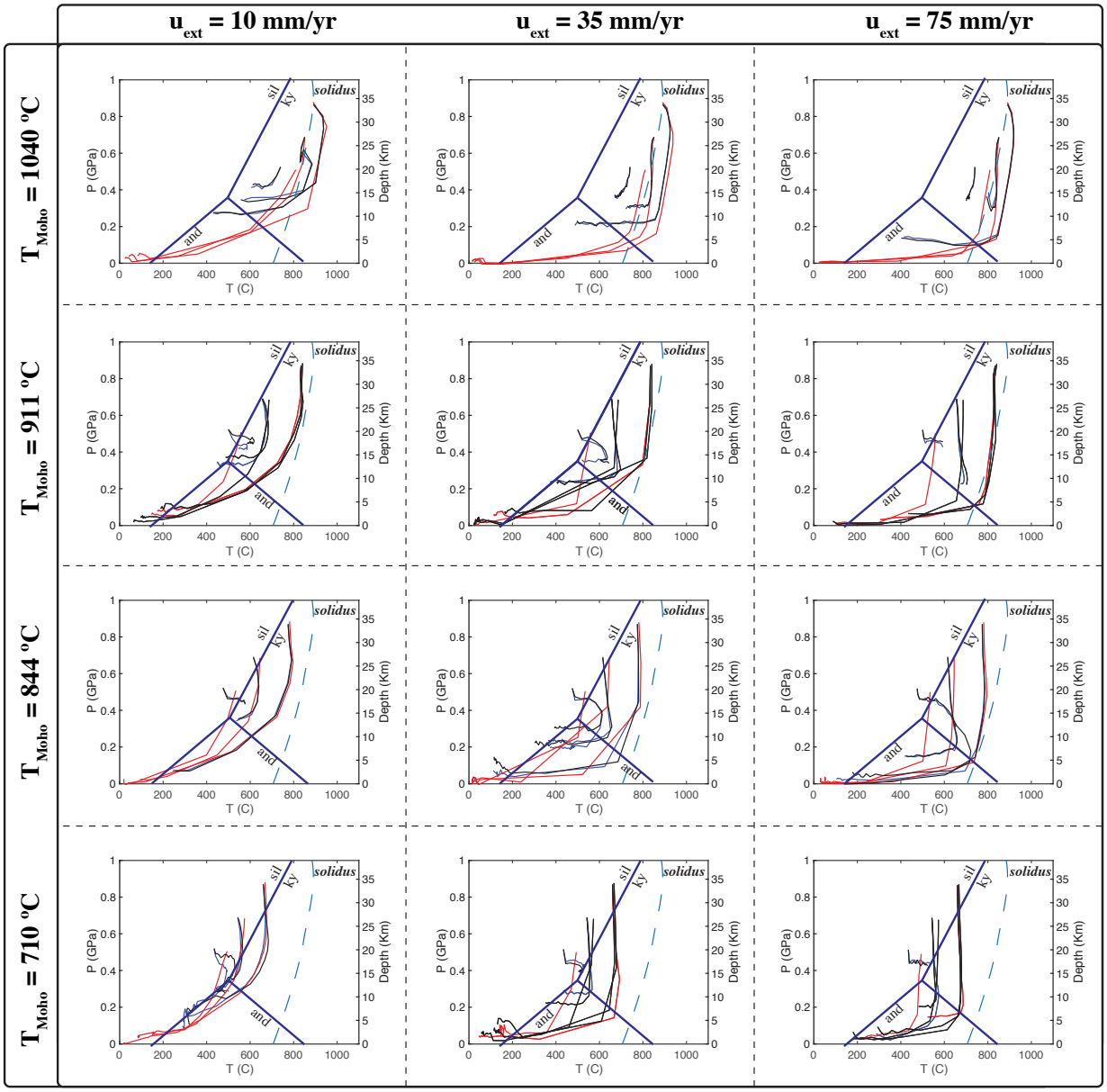

Figure 4: p-T paths corresponding to Solidus B

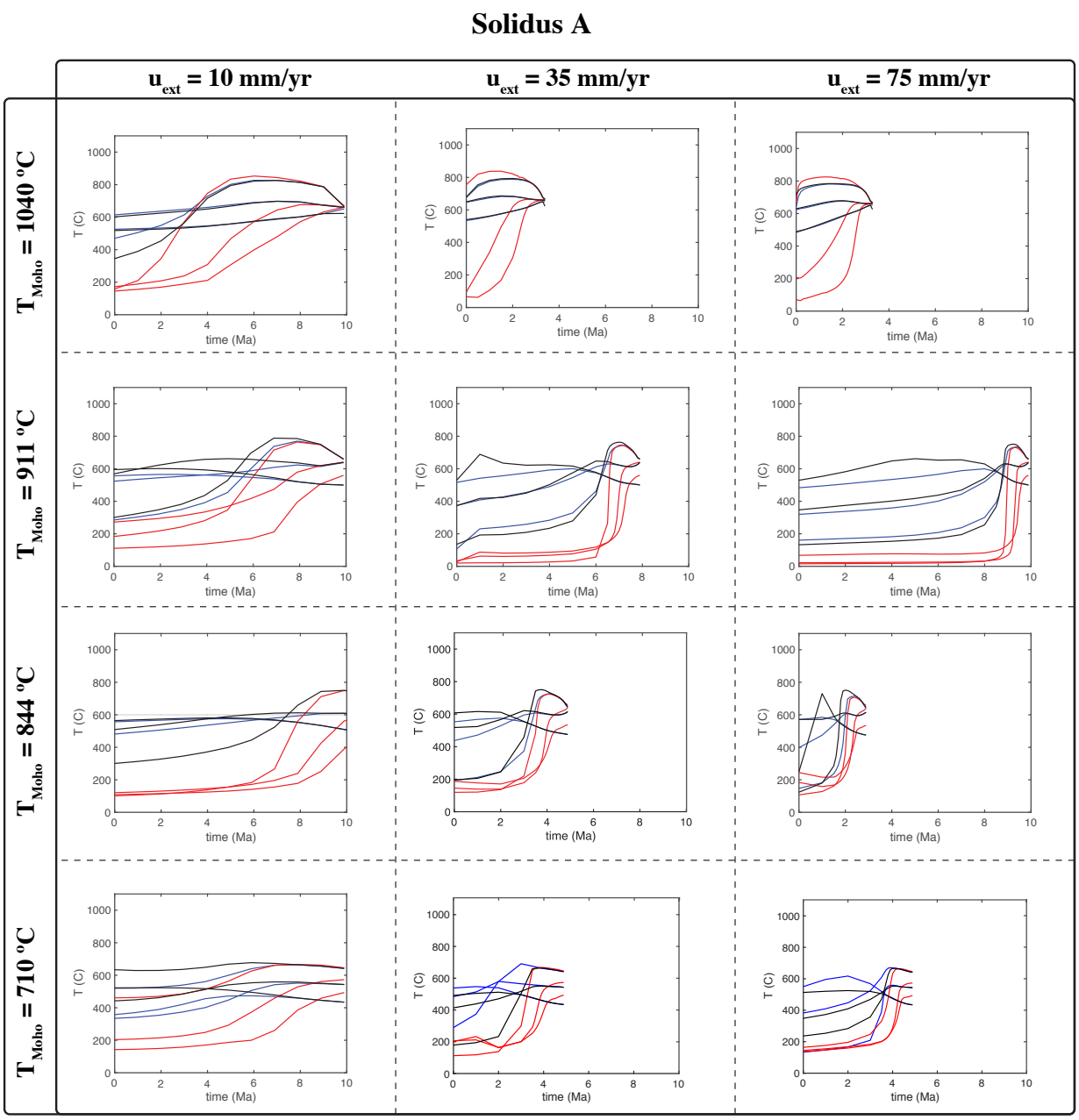

Figure 5: T-t paths corresponding to Solidus A.

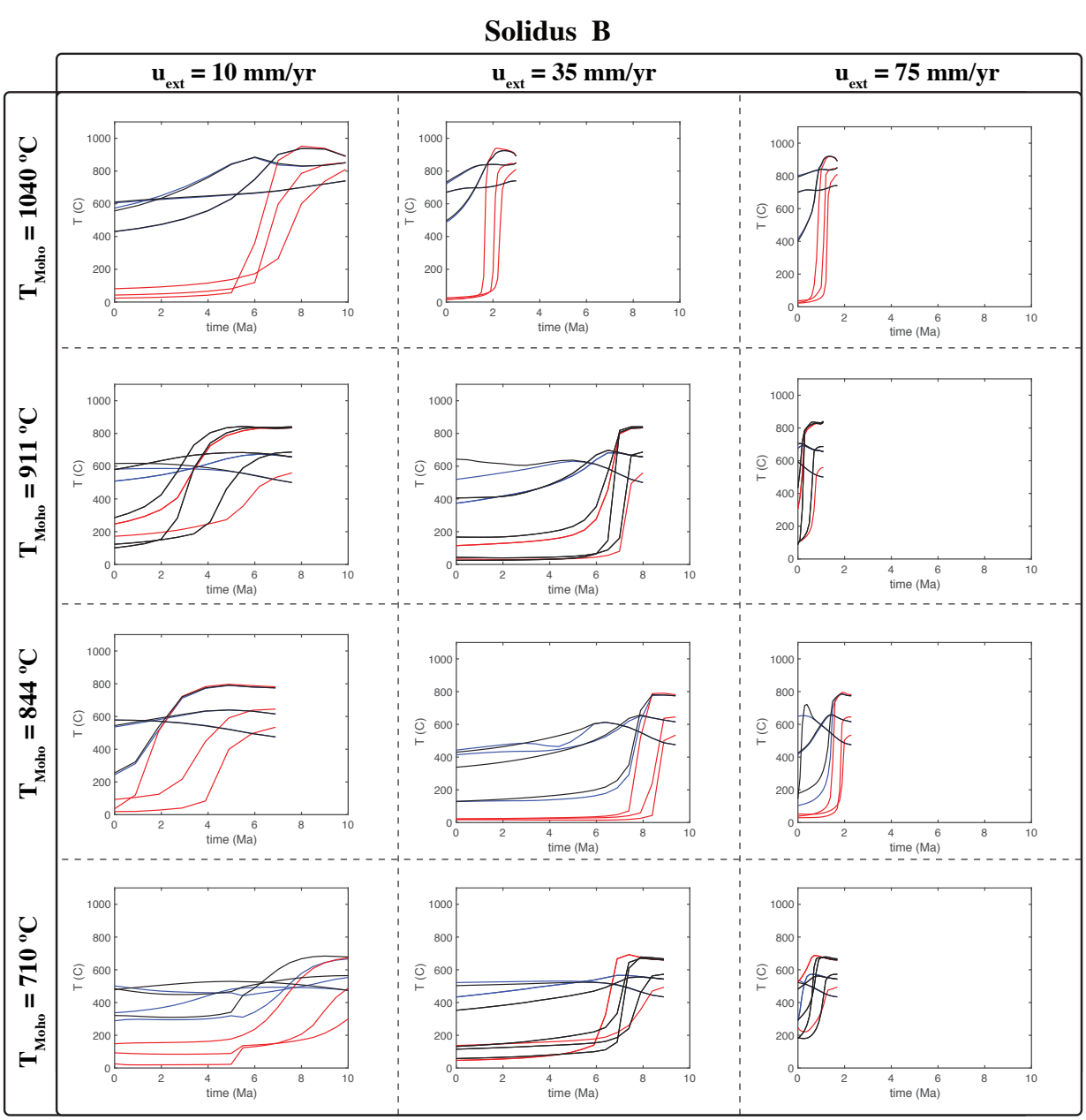

Figure 6: T-t paths corresponding to Solidus B

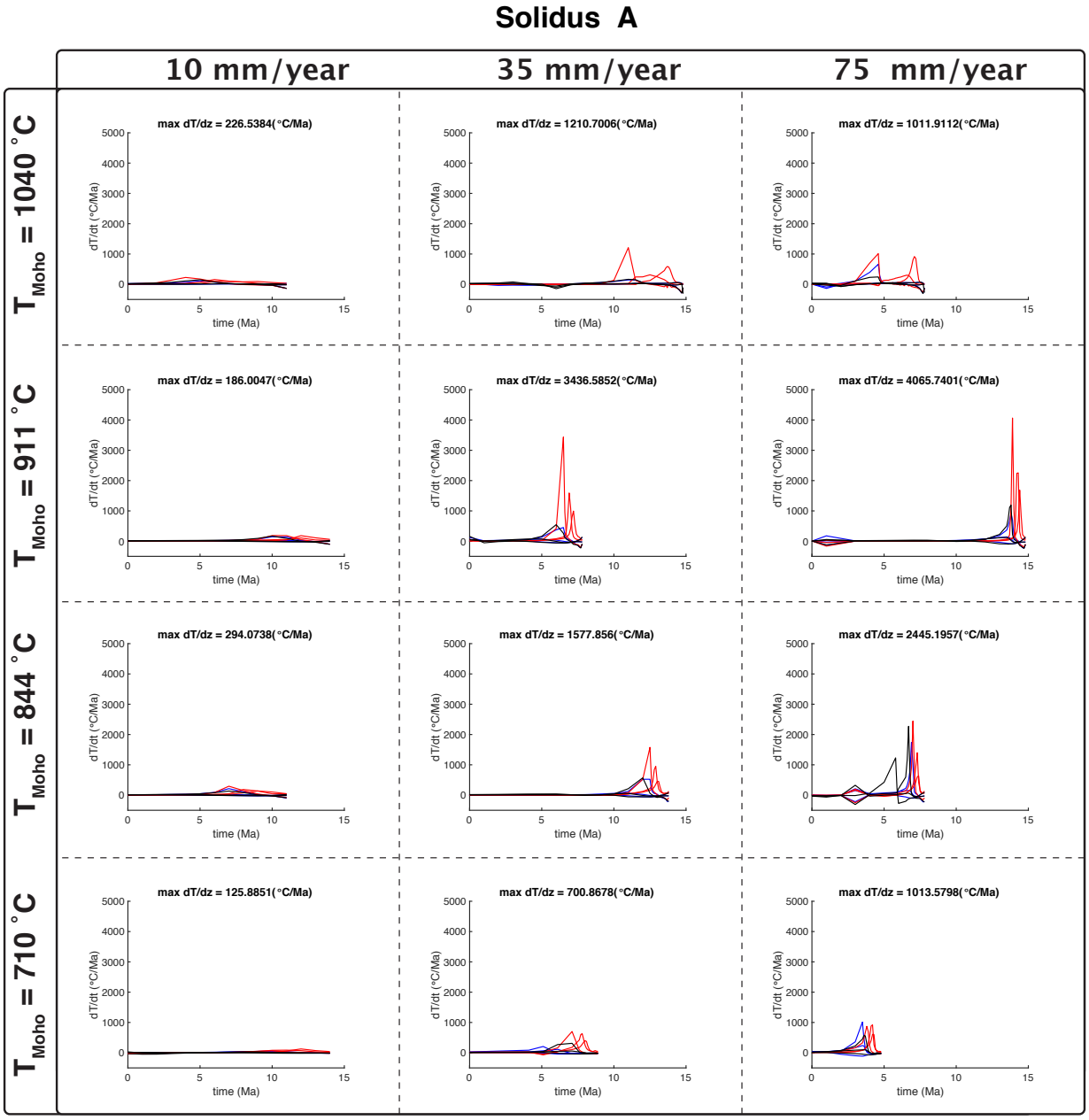

Figure 7: dT/dt paths corresponding to Solidus A.

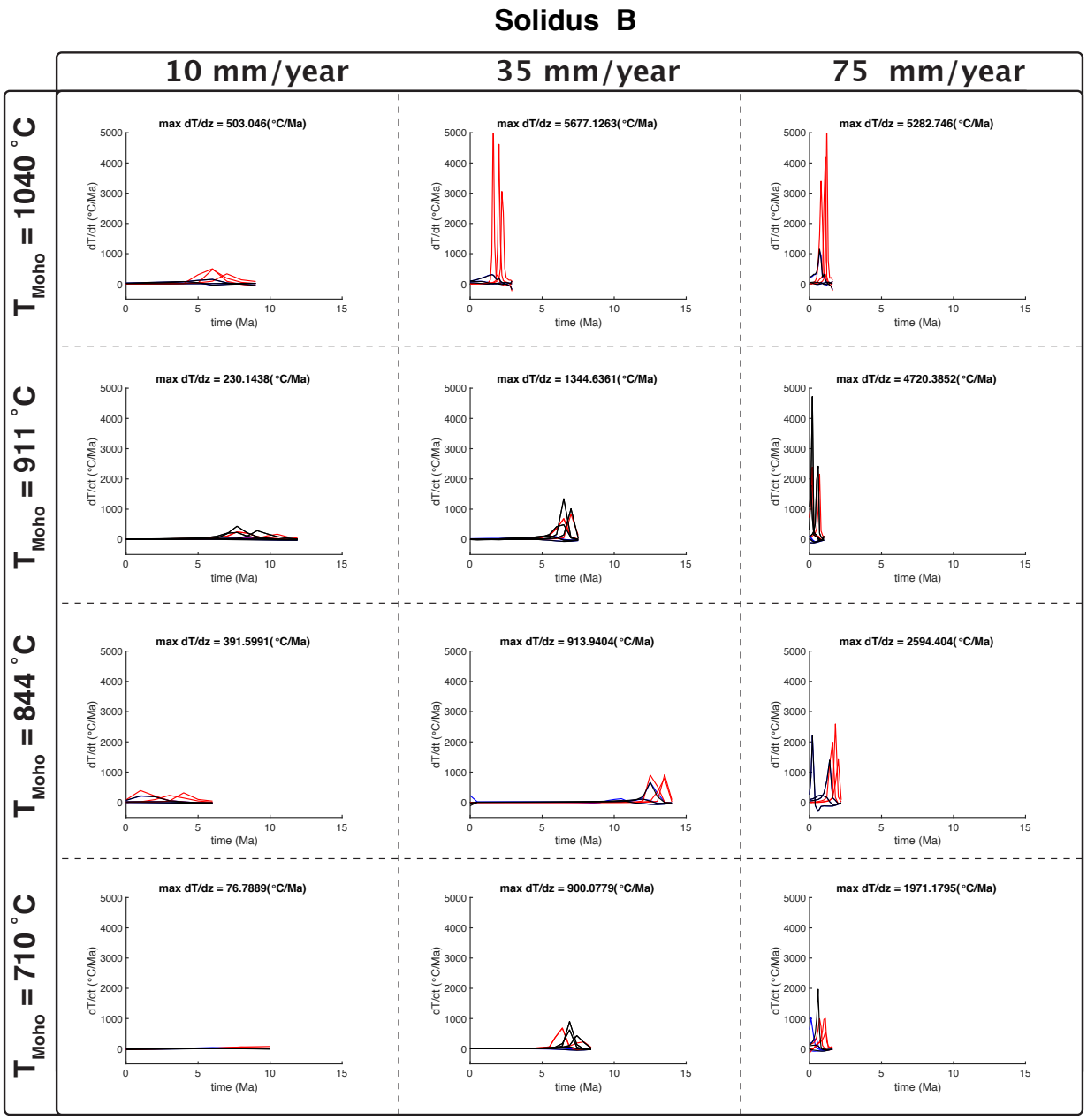

Figure 8: dT/dt paths corresponding to Solidus B

6 | Discussion

6.1 Numerical modelling of tectonic processes: critical evaluation

In Chapter 3, the formulation and benchmarks for the fully compressible code LaCoDe are presented. The compressible Stokes equations are solved in an implicit manner using the Augmented Lagrangian Method (ALM) [Rockafellar, 1974]. This approach has proven to be numerically stable and passed accurately all the benchmarks and numerical experiments in Chapters 3 and 4. In the current state of the code, all the non-linearities are treated using Picard iterations. Heister et al. [2017] showed that, using a Generalized Minimal Residual Method (GMRES) scheme, a 'more implicit' formulation requires fewer non-linear iterations, whereas a 'more explicit' formulation required fewer linear iterations because better preconditioners can be used. These authors concluded that, for stationary computations, the implicit approach is computationally cheaper and more stable; however, for time-dependent problems the explicit approach may become cheaper as, after few time steps, a good approximation of the solution from the previous time step will be available. This conclusion reaffirms the implicit formulation of the continuity equation used in LaCoDe as a valid and efficient approach to solve time-dependent problems in geodynamics. However, some considerations could be considered in the future to improve the robustness, efficiency and versatility of the code.

In the next sections I discuss some aspects of LaCoDe where there is still room for improvement, and some potential implementations that would make this code completer and more versatile.

6.1.1 Solution scheme

As mentioned above, the governing equations of a compressible visco-elastic flow are solved using the ALM, and the non-linearities that appear in the continuity equation due are treated using Picard iterations. If the rheology is non-linear (i.e. non-Newtonian and/or plastic), an outer level of Picard iterations is added to the solution scheme. This split of the non-linearities in two different Picard levels has proven to be a stable scheme for highly non-linear problems.

In order to improve the performance of the code solving non-linear problems, two options might be worth of consideration. First, as illustrated in Popov and Sobolev [2008], and discussed in further details in Spiegelman et al. [2016], a Newton-Raphson solution scheme accelerates and improves the convergence for non-linear problems that include plastic deformation. Both studies show how the Newton-Raphson scheme offers a quadratic convergence for visco-plastic problems, whereas Picard iterations show linear convergence and might stall around a non-converged solution. However, the implementation of such a method would require the calculation of the derivative of the stiffness matrix (either analytically or numerically), which would lead to a reformulation of the governing equations.

The second option consists in parallelising additional parts of the code. The most computationally expensive operations are the assembly and inversion of the block matrices that comprise the global stiffness matrix, and the Cholesky factorization of the latter. LaCoDe uses the Mutils package [Krotkiewski and Dabrowski, 2013] to perform the Cholesky factorisation, which already works in parallel. This done, a parallelisation of the matrices assembly would considerably reduce the computational cost per time step. This technique would not require a reformulation of the governing equations, but the matrix assembly algorithm should be rewritten.

6.1.2 Spatial discretisation

The spatial discretisation of the domain is carried out using the package Triangle [Shewchuk, 1996] to create a mesh of triangular elements. During the mesh generation, a set of regions with different numerical resolutions are defined, according to the degree of interest in each region. For example, in models aiming at studying continental rifting at a lithospheric scale, a fine spatial resolution is of higher necessity in the upper crust than in the deeper mantle. During the evolution of the model, the interface between different rheological layers is tracked so that the resolution after remeshing is as constant as possible.

However, a robust adaptive mesh would be a very interesting and convenient feature to be implemented in LaCoDe. This mesh generation tool consists in performing a mesh refinement in specific regions of interest, given a certain constraint or set of constraints. For example, this method can used to created highly refined areas that follow the upwelling of a mantle plume by forcing the mesh to have a higher resolution where temperature gradient is the highest. Furthermore, it may help to reduce the mesh-dependency of localisation problems in plasticity [Zienkiewicz et al., 1995]. An adaptive mesh has already been implemented in some geodynamic codes, such as ASPECT [Kronbichler et al., 2012] or I2ELVIS [Gerya et al., 2013].

6.1.3 Rheological laws

The results of any mechanical model are ultimately defined by a common denominator: the rheology of the material. Hence the development and employability of the appropriate rheological law is of paramount importance for numerical modelling of any thermo-mechanical process. LaCoDe includes a very complete set of rheological laws aiming at mimicking the physical behaviour of rocks: 1) linear elasticity, 2) dislocation creep, 3) diffusion creep, 4) non-dilatant plasticity using a Prandtl-Reus flow rule, and 5) dilatant plasticity using an associated flow rule.

Linear elasticity is presumably the simplest rheological law, and its mathematical description and applicability to all sort of mechanical processes is far beyond any doubts. Furthermore, the elastic parameters of Earth's interior are fairly well constrained. Non-Newtonian power-laws such as dislocation and diffusion creep have been extensively studied, and the physical parameters defining them have also been fairly well constrained by triaxial laboratory experiments [Wilks and Carter, 1990; Gleason and Tullis, 1995; Hirth and Kohlstedt, 1996; Rybacki and Dresen, 2000; Hirth and Kohlstedt, 2003]. Nonetheless, one should be cautious as these experiments were performed at relatively low deviatoric stresses (the order of 100 MPa) and high strain rates (10^{-1} to 10^{-5} s^{-1}), and yet they are used in models where deviatoric stresses can be almost an order of magnitude higher and strain rates may be several order of magnitude lower with respect to laboratory experiments. Thus, uncertainties resulting from the upscaling to geological processes should expected.

Plasticity limits the maximum stress that a material can withstand, and it is employed to simulate brittle failure at lithospheric depths, i.e. shear zones and faults [e.g. Buck, 1991; Poliakov et al., 1994; Fullsack, 1995; Buiter et al., 2006; Gerya and Yuen, 2007; Huismans and Beaumont, 2007; Braun et al., 2008; Choi

et al., 2013; Ros et al., 2017]. As in elasticity and non-Newtonian flows, the physical plastic parameters, namely friction angle and cohesion, are also well constrained from laboratory experiments. During the calculation of the plastic strain, the effective viscosity is corrected so that the stress field is modified, and the yield stress is never exceeded. More over, plastic strain in geodynamics is often defined by a pressure-sensitive yield surface. Because the effective viscosity is updated via non-linear iterations, the pressure in each one of these iterations will not be the same. Hence plasticity introduces two non-linearities into the system: a first one due to the correction of the effective viscosity and a second one derived from the dependency of the yield criterion on the pressure. The convergence of such a highly non-linear problem is still under debate [Spiegelman et al., 2016] and further research needs to be conducted in this topic.

It is further known that plastic deformation of geomaterials is usually accompanied by a volumetric increase. Yet this feature is typically ignored in geodynamic models and has only been briefly discussed in Choi and Petersen [2015]; however, these authors focused only on the orientation of shear bands, and a deeper study of the effects of dilatant plasticity on tectonic processes is still lacking. In Chapter 4 I propose and discuss a new visco-elastic-plastic constitutive law for geodynamic models that includes volumetric plastic strains via an associative Drucker-Prager flow rule. The robustness of this model is demonstrated by its capability to yield shear bands at orientations predicted by the bifurcation study of Rudnicki and Olsson [1998], where he derived an analytical expression for shear band orientation using the Drucker-Prager's failure criterion. To test the impact of plastic dilation on tectonic processes, I designed a rift-like scenario with different values of dilatancy angle, and two end-members of lower crustal strength: 1) a weak wet quartzite lower crust, and 2) a strong mafic granulitic lower crust. The results show that even though plastic dilation is not likely to play a key role in shaping the faulting history of continental crust, it leads to a hardening of the crust that slows down the evolution of the rifted margins, and thus promotes a faster cooling of the model and yields lower values of surface heat flow. For simplicity, partial melt production was not computed in these models; nonetheless, plastic dilation might potentially have a negative feedback with partial melt occurring in the mantle, as it may enhance the cooling of the raising asthenospheric material. Whether it affects the onset and/or the amount of partial melt, needs to be further investigated.

Despite the fairly complex set of constitutive laws included in LaCoDe, I believe there is a long way to go for the geodynamic community to develop advanced rheological models to better describe the tectonic history of the Earth, and the geodynamic community would largely benefit from models and techniques that are used more frequently in engineering. Some of those that might be useful for modelling geological processes are damage models [e.g. Kachanov, 1958; Simo and Ju, 1987; Oller et al., 1995], Bingham or Perzyna visco-plastic models, viscous and elastic anisotropy/orthotropy, and anistropic yield surfaces [e.g. Moresi and Mühlhaus, 2006].

6.1.4 Strain hardening and softening

After reaching yield conditions, a perfect plastic body will maintain a constant stress as strain increases. This behaviour is characteristic of some metals; however, after onset of inelastic deformation, geomaterials are characterised by a brief period where stress still grows with increasing strain, the so-called *strain hardening*, followed by a stress drop, referred as *strain weakening* or *strain softening*. While strain hardening does not always occur (serpentinite is one example [Escartin et al., 1997]) strain weakening is a crucial mechanism to better understand the post-failure behaviour of rocks and other granular materials.

As discussed in Chapter 4, strain hardening is not implemented as an intrinsic material property; instead, the increase of volume produced by dilatant plasticity leads to a structural hardening. On the other hand, strain softening is accounted for by introducing a dependence of the plastic parameters (cohesion, friction angle

and dilatancy angle) on the softening parameter h. The plastic parameters are the friction angle, cohesion and the dilatancy angle. In order to reduce the complexity of the problem, strain softening is only applied to the friction ($\phi = \phi(h)$) and dilatancy angles ($\psi = \psi(h)$); nevertheless, it is common to find strain softening applied also to the cohesion [e.g. Huismans and Beaumont, 2007; Choi and Petersen, 2015; Tetreault and Buiter, 2017].

A good parametrisation of the strain softening behaviour is important to reproduce the post-peak behaviour of different materials, and while there is an extensive amount of studies addressing the topic [Sibson, 1990; Rice, 1992; Ridley, 1993; Streit, 1997; Ingebritsen and Manning, 1999; Bos and Spiers, 2002; Handy and Stünitz, 2002], more laboratory experiments are needed in order to further constrain the physical parameters defining the strain softening curve.

The implementation of strain softening also introduces interesting numerical complications. Let us consider a rectangular domain subject to tensile stress at its edges and with a small mechanically weaker region located at its centre. When stresses reach the weaker region, softening begins, stress drops, and the material around this region must unload elastically. As a consequence, the softening region is defined by the size of the region with the minimum strength. This leads to two major drawbacks: 1) to solve the Stokes equations, the domain is subdivided in cells or elements with a finite size; consequently the size of these elements will define the strain softening regions and influence the solution; and, 2) strain softening leads to the loss of ellipticity of the governing equations and the boundary problem becomes ill-posed, i.e. an infinitesimal change in the stiffness matrix leads to a large change of the solution.

To my knowledge, the only solution applied to geodynamics was given by Lavier et al. [2000], who proposed the addition of a mesh-independent length scale to define the area of influence of strain softening. In Chapter 4 I have further discussed alternative solutions to the mesh dependency such as non-local continuum techniques. As remarked in Section 6.1.3, modelling of geological processes will largely benefit from importing some of these solutions common in engineering.

6.1.5 Dilatancy angle

During tectonic processes, the strain of the cold lithospheric rocks can go far beyond peak conditions. Therefore, having a model that captures the whole stress-strain post-peak curve will help to produce more realistic results. The post-failure strength behaviour is controlled by the strain softening, discussed in Section 6.1.4, and the dilatancy angle. Since, in rock mechanics, many problems are solved by avoiding failure, the dilatancy angle has not received a great deal of attention and, when used, it has been frequently considered in a simple way either as an associated flow rule ($\psi = \phi$) or fully non-associated ($\psi = 0^\circ$) [Alejano and Alonso, 2005]. However, Vermeer and De Borst [1984] pointed out that an associated flow does not represent well the post-peak behaviour for soils, rocks and concrete and concluded that, for rocks, the dilatancy angle had to be $\psi \leq \phi - 20^\circ$. Later on, Detournay [1986] noted the inappropriateness of this approach and proposed a dilatancy angle that depended on the shear plastic strain. Additionally, Medhurst [1997] and Ribacchi [2000] found out that the dilatancy angle further depends on the confining stress.

One could attempt to reproduce features of post-peak curves mentioned above by writing complex expressions for the dilatancy angle [e.g. Alejano and Alonso, 2005], so that the results would fit the stress-strain curves obtained from laboratory experiments. However, the level of uncertainty surrounding the modelling of tectonic processes is already very elevated and attempting to upscale every single detail featured in results derived from laboratory experiments might be unnecessary. In Chapter 4 I attempted to capture the main features previously mention in a simple manner by introducing a linear dependency of the dilatancy angle on the softening parameter h and on the depth to approximate the pressure-dependency. Interestingly,

results with different degrees of the depth dependency yielded different faulting histories. Thus, further investigations are required in order to better constrain the depth dependency of the dilatancy angle.

6.1.6 Serpentinisation and magmatism

The rationale behind the implementation of a fully consistent compressible formulation for viscous flows was not only to include volumetric strain derived from pressure and temperature changes with respect to the reference state (which has obvious implications in, for example, mantle convection and subducting slabs), but also to account for volumetric changes linked to phase changes (e.g. expansion caused by serpentinisation reactions during mantle exhumation in magma-poor conjugate margins, or during slab fault bending; or contraction caused by deserpentinisation reactions or removal of mass in the form of fluid or melt).

Serpentinisation

Serpentinisation reaction of peridotites is an important process involved in both rifting of continental crust and slab subduction that produces an increase of volume [Gresens, 1967; O'Hanley, 1992]. The volumetric strain is known to reduce the crustal strength [Escartin et al., 1997, 2001] and plays and important role during continental break-up by controlling part of the formation of continent-ocean transition and oceanisation. It has also been hypothesised that the volume increase linked to serpentinisation of the subducting slab enhances fault-bending [Phipps Morgan, 2001a], hence aiding the process of subduction initiation.

As described in Section 2.4.2, I have implemented parametrisation of serpentinisation and deserpentinisation reactions based on the work of Malvoisin et al. [2012]. For completeness, this should be coupled with the Darcy equations to properly quantify the amount of water circulating within the lithosphere and also the spatial distribution with time. Unfortunately, during my Ph.D. I did not further investigate the implications of volumetric changes in geodynamic models. Development and design of models aiming at studying these processes, along with the coupling the equation of flow in a porous media, remains one of the major topics to be further studied with LaCoDe.

Magmatism

The buoyancy of migmatites is believed to have an active role in exhuming mid-crustal rocks and in supporting vertical motion in metamorphic core complexes [e.g. Gautier et al., 1990; Burg and Vanderhaeghe, 1993; Ledru et al., 2001]. Furthermore, partial melting of the mid-lower crust is likely to promote strain localisation as the viscosity lowers (if one assumes that the partially molten crust moves *en mass* along with the non-molten material). Hence, there has been the argument around whether magmatism promotes and facilitates the formation of core complexes, or whether these are a result of extension [Gans, 1989; Lee Armstrong and Ward, 1991; Lister and Baldwin, 1993; Spencer et al., 1995; Foster et al., 2001; Tucholke et al., 2008; Olive et al., 2010].

In Chapter 5 I have tested the influence of melting in the formation of metamorphic complexes by using solidus curves corresponding to 1) an hydrated granite [Boettcher and Wyllie, 1968] and 2) a fluid-absent MORB-derived amphibolite [López and Castro, 2001]; see Fig. 2.5 for a representation of the correspondent solidus curves. Models using the first solidus curve to define crustal melting produce a higher amount of partial melt at mid-lower crustal depths as melting occurs at 600-700 °C at 1 GPa, whereas the fluid-absent amphibolite requires temperatures of around 900 °C at similar pressures. It is therefore easier to produce partial melting in the crust if the source is a hydrated MORB and it will lead to higher amounts of partial

melt volume. However, the results shown in Chapter 5 suggest that the amount of partial melting does not play a crucial role in the development of the metamorphic complex. The appreciable effect of the amount of melting is observed in the p-T paths, where at very high geotherms, the amphibolite leads to near-isothermal decompression of lower crustal rocks of the metamorphic complex. These results are in agreement with the observations of Rey et al. [2009b], who concluded that metamorphic complexes develop both in the presence and absence of crustal melting.

6.1.7 Weak Seeds

Tectonic models are almost always designed so that the rheological layers are laterally homogeneous. Therefore, upon prescription of the boundary conditions, strain is likely to localise at a non-desired region. For example, in models of stretching of continental lithosphere where the domain is laterally homogeneous, strain might localise at geometrical singularities, such as the corners of the model. A simple solution is to introduce the so-called *weak seed*, which consists of a thermo-mechanical heterogeneity. This artificial weakness is commonly used in tectonic models to enforce strain localisation within a desired region. In rifting models, these heterogeneities are typically small regions where the temperature is anomalously higher [e.g. Brune et al., 2012; Ros et al., 2017] or plastic parameters are lower than the surrounding material [e.g. Buck, 1991; Huismans and Beaumont, 2007; Tetreault and Buiter, 2017]. On the other hand, in models aiming at studying subduction zones, it is common to define a weak zone between the subducting slab and the overriding plate [e.g. Gerya and Yuen, 2003; Warren et al., 2008; Taramón et al., 2015]. I must note that one must be careful when introducing mechanical heterogeneities in any model, as the nature and location of the weak seed might have a large influence on the results [Dyksterhuis et al., 2007].

Of particular interest are the weak seeds used to reproduce the development of metamorphic core complexes. A frequent way to force the models to produce metamorphic core complexes is by imposing a fault-like region of low viscosity or plastic parameters that cuts through the crust [e.g. Lavier and Buck, 2002; Rey et al., 2009b,a; Whitney et al., 2013]. Contrary to this trend, other authors choose not to prescribe a weak seed [Schenker et al., 2012]. While the first approach assumes the pre-existence of a normal fault cutting through the crust is a condition for the development of metamorphic complexes, it is not clear the role of boundary effects in the absence of a weak seed. Due to the uncertainties around the hypotheses adopted by these two approaches, in Chapter 5 I decided to use a Gaussian-shaped perturbation of the thermal field located at mid-crustal depths and found that, when combined with a weak and ductile lower crust, it results in the formation and exhumation of lower crustal domes that resembles the metamorphic complexes. In this way, the metamorphic complex develops without the necessity of a pre-existent fault and boundary effects are avoided.

6.2 Future work

Several questions arise from the work presented in this Ph.D. thesis, some related to numerical and/or theoretical concepts, and some others related geological processes that have not been addressed throughout this thesis.

Many of the technical aspects to be considered have already been discussed in Section 6.1, such as the implementation of a Newton-like solution scheme and an adaptive mesh, or importing engineering solutions to overcome the issue of a mesh-dependent solution in strain localisation problems. However, the implementation of the fully compressible Stokes equations opens the doors to investigate a wide spectrum

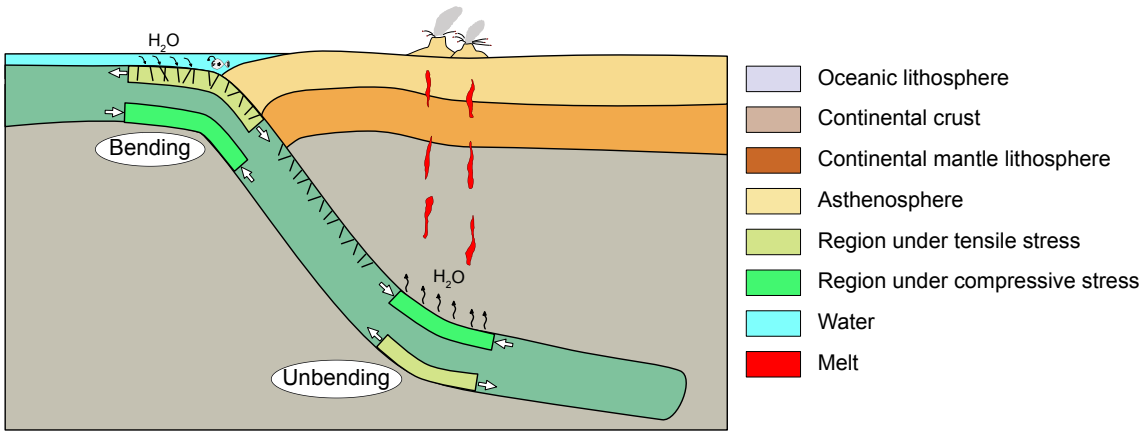

Fig. 6.1 *Schematic representation of bending (and consequent faulting) and unbending of the subducted slab due to hydration and dehydration reactions.*

of geological processes that, to my knowledge, have not been studied from a numerical point of view, or received very little attention: the study of the mechanical effects of volume-changing processes.

One of these processes are the consequences of serpentinisation and deserpentinisation reactions on different tectonic processes. In Section 6.1.6 I have briefly discussed its potential effects on rifted margins and aiding subduction initiation. However, serpentinisation may play an important role in other geological scenarios. For example, dehydration of the subducted slab would lead to deserpentinisation reactions, reverting the increase of volume produced at shallow depths. This would produce a contraction at the upper *face* of the subducted slab, potentially forcing it to unbend.

Another scenario related to this process are transform faults in rifted margins, i.e. East Pacific and Atlantic Ocean. Cross-sections of transform faults typically display a narrow area at the centre that is topographically depressed (up to a few hundred meters) with respect to the surrounding region and surrounded by two elevated bulges at its sides. Furthermore, the blocks at each side of the valley have different depths. The differential depth of the blocks can easily be explained by the offset of their thermal age. On the other hand, the presence of the valley and the bulges supports the idea of the existence of some tectonic activity, as one of the blocks is likely to have rotated due to flexure caused by extension.

A possible driver mechanism for extension is the presence of a mechanically weaker region between the blocks of the transform fault, caused by serpentinisation reactions. Cooling down of the lithosphere will lead to a differential thermal subsidence at both sides of the transform fault, and the weak region will promote strain localisation and extension in the surroundings of the fault. This hypothesis could easily be tested using the current state of LaCoDe and will be addressed in the near future. Furthermore, mid-ocean-ridges are characterised by several transform faults, making this a highly three-dimensional process. The interaction between adjacent transform faults and the degree of obliquity of extension remains to be further investigated using a three-dimensional approach.

These geological scenarios are only some of examples where volume changes can become relevant and should not be neglected if one aims at studying geological processes with the maximum possible degree of complexity. Unfortunately, this has not been possible during my Ph.D. and will be the subject of future research using the numerical code developed here.

In Chapter 5 I have shown how the high cooling and exhumation rates of metamorphic complexes found in Sulawesi can be explained by extension rates that are higher with respect to the ones that lead to the development of other extensively studied metamorphic complexes. Furthermore, these anomalously rapid

exhumation processes are not endemic of Sulawesi, but they are likely to be widespread along the Banda Sea region. Recent studies suggests similar or even higher rates [Pownall et al., 2013, 2014; Pownall, 2015] for metamorphic complexes found Seram (located at the Banda Sea, between Sulawesi and West Papua New Guinea) which are age-comparable to the events in Sulawesi. Therefore, more numerical (and field) studies are required to constrain the cause of such rapid process and verify whether they are all related to the same tectonic event (e.g. roll-back of the Banda trench and consequent opening of the Banda Sea) or they are independent.

7 | Conclusions

7.1 Conclusions

- The solvability and accuracy of a general expression of the compressible Stokes equations using an iterative Augmented Lagrangian Method using an implicit approach has been demonstrated. This approach has passed several benchmarks for elastic and viscous deformation with errors comparable to other available codes.
- The density dependence of the continuity equation introduces a non-linearity into the problem that is lacking in the incompressible approximations. Hence the total number of iterations per time step will be substantially more elevated. I find that for non-linear rheologies, one could treat all the non-linearities in one single level of Picard iterations. However, as the complexity of the model increases, it is more convenient to split the non-linearities arising from the rheology and the continuity equation into two levels of Picard iterations, leading to faster convergence rates and better resolved solutions.
- While the Boussinesq approximation is a valid hypothesis for simple modelling of crustal deformation, more complex models that aim to study processes such as phase changes or partial melting will require a modification of the Boussinesq approximation to accommodate the effects of volumetric strains and volume-change-linked stresses.
- The inclusion of a self-consistent volume change source term is a powerful tool that opens an opportunity to study the effects of overpressure caused by the inflow and outflow of mass into geological features (e.g. serpentinisation and melt extraction.
- Plastic models with a Drucker-Prager yield function and an associative flow rule yield shear bands dipping at Coulomb angles. On the other hand, a non-associative deviatoric Prandtl-Reus flow rule yields shear band orientations scattered within the range of Coulomb-Arthur-Roscoe angles.
- Volumetric expansion within the shear bands results in a structural hardening of the domain. However, the evolution and final geometry of the rift do not present significant differences between dilatant and non-dilatant models.
- The slower vertical motion of mantle upwelling induced by the structural hardening of the lithosphere promotes a cooling of the models, whereas volumetric plastic strain introduces an extra source of heat derived from inelastic work. The thermal structure and surface heat flow in dilatant models is therefore altered with respect non-dilatant models. For a strong lower crust, brittle deformation is highly effective and dilatant models yield similar temperature fields for the range of dilatancy angles considered in this paper. However, plasticity is less effective in models with a weak lower crust and shear heating dominates for $\psi_0 = 15^\circ$, whereas the model with $\psi_0 = 30^\circ$ is cooler, due to the slower upwelling of mantle material.

- The evolution of the faults and shear zones of a model with a depth-dependent dilatancy angle with $\psi_0 = \phi_0$ at null confining pressure represents and intermediate state between using constant $\psi_0 = 30^\circ$ and $\psi_0 = 15^\circ$. During the early stages of extension, this model is very similar to a model with constant $\psi_0 = 30^\circ$ and it evolves towards a similar strain rate state as the model with $\psi_0 = 15^\circ$ as strain softening kicks in.
- Our numerical results on extension of thinned crust with different permutations of initial thermal structure and extension rates considered in this work yield formation of lower crustal domes, suggesting that anomalously elevated thermal conditions are not a pre-requisite for the formation of metamorphic core complexes (MCCs) in thinned crust.
- Three different final modes of model architecture are observed: 1) localised doming of the lower crust with synchronous upwelling of the asthenosphere, followed by crustal break up and resulting in two conjugate margins; 2) localised doming of the lower crust accompanied by doming of the Moho, occasionally followed by secondary asthenospheric-heat induced lower crustal dome; and 3) doming of the lower crust and a flat Moho.
- Two different kinds of lower crustal domes are identified in intermediate temperature ($T_{Moho} = 844$ °C) models under fast extension (≥ 35 mm/yr): 1) a primary lower crustal dome driven by far-field forces and lower crustal flow; and 2) a secondary asthenospheric-heat induced MCC. Rocks comprising these lower crustal domes record different p-T-t histories: primary lower crustal dome rocks show very rapid vertical ascend towards the surface reflected by near-isothermal p-T paths followed by rapid cooling at shallow depths, whereas asthenospheric-heat induced MCC rocks experience isobaric heating at intermediate pressure and 400-600 °C followed by decompression heating to peak conditions (c. 0.2 GPa and 700-750 °C).
- Extension rate defines the shape of the p-T and T-t paths of lower crustal rocks of MCC, promoting near-isothermal decompression and shorter periods of rapid cooling. The final architecture of the models and volume of partial melt is also affected by the extension rate. This dependence on extension rate is reduced with hotter initial conditions.
- Rocks with a solidus similar to a hydrated MORB are weakened by partial melt even for the lowest Moho temperature considered here. Rocks with a lower water content require hotter conditions in order to be partially molten, and they remain stronger. The geometry is affected by the volume of crustal melting, however, MCCs are still predicted when there is no partial melting of the crust. This suggests that advection of lower crust towards the surface is driven by the ductile flow of hot lower crust that fills the space left by the stretching and break-up of the lower crust, rather than by buoyancy forces alone.

Bibliography

Alejano, L. and Alonso, E. (2005). Considerations of the dilatancy angle in rocks and rock masses. *International Journal of Rock Mechanics and Mining Sciences*, 42(4):481–507.

Bathe, K.-J. (2006). *Finite element procedures*. Klaus-Jurgen Bathe.

Bayrakci, G., Minshull, T., Sawyer, D., Reston, T. J., Klaeschen, D., Papenberg, C., Ranero, C., Bull, J., Davy, R., Shillington, D., et al. (2016). Fault-controlled hydration of the upper mantle during continental rifting. *Nature Geoscience*, 9(5):384.

Bercovici, D., Schubert, G., and Glatzmaier, G. A. (1992). Three-dimensional convection of an infinite-Prandtl-number compressible fluid in a basally heated spherical shell. *Journal of Fluid Mechanics*, 239:683–719.

Boettcher, A. and Wyllie, P. (1968). Melting of granite with excess water to 30 kilobars pressure. *The Journal of Geology*, 76(2):235–244.

Bos, B. and Spiers, C. J. (2002). Frictional-viscous flow of phyllosilicate-bearing fault rock: Microphysical model and implications for crustal strength profiles. *Journal of Geophysical Research: Solid Earth*, 107(B2).

Braun, J., Thieulot, C., , P., DeKool, M., Beaumont, C., and Huismans, R. (2008). DOUAR: A new three-dimensional creeping flow numerical model for the solution of geological problems. *Physics of the Earth and Planetary Interiors*, 171(1-4):76–91.

Braun, M. G., Hirth, G., and Parmentier, E. (2000). The effects of deep damp melting on mantle flow and melt generation beneath mid-ocean ridges. *Earth and Planetary Science Letters*, 176(3-4):339–356.

Brune, S., Popov, A. A., and Sobolev, S. V. (2012). Modeling suggests that oblique extension facilitates rifting and continental break-up. *Journal of Geophysical Research: Solid Earth*, 117(B8).

Buck, W. R. (1991). Modes of continental lithospheric extension. *Journal of Geophysical Research: Solid Earth*, 96(B12):20161–20178.

Buiter, S. J., Babeyko, A. Y., Ellis, S., Gerya, T. V., Kaus, B. J., Kellner, A., Schreurs, G., and Yamada, Y. (2006). The numerical sandbox: comparison of model results for a shortening and an extension experiment. *Geological Society, London, Special Publications*, 253(1):29–64.

Burg, J.-P. and Vanderhaeghe, O. (1993). Structures and way-up criteria in migmatites, with application to the Velay dome (French Massif Central). *Journal of Structural Geology*, 15(11):1293–1301.

Cann, J., Blackman, D., Smith, D., McAllister, E., Janssen, B., Mello, S., Avgerinos, E., Pascoe, A., and Escartin, J. (1997). Corrugated slip surfaces formed at ridge–transform intersections on the Mid-Atlantic Ridge. *Nature*, 385(6614):329.

Choi, E. and Petersen, K. D. (2015). Making coulomb angle-oriented shear bands in numerical tectonic models. *Tectonophysics*, 657:94–101.

Choi, E., Tan, E., Lavier, L., and Calo, V. M. (2013). DynEarthSol2D: An efficient unstructured finite element method to study long-term tectonic deformation. *Journal of Geophysical Research: Solid Earth*, 118(5):2429–2444.

Coney, P. J. (1974). Structural analysis of the Snake Range 'Décollement,'east-central Nevada. *Geological Society of America Bulletin*, 85(6):973–978.

Coulomb, C. (1773). Test on the applications of the rules of maxima and minima to some problems of statics related to architecture. *Mem. Math. Phys*, 7:343–382.

Crouzeix, M. and Raviart, P.-A. (1973). Conforming and nonconforming finite element methods for solving the stationary Stokes equations I. *Revue française d'automatique, informatique, recherche opérationnelle. Mathématique*, 7(3):33–75.

Dabrowski, M., Krotkiewski, M., and Schmid, D. W. (2008). MILAMIN: MATLAB-based finite element method solver for large problems. *Geochemistry, Geophysics, Geosystems*, 9(4):1–24.

de Souza Neto, E. A., Peric, D., and Owen, D. R. (2011). *Computational methods for plasticity: theory and applications*. John Wiley & Sons.

Detournay, E. (1986). Elastoplastic model of a deep tunnel for a rock with variable dilatancy. *Rock Mechanics and Rock Engineering*, 19(2):99–108.

Donea, J. and Huerta, A. (2003). *Finite Element Methods for flow problems*. John Wiley & Sons.

Drucker, D. C. and Prager, W. (1952). Soil mechanics and plastic analysis or limit design. *Quarterly of applied mathematics*, 10(2):157–165.

Du Toit, A. L. (1937). *Our wandering continents: an hypothesis of continental drifting*. Oliver and Boyd.

Dyksterhuis, S., Rey, P., Müller, R., and Moresi, L. (2007). Effects of initial weakness on rift architecture. *Geological Society, London, Special Publications*, 282(1):443–455.

Emmanuel, S. and Berkowitz, B. (2006). Suppression and stimulation of seafloor hydrothermal convection by exothermic mineral hydration. *Earth and Planetary Science Letters*, 243(3):657–668.

Escartin, J., Hirth, G., and Evans, B. (1997). Effects of serpentinization on the lithospheric strength and the style of normal faulting at slow-spreading ridges. *Earth and Planetary Science Letters*, 151(3):181–189.

Escartin, J., Hirth, G., and Evans, B. (2001). Strength of slightly serpentinized peridotites: Implications for the tectonics of oceanic lithosphere. *Geology*, 29(11):1023–1026.

Faccenda, M., Gerya, T. V., Mancktelow, N. S., and Moresi, L. (2012). Fluid flow during slab unbending and dehydration: Implications for intermediate-depth seismicity, slab weakening and deep water recycling. *Geochemistry, Geophysics, Geosystems*, 13(1).

Forte, A. M. and Mitrovica, J. X. (1996). New inferences of mantle viscosity from joint inversion of long-wavelength mantle convection and post-glacial rebound data. *Geophysical Research Letters*, 23(10):1147–1150.

Foster, D. A., Schafer, C., Fanning, C. M., and Hyndman, D. W. (2001). Relationships between crustal partial melting, plutonism, orogeny, and exhumation: Idaho–Bitterroot batholith. *Tectonophysics*, 342(3-4):313–350.

Fullsack, P. (1995). An arbitrary Lagrangian-Eulerian formulation for creeping flows and its application in tectonic models. *Geophysical Journal International*, 120(1):1–23.

Galerkin, B. G. (1915). Series solution of some problems of elastic equilibrium of rods and plates. *Vestn. Inzh. Tekh*, 19:897–908.

Gans, P. B. (1989). *Synextensional magmatism in the Basin and Range province: A case study from the eastern Great Basin*, volume 233. Geological Society of America.

Gautier, P., Ballèvre, M., Brun, J.-P., and Jolivet, L. (1990). Extension ductile et bassins sédimentaires mio-pliocènes dans les Cyclades (îles de Naxos et Paros). *Comtes Rendus de l'acad des Sciences Paris*, 310:147–153.

Gerya, T., May, D., and Duretz, T. (2013). An adaptive staggered grid finite difference method for modeling geodynamic Stokes flows with strongly variable viscosity. *Geochemistry, Geophysics, Geosystems*, 14(4):1200–1225.

Gerya, T. V. and Meilick, F. (2011). Geodynamic regimes of subduction under an active margin: effects of rheological weakening by fluids and melts. *Journal of Metamorphic Geology*, 29(1):7–31.

Gerya, T. V. and Yuen, D. A. (2003). Rayleigh–Taylor instabilities from hydration and melting propel 'cold plumes' at subduction zones. *Earth and Planetary Science Letters*, 212(1-2):47–62.

Gerya, T. V. and Yuen, D. A. (2007). Robust characteristics method for modelling multiphase visco-elasto-plastic thermo-mechanical problems. *Physics of the Earth and Planetary Interiors*, 163(1-4):83–105.

Glatzmaier, G. A. (1988). Numerical simulations of mantle convection: Time-dependent, three-dimensional, compressible, spherical shell. *Geophysical & Astrophysical Fluid Dynamics*, 43(2):223–264.

Gleason, G. C. and Tullis, J. (1995). A flow law for dislocation creep of quartz aggregates determined with the molten salt cell. *Tectonophysics*, 247(1-4):1–23.

Gresens, R. L. (1967). Composition-volume relationships of metasomatism. *Chemical geology*, 2:47–65.

Hall, R. (2002). Cenozoic geological and plate tectonic evolution of SE Asia and the SW Pacific: computer-based reconstructions, model and animations. *Journal of Asian Earth Sciences*, 20(4):353–431.

Handy, M. and Stünitz, H. (2002). Strain localization by fracturing and reaction weakening—a mechanism for initiating exhumation of subcontinental mantle beneath rifted margins. *Geological Society, London, Special Publications*, 200(1):387–407.

Hansen, L., Zimmerman, M., and Kohlstedt, D. (2012). Laboratory measurements of the viscous anisotropy of olivine aggregates. *Nature*, 492(7429):415–418.

Hashiguchi, K. and Yamakawa, Y. (2012). *Introduction to finite strain theory for continuum elasto-plasticity*. John Wiley & Sons.

Heister, T., Dannberg, J., Gassmöller, R., and Bangerth, W. (2017). High accuracy mantle convection simulation through modern numerical methods–ii: realistic models and problems. *Geophysical Journal International*, 210(2):833–851.

Hennig, J., Hall, R., Forster, M. A., Kohn, B. P., and Lister, G. S. (2017). Rapid cooling and exhumation as a consequence of extension and crustal thinning: Inferences from the Late Miocene to Pliocene Palu Metamorphic Complex, Sulawesi, Indonesia. *Tectonophysics*, 712:600–622.

Hess, H. H. (1962). History of ocean basins. *Petrologic studies*.

Hestenes, M. R. (1969). Multiplier and gradient methods. *Journal of optimization theory and applications*, 4(5):303–320.

Hirth, G. and Kohlstedt, D. (2003). Rheology of the upper mantle and the mantle wedge: A view from the experimentalists. *Inside the subduction Factory*, pages 83–105.

Hirth, G. and Kohlstedt, D. L. (1996). Water in the oceanic upper mantle: implications for rheology, melt extraction and the evolution of the lithosphere. *Earth and Planetary Science Letters*, 144(1-2):93–108.

Holmes, A. (1931). Radioactivity and earth movements. *Nature*, 128(3229):496.

Huet, B., Le Pourhiet, L., Labrousse, L., Burov, E., and Jolivet, L. (2011). Formation of metamorphic core complex in inherited wedges: A thermomechanical modelling study. *Earth and Planetary Science Letters*, 309(3-4):249–257.

Hughes, T. (1987). *The finite element method: linear static and dynamic finite element analysis*. Englewood Cliffs: Prentice-Hall, 1st edition.

Huismans, R. and Beaumont, C. (2007). Roles of lithospheric strain softening and heterogeneity in determining the geometry of rifts and continental margins. *Geological Society, London, Special Publications*, 282(1):111–138.

Ingebritsen, S. and Manning, C. E. (1999). Geological implications of a permeability-depth curve for the continental crust. *Geology*, 27(12):1107–1110.

Jarvis, G. T. and McKenzie, D. P. (1980). Convection in a compressible fluid with infinite Prandtl number. *Journal of Fluid Mechanics*, 96(3):515–583.

Jeffreys, H. (1924). *The Earth: its origins, history and physical constitution*. University Press.

Kachanov, L. M. (1958). Time of the rupture process under creep conditions. *Nank SSR Otd Tech Nauk*, 8:26–31.

Karato, S.-i., Riedel, M. R., and Yuen, D. A. (2001). Rheological structure and deformation of subducted slabs in the mantle transition zone: implications for mantle circulation and deep earthquakes. *Physics of the Earth and Planetary Interiors*, 127(1):83–108.

Karato, S.-i. and Wu, P. (1993). Rheology of the upper mantle: A synthesis. *Science*, 260(5109):771–778.

Kaus, B. J. (2010). Factors that control the angle of shear bands in geodynamic numerical models of brittle deformation. *Tectonophysics*, 484(1-4):36–47.

Kern, H., Gao, S., and Liu, Q.-S. (1996). Seismic properties and densities of middle and lower crustal rocks exposed along the North China Geoscience Transect. *Earth and Planetary Science Letters*, 139(3-4):439–455.

King, S. D., Lee, C., Van Keken, P. E., Leng, W., Zhong, S., Tan, E., Tosi, N., and Kameyama, M. C. (2010). A community benchmark for 2-d cartesian compressible convection in the earth's mantle. *Geophysical Journal International*, 180(1):73–87.

Kronbichler, M., Heister, T., and Bangerth, W. (2012). High accuracy mantle convection simulation through modern numerical methods. *Geophysical Journal International*, 191(1):12–29.

Krotkiewski, M. and Dabrowski, M. (2013). MUTILS-a set of efficient modeling tools for multi-core CPUs implemented in MEX. In *EGU General Assembly Conference Abstracts*, volume 15.

Lavier, L. L. and Buck, W. R. (2002). Half graben versus large-offset low-angle normal fault: Importance of keeping cool during normal faulting. *Journal of Geophysical Research: Solid Earth*, 107(B6).

Lavier, L. L., Buck, W. R., and Poliakov, A. N. (2000). Factors controlling normal fault offset in an ideal brittle layer. *Journal of Geophysical Research: Solid Earth*, 105(B10):23431–23442.

Ledru, P., Courrioux, G., Dallain, C., Lardeaux, J., Montel, J., Vanderhaeghe, O., and Vitel, G. (2001). The Velay dome (French Massif Central): melt generation and granite emplacement during orogenic evolution. *Tectonophysics*, 342(3-4):207–237.

Lee Armstrong, R. and Ward, P. (1991). Evolving geographic patterns of Cenozoic magmatism in the North American Cordillera: The temporal and spatial association of magmatism and metamorphic core complexes. *Journal of Geophysical Research: Solid Earth*, 96(B8):13201–13224.

Lister, G. S. and Baldwin, S. L. (1993). Plutonism and the origin of metamorphic core complexes. *Geology*, 21(7):607–610.

Lister, G. S. and Davis, G. A. (1989). The origin of metamorphic core complexes and detachment faults formed during Tertiary continental extension in the northern Colorado River region, USA. *Journal of Structural Geology*, 11(1-2):65–94.

Liu, L., Morgan, J. P., Xu, Y., and Menzies, M. (2018). Craton destruction part i: Cratonic keel delamination along a weak mid-lithospheric discontinuity layer. *Journal of Geophysical Research: Solid Earth*.

López, S. and Castro, A. (2001). Determination of the fluid–absent solidus and supersolidus phase relationships of MORB-derived amphibolites in the range 4–14 kbar. *American Mineralogist*, 86(11-12):1396–1403.

Malkus, D. S. and Hughes, T. J. (1978). Mixed finite element methods—reduced and selective integration techniques: a unification of concepts. *Computer Methods in Applied Mechanics and Engineering*, 15(1):63–81.

Malvoisin, B., Brunet, F., Carlut, J., Rouméjon, S., and Cannat, M. (2012). Serpentinization of oceanic peridotites: 2. Kinetics and processes of San Carlos olivine hydrothermal alteration. *Journal of Geophysical Research: Solid Earth*, 117(B4).

Medhurst, T. P. (1997). *Estimation of the in situ strength and deformability of coal for engineering design*.

Miller, D. J. and Christensen, N. L. (1994). Seismic signature and geochemistry of an island arc: A multidisciplinary study of the Kohistan accreted terrane, northern Pakistan. *Journal of Geophysical Research: Solid Earth*, 99(B6):11623–11642.

Mises, R. v. (1913). Mechanik der festen Körper im plastisch-deformablen Zustand. *Nachrichten von der Gesellschaft der Wissenschaften zu Göttingen, Mathematisch-Physikalische Klasse*, 1913(4):582–592.

Mitrovica, J. and Forte, A. (2004). A new inference of mantle viscosity based upon joint inversion of convection and glacial isostatic adjustment data. *Earth and Planetary Science Letters*, 225(1-2):177–189.

Moresi, L., Dufour, F., and Mühlhaus, H.-B. (2003). A lagrangian integration point finite element method for large deformation modeling of viscoelastic geomaterials. *Journal of Computational Physics*, 184(2):476–497.

Moresi, L. and Mühlhaus, H.-B. (2006). Anisotropic viscous models of large-deformation Mohr–Coulomb failure. *Philosophical Magazine*, 86(21-22):3287–3305.

Morgan, W. J. (1968). Rises, trenches, great faults, and crustal blocks. *Journal of Geophysical Research*, 73(6):1959–1982.

Müller, R. D., Sdrolias, M., Gaina, C., and Roest, W. R. (2008). Age, spreading rates, and spreading asymmetry of the world's ocean crust. *Geochemistry, Geophysics, Geosystems*, 9(4).

Musacchio, G., Mooney, W. D., Luetgert, J. H., and Christensen, N. I. (1997). Composition of the crust in the Grenville and Appalachian Provinces of North America inferred from Vp/Vs ratios. *Journal of Geophysical Research: Solid Earth*, 102(B7):15225–15241.

Nielsen, T. K. and Hopper, J. R. (2004). From rift to drift: Mantle melting during continental breakup. *Geochemistry, Geophysics, Geosystems*, 5(7).

O'Hanley, D. S. (1992). Solution to the volume problem in serpentinization. *Geology*, 20(8):705–708.

Olive, J.-A., Behn, M. D., and Tucholke, B. E. (2010). The structure of oceanic core complexes controlled by the depth distribution of magma emplacement. *Nature Geoscience*, 3(7):491.

Oller, S., Botello, S., Miquel, J., and Oñate, E. (1995). An anisotropic elastoplastic model based on an isotropic formulation. *Engineering Computations*, 12(3):245–262.

Peltier, W. R. (1996). Mantle viscosity and ice-age ice sheet topography. *Science*, 273(5280):1359–1364.

Pérez-Gussinyé, M. and Reston, T. J. (2001). Rheological evolution during extension at nonvolcanic rifted margins: onset of serpentinization and development of detachments leading to continental breakup. *Journal of Geophysical Research: Solid Earth*, 106(B3):3961–3975.

Phipps Morgan, J. (2001a). The role of serpentinization and serpentinization in bending and unbending the subducting slab. *AGU*, 82:F1154.

Phipps Morgan, J. (2001b). Thermodynamics of pressure release melting of a veined plum pudding mantle. *Geochemistry, Geophysics, Geosystems*, 2(4).

Poirier, J.-P. (1985). *Creep of crystals: high-temperature deformation processes in metals, ceramics and minerals*. Cambridge University Press.

Poliakov, A. N., Herrmann, H. J., Podladchikov, Y. Y., and Roux, S. (1994). Fractal plastic shear bands. *Fractals*, 2(04):567–581.

Popov, A. A. and Sobolev, S. V. (2008). SLIM3D: A tool for three-dimensional thermomechanical modeling of lithospheric deformation with elasto-visco-plastic rheology. *Physics of the Earth and Planetary Interiors*, 171(1-4):55–75.

Powell, M. J. (1967). *A method for non-linear constraints in minimization problems*. UKAEA.

Pownall, J. (2015). UHT metamorphism on Seram, eastern Indonesia: reaction microstructures and P–T evolution of spinel-bearing garnet–sillimanite granulites from the Kobipoto Complex. *Journal of Metamorphic Geology*, 33(9):909–935.

Pownall, J., Hall, R., and Watkinson, I. (2013). Extreme extension across Seram and Ambon, eastern Indonesia: evidence for Banda slab rollback. *Solid Earth*, 4(2):277.

Pownall, J. M., Hall, R., Armstrong, R. A., and Forster, M. A. (2014). Earth's youngest known ultrahigh-temperature granulites discovered on Seram, eastern Indonesia. *Geology*, 42(4):279–282.

Ranero, C. R., Morgan, J. P., McIntosh, K., and Reichert, C. (2003). Bending-related faulting and mantle serpentinization at the middle america trench. *Nature*, 425(6956):367.

Ranero, C. R. and Reston, T. J. (1999). Detachment faulting at ocean core complexes. *Geology*, 27(11):983–986.

Rey, P., Teyssier, C., and Whitney, D. (2009a). Extension rates, crustal melting, and core complex dynamics. *Geology*, 37(5):391–394.

Rey, P., Teyssier, C., and Whitney, D. (2009b). The role of partial melting and extensional strain rates in the development of metamorphic core complexes. *Tectonophysics*, 477(3-4):135–144.

Ribacchi, R. (2000). Mechanical tests on pervasively jointed rock material: insight into rock mass behaviour. *Rock mechanics and rock engineering*, 33(4):243–266.

Rice, J. R. (1992). Fault stress states, pore pressure distributions, and the weakness of the San Andreas fault. In *International geophysics*, volume 51, pages 475–503. Elsevier.

Ridley, J. (1993). The relations between mean rock stress and fluid flow in the crust: with reference to vein-and lode-style gold deposits. *Ore Geology Reviews*, 8(1-2):23–37.

Rockafellar, R. T. (1974). Augmented Lagrange multiplier functions and duality in nonconvex programming. *SIAM Journal on Control*, 12(2):268–285.

Ros, E., Pérez-Gussinyé, M., Araújo, M., Thoaldo Romeiro, M., Andrés-Martínez, M., and Morgan, J. P. (2017). Lower crustal strength controls on melting and serpentinization at magma-poor margins: potential implications for the South Atlantic. *Geochemistry, Geophysics, Geosystems*.

Rudnicki, J. and Olsson, W. (1998). Reexamination of fault angles predicted by shear localization theory. *International Journal of Rock Mechanics and Mining Sciences*, 35(4-5):512–513.

Rüpke, L. H. and Hasenclever, J. (2017). Global rates of mantle serpentinization and h2 production at oceanic transform faults in 3-d geodynamic models. *Geophysical Research Letters*, 44(13):6726–6734.

Rüpke, L. H., Morgan, J. P., Hort, M., and Connolly, J. A. (2004). Serpentine and the subduction zone water cycle. *Earth and Planetary Science Letters*, 223(1-2):17–34.

Rüpke, L. H., Schmid, D. W., Perez-Gussinye, M., and Hartz, E. (2013). Interrelation between rifting, faulting, sedimentation, and mantle serpentinization during continental margin formation—including examples from the norwegian sea. *Geochemistry, Geophysics, Geosystems*, 14(10):4351–4369.

Rybacki, E. and Dresen, G. (2000). Dislocation and diffusion creep of synthetic anorthite aggregates. *Journal of Geophysical Research: Solid Earth*, 105(B11):26017–26036.

Schenker, F., Gerya, T., and Burg, J.-P. (2012). Bimodal behavior of extended continental lithosphere: Modeling insight and application to thermal history of migmatitic core complexes. *Tectonophysics*, 579:88–103.

Schmeling, H. (1989). Compressible convection with constant and variable viscosity: The effect on slab formation, geoid, and topography. *Journal of Geophysical Research: Solid Earth*, 94(B9):12463–12481.

Shewchuk, J. R. (1996). Triangle: Engineering a 2D quality mesh generator and Delaunay triangulator. In *Applied computational geometry towards geometric engineering*, pages 203–222. Springer.

Sibson, R. H. (1990). Conditions for fault-valve behaviour. *Geological Society, London, Special Publications*, 54(1):15–28.

Simo, J. and Ju, J. (1987). Strain-and stress-based continuum damage models—ii. computational aspects. *International journal of solids and structures*, 23(7):841–869.

Sobolev, S. V. and Babeyko, A. Y. (1994). Modeling of mineralogical composition, density and elastic wave velocities in anhydrous magmatic rocks. *Surveys in geophysics*, 15(5):515–544.

Spencer, J. E., Richard, S. M., Reynolds, S. J., Miller, R. J., Shafiqullah, M., Gilbert, W. G., and Grubensky, M. J. (1995). Spatial and temporal relationships between mid-Tertiary magmatism and extension in southwestern Arizona. *Journal of Geophysical Research: Solid Earth*, 100(B6):10321–10351.

Spiegelman, M., May, D. A., and Wilson, C. R. (2016). On the solvability of incompressible Stokes with viscoplastic rheologies in geodynamics. *Geochemistry, Geophysics, Geosystems*, 17(6):2213–2238.

Streit, J. E. (1997). Low frictional strength of upper crustal faults: a model. *Journal of Geophysical Research: Solid Earth*, 102(B11):24619–24626.

Tackley, P. J. (1996). Effects of strongly variable viscosity on three-dimensional compressible convection in planetary mantles. *Journal of Geophysical Research: Solid Earth*, 101(B2):3311–3332.

Taramón, J. M., Rodríguez-González, J., Negredo, A. M., and Billen, M. I. (2015). Influence of cratonic lithosphere on the formation and evolution of flat slabs: Insights from 3-D time-dependent modeling. *Geochemistry, Geophysics, Geosystems*, 16(9):2933–2948.

Taylor, F. B. (1910). Bearing of the Tertiary mountain belt on the origin of the Earth's plan. *Bulletin of the Geological Society of America*, 21(1):179–226.

Tetreault, J. and Buiter, S. (2017). The influence of extension rate and crustal rheology on the evolution of passive margins from rifting to break-up. *Tectonophysics*.

Tucholke, B. E., Behn, M. D., Buck, W. R., and Lin, J. (2008). Role of melt supply in oceanic detachment faulting and formation of megamullions. *Geology*, 36(6):455–458.

van der Wal, W., Whitehouse, P. L., and Schrama, E. J. (2015). Effect of GIA models with 3D composite mantle viscosity on GRACE mass balance estimates for Antarctica. *Earth and Planetary Science Letters*, 414:134–143.

Vermeer, P. A. and De Borst, R. (1984). Non-associated plasticity for soils, concrete and rock. *HERON, 29 (3), 1984*.

Warren, C., Beaumont, C., and Jamieson, R. A. (2008). Modelling tectonic styles and ultra-high pressure (UHP) rock exhumation during the transition from oceanic subduction to continental collision. *Earth and Planetary Science Letters*, 267(1-2):129–145.

Wegener, A. (1946). *The origin of continents and oceans*. New York: Dover Publications.

Whitney, D. L., Teyssier, C., Rey, P., and Buck, W. R. (2013). Continental and oceanic core complexes. *Bulletin*, 125(3-4):273–298.

Wilks, K. R. and Carter, N. L. (1990). Rheology of some continental lower crustal rocks. *Tectonophysics*, 182(1-2):57–77.

Zienkiewicz, O. (1985). Iterative method for constrained and mixed approximation. An inexpensive improvement of F.E.M. performance. *Computer Methods in Applied Mechanics and Engineering*, 51:3–29.

Zienkiewicz, O., Huang, M., and Pastor, M. (1995). Localization problems in plasticity using finite elements with adaptive remeshing. *International Journal for Numerical and Analytical Methods in Geomechanics*, 19(2):127–148.

Zienkiewicz, O. C. and Taylor, R. L. (2005). *The Finite Element Method for Solid and Structural Mechanics*. Elsevier, 6th edition.

A | Appendix

A.1 The Finite Element Method

The description of the FEM presented here is based on Hughes [1987]. I will adopt Einstein index notation (i.e. repeated indices indicates the sum: $u_{ii} = u_{11} + u_{22} + u_{33}$), and the following notation for partial derivatives:

$$u_{i,j} = \frac{\partial u_i}{\partial x_j} \tag{A.1}$$

so that $u_{i,j}$ denotes de derivative of the i-component of u respect to j. When appropriate, I will also use a compact matrix notation. Let us consider a simple 1D boundary problem described by the following PDE in the domain $\Omega = [0,1]$:

$$u_{,xx} + f(x) = 0 \tag{A.2}$$

with the following boundary conditions on the boundary Γ:

$$u(1) = g \quad on \quad \Gamma_d \tag{A.3}$$

and

$$-u_{,x}(0) = h \quad on \quad \Gamma_n \tag{A.4}$$

Eqs. (A.3) (A.4) are commonly known as *Dirichlet* and *Neumann boundary conditions*, respectively. Eq.(A.2) is known as the *strong form* of the problem. The FEM is based on solving the integral form of the given PDE, the so-called *weak form*. To build the weak form of eq. (A.2) we need to define a set of trial solutions $\mathscr{U}$ that satisfy eq. (A.2), and a set of weighting functions $\mathscr{W}$ that satisfy $w(1) = 0$:

$$\mathscr{U} = \{u | u \in H^1, u(1) = g\} \tag{A.5}$$

$$\mathscr{W} = \{w | w \in H^1, w(1) = 0\} \tag{A.6}$$

where H^1 means that the derivatives must be square-integrable. To obtain the weak form, the strong form is first pre-multiplied by the weighting functions and integrated over the domain:

$$\int_\Omega w u_{,xx} d\Omega + \int_\Omega w f d\Omega = 0 \tag{A.7}$$

Eq.(A.7) is then reduced by performing an integration by parts:

$$\int_\Omega w_{,x} u_{,x} d\Omega = \int_\Omega w f d\Omega + w(0)u_{,x}(0) - w(1)u_{,x}(1) \tag{A.8}$$

It shall be noted that Neumann boundary conditions (the new terms in the right-hand-side) appear in a natural way after integrating the weak form by parts. In this particular case we have:

$$w(0)u_{,x}(0) = w(0)h \tag{A.9}$$

$$w(1)u_{,x}(1) = 0 \tag{A.10}$$

Hence the weak form of eq.(A.2) yields:

$$\int_\Omega w_{,x}u_{,x}d\Omega = \int_\Omega wfd\Omega + w(0)h \tag{A.11}$$

The strong and weak forms are equivalent and have identical solutions. The latter is solved by approximating the trial solutions and the weighting functions as a set of functions multiplied by unknown parameters a_n and b_n:

$$u(x) \approx \widetilde{u}(x) = \sum_{n=1}^{d} \phi_n a_n + g\phi_{n+1} \tag{A.12}$$

$$w(x) \approx \widetilde{w}(x) = \sum_{m=1}^{d} \psi_m b_m \tag{A.13}$$

where $n = 1,2,...,d$, d is the number of unknowns in the problem, the functions ϕ_n and ψ_n (often referred as *shape functions*) are assumed to be zero at all locations where the boundary conditions are prescribed, and the term $g\phi_{n+1}$ must satisfy the boundary conditions. Different choices for the functions ϕ_n and ψ_m exist. However, throughout all this study the Galerkin method [Galerkin, 1915] is employed; therefore $\phi_n = \psi_n$. The advantage of this method is that it usually leads to symmetric matrices. To simplify the notation, I adopt the standard symbol of the shape functions $N_n = \phi_n = \psi_n$. The approximate Galerkin solution of the weak form is obtained substituting eqs. (A.12) and (A.13) into eq. (A.11):

$$\int_\Omega \sum_{n=1}^{d} N_{m,x}b_m \sum_{n=1}^{d} N_{n,x}a_n d\Omega = \int_\Omega \sum_{m=1}^{d} N_n b_m f d\Omega + \sum_{m=1}^{d} N_n b_m(0)h - \int_\Omega \sum_{m=1}^{d} b_m N_{n,x} g N_{n+1} \tag{A.14}$$

Using the bilinearity of the integrals in A.11, the problem is rewritten as:

$$0 = \sum_{m=1}^{d} b_m G_m \tag{A.15}$$

with

$$G_m = \sum_{n=1}^{d} \int_\Omega N_{m,x}N_{n,x}a_n d\Omega - \int_\Omega N_n f d\Omega - N_n b_m(0)h + \int_\Omega N_{n,x} g N_{n+1} d\Omega \tag{A.16}$$

Eq. (A.15) must hold for all the weighting functions $w \in \mathscr{W}$. Given the arbitrariness of the coefficients b_n, it is necessary that each G_m, with $m = 1,2,...,d$, is equal to zero. Thus the weak form becomes:

$$\sum_{n=1}^{d} \int_\Omega N_{m,x}N_{n,x}a_n d\Omega = \int_\Omega N_n f d\Omega + N_n b_m(0)h - \int_\Omega N_{n,x} g N_{n+1} d\Omega \tag{A.17}$$

Finally, the original strong form has been reduced to a set of d ordinary differential equations (A.17) that can be expressed as:

$$\sum_{n=1}^{d} K_{mn}a_n = f_m \tag{A.18}$$

$$\tag{A.19}$$

where

$$K_{mn} = \int_{\Omega} N_{m,x} N_{n,x} d\Omega \tag{A.20}$$

$$f_m = \int_{\Omega} N_n f d\Omega + N_n b_m(0) h - \int_{\Omega} N_{n,x} g N_{n+1} d\Omega \tag{A.21}$$

or using a compact matrix notation:

$$\mathbf{Ka} = \mathbf{f} \tag{A.22}$$

The physical interpretation of the matrix $\mathbf{K}$ and the vector $\mathbf{f}$ depends on the nature of the problem described by the set of PDEs. For instance, in elasticity or viscous flow problems, $\mathbf{K}$ is the so-called stiffness matrix and $\mathbf{f}$ is the force vector; for thermal advection and diffusion, $\mathbf{K}$ is the conductivity matrix and $\mathbf{f}$ is the heat flow vector; and $\mathbf{K}$ is the permeability matrix in porous flow problems.

The parameters a_n are obtained solving the linear system of equations in (A.22). Once a_n is obtained, u can be calculated at any point $x \in \Omega$:

$$u(x) = \sum_{n=1}^{d} N(x)_n a_n \tag{A.23}$$

A convenient way to approximate N consists in constructing a *mesh* formed by set of discrete points that subdivide the domain Ω. These points are called *nodes* and each one of the nodes is connected to the neighbouring nodes, defining the so-called *elements*. These elements may have different shapes, and the appropriateness of a specific shape is ultimately determined by the nature of the problem. Each shape function is defined so that $N_n = 1$ at the node n and $N_m = 0$ at the nodes $n \neq m$. Common elements shapes are one dimensional bars for 1D problems; triangles and quadrilaterals for 2D problems; and tetrahedron and hexahedrons for 3D problems. The accuracy of the solution obtained with the FEM depends on the number and spatial distribution of the nodes of the mesh and the definition of the shape functions.

The number of nodes in an element defines the polynomial order of the shape functions. For example, a 2D triangular element with 3 nodes has linear shape functions that are constructed from piecewise linear approximations. If one needed N to be quadratic, the 2D triangular element requires of 6 nodes. The choice of the polynomial order of N is not trivial and depends on the physical problem described by the PDE. To obtain an accurate FEM solution, the order of N should be equal or higher than the order of the partial derivatives of the PDE.

A.2 Weak formulation of the Stokes equations

A.2.1 Thermal diffusion

The Lagrangian time-dependent diffusion equation in a domain Ω is defined by the following boundary problem:

$$\rho C_p \frac{DT}{Dt} = \kappa \nabla^2 T + Q \tag{A.24}$$

with the boundary conditions

$$T = g \qquad \text{on } \Gamma_D \tag{A.25}$$

$$-\mathbf{n}\kappa T = q \qquad \text{on } \Gamma_N \tag{A.26}$$

where n is the unit outward normal vector to the boundary Γ and q is the heat flux. As described in Section A.1, to obtain the weak forms we first need to pre-multiply eq. (A.24) by the weighting function and integrate over the Ω:

$$\int_\Omega w\rho C_p \frac{DT}{Dt} d\Omega = \int_\Omega w\kappa\nabla^2 T d\Omega + \int_\Omega wQ d\Omega \tag{A.27}$$

The temperature field is then approximated as a linear combination of the shape functions and unknown parameters:

$$T \approx \sum_{n=1}^{d} N_n \widetilde{T}_n \tag{A.28}$$

Employing the Galerkin method, the strong form of eq. (A.27) yields:

$$\int_\Omega \mathbf{N}\rho C_p \frac{D(\mathbf{N}\widetilde{T})}{Dt} d\Omega = \int_\Omega \mathbf{N}^T \kappa\nabla^2(\mathbf{N}\widetilde{T}) d\Omega + \int_\Omega \mathbf{N}Q d\Omega \tag{A.29}$$

Eq. (A.29) is integrated by parts to reduce the order of the second derivatives:

$$\int_\Omega \mathbf{N}\rho C_p \frac{D(\mathbf{N}\widetilde{T})}{Dt} d\Omega = -\int_\Omega (\nabla\,\mathbf{N}^T)\kappa(\nabla\mathbf{N}\widetilde{T}) d\Omega + \int_\Omega \nabla(\mathbf{N}^T\kappa\nabla N\widetilde{T}) d\Omega + \int_\Omega NQ d\Omega \tag{A.30}$$

and using the divergence theorem we finally obtain the strong form of the equation of heat diffusion:

$$\int_\Omega \mathbf{N}\rho C_p \frac{D(\mathbf{N}\widetilde{T})}{Dt} d\Omega + \int_\Omega (\nabla\mathbf{N}^T)\kappa(\nabla N\widetilde{T}) d\Omega = \int_\Omega \mathbf{N}Q d\Omega - \int_{\Gamma_N} \mathbf{N}q d\Gamma_N \tag{A.31}$$

A.2.2 Conservation of momentum and conservation of mass

The resulting set of governing equations of the problem is solved numerically using the FEM to generate a system of linear equations. The governing equations (A.48) and (A.49) are transformed into their weak forms with help of the trial solutions and weighting functions. As explained previously in this chapter, the first step consists in integrating the Stokes equations over the domain Ω and pre-multiplying them by two sets of weighting functions: w for the velocity field; and q for the pressure. For the conservation of momentum, that is:

$$\int_\Omega w\tau_{ij,j} d\Omega - \int_\Omega q p_{,j} d\Omega = -\int_\Omega w\rho g_i d\Omega \tag{A.32}$$

Integrating (A.32) by parts we obtain:

$$\int_\Omega (w\tau_{ij})_{,j} d\Omega - \int_\Omega w_{,j}\tau_{ij,j} d\Omega + \int_\Omega q_{,j} p d\Omega = -\int_\Omega w\rho g_i d\Omega \tag{A.33}$$

The primary variables u and p are then approximated using the shape functions N_u for the velocity field and N_p for pressure:

$$u(x,y) \approx \sum_{n=1}^{d} N_u^n(x,y)\widetilde{u}_n \tag{A.34}$$

$$p(x,y) \approx \sum_{n=1}^{d} N_p^n(x,y)\widetilde{p}_n \tag{A.35}$$

where the subindex n is the nodal index and nn is the number of nodes in the element and $\widetilde{u}_n$ and $\widetilde{p}_n$ are the trial solutions of velocity and pressure, respectively. Employing the Galerkin procedure, the governing

equations (2.16) and (2.17) are transformed into their weak forms using the shape functions as trial functions. Substituting the Galerkin approximations of the primary fields (A.34) and (A.35) into the corresponding weak forms, and following the same procedure as in the thermal diffusion problem, we obtain:

$$\int_\Omega N_{u,j}\left(2\eta\left[\dot{\varepsilon}_{ij}-\frac{1}{3}\dot{\varepsilon}_{kk}\delta_{ij}\right]\right)d\Omega-\int_\Omega N_{p,j}p d\Omega= \int_\Omega N_u\rho g_i d\Omega-\int_\Omega N_{u,j}\chi\widehat{\tau}_{ij}d\Omega+\int_{\Gamma_N}N_u n_i t d\Gamma \tag{A.36}$$

$$\int_\Omega N_p u_{i,i}d\Omega=0 \tag{A.37}$$

or

$$\int_\Omega(\nabla\mathbf{N}_u)^T\left(2\eta\left[\dot{\varepsilon}-\frac{1}{3}tr(\dot{\varepsilon})\mathbf{I}\right]\right)d\Omega-\int_\Omega\nabla\mathbf{N}_p\,\mathbf{p}d\Omega= \int_\omega\mathbf{N}_u\rho\mathbf{g}d\Omega-\int_\Omega\nabla\mathbf{N}_u\chi\widehat{\tau}d\Omega+\int_{\Gamma_N}\mathbf{N}_u\mathbf{n}t d\Gamma \tag{A.38}$$

$$\int_\Omega\mathbf{N}_p\nabla\mathbf{u}d\Omega \tag{A.39}$$

A.3 Mathematical description of a visco-elastic flow

The deformation of lower mantle material is dominated by viscous flow, whereas lithospheric and upper mantle materials have a non-negligible contribution of elastic stresses. Elastic deformation is incorporated by employing a Maxwell material model, where the deviatoric strain rate is the summation of the viscous and elastic strain rates:

$$\dot{\varepsilon}'_{ij}=\dot{\varepsilon}'^{(viscous)}_{ij}+\dot{\varepsilon}'^{(elastic)}_{ij}=\frac{\tau_{ij}}{2\eta}+\frac{1}{2G}\frac{D\tau_{ij}}{Dt} \tag{A.40}$$

where G is the shear modulus and $D\tau_{ij}/Dt$ is the objective deviatoric stress rate. The Zaremba-Jaumann derivative (e.g. Hashiguchi and Yamakawa [2012]) is used to compute the objective deviatoric stress rate in eq. (A.40):

$$\frac{D\tau_{ij}}{Dt}=\frac{\partial\tau_{ij}}{\partial t}+u_k\tau_{ij,k}-\omega_{ik}\tau_{kj}+\tau_{ik}\omega_{kj} \tag{A.41}$$

where the spin tensor ω_{ij} is the skew-symmetric part of the velocity gradient tensor:

$$\omega_{ij}=\frac{1}{2}\left(u_{i,j}-u_{j,i}\right) \tag{A.42}$$

Because a Lagrangian formulation is used, the advection term $u_k\tau_{ij,k}$ in the right-hand-side of eq. (A.41) vanishes. Following the implementation of large-strain elastic deformation described by Moresi et al. [2003] and Kaus [2010], eq. (A.41) is approximated in an implicit manner:

$$\frac{D\tau_{ij}}{Dt}\approx\frac{\tau^{n+1}_{ij}-\tau^{n}_{ij}}{\Delta t}+\tau^{rot}_{ij} \tag{A.43}$$

where $\tau^{rot}_{ij}=-\omega^n_{ik}\tau^n_{kj}+\tau^n_{ik}\omega^n_{kj}$ are the terms of eq. (A.43) associated with rotation of the stress field, and the superscript n denotes the time step. Substitution of eq. (A.43) into eq. (A.40) followed by the rearrangement of its terms leads to the visco-elastic constitutive law:

$$\tau_{ij}=2\eta_{eff}\left(\dot{\varepsilon}_{ij}-\frac{1}{3}\dot{\varepsilon}_{kk}\delta_{ij}\right)+\chi\widehat{\tau}_{ij} \tag{A.44}$$

where

$$\eta_{eff} = \frac{1}{\frac{1}{\eta} + \frac{1}{G\Delta t}} \tag{A.45}$$

$$\chi = \frac{1}{1 + \frac{G\Delta t}{\eta}} \tag{A.46}$$

$$\widehat{\tau}_{ij} = \tau_{ij}^n + (\omega_{ik}^n \tau_{kj}^n - \tau_{ik}^n \omega_{kj}^n)\Delta t \tag{A.47}$$

Here η_{eff} is the effective viscosity and Δt is the time step. A pure viscous rheology is recovered if $\Delta t \to \infty$. Note that the visco-elastic deformation obtained per time step depends on the time step size. However, the deformation after a certain simulation time has to be independent of the chosen time step. The Stokes flow problem for a visco-elastic fluid in Ω is determined by:

$$\tau_{ij,j} - p_{,j} = -\rho g_i \tag{A.48}$$

$$u_{i,i} = 0 \tag{A.49}$$

and the boundary conditions

$$u_i = h_i \qquad \text{on } \Gamma_D \tag{A.50}$$

$$\sigma_{ij} n_j = t_i \qquad \text{on } \Gamma_N \tag{A.51}$$

Now we can substitute eq. (A.44) in eq. (A.48) and obtain the following expressions for the x axis:

$$2\eta_{eff}\left(\dot{\varepsilon}_{xx} - \frac{1}{3}\dot{\varepsilon}_{kk}\delta_{ij}\right)_{,x} + \left(2\eta_{eff}\dot{\varepsilon}_{xz}\right)_{,z} - p_{,x} = -\chi\left(\widehat{\tau}_{xx,x} + \widehat{\tau}_{xz,z}\right) \tag{A.52}$$

and for the z axis:

$$2\eta_{eff}\left(\dot{\varepsilon}_{zz} - \frac{1}{3}\dot{\varepsilon}_{kk}\delta_{ij}\right)_{,z} + \left(2\eta_{eff}\dot{\varepsilon}_{zx}\right)_{,x} - p_{,z} = -\chi\left(\widehat{\tau}_{xz,x} + \widehat{\tau}_{zz,z} - \frac{1}{3}\dot{\varepsilon}_{kk,z}\widehat{\tau}_{zz,z}\right) - \rho g_z \tag{A.53}$$

and using the definition of the strain tensor we obtain the strong forms of the conservation of momentum:

$$\eta_{eff}\left(\frac{4}{3}u_{x,x} - \frac{2}{3}u_{z,z}\right)_{,x} + \eta_{eff}\left(u_{x,z} + u_{z,x}\right)_{,z} - p_{,x} = -\chi\left(\widehat{\tau}_{xx,x} + \widehat{\tau}_{xz,z}\right) \tag{A.54}$$

for the x axis, and:

$$\eta_{eff}\left(\frac{4}{3}u_{z,z} - \frac{2}{3}u_{x,x}\right)_{,z} + \eta_{eff}\left(u_{x,z} + u_{z,x}\right)_{,z} - p_{,z} = -\chi\left(\widehat{\tau}_{zx,x} + \widehat{\tau}_{zz,z}\right) - \rho g_z \tag{A.55}$$

for the z axis. Eqs.(A.54) and (A.55) are then transformed into weak form and solved using the FEM. Note that the visco-elastic Stokes problem is very similar to a purely viscous Stokes flow. The main difference lay in the substraction of the rotated stress from the previous time step in the right-hand-side of the momentum equation. The "purely viscous" viscosity is also substituted by new effective viscosity that averages the resistance of the material to viscous and elastic strain. and using the divergence theorem:

$$\int_\Omega w_{,j}\tau_{ij}d\Omega - \int_\Omega q_{,j}pd\Omega = \int_\Omega w\rho g_i d\Omega + \int_{\Gamma_N} w\tau_{ij}n_j d\Gamma \tag{A.56}$$

The weak form of the incompressible constraint is:

$$\int_\Omega q u_{i,i} d\Omega = 0 \tag{A.57}$$

The variational form of the visco-elastic Stokes flow is then described as follows:

$$\int_\Omega w_{,j}\tau_{ij}d\Omega - \int_\Omega q_{,j}p d\Omega - \int_\Omega q u_{i,i}d\Omega = \int_\Omega w\rho g_i d\Omega + \int_{\Gamma_N} w t_i d\Gamma \tag{A.58}$$

Using the constitutive relationship (A.44), eq. (A.58) yields:

$$\overbrace{\int_\Omega w_{,j}\left(2\eta\left[\dot{\varepsilon}_{ij} - \frac{1}{3}\dot{\varepsilon}_{kk}\delta_{ij}\right]\right)d\Omega}^{\text{stress-strain relationship}} - \overbrace{\int_\Omega q_{,j}p d\Omega}^{\text{pressure}} - \overbrace{\int_\Omega q u_{i,i}d\Omega}^{\text{incompressibility constrain}} = \underbrace{\int_\Omega w\rho g_i d\Omega}_{\text{buoyancy forces}} - \underbrace{\int_\Omega w_{,j}\chi\widehat{\tau}_{ij}d\Omega}_{\text{rotated stresses}} + \underbrace{\int_{\Gamma_N} w t_i d\Gamma}_{\text{Neumann BC}} \tag{A.59}$$